
SEARCHES FOR
COLOURED SUSY
WITH ATLAS
AT √s = 8 TeV, 13 TeV, AND 14 TeV
Ingrid Deigaard

Searches for Coloured Supersymmetry with ATLAS at $\sqrt{s} = 8$ TeV, 13 TeV, and 14 TeV

Ingrid Deigaard

Searches for Coloured Supersymmetry with ATLAS at $\sqrt{s} = 8$ TeV, 13 TeV, and 14 TeV

academisch proefschrift

ter verkrijging van de graad van doctor
aan de Universiteit van Amsterdam
op gezag van de Rector Magnificus
prof. dr. ir. K.I.J.Maex
ten overstaan van een door het College voor Promoties ingestelde commissie,
in het openbaar te verdedigen in de Agnietenkapel
op woensdag 30 november 2016, te 10:00 uur

door

Ingrid Deigaard

geboren te Hørsholm, Denemarken

PROMOTOR	prof. dr. ir. P.J. de Jong (Universiteit van Amsterdam)
COPROMOTOR	dr. M. Vranjes Milosavljevic (Univerzitet u Beogradu)
OVERIGE LEDEN	prof. dr. E.L.M.P. Laenen (Universiteit van Amsterdam)
	prof. dr. P.M. Kooijman (Universiteit van Amsterdam)
	prof. dr. O.B. Igonkina (Radboud Universiteit Nijmegen)
	prof. dr. M.H.M. Merk (Vrije Universiteit Amsterdam)
	dr. D. Berge (Universiteit van Amsterdam)
	dr. I.B. van Vulpen (Universiteit van Amsterdam)
	dr. S. Caron (Radboud Universiteit Nijmegen)

Faculteit der Natuurwetenschappen, Wiskunde en Informatica

Searches for Coloured Supersymmetry with ATLAS at $\sqrt{s} = 8$ TeV, 13 TeV, and 14 TeV

ISBN 978·94·6233·452·6

Set in 9/12 pt using pdfLaTeX
Cover design by Buro Brouns
Printed in the Netherlands by Gildeprint

This work is part of the research programme of the *Stichting voor Fundamenteel Onderzoek der Materie* (FOM), which is financially supported by the *Nederlandse Organisatie voor Wetenschappelijk Onderzoek* (NWO). It was carried out at the *Nationaal Instituut voor Subatomaire Fysica* (Nikhef) in Amsterdam, the Netherlands. The research has been supported financially by a FOM-Projectruimte grant titled "Mind the gap! Generalizing dark matter searches at the LHC" of prof. dr. ir. P.J. de Jong.

Hele Verden er en Række af Underværker,
men vi ere saa vante til dem, at vi kalde dem Hverdagsting.

— H. C. Andersen, *Marionetspilleren*

Contents

Introduction

What are the fundamental building blocks of Nature and which laws govern their interactions? A theory which can answer this question is one of the primary goals of modern, theoretical physics.

The Standard Model of particle physics is an attempt to answer the question. At energy scales accessible to current experiments, it is very successful. With the discovery of the Higgs boson,the Standard Model is complete. However, it falls short: it does not describe all four fundamental forces. While it successfully provides a description of the electromagnetic, weak, and strong forces, the fourth force, gravity, cannot be included in the theory. Other things are left unexplained by the Standard Model as well: For example if observations have shown that only 5% of the matter in the Universe can be explained by the particles of the Standard Model what is then the origin of the remaining 95% referred to as Dark Energy and Dark Matter?

The Standard Model is based on symmetries. Global space-time symmetries ensure conservation of energy and momentum, while local gauge symmetries dictate the interactions of the elementary particles through force carrying vector bosons. It is possible to extend the symmetries of the Standard Model with an entire new type of symmetry: supersymmetry which is a symmetry between the two types of particles, fermions and bosons. Supersymmetry predicts a fermionic partner for each boson in the Standard Model and vice versa and thereby doubles the particle content of the Standard Model. Supersymmetry provides a possible answer to some of the previously described shortcomings of the Standard Model.

If supersymmetry would be an exact symmetry at our energy scale, then the masses of the supersymmetric particles would be identical to the masses of their Standard Model partners. As the supersymmetric partners have not been observed, supersymmetry must be broken at a higher energy scale. This results in heavier masses of the supersymmetric particles. The exact masses are determined by some of the 105 additional free parameters introduced by the symmetry breaking in the minimal supersymmetric extension of the Standard Model as the nature of the breaking mechanism is unknown.

The search for direct production of supersymmetric particles in particle collisions has been ongoing for decades. Throughout the years many experiments at different particle colliders have looked in vain for hints of supersymmetry: in the 1980's at the Super Proton Synchroton, a proton-antiproton collider located at the european research centre for particle physics, CERN, in the 1990's

at the Large Electron-Positron collider also located at CERN, and in the 2000's at the Tevatron, a proton-antiproton collider located at the american particle physics laboratory, Fermilab.

The newest and most powerful particle accelerator and collider is the Large Hadron Collider, LHC, located at CERN. It is designed to collide protons at a centre-of-mass energy of $\sqrt{s} = 14$ TeV. The protons collide at four interaction points where large detectors are located to record the results of the collisions. One of the detectors is the ATLAS detector which is designed to measure properties of the Standard Model and search for physics beyond the Standard Model such as supersymmetry.

The LHC began its operation in 2009 with proton-proton collisions at a centre-of-mass energy of $\sqrt{s} = 7$ TeV. The collision energy was increased to $\sqrt{s} = 8$ TeV in 2012 and the end of that year marked the end of a successful first run of the LHC with a dataset of 20.3 fb^{-1} collected by the ATLAS experiment. After a scheduled shutdown of two years, the LHC resumed proton collisions in 2015 at an even higher energy, $\sqrt{s} = 13$ TeV, and 3.2 fb^{-1} had been collected by the ATLAS experiment by the end of the year. The LHC is foreseen to run for many years ahead providing in total 300 fb^{-1} of proton collisions at $\sqrt{s} = 14$ TeV. With an upgrade of the LHC to the High-Luminosity LHC, HL-LHC, by 2026, the size of the dataset will increase to 3000 fb^{-1}.

With its high energy proton collisions and large datasets, the LHC provides a great opportunity to search for supersymmetry as it opens up sensitivity to yet unexplored parts of the supersymmetric phase space.

The hunt for supersymmetry at the LHC has begun...

Outline of the Thesis and the Author's Contribution

This thesis is divided into 8 chapters and this introduction. In the following the content of the chapters and the contribution from the author are stated.

Chapter 1 provides an overview of the Standard Model of particle physics and its shortcomings. Supersymmetry is introduced and it is discussed how it provides a solution to the shortcomings of the Standard Model. A summary of the current constraints of supersymmetry is given.

Chapter 2 gives an overview of the Large Hadron Collider and the ATLAS experiment that collected the data used in the analyses presented in this thesis. The performance of the Large Hadron collider and the ATLAS experiment is summarised. I have contributed in the trigger group through efficiency studies of jet triggers and by contributing to the simulation of the LITOPO triggers introduced in Run-2. This work is not included in this thesis.

Chapter 3 provides a description of the reconstruction and identification of particles in the datasets collected by the ATLAS experiment.

Chapter 4 contains a description of the method used to obtain the results of the analyses presented in this thesis. The concept of signal, control, and validation regions as well as the statistical methods used to obtain the background estimate and place limits are introduced.

Chapter 5 describes a search for squarks and gluinos in events with jets and missing transverse momentum in a dataset collected at $\sqrt{s} = 8$ TeV. The results of the analysis are published in Refs. [1, 2]. I studied the sensitivity to a pMSSM model with left-handed squark-pair production. I worked on the generation of the signal samples, the inclusion of two additional signal regions optimised for the pMSSM model, the background-fit and model independent limits in the new signal regions, and finally the exclusion limits on the pMSSM model using all 17 signal regions of the analysis.

Chapter 6 provides a description of a search for squarks and gluinos with data collected in 2015 at $\sqrt{s} = 13$ TeV published in Ref. [3]. The search is very similar to the analysis presented in Chapter 5. I worked on the calculation of the signal cross section, optimisation of a signal region targeting a small mass difference between the lightest neutralino and the squark or gluino, and producing the final plots for the paper.

Chapter 7 presents a prospect study of searches for squarks and gluinos with the full dataset of an upgraded LHC, the High-Luminosity LHC. The results are published in Ref. [4].

Chapter 8 contains concluding remarks on the results presented in previous chapters and an overview of the status of supersymmetry after the entire first run and the beginning of the second run of the LHC.

1

The Standard Model and Supersymmetry

The theory of particle physics is the theory of the smallest constituents of the Universe, the elementary particles, and their interactions. It is described by the Standard Model (SM), a theory developed through decades in the 20th century. The Standard model has been a great success with precise predictions agreeing well with experimental observations at all energy scales explored so far. However, the Standard Model has limitations, thus the need of a new theory at a higher energy-scale is inevitable. One group of extensions of the Standard Model is Supersymmetric (SUSY) theories.

This chapter will give a short introduction to the Standard Model, a discussion of its shortcomings, and introduce SUSY as a possible solution to the questions posed by the Standard Model.

1.1 The Standard Model

The Standard Model [5–11] is a relativistic quantum field theory. It is based on symmetry assumptions and its interactions arise on requiring gauge invariance based on the $SU(3)_C \times SU(2)_L \times U(1)_Y$ symmetry group.

1.1.1 Particle content of the Standard Model

The Standard model describes the matter particles, fermions, and their interactions through exchange of force carrying particles, vector bosons. Three of the four fundamental forces are described by the Standard Model - the electromagnetic force, the weak force, and the strong force - and each force is mediated by a single or several gauge bosons. A description of the fourth fundamental force, gravity, is not included.

The matter particles are divided into two groups, leptons and quarks. The leptons interact through the electromagnetic and weak forces, while the quarks carry colour-charge and are thus interacting through the strong force as well. Quarks are never observed freely, but appear in colourless, bound states called hadrons. The hadrons are divided into mesons composed of a $q\bar{q}$-pair and baryons consisting of $qqq/\bar{q}\bar{q}\bar{q}$-triplets. The quarks and leptons are divided into three

	Leptons				Quarks			
	Particle		Mass [MeV]	Q [e]	Particle		Mass [MeV]	Q [e]
1st Generation	electron	e	0.511	−1	up	u	~ 3	+2/3
	electron neutrino	ν_e	$< 2 \cdot 10^{-6}$	0	down	d	~ 5	-1/3
2nd Generation	muon	μ	106	−1	charm	c	~ 100	+2/3
	muon neutrino	ν_μ	< 0.19	0	strange	s	$\sim 1.3 \cdot 10^3$	-1/3
3rd Generation	tau	τ	1777	−1	top	t	$173 \cdot 10^3$	+2/3
	tau neutrino	ν_τ	< 18.2	0	bottom	b	$\sim 4.2 \cdot 10^3$	-1/3

Table 1.1 · The matter particles of the Standard Model, their masses, and their electrical charges (Q). The numbers are taken from Ref. [12]

families of identical quantum numbers, but with different masses. The first family consists of the electron (e), the electron-neutrino (ν_e), and the up (u) and down (d) quark forming the proton (p) and the neutron (n), thus accounting for the stable, visible matter in the Universe. The particles of the second and third family are unstable and will decay. A summary of the quantum numbers of quarks and leptons can be seen in Table 1.1.

The four types of force carrying particles are the photon, γ, the massive $W^\pm$ and Z bosons, and the gluon, g. The photon is responsible for the electromagnetic force and couples only to charged particles. The weak force is mediated by the $W^\pm$ and the Z bosons which couple to all matter particles. The gluon is the carrier of the strong force and couples only to particles that carry colour-charge including itself. There are eight gluons with different combinations of colour charges. The quantum numbers of the vector bosons can be seen in Table 1.2.

In order for the $W^\pm$ and Z boson to be massive, a scalar particle, the Higgs boson, is introduced. The Higgs boson couples only to massive particles with a coupling strength depending on the mass of the other particle. The search for the Higgs boson has taken years, but in 2012 a discovery of a new particle was announced by experiments at the Large Hadron Collider at CERN [13, 14]. Properties of the newly discovered particle, including its mass of 125.09 ± 0.24 GeV [15], has been measured to be in agreement with a Higgs boson. The quantum numbers of the Higgs boson can be found in Table 1.2.

1.1.2 Symmetries of the Standard Model

Symmetries have played a major role in the description of modern particle physics. It is the fundament on which the Standard Model is built.

A theory is said to be symmetric if the Lagrangian describing the system is left invariant by a transformation. Symmetries are described by transformation groups such as the group of

Particle Name		EM Charge [e]	Weak Charge (Isospin)	Strong Charge (Color)	Mass [MeV]
photon	γ	0	no	no	0
Z boson	Z^0	0	yes	no	$91.188 \cdot 10^3$
W boson	$W^\pm$	± 1	yes	no	$80.4 \cdot 10^3$
gluon	g	0	no	yes	0
Higgs	H^0	0	yes	no	$125.09 \cdot 10^3$

Table 1.2 · The force particles and the Higgs boson of the Standard Model and their charges. The numbers are taken from Ref. [12], except for the mass of the Higgs boson which is taken from Ref. [15].

rotations or the group of translations. If the symmetry is continuous, Noether's theorem states that a corresponding conserved current, $j^\mu(x)$, will exist fulfilling [16]

$$\partial_\mu j^\mu(x) = 0. \tag{1.1}$$

Equation 1.1 implies that the zero-component integral over a large space will be constant. This is known as the constant charge, Q, of the current. For example, the symmetry charge of rotational symmetries is the angular momentum.

External and Internal Symmetries

The Standard Model is built on symmetries, global and local, discrete and continuous. The symmetries of the Standard Model can be divided into two categories, external and internal symmetries.

External Symmetries

The external symmetries of the Standard Model are related to spacetime transformations. There are two groups of symmetries, the discrete symmetries such as charge conjugation C, parity P, and time reversal T, and the continuous symmetries of the Poincaré group.

The Standard Model is invariant under the combination of the three discrete symmetries C, P, and T. However, the SM is not invariant under any of the discrete symmetries separately.

The Poincaré symmetry group consists of the Lorentz transformations, rotations and boosts, combined with translations. By requiring invariance under the Poincaré group, the fields that enter the Lagrangian must transform as tensors under the Poincaré transformations. This is why fields as scalars, spinors, vectors, etc. are the constituents of the Lagrangian.

Internal Symmetries

Internal symmetries originate from multiple fields in the Lagrangian appearing in a symmetric fashion. Considering a Lagrangian for two Klein-Gordon scalars, ϕ_1 and ϕ_2,

$$\mathcal{L} = \tfrac{1}{2}\partial_\mu\phi_1(x)\partial^\mu\phi_1(x) + \tfrac{1}{2}\partial_\mu\phi_2(x)\partial^\mu\phi_2(x) - \frac{m^2}{2}\left(\phi_1(x)\right)^2 - \frac{m^2}{2}\left(\phi_2(x)\right)^2, \tag{1.2}$$

it is seen that the fields appear symmetric. The Lagrangian is invariant under a mixing of the two fields by

$$\begin{aligned}\phi_1 &\to \phi_1' = \cos\alpha\phi_1 + \sin\alpha\phi_2 \\ \phi_2 &\to \phi_2' = \cos\alpha\phi_2 - \sin\alpha\phi_1.\end{aligned} \tag{1.3}$$

Such a transformation of two fields leaving the Lagrangian invariant is an internal symmetry.

The internal symmetries of the Standard Model are the global symmetries of flavour and isospin as well as the (local) gauge symmetries, $U(1)_Y$ of hypercharge and $SU(2)$ of weak interactions joining together to form the electroweak interactions, and $SU(3)$ of the strong force.

Internal symmetries commute with the generators of the Poincaré group leading to the conclusion that all particles related through an internal symmetry must have the same mass and spin.

1.1.3 The Electroweak Theory and Spontaneous Symmetry Breaking

The electroweak (EW) theory is the unification of the electromagnetic and weak forces. The theory of the EW unification was described by Glashow, Salam, and Weinberg for which they were awarded the Nobel Prize in 1979 [5–7]. With the discovery of the massive $W^{\pm}$ and Z bosons in 1983 [17–20], the EW theory consolidated itself.

The electroweak theory is invariant under $SU(2)_T \times U(1)_Y$ gauge transformations where T is the weak isospin and Y is the weak hypercharge. $SU(2)_T \times U(1)_Y$ is spontaneously broken into $U(1)_{\text{em}}$ in order for the gauge bosons of the weak interaction, Z and W, to be massive.

Fermion Fields

The gauge bosons of the weak force couple with different strength to left-handed and right-handed particles. The left- and right-handed components of a four component bi-spinor, ψ can be obtained by the projection operators P_L and P_R, respectively:

$$\psi_L = P_L\psi = \tfrac{1}{2}\left(1-\gamma^5\right)\psi, \qquad \psi_R = P_R\psi = \tfrac{1}{2}\left(1+\gamma^5\right)\psi, \tag{1.4}$$

where γ^5 is a product of the four Dirac matrices, γ^μ.

A clear distinction through two different representations is needed depending on the chirality of the fermion. The left-handed fermions are arranged in weak isospin doublets while the right-handed fermions are arranged in isospin singlets:

$$L = \begin{pmatrix} \nu_{\text{L}} \\ e_{\text{L}} \end{pmatrix}, \quad e_{\text{R}}, \qquad Q = \begin{pmatrix} u_{\text{L}} \\ d_{\text{L}} \end{pmatrix}, \quad u_{\text{R}}, \quad d_{\text{R}}, \tag{1.5}$$

and similarly for the remaining two generations. The right-handed neutrinos and left-handed anti-neutrinos are not included in the singlets.[1]

[1] Experimental evidence shows that neutrinos oscillate between flavour eigenstates. This proves that they are massive, but the mechanism behind is unknown. For the remainder of the thesis, neutrinos are assumed to be massless, and right-handed neutrinos not to exist. Although this is technically incorrect, it does not affect the production of supersymmetric particles at the LHC in the models considered in this thesis.

Another thing to take into account when dealing with fermions in the EW theory is the difference between the mass-eigenstates and the eigenstates of weak isospin of the quarks. The weak isospin eigenstates are obtained by transforming the lower component of the quark doublets, d, s, and b, using the unitary Cabibbo-Kobayashi-Maskawa (CKM) mixing matrix [21, 22]

$$\begin{pmatrix} d' \\ s' \\ b' \end{pmatrix} = \begin{pmatrix} V_{ud} & V_{cd} & V_{td} \\ V_{us} & V_{cs} & V_{ts} \\ V_{ub} & V_{cb} & V_{tb} \end{pmatrix} \begin{pmatrix} d \\ s \\ b \end{pmatrix}. \tag{1.6}$$

The biggest mixing of the quark states appear in the first two generations, d, and s, while the mixing with b-quarks is very small.

The Electroweak Lagrangian

The Electroweak Lagrangian must be invariant under $SU(2) \times U(1)$ transformations, thus four gauge fields are introduced, W_μ^1, W_μ^2, W_μ^3 from the $SU(2)$-group, and B_μ from the $U(1)$-group. The W_μ-fields couple only to left-handed fermions, while the B_μ-field couples with equal strength to both chirality states.

The EW Lagrangian is written in terms of the gauge fields as [23]

$$\begin{aligned} \mathcal{L} = & \sum_{\text{generations}} \left[i\bar{L}\not{D}L + i\bar{Q}\not{D}Q + i\bar{e}_R\not{D}e_R + i\bar{u}_R\not{D}u_R + i\bar{d}_R\not{D}d_R \right] \\ & - \tfrac{1}{4}W^a_{\mu\nu}W^{a\mu\nu} - \tfrac{1}{4}B_{\mu\nu}B^{\mu\nu}, \end{aligned} \tag{1.7}$$

where $\not{D}$ is the covariant derivative, D_μ contracted with the gamma-matrices, γ^μ. Since the W_a^μ-field only couples to left-handed fermions, two different covariant derivative are defined based on the chirality of the fermion:

$$i\bar{L}\not{D}L = \bar{L}\gamma^\mu \left(i\partial_\mu - \frac{g}{2}\tau^a W_\mu^a - g' Y_W B_\mu \right) L \tag{1.8a}$$

$$i\bar{e}_R\not{D}e_R = \bar{e}_R\gamma^\mu \left(i\partial_\mu - g' Y_W B_\mu \right) e_R, \tag{1.8b}$$

and likewise for the quarks. g and g' are the coupling constants of the weak isospin current and the W and B fields respectively, and τ^a is the generator of the $SU(2)$ group represented by the Pauli spin matrices.

The interaction terms of the four gauge bosons given in the second part of Equation 1.7 are given as

$$W^a_{\mu\nu} = \partial_\mu W^a_\nu - \partial_\nu W^a_\mu + g\epsilon^{abc} W^b_\mu W^c_\nu \tag{1.9a}$$

$$B_{\mu\nu} = \partial_\mu B_\nu - \partial_\nu B_\mu, \tag{1.9b}$$

where ϵ^{abc} is the Levi-Civita symbol. The gauge-fields, W_μ^a, and B_μ, describe the force carrying bosons of the electroweak theory, $W^\pm$, Z^0, and the photon.

Spontaneous Symmetry Breaking

The four gauge-bosons entering in Equation 1.7 are all massless, and thus in disagreement with experimental observations of the massive $W^{\pm}$ and Z boson with masses of 80.4 GeV and 91.2 GeV, respectively. Simply adding a mass-term for the gauge bosons of $\frac{1}{2}m^2 W_\mu^a W^{a\mu}$ cannot be the solution, as this will ruin the gauge invariance of the Lagrangian.

A solution that will conserve the gauge invariance of the Lagrangian is to spontaneously break the electroweak symmetry through the Brout-Englert-Higgs mechanism [8, 9]. An isospin doublet of a complex scalar field, ϕ, is introduced with Lagrangian term

$$\begin{aligned}\mathcal{L}_{\text{Higgs}} &= |D_\mu \phi|^2 - V(\phi) \\ &= |D_\mu \phi|^2 + \mu^2 \phi^\dagger \phi - \lambda \left(\phi^\dagger \phi\right)^2 .\end{aligned} \tag{1.10}$$

By requiring that $\mu^2 > 0$ in the potential of the scalar field described in Equation 1.10, the Higgs field, ϕ, obtains a non-zero vacuum expectation value (VEV) at

$$v = \sqrt{\frac{\mu^2}{\lambda}}, \tag{1.11}$$

and the vacuum state of the scalar field can be written as

$$\langle \phi \rangle = \frac{1}{\sqrt{2}} \begin{pmatrix} 0 \\ v \end{pmatrix}. \tag{1.12}$$

The non-zero VEV of the Higgs field breaks the symmetry of the Lagrangian and by the choice of gauge generates three massive and one massless vector boson. The four physical gauge bosons are combinations of the original W_μ^a and B_μ-bosons:

$$W_\mu^{\pm} = \left(W_\mu^1 \mp i W_\mu^2\right)/\sqrt{2} \qquad M_W = \frac{1}{2} v g \tag{1.13a}$$

$$Z_\mu^0 = \cos\theta_W W_\mu^3 - \sin\theta_W B_\mu \qquad M_Z = \frac{v}{2}\sqrt{g^2 + g'^2} \tag{1.13b}$$

$$A_\mu = \cos\theta_W W_\mu^3 + \sin\theta_W B_\mu \qquad M_A = 0, \tag{1.13c}$$

where θ_W is the weak mixing angle given by

$$\sin\theta_W = \frac{g}{\sqrt{g^2 + g'^2}}, \qquad \cos\theta_W = \frac{g'}{\sqrt{g^2 + g'^2}}. \tag{1.14}$$

A relic from the spontaneous symmetry breaking is the Higgs boson, a massive scalar particle coupling to particles with strength depending on their mass. The mass of the Higgs boson depends on the parameters in the potential in Equation 1.10, $M_H = \sqrt{2}\mu = \sqrt{2\lambda}v$. The mass of the Higgs boson discovered in 2012 has been measured to be ~ 125 GeV.

A milestone for the Standard Model was the prove by 't Hooft and Veltman in 1972 that with the Higgs mechanism included in the theory, it is renormalizable [24], i. e. divergencies arising at a certain order of calculation can be isolated and will be canceled by higher-order effects.

Yukawa Interactions

A mass-term of the fermions must be of the form

$$\mathcal{L}_{m_f} = -m_f \left(\bar{f}_L f_R + \bar{f}_R f_L\right). \tag{1.15}$$

Since the left-handed and right-handed components of the fermions are described by two different representations and thus have different gauge quantum numbers, a simple mass term as in Equation 1.15 will violate gauge invariance.

As for the masses of the gauge bosons, the mass-terms for the fermions can arise from spontaneous symmetry breaking. The scalar-field introduced to solve the problem of the gauge boson masses possesses the correct gauge quantum numbers and have gauge invariant Yukawa couplings of the form [16]

$$\mathcal{L}_{\text{Yukawa}} = \sum_{\text{generations}} \left[-\lambda_e \bar{L}\cdot\phi e_R - \lambda_d \bar{Q}\cdot\phi d_R - \lambda_u \epsilon^{ab}\bar{Q}_a\phi_b^\dagger u_R + \quad \text{h.c.}\right], \tag{1.16}$$

where ϵ^{ab} is the completely asymmetric $SU(2)$ tensor with $\epsilon^{12} = 1$ and λ_f is a dimensionless coupling constant.

By breaking the $SU(2)$ symmetry and replace ϕ with its VEV, v, mass-terms of the form in Equation 1.15 appear with fermion masses depending on λ_f

$$m_f = \frac{1}{\sqrt{2}}\lambda_f v. \tag{1.17}$$

The Higgs boson couples to fermions depending on their mass through a Yukawa-coupling. A term

$$\mathcal{L}_{\text{Yukawa}} = -\sum_f \frac{\lambda_f}{\sqrt{2}}\bar{f}fH \tag{1.18}$$

is added to the Lagrangian. In principle λ_f is a matrix related to the CKM matrix introduced in Eq. 1.6. When the fermions are represented in their mass-eigenstate basis, then λ_f is diagonal and the CKM matrix will have non-zero off-diagonal terms. If the fermions are instead represented in the basis of weak isospin eigenstates, the CKM matrix is diagonal and λ_f will then have non-zero off-diagonal terms. In the remainder of this thesis, the fermions are written in their mass-eigenstates.

1.1.4 Quantum Chromodynamics

Quantum chromodynamics (QCD) is the theory of the strong interaction described by the gauge group $SU(3)$ [10, 11]. The (anti-)quarks are arranged in colour-triplets of (anti-)Red, (anti-)Green, and (anti-)Blue. The leptons are colour-singlets and thus do not couple through the strong force. The force carrying particle of the strong force is the gluon which itself carries colour charge. There are eight different colour combinations for gluons.

The Lagrangian describing QCD is given by

$$\mathcal{L}_{QCD} = \sum_{j=\text{flavours}} \bar{q}_j \left(i \not{D} - m_j\right) q_j - \tfrac{1}{4} G^a_{\mu\nu} G^{\mu\nu a}, \tag{1.19}$$

where $\not{D}$ is the covariant derivative, D_μ, contracted with the gamma-matrices, γ^μ, given by:

$$i\bar{q}_j \not{D} q_j = i\bar{q}_j \gamma^\mu \left(\partial_\mu - i g_s G^a_\mu T^a\right) q_j, \tag{1.20}$$

where g_s is the strong coupling, G^a_μ is the gluon field, and T^a is the generators of the $SU(3)$ group related to the eight Gell-Man matrices, $T^a = \lambda^a/2$. The second part of Eq. 1.19 containing $G^a_{\mu\nu}$ is describing the interactions of the gluon field:

$$G^a_{\mu\nu} = \partial_\mu G^a_\nu - \partial_\nu G^a_\mu + g_s f^{abc} G^b_\mu G^c_\nu, \tag{1.21}$$

where f^{abc} is the structure constant of the $SU(3)$ group.

Unlike the electroweak theory, QCD is an unbroken symmetry which leaves the gluon massless like the photon. However, unlike the photon, the gluon couples to itself. The gluon self-coupling arises from the $-\frac{1}{4} G^a_{\mu\nu} G^{\mu\nu a}$-term in the Lagrangian leading to triple and quartic self-couplings.

The behaviour of the coupling constant of the strong force, $\alpha_s = g_s^2/4\pi$, differs from that of the electromagnetic force. As for the interaction strengths of the electromagnetic and weak forces, the interaction strength of the strong force depends on the energy at which it is probed. The difference between the couplings lie in the behaviour as a function of the distance between particles; the electromagnetic force decrease with increasing distance, the strength of the strong force increases with increasing distance similar to the weak force. Thus at small distances, the quarks do not feel the strong force between them and can move freely. This is known as asymptotic freedom.

When the distance between a pair of quarks grows, the force grows as well until there is enough energy in the system to create a new quark-antiquark pair from the vacuum. In this way, observation of a single quark is never possible and they will always be observed confined in hadrons.

If free high-energetic quarks or gluons are produced in particle collisions, they will not be observed directly due to confinement. To screen their colour charge the quarks and gluons will both radiate gluons which split into $q\bar{q}$-pairs forming many light hadrons, they hadronise. The hadrons will be collimated in a cone forming a detector signal known as a jet. The exact mechanism behind hadronisation is not fully understood, but there are models used for simulation describing the process.

1.1.5 Particle Collisions at Hadron Colliders

Several hadron colliders have been built. The most recent one to begin operation is the Large Hadron Collider (LHC) at CERN colliding protons at unprecedented energies.

The proton consists of three valence quarks, two u-quarks and one d-quark, and a sea of quarks, anti-quarks, and gluons. When colliding protons, it is the constituents of the protons, the partons, that collide.

Parton Distribution Functions

In order to produce new heavy particles, the partons colliding must have a high energy: a hard process must occur. The hard process is characterised by a large momentum transfer between the interacting partons. When the energy of the hard process is much larger than the QCD binding energy, Λ_{QCD}, the proton can be approximated with a collection of free partons [25]. Apart from the hard scattering, multiple other things happen in a hadron collision. The remaining partons will interact creating many low energy particles, a process known as the underlying event. The initial state partons can radiate off photons, gluons or quarks creating jets known as initial state radiation (ISR). Just as the initial state particles, the final state particles might radiate off particles as well creating final state radiation (FSR).

To study parton-parton interactions, parton distribution functions (PDFs) are introduced. To the lowest order, a parton distribution function, $f_i(x, \mu^2)$, describes the probability of selecting a certain parton with a momentum fraction x given by

$$x = \frac{|\vec{p}_{\text{parton}}|}{|\vec{p}_{\text{proton}}|}, \tag{1.22}$$

at a resolution scale, μ^2. The resolution scale is a measure of the energy at which the proton is probed. The higher the μ^2, the more "closely" the proton is studied.

The x-dependence of the parton distribution functions are obtained experimentally. There is a big variety of PDF-sets available provided by several collaborations using data from many different experiments, e. g. experiments at HERA, Tevatron, and LHC [26–33]. The most commonly used PDF-sets at the LHC are MSTW [34], NNPDF [35], CT10 [36], and CTEQ6.6 [37]

The parton distribution functions for two different resolution scales are shown in Fig. 1.1. At low values of x, the gluon distribution dominates while at higher values of x, the PDFs of the valence quarks, u and d are the biggest. By increasing the energy at which the proton is probed, the PDFs of the sea-quarks and especially the gluon increase while the PDFs of the valence quarks decrease at high x.

Factorisation

The probability of a process, $pp \to X$, to occur is given by the cross section, σ, of the process. The cross section of a hard scattering is normally calculated from known initial states at the parton level, $ab \to X$. The quadratic energy of a hard scattering, $\hat{s}$, restricts the momentum fractions carried by the two partons

$$\hat{s} = x_a x_b s, \tag{1.23}$$

where s is the total quadratic energy of the two protons, and x_a and x_b are the momentum fractions carried by the two partons participating in the process.

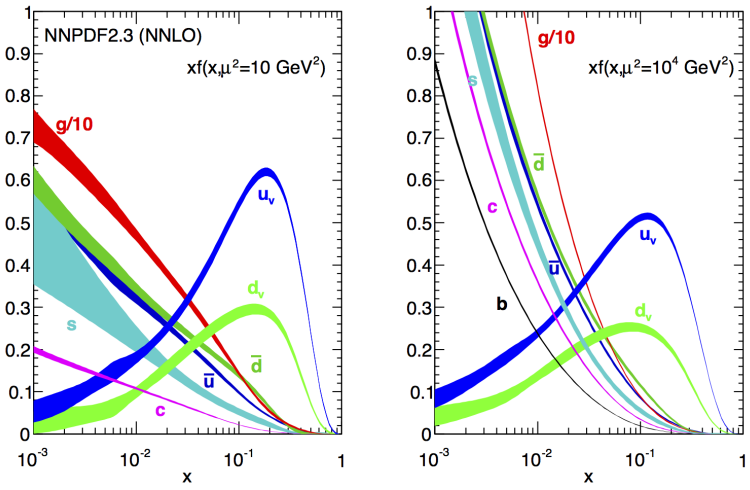

Fig. 1.1 · Parton distribution functions at two different resolutions scales, $\mu^2 = 10\ \text{GeV}^2$ and $\mu^2 = 10^4\ \text{GeV}^2$. This set of parton distribution functions are provided by the NNPDF collaboration [35].

When $\sqrt{\hat{s}} \gg \Lambda_{\text{QCD}}$ and the proton is approximated to a collection of free partons, the cross section of $pp \to X$ can be written in terms of the cross section at parton level, $\sigma(ab \to X)$ convoluted with the PDFs of parton a and b [38]

$$\sigma\left(p_A p_B \to X\right) = \int_0^1 \int_0^1 \sum_a \sum_b dx_a dx_b f_a\left(x_a, \mu^2\right) f_b\left(x_b, \mu^2\right) \sigma\left(ab \to X\right). \tag{1.24}$$

The cross section is related to the scattering amplitudes calculated from Feynman diagrams. The Feynman diagrams are drawn to a certain order in the strong coupling constant, α_s. The lowest order is leading order in α_s (LO), followed by the next-to-leading order in α_s (NLO) taking into account single loop-corrections, and so forth. The cross sections are calculated at a certain order, the higher the order, the more precise the cross section is expected to be. In order to make the cross section even more accurate, a resummation of soft gluon emission at the next-to-leading logarithm (NLL) [39] or even next-to-next-to-leading logarithm (NNLL) accuracy level can be performed.

At hadron colliders it is possible to study many different energies up to $\hat{s} \approx s$. This makes them ideal for searching for new, heavy particles of unknown mass as a wide energy range can be explored.

1.2 Shortcomings of the Standard Model

The Standard Model has proven a success agreeing with a wide variety of observations spanning over twelve orders of magnitude in energy. Despite its great triumph, the Standard Model fails to answer several questions, both experimental and theoretical. A short summary of some of the shortcomings are listed here.

1.2.1 What is in the darkness?

The precise measurements of the Cosmological Microwave Background by Planck [40, 41] and WMAP [42, 43] interpreted in a Λ_{CDM}-model, show that only $\sim$ 5% of energy in the Universe is attributed to baryonic matter such as atoms. The rest of the energy of the Universe comes from Dark Matter (DM) and Dark Energy constituting $\sim$ 26% and $\sim$ 69% of the total energy, respectively.

Dark Matter is invisible and has so far only been detected through gravitational interactions. Dark Matter was first postulated to account for rotational speed of galaxies in the 1930's that could not be explained by the visible matter [44]. Later more evidence of the existence of DM has been observed. What exactly DM is, is still a mystery. However, it cannot be electrically charged, otherwise it would be visible. Dark Matter could be a new particle that only interacts through gravity and perhaps the weak force.

Dark Energy accounts for the majority of the energy in the Universe and results in an accelerated expansion of the Universe. Supernovae with large redshifts have been measured to be further away than expected suggesting that the expansion of the Universe is accelerating, i. e. suggesting the presence of Dark Energy [45]. The exact nature of Dark Energy is not understood, but it could be explained by the cosmological constant, Λ, first postulated by Einstein.

1.2.2 Why is the Higgs so light?

The measured mass of the Higgs boson receives quantum corrections to the SM-parameter m_H^2 through loop diagrams with big correction factors.

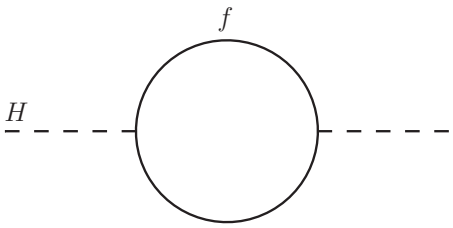

Fig. 1.2 · One-loop quantum corrections to the Higgs propagator containing a Dirac fermion, f.

A fermion one-loop correction to m_H^2, as shown in Figure 1.2, will occur through the Yukawa interaction defined in Equation 1.18. In principle, the fermion in the loop can have any four-momentum, k^μ, and thus the contribution from the loop should be integrated from $-\infty$ to $+\infty$. By studying large loop-momentum, the mass of the fermion and the initial momentum of the Higgs can be ignored, given a correction to m_H^2 [46]

$$\Delta m_H^2 \sim \int_0^\infty \lambda \mathrm{d}\lambda \quad \text{where} \quad \lambda = |k| = \sqrt{k_\mu k^\mu}. \tag{1.25}$$

This integral clearly diverges as $\lambda \to \infty$. It can be regularised by introducing a cutoff scale, Λ_{UV}, making

$$\Delta m_H^2 = -\frac{|\lambda_f|^2}{8\pi^2}\Lambda_{UV}^2 + \dots. \tag{1.26}$$

All the massive fermions of the Standard Model contribute to the loop, but since the strength of the Yukawa-coupling depends on the mass of the particle, the top quark gives the largest contribution.

The UV cutoff scale is the energy scale where new physics beyond the Standard Model appears. Assuming that the Standard Model without any modifications holds up to the Planck scale where gravity becomes strong, the cutoff-scale will be $M_{\text{Planck}} \sim 1.22 \cdot 10^{19}$ GeV. The only way we can have an observed Higgs mass of ~ 125 GeV, is by finetuning the Standard Model parameter m_H^2 to be the size of M_{Planck} through 17 orders of magnitude. This is known as the hierarchy problem.

The hierarchy problem can be solved by new particles entering in the loops canceling the quartic divergence in the quantum corrections in Equation 1.25.

1.2.3 That GUT-feeling ...

The entire composition of the Standard Model seems rather random. There are 19 free parameters arising from the CKM matrix, the masses of the particles, the gauge couplings and the vacuum expectation value of the Higgs potential. The 19 free parameters are not constrained by theory and can only be determined through measurements. Aside from the 19 parameters, the choice of gauge group and different fermion representations depending on the fields seem arbitrary as well.

The arbitrariness of the Standard Model is not a real problem of the theory, but more an aesthetic consideration. It could be that the Standard Model is simpler at higher energies; that at high energies the gauge groups are unified under one larger symmetry group. This set of theories are called Grand Unified Theories (GUT) [47–49]. For the gauge groups to unify at a higher energy, the running couplings of the gauge group must approach each other at the unification scale. By evolving the gauge couplings with their respective renormalisation group equations, it is found that the couplings do approach each other at an energy around 10^{16} GeV, but they do not get close enough that a direct unification of all three forces is a possibility. This implies that either the unification occurs in two steps where two forces are unified at a lower scale, or that there simply is no unification in the Standard Model.

Physics beyond the Standard Model could alter the running of the couplings allowing them to meet at the unification scale.

1.2.4 How does gravity fit in?

The fourth fundamental force, gravity, is not included in the Standard Model. Gravity is described classically by Einstein's theory of general relativity. Many attempts have been made in formulating a theory of quantum gravity similar to quantum electrodynamics with a massless spin-2 boson, the graviton, being the mediator of the force. This, however, leads to an unrenormalisable theory with infinite probabilities for some sub-processes [50].

Even though gravity is one of the fundamental forces most directly visible in everyday life, it is the weakest of the four fundamental forces. At the Planck scale, $\Lambda_{\text{Planck}} \sim 1.22 \cdot 10^{19}$ GeV, the strength of gravity becomes of the same order as the weak force, and the Standard Model breaks down. At this energy a new theory including gravity is needed.

1.2.5 Where did all the antimatter go?

It is a natural assumption that in the very early Universe, there were equal amounts of matter and antimatter. Observations show that we now live in a matter dominated Universe. This leaves the question of what happened to the antimatter?

Though the Standard Model contains CP-violating processes that can account for part of the matter-antimatter asymmetry, these are not strong enough to explain all of the observed asymmetry [51].

1.3 Possible Extensions of the Symmetry Groups of the Standard Model

Since the Standard Model is built on a basis of external and internal symmetries, a natural question to ask is these are the only two possible types of symmetries? Maybe it is possible to combine the external and internal symmetries in a non-trivial way into a new kind of symmetry.

Before the discovery of the substructure of hadrons, i.e. quarks and gluons, the hadrons were organised in different representations of $SU(3)$ dependent on their spin. This seemed to form a correlation between an external symmetry (spin) and an internal symmetry ($SU(3)$ representations). This led to the search of an extension of the symmetry group.

In 1967, Coleman and Mandula published a paper proving, under reasonable assumptions, that it is not possible to combine external and internal symmetries [52]. Adding an extra type of symmetry would lead to an over-constrained theory with unphysical two-particle scatterings. This is known as the Coleman-Mandula no-go theorem. This seemed to put an end to exploring possible extensions of the Poincaré group.

While scrutinising the assumptions of the Coleman-Mandula no-go theorem, it was found that it contained a hidden restriction - only bosonic symmetries were considered by the theorem. It was not a strange assumption as all symmetries of the Standard Model were bosonic. However, it meant that spinoral symmetries whose generators have half-integer spin had not been considered by Coleman and Mandula. It was later found by Haag, Łuposzański, and Sohnius that the Poincaré group could be extended by a new symmetry with spin-$\frac{1}{2}$ generators [53]. This fermionic extension is known as supersymmetry (SUSY).

1.4 Supersymmetry

Supersymmetry (SUSY) is the extension of the Poincaré symmetry group to include fermionic symmetries. The extended symmetry group is called the super-Poincaré group.

The generators of supersymmetry, Q_α and its conjugate $\bar{Q}^{\dot{\alpha}}$, are called supercharges. They are spin-$\frac{1}{2}$ operators and carry a spin index, $\alpha/\dot{\alpha}$, which are themselves 2-component Weyl spinors.

Since the supercharges are described by fermion statistics, two supercharges, Q_α and Q_β, will anticommute, while a supercharge and its conjugate fulfills [46]

$$\{Q_\alpha, \bar{Q}_{\dot{\alpha}}\} = 2\sigma^\mu_{\alpha\dot{\alpha}} P_\mu, \tag{1.27}$$

where $\sigma^\mu_{\alpha\dot{\alpha}}$ is a specific matrix element of the Pauli-spin matrices. This shows that performing two SUSY transformations generates a space-time translation.

When acting on a particle-state, fermion or boson, with a SUSY transformation, Q, the spin is changed by $\pm\frac{1}{2}$, such that

$$Q|\text{Fermion}\rangle = |\text{Boson}\rangle \qquad \text{and} \qquad Q|\text{Boson}\rangle = |\text{Fermion}\rangle. \tag{1.28}$$

A supersymmetric theory will thus be symmetric when interchanging fermions and bosons. This leads to a prediction of a supersymmetric partner for every SM particle with identical quantum numbers except the spin differing by $\pm\frac{1}{2}$. The particle content of the Universe is doubled by requiring supersymmetry.

The SUSY partners are known as sparticles and if supersymmetry is an exact symmetry they will have a mass identical to their SM partner. In supersymmetry, each chiral SM fermion forms together with its supersymmetric partner, a complex scalar, a chiral supermultiplet. Similarly, the Higgs forms together with its SUSY partner, a chiral fermion, a chiral supermultiplet. The SM gauge bosons each have a fermion as their SUSY partner and together they form gauge supermultiplets.

Since the sparticles and their SM partners have not been observed to have identical masses, SUSY must be broken. This can lead to sparticles with masses in the TeV-range.

1.4.1 SUSY to the rescue

Supersymmetry addresses several of the shortcomings of the Standard Model described in Section 1.2.

Dark Matter Candidate

As suggested by the name, dark matter does not emit light and must therefore be electrical neutral. The dark matter observed in the Universe can be described by particles that interact through gravity and perhaps through the weak interaction. There are different hypotheses of what could make up dark matter. One hypothesis is that it consists of electrically neutral, massive, stable particles only interacting weakly.

Since supersymmetry doubles the particle content of the Universe, it provides candidates for dark matter. The supersymmetric partners of the neutral gauges bosons and the Higgs boson are massive, weakly interacting particles. The dark matter candidate must be stable or have a lifetime at least in the order of the age of the Universe. This is also possible in SUSY.

Higgs finetuning

A heavy, complex scalar, S, that couples to the Higgs with the Lagrange-term $-\lambda_S |H|^2 |S|^2$ will contribute to the measured Higgs mass to first order with a one-loop correction as shown in Figure 1.3. This will give rise to a correction term [46]

$$\Delta m_H^2 = \frac{\lambda_S}{16\pi^2}\left[\Lambda_{UV}^2 - 2m_S \ln\left(\Lambda_{UV}/m_S\right) + \ldots\right], \tag{1.29}$$

depending on the cut-off scale, Λ_{UV}, and the mass of the scalar, m_S. The second term is a logarithmic divergence, similar to the correction of the electron mass. Logarithmic divergencies are a lot less severe than quartic divergencies.

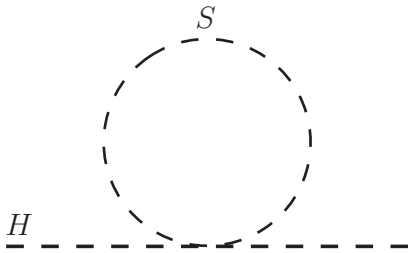

Fig. 1.3 · One-loop qunatum coorections to the Higgs propagator containing a scalar, S.

Supersymmetry states that for every chiral fermion, a complex scalar exists. Combing Equations 1.25 and 1.29, one arrives at

$$\Delta m_H^2 = \frac{1}{8\pi^2}\left(|\lambda_f|^2 - \lambda_S\right)\Lambda_{UV} + \ldots. \tag{1.30}$$

It is seen that by requiring $|\lambda_f|^2 = \lambda_S$, the quartic divergence disappears. In unbroken supersymmetry that relation holds and the Higgs mass no longer needs excessive finetuning to stay light. There exists SUSY breaking mechanisms where the cancellation holds, known as soft SUSY breaking [54].

Grand Unified Theories

As discussed in Section 1.2.3, the introduction of new particles can alter the running of the gauge coupling constants. By including supersymmetry, the running of the couplings can be changed so they all meet in one point provided the masses of the sparticles are in the range of 100 GeV to 10 TeV [55]. This allows for a direct unification of all three forces at the GUT energy scale of 10^{16} GeV.

Gravity

Supersymmetry as a global symmetry does not in itself describe gravity. By making SUSY local, one is forced to introduce a massless spin-2 particle, the graviton, and its superpartner, the gravitino [55]. This local supersymmetry will describe the dynamics of Einstein's theory of general relativity through supergravity. Supergravity is unfortunately not a renormalisable theory.

Supermultiplet	Bosons	Fermions	$SU(3)_C$	$SU(2)_L$	$U(1)_Y$
Chiral multiplets	spin-0	spin-$\frac{1}{2}$			
quarks, squarks	$(\tilde{u}_L, \tilde{d}_L)$	(u_L, d_L)	3	2	$\frac{1}{3}$
(Three families)	$\tilde{u}_R^\dagger$	u_R^c	$\bar{3}$	1	$-\frac{4}{3}$
	$\tilde{d}_R^\dagger$	d_R^c	$\bar{3}$	1	$\frac{2}{3}$
leptons, sleptons	$(\tilde{\nu}_{eL}, \tilde{e}_L)$	(ν_{eL}, e_L)	1	2	-1
(Three families)	$\tilde{e}_R^\dagger$	e_R^c	1	1	2
Higgs, Higgsinos	(H_u^+, H_u^0)	$(\tilde{H}_u^+, \tilde{H}_u^0)$	1	2	1
	(H_d^0, H_d^-)	$(\tilde{H}_d^0, \tilde{H}_d^-)$	1	2	-1
Gauge multiplets	spin-1	spin-$\frac{1}{2}$			
Gluons, gluinos	g	$\tilde{g}$	8	1	0
W bosons, winos	$W^\pm, W^0$	$\widetilde{W}^\pm, \widetilde{W}^0$	1	3	0
B bosons, binos	B	$\tilde{B}$	1	1	0

Table 1.3 · The chiral and gauge supermultiplets of the MSSM and their quantum numbers.

Aside from supergravity, many attempts to include gravity in the quantum world rely on the existence of SUSY as for example string theory.

1.4.2 The Minimal Supersymmetric Standard Model (MSSM)

The Minimal Supersymmetric Standard Model (MSSM) [56, 57] is an extension of the Standard Model with one set of SUSY generators, a so-called $\mathcal{N} = 1$ supersymmetry. Even though it is the most simple full supersymmetric extension of the Standard Model it comes with an additional 105 free parameters originating from sparticle masses and mixing.

The Standard Model particles and their SUSY partners form supermultiplets. The SM fermions will have scalar superpartners and they will form chiral supermultiplets. The naming convention of the superpartners of the fermions is to add an "s" for "scalar" in front of the SM fermion names, e.g. squarks, sleptons, etc. The gauge bosons form together with their fermion superpartners gauge supermultiplets. The naming convention for the superpartners of gauge bosons is to add "ino" to the end of the Standard Model gauge boson names. The superpartners of the electroweak gauge bosons, $W^\pm$, W^0, and B, are called winos and the bino, while the superpartner of the gluon is called the gluino. The Higgs boson is a scalar particle and forms a chiral supermultiplet with its chiral fermion SUSY partner, the higgsino. The particle content of the MSSM is summarised in Table 1.3.

In the Standard Model, the up-type fermions gain their mass through Yukawa-interactions with the conjugate of the Higgs field, $\phi^\dagger$, as described in Equation 1.18. In Supersymmetry, the Lagrangian cannot depend on both scalar fields and their conjugate. This is solved by adding

an extra Higgs field, H_u, to the MSSM coupling only to the up-type fermions, whereas the "old" Higgs field, ϕ, is renamed to H_d and couples only to down-type fermions.

Soft SUSY Breaking

The Standard Model particles and their respective supersymmetric partners would have identical masses if supersymmetry was an exact symmetry. Since no superpartners have been discovered at the explored energy ranges, supersymmetry must be broken allowing the sparticles to have higher masses than their Standard Model partners.

The origin of SUSY breaking is not known. To keep the cancellation of the quartic divergencies described in Section 1.4.1, SUSY is assumed to be broken softly in the MSSM. As the exact mechanism behind the soft SUSY breaking is unknown, all terms allowed after soft SUSY breaking are included in the Lagrangian [46]:

$$\begin{aligned}\mathscr{L}_{\text{soft}}^{\text{MSSM}} = &-\tfrac{1}{2}\left(M_3\tilde{g}\tilde{g} + M_2\tilde{W}\tilde{W} + M_1\tilde{B}\tilde{B} + \text{c.c.}\right)\\ &-\left(\tilde{\bar{u}}\mathbf{a_u}\tilde{Q}H_u - \tilde{\bar{d}}\mathbf{a_d}\tilde{Q}H_d - \tilde{\bar{e}}\mathbf{a_e}\tilde{Q}H_d + \text{c.c.}\right)\\ &-\tilde{Q}^\dagger\mathbf{m}_{\mathbf{Q}}^2\tilde{Q} - \tilde{L}^\dagger\mathbf{m}_{\mathbf{L}}^2\tilde{L} - \tilde{\bar{u}}\mathbf{m}_{\bar{\mathbf{u}}}^2\tilde{\bar{u}}^\dagger - \tilde{\bar{d}}\mathbf{m}_{\bar{\mathbf{d}}}^2\tilde{\bar{d}}^\dagger - \tilde{\bar{e}}\mathbf{m}_{\bar{\mathbf{e}}}^2\tilde{\bar{e}}^\dagger\\ &-m_{H_u}^2H_u^*H_u - m_{H_d}^2H_d^*H_d - (bH_uH_d + \text{c.c.})\,.\end{aligned} \tag{1.31}$$

The first line of Equation 1.31, describes the masses of the gauginos: gluino (M_3), winos (M_2) and bino (M_1). The second line contains terms of trilinear scalar couplings between the sfermions and the Higgs bosons, much like the Yukawa coupling of the Standard Model. The **a**'s are complex 3×3 matrices. The third line contains the sfermion mass terms with **m**'s being the hermitian, possibly complex 3×3 mass matrices. Finally, the fourth line contains the terms contributing to the Higgs potential. While m_{H_u} and m_{H_d} are real, b can be complex. Many of the free parameters in the MSSM originates from the matrices of the soft breaking terms.

R-parity

The Lagrangian of the MSSM contains terms which would allow the proton to decay through a SUSY particle at a measurable rate. Proton decays have, however, never been discovered and as such an lower limit on the lifetime of the proton of $5.9 \cdot 10^{33}$ years is set [58].

This problem can be solved by fixing the couplings of the interactions allowing for the proton to decay to zero. A more satisfactory solution seems to be the addition of a new discrete symmetry, R-parity [59] with the multiplicative quantum number R

$$R = (-1)^{3(B-L)+2s}\,, \tag{1.32}$$

where B is the baryon number, L is the lepton number, and s is the spin of the particle. SUSY particles will have $R = -1$, while SM particles will have $R = +1$.

By requiring R-parity conservation, the three-particle interactions allowing the proton to decay will be forbidden as they contain only one SUSY particle. The assumption of R-parity conservation has additional consequences:

- SUSY particles can only be pair-produced. Since SUSY particles have $R = -1$, an even number will need to be produced from a SM particle with $R = +1$ for R-parity to be conserved.
- A SUSY particle must decay into an odd number of sparticles with $R = -1$ and additional SM particles.
- The lightest SUSY particle (LSP) will be stable since SUSY particles have to decay into particles with $R = -1$. All SUSY particles eventually decay into the LSP.

If the LSP is electrical neutral and only weakly interacting, it is a candidate for dark matter as described in Section 1.4.1.

Electroweak Symmetry Breaking in the MSSM

In EW symmetry breaking in the MSSM, the scalar potential, V, contains both Higgs doublets. The charged components of the Higgs doublets are chosen to be zero, $H_u^+ = H_d^- = 0$. This simplifies the expression of V to [46]

$$\begin{aligned} V = &\left(|\mu|^2 + m_{H_u}^2\right)|H_u^0|^2 + \left(|\mu|^2 + m_{H_d}^2\right)|H_d^0|^2 - \left(bH_u^0 H_d^0 + \text{c.c.}\right) \\ &+ \tfrac{1}{8}\left(g^2 + g'^2\right)\left(|H_u^0|^2 - |H_d^0|^2\right)^2 . \end{aligned} \tag{1.33}$$

Both b and the vacuum expectation values of H_u^0 and H_d^0 can be chosen to be real and positive.

The two Higgs doublets acquire different vacuum expectation values, v_u and v_d. The relation between the VEVs is normally referred to as

$$\tan\beta \equiv v_u / v_d . \tag{1.34}$$

$\tan\beta$ is a free parameter in the MSSM. As the VEVs of both Higgs doublets are assumed to be positive, $0 < \beta < \pi/2$ must be fulfilled.

There are eight degrees of freedom arising from the two Higgs doublets. After spontaneous symmetry breaking, three degrees of freedom become the longitudinal modes of the massive $W^\pm$ and Z bosons. The remaining five degrees of freedom are manifested as five Higgs bosons; the CP-even neutral scalars h^0 and H^0, the CP-odd neutral scalar A^0, and two charged Higgs bosons H^+ and H^-. The masses of four of the Higgs bosons, H^0, A^0, and $H^\pm$, can be arbitrarily large. The mass of the lightest Higgs, h^0, has a theoretical upper limit given at tree-level by

$$m_{h^0} < m_Z |\cos(2\beta)| . \tag{1.35}$$

This is in disagreement with the observed Higgs mass of ~ 125 GeV. Radiative corrections to the mass of h^0 will increase its upper limit. Due to its large Yukawa coupling, the radiative corrections originating from the top-squarks, $\tilde{t}_1$ and $\tilde{t}_2$, are found to be the largest. It is given by [12]:

$$\Delta m_{h^0}^2 = \frac{3g^2 m_t^4}{8\pi^2 M_W^2}\left[\ln\left(\frac{m_{\tilde{t}_1} m_{\tilde{t}_2}}{m_t^2}\right) + a^2\left(1 - \frac{a^2}{12}\right)\right], \tag{1.36}$$

where a^2 is a dimensionless number related to the trilinear couplings of the top sector to h_0 with a maximum value of $\sqrt{6}$. By including the radiative corrections, the upper limit of the mass of h^0 can be increased to $m_{h^0} \lesssim 135$ GeV which is in agreement with the observed Higgs mass.

Gaugino Mixing

The electroweak gauginos and higgsinos will mix into mass eigenstates due to the electroweak symmetry breaking, just as the W^0 and B mix into the photon and the Z boson. The four neutral bosinos, $\tilde{H}_u^0$, $\tilde{H}_d^0$, $\widetilde{W}^0$, and $\tilde{B}$, will combine into four mass eigenstates referred to as neutralinos, $\tilde{\chi}_1^0$, $\tilde{\chi}_2^0$, $\tilde{\chi}_3^0$, and $\tilde{\chi}_4^0$. The two charged gauginos ($\widetilde{W}^{\pm}$) will mix together with the two charged higgsinos ($\tilde{H}_u^+$ and $\tilde{H}_u^-$) to form four charged mass eigenstates, $\tilde{\chi}_1^{\pm}$ and $\tilde{\chi}_2^{\pm}$. The mass-ordering of the neutralinos and charginos follows the indices, i, such that $m(\tilde{\chi}_4^0) > m(\tilde{\chi}_3^0) > m(\tilde{\chi}_2^0) > m(\tilde{\chi}_1^0)$ and $m(\tilde{\chi}_2^{\pm}) > m(\tilde{\chi}_1^{\pm})$. The lightest neutralino, $\tilde{\chi}_1^0$, is often assumed to be the lightest supersymmetric particle (LSP) described earlier.

The mixing of the higgsinos and gauginos into neutralinos and charginos depends on the parameters M_1 and M_2 from Equation 1.31, μ from Equation 1.33, and the relation between the VEVs of the two Higgs doubles, $\tan\beta$ [60]. The hierarchy of the mass-parameters will to a large extend determine the mixing components of the various mass eigenstates.

If $|\mu| \gg |M_{1,2}| \gg M_Z$, the two lightest neutralinos, $\tilde{\chi}_{1,2}^0$, and the lightest chargino, $\tilde{\chi}_1^{\pm}$, are gaugino dominated. The two lightest neutralinos are said to be "bino"- and "wino"-like, while the lightest chargino is only "wino"-like. The two heavier neutralinos, $\tilde{\chi}_{3,4}^0$, and the heaviest chargino, $\tilde{\chi}_2^{\pm}$ are dominated by the neutral and charged higgsinos, respectively. They are said to be "higgsino"-like.

If instead $|\mu| \ll |M_{1,2}|$, then the two lightest neutralinos, $\tilde{\chi}_{1,2}^0$, and the lightest chargino, $\tilde{\chi}_1^{\pm}$, are "higgsino"-like, while the two heavier neutralinos, $\tilde{\chi}_{3,4}^0$, and the heaviest chargino, $\tilde{\chi}_2^{\pm}$ are largely gaugino dominated.

If the mass parameters are of the same order, $|\mu| \simeq M_2$ or $|\mu| \simeq M_1$, then the neutralinos and charginos will contain an almost equal amount of the gauginos and higgsinos.

The ordering of the mass-parameters does not only determine the masses of the neutralinos and charginos, but also their interactions with (s)fermions. This is similar to the V-A structure of the Z boson in the Standard Model arising from the mixing of the W^0 and B fields after the EW spontaneous symmetry breaking.

1.4.3 Other SUSY Models

Many simplifications of the MSSM exist. There are both more complex models and very simple models. The more complex models make assumptions on the nature of the SUSY breaking mechanism and calculate the mass spectrum of the sparticles from that. In the simpler models, it is assumed that SUSY has been broken at some scale without any assumptions on the nature behind it making the SUSY particles light enough to be produced at colliders.

Here follows a short description of a selection of SUSY models with emphasis on the models studied in this thesis (the phenomenological MSSM and simplified models).

mSUGRA/CMSSM

The minimal supergravity or constrained MSSM (mSUGRA/CMSSM)[61–63], is a set of theories where SUSY is assumed to be broken at the GUT scale by a hidden sector through a supersymmetric Higgs mechanism. The SUSY breaking is mediated from the hidden to the visible sector by gravity.

mSUGRA/CMSSM can be described by only five free parameters arising from the symmetry breaking: an universal mass for scalar particles (m_0), an universal mass of fermionic particles ($m_{1/2}$), the trilinear coupling (A_0), the relation between the vacuum expectation values of the two Higgs doublets ($\tan\beta$), and the sign of the higgsino mass parameter μ. The mass parameters are defined at the GUT scale and are evolved to the energy scales of current colliders through renormalisation group equations.

Gauge-mediated and Anomaly-mediated SUSY Breaking Models

In gauge-mediated SUSY breaking (GMSB) models [64–66] supersymmetry is broken in a similar way as mSUGRA/CMSSM in a hidden sector. Instead of only gravity mediating the SUSY breaking to the visible sector, a new chiral supermultiplet is introduced as the messenger coupling the SUSY breaking and the SUSY particles through the gauge interactions of the Standard Model. Gravity will be a mediator as well, but the chiral supermultiplet will have much stronger couplings.

In GMSB models, the gravitino is the LSP giving a special role to the next-to-lightest SUSY particle (NLSP) as it defines the phenomenology of the final state.

Anomaly-mediated SUSY breaking (AMSB) models [67, 68] is another set of theories of supergravity, where the SUSY breaking is due to violation of the extended scale invariance described by conformal symmetry.

The Phenomenological MSSM

The amount of free parameters in the MSSM is too big for feasible systematic, phenomenological studies. With 105 parameters arising from the soft SUSY breaking terms and 19 from the Standard Model, the MSSM has a 124-dimensional parameter space.

The phenomenological Minimal Supersymmetric Standard Model (pMSSM) [69, 70], is a simplification of the MSSM. The number of free parameters arising from soft SUSY breaking is reduced from 105 in the MSSM to 19 in the pMSSM. The reduction is based on three assumptions:

1. There are no new sources of CP-violation. New sources of CP-violations are eliminated by assuming that all the phases in the soft SUSY breaking Lagrangian are zero. This reduces the amount of free parameters significantly.

2. There are no flavour changing neutral currents (FCNC). The off-diagonal terms in the sfermion mass-matrices and the trilinear scalar couplings in Equation 1.31, can lead to large FCNC already heavily constrained by experiment. Both the sfermion mass matrices and the trilinear couplings are assumed to be diagonal to ensure that FCNC-terms do not arise.

3. First and second generation of sfermions are mass-degenerate. The mass-splitting between the first and the second generation of squarks is limited by experimental data. The first

two generations are therefore assumed to have the same mass. There can, however, be mass difference between the "left"-handed and "right"-handed sfermions[1]. Furthermore, the trilinear couplings in Equation 1.31 of the first two generations are assumed to be zero since they depend on the mass of the Standard Model partners to the sfermions.

The three assumptions have reduced the number of free parameters to:

- $\tan\beta$: The ratio of the vacuum expectation values of the two Higgs doublets.
- μ: The higgsino mixing parameter.
- M_A: The mass of the pseudo-scalar Higgs, A^0.
- M_1, M_2, and M_3: The gaugino mass parameters.
- $m_{\tilde{q}_L}$, $m_{\tilde{u}_R}$, $m_{\tilde{d}_R}$, $m_{\tilde{l}_L}$, and $m_{\tilde{e}_R}$: The mass parameters of the first two generations of sfermions.
- $m_{\tilde{Q}_L}$, $m_{\tilde{t}_R}$, $m_{\tilde{b}_R}$, $m_{\tilde{L}_L}$, and $m_{\tilde{\tau}_R}$: The mass parameters of the third generation of sfermions.
- A_t, A_b, and A_τ: The trilinear couplings for the third generation.

Having reduced the number of free parameters to 19, it is easier to study the phenomenology of sparticle production and interactions more systematically. Especially since for most model-building normally, only a subset of the 19 parameters are varied.

Simplified Models

In simplified models no assumption on SUSY breaking parameters are made except that SUSY breaking has occurred at an energy that has made only a few sparticles light enough to be produced at colliders [71–73]. A simplified model will normally deal with pair-production of only one or maybe two types of sparticles. Unlike simplifications of the MSSM such as the MSUGRA/CMSSM and the pMSSM containing many different decay-chains of sparticles, the pair-produced sparticles in simplified models will normally only have one decay mode with a 100% branching fraction. The decay of the sparticles are motivated by similar decays in the MSSM. The number of free parameters in simplified models is normally reduced to two, the mass of the sparticle created and the mass or the mass difference between sparticles in the decay chain.

In Figure 1.4, simplified models are shown for squark and gluino pair-production decaying directly with a 100% branching fraction into $q\tilde{\chi}_1^0$ and $q\bar{q}\tilde{\chi}_1^0$, respectively. In both models all other sparticles than the ones created and the LSP are decoupled. The free parameters are the mass of the squark/gluino, $m_{\tilde{q}/\tilde{g}}$, and the mass of the LSP, $m_{\tilde{\chi}_1^0}$. These two examples of simplified models would lead to distinct signatures in our detector.

Simplified models are not, as the name might suggest, full SUSY models. They oversimplify the SUSY parameter space, and are thus not descriptive of most SUSY scenarios. However, they

[1] Scalar particles are not chiral states and the squarks are therefore neither right- or left-handed. The notation is used to refer to the chirality of the SM partner of the squarks.

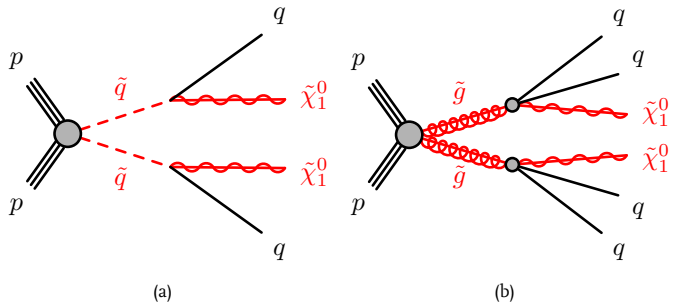

Fig. 1.4 · Examples of diagrams for simplified models of squark and gluino pair-production with direct decays.

are useful when searching for SUSY particles at the LHC, as the heavily reduced parameter space can be fully explored and they predict very specific detector responses. Furthermore, results in simplified models can be reported as upper limits on the cross section of the processes which they describe, e. g. squark-pair production with direct decays. This can be interpreted in larger models in which this process occur. This is why, even though they are not complete SUSY models, they are widely used when searching for supersymmetry at the LHC.

1.4.4 Experimental Constraints on Supersymmetry

There are several experimental constraints on supersymmetry. They arise both through direct searches looking for production of SUSY particles and indirectly from measurements that would differ from the Standard Model expectation value if SUSY would play a role.

The direct searches for supersymmetry are performed at collider experiments, where high-energetic particles collide to create heavier particles. Searches for supersymmetry has been performed both at hadron colliders and at e^+e^--colliders.

At the Large Electron-Positron collider (LEP) operating at CERN in the 1990's searches for supersymmetry were mainly focussed on the sleptons, and charginos produced by Z/γ-decays [74–77]. Furthermore, through precise measurement of the width and branching fraction of the Z boson by the LEP experiments, limits on the mass of an LSP coupling to the Z boson can be placed at 47 GeV.

The strong sector as well as the electroweak sector of supersymmetry can be searched for at hadron colliders such as the proton-anti-proton collider Tevatron operating at $\sqrt{s} = 1.96$ TeV and the proton-proton collider LHC operating at $\sqrt{s} = 7,\ 8,$ and 13 TeV.

The two experiments at the Tevatron, CDF and DØ, have placed limits on many different SUSY models containing a big variety of SUSY particles. The searches for squarks and gluinos in events with jets and missing transverse momentum have resulted in limits of the squark and gluino masses in mSUGRA/CMSSM models up to $\sim$ 400 GeV, exceeding the limits placed by LEP [78, 79]. With the increase in collision-energy, the experiments at the LHC can search for even heavier

SUSY particles. The results of the searches for supersymmetry by the ATLAS and CMS experiments will be discussed later in this thesis.

Precision-measurements from flavour physics and observables in the electroweak sector of the Standard Model constrains supersymmetry indirectly. The observation of rare b-decays such as $b \to s\gamma$ [80], and $B_s^0 \to \mu^+\mu^-$ [81] at a rate in agreement with the Standard Model restricts the SUSY phase space. The observed Standard Model rate of $b \to s\gamma$ restricts the off-diagonal mass matrix terms for squarks, whereas an agreement of the $B_s^0 \to \mu^+\mu^-$ with the Standard Model was prophesied to rule out supersymmetry, but in reality disfavoured the same SUSY models as the observed Higgs boson with a mass of 125 GeV [82]. The measured value of the anomalous magnetic moment of the muon [83] disagrees with the Standard Model at a 2.2σ-level favouring SUSY models with light smuons and $\tan\beta \geq 3$ [84].

The observation of a Higgs boson with a mass of 125 GeV is critical for supersymmetry as shown by the requirement in Equation 1.35. The requirement is loosened by radiative corrections to $m_{h^0} < 135$ GeV which is in agreement with the mass of the observed Higgs boson. However, GMSB and AMSB models require the Higgs boson to be lighter than 121.5 GeV and 121 GeV, respectively, clearly disfavouring these sets of SUSY models [85]. There is however a work-around this constraint on AMSB and GMSB: if the top squark is heavy ($m_{\tilde{t}} > 2$ TeV), then the mass of the Higgs boson can reach 125 GeV.

Constraints arising from astrophysical observations are mainly placing restrictions on the LSP assuming that it is the origin of dark matter. From searches for dark matter through direct detection by dark matter scattering off nuclei, limits on both spin-dependent and spin-independent cross sections of dark matter particles interacting with Standard Model particles are found. The DAMA/LIBRA [86] and CoGent [87] experiments look for dark matter in the annual modulation of events arising from the Earth going through a cloud of dark matter. They both find an excess in agreement with light dark matter particles. An excess of positrons over electrons are observed by both PAMELA [88] and AMS [89, 90]; a possible sign of dark matter annihilation. These interpretations of the results are, however, ruled out by the limits on dark matter-nucleus cross section set by XENON100 [91] and LUX [92].

A strong constraint on supersymmetry is the relic density of cold dark matter in the Universe. It is assumed that dark matter was existing in the early Universe and that there was a thermal equilibrium between the annihilation and the creation of dark matter. As the Universe expanded and cooled down, the equilibrium broke and dark matter could no longer be created, it could only annihilate. As the Universe kept expanding and cooled even more, the annihilation process stopped leading to a "freeze-out" of Dark Matter. In the Universe today there is still dark matter present from the early Universe, this is known as the relic density of dark matter. The relic density of cold dark matter has been observed to be $\Omega_c h^2 = 0.1148 \pm 0.0019$ by WMAP [43] and $\Omega_c h^2 = 0.1199 \pm 0.0022$ by Planck [41]. In SUSY models with a pure bino LSP the annihilation cross section will be too small resulting in a relic density which is larger than the observed, while SUSY models with a wino-like or higgsino-like LSP have a larger annihilation cross section resulting in a lower relic density [93]. The gaugino mixing of the LSP is therefore important in

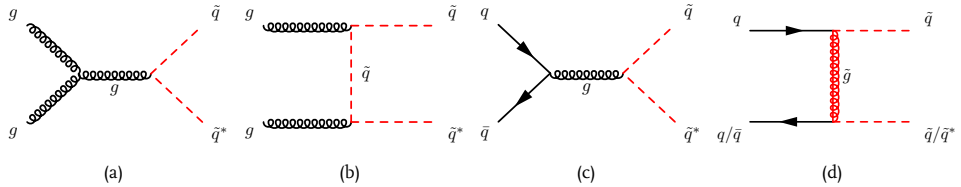

Fig. 1.5 · Feynman diagrams for squark-pair production. The sparticles are marked with red.

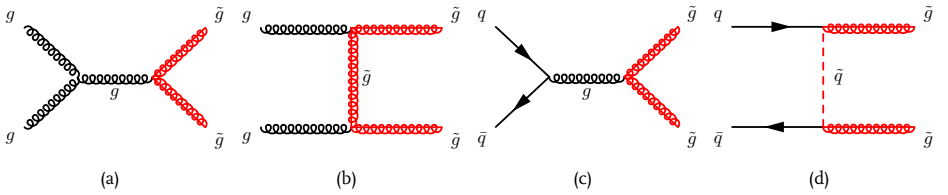

Fig. 1.6 · Feynman diagrams for gluino-pair production. The sparticles are marked with red.

order to get an annihilation cross section which will result in the observed relic density of Dark Matter.

Despite the experimental constraints mentioned here, supersymmetry has a vast number of parameters and can avoid many of the restrictions imposed by these observations.

1.5 Squark and Gluino Production at Hadron Colliders and Their Decay

Squarks and gluinos are coloured and can therefore interact through the strong force. This makes the search for squarks and gluinos at hadron colliders such as the LHC very important. When discussing squarks, a distinction is made between the first two generation of squarks, normally referred to as simply squarks, and the third generation squarks, referred to as the stop and the sbottom. This section will describe some of the phenomenology related to squark and gluino production and their subsequent decay.

1.5.1 Squark and Gluino Production

Squarks and gluinos will be produced in pairs due to R-parity conservation. They will be produced in quark and gluon interactions.

Squark-pairs can be produced through s-, t- and u-channel diagrams both from gluon and quark initial states if the gluinos are not too heavy. The Feynman diagrams for squark-pair production at tree-level through the s- and t-channel are shown in Figure 1.5. If the gluino is decoupled, i.e. very heavy, the diagram in Figure 1.5d is heavily suppressed and can be safely ignored. The kinematics of the produced squarks depends on whether the t-channel containing gluino mediation is available or not and only when that diagram is available can squark-squark-pairs be created.

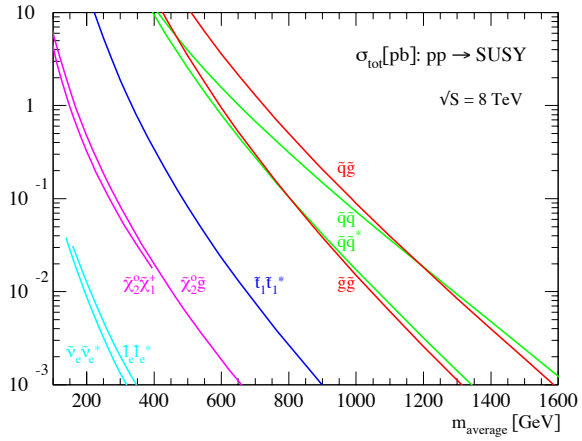

Fig. 1.7 · Cross sections of various sparticles as a function of their mass in proton-proton collisions at $\sqrt{s} = 8$ TeV. Figure taken from Ref. [94].

Just as squarks, gluinos can be pair-produced through both s-, t-, and u-channel diagrams from quark and gluon initial states. The tree-level Feynman diagrams describing gluon-pair production through the s- and t-channel are shown in Figure 1.6. The diagram in Figure 1.6d is only available if the squarks are not decoupled.

Squark and gluinos have, if they are light enough to be produced at hadron colliders, larger cross sections than other sparticles with the same mass. A comparison of cross sections of pair-production of various SUSY particles at $\sqrt{s} = 8$ TeV is shown in Figure 1.7. The cross section of squark-pair production is larger than the stop-pair production by a factor of ~ 100. The squark-pair production cross section is calculated with eight mass-degenerate squarks compared to the cross section of the stop-pair production calculated with a single, light stop. This, however, only accounts for a factor 8 difference between the two cross section. As there are no top quarks present in the proton, the t-channel diagram with gluino exchange in Figure 1.5d is not available for stop-pair production leading to an even a lower cross section. These two effects explain the lower cross section of stop-pair production compared to squark pair production. Since the charginos and neutralinos only interact though the electroweak forces, the production cross sections of chargino and neutralino production are much lower than the squark and gluino production cross sections, where s-channel diagrams with gluinos are major contributors in the production process. In addition, squarks and gluinos carry colour charge which further enhances their cross section.

1.5.2 Squark and Gluino Decay

In R-parity conserving supersymmetry, squarks and gluinos are unstable and will decay immediately after being produced into a final state eventually consisting of Standard Model particles and the LSP.

Squarks will preferably decay into a gluino, $\tilde{q} \to q\tilde{g}$, if the decay channel is available due to the strong gluino-squark-quark coupling. If the gluino is heavier than the squarks, the squarks will decay into a quark and a neutralino, $\tilde{q} \to q\tilde{\chi}_i^0$, or a quark and a chargino, $\tilde{q} \to q'\tilde{\chi}_i^\pm$. Depending on the mass and the mixing of the neutralinos and the charginos as well as whether the squark is "right"- or "left"-handed, different decay chains will be favoured. The simplest decay, $\tilde{q} \to q\tilde{\chi}_1^0$, is kinematically favoured, and may be preferred by the right-handed squark. If the decay through wino-like $\tilde{\chi}_2^0$ and $\tilde{\chi}_1^\pm$ is allowed the left-handed squarks may prefer the longer decay-chain to the direct decay. The higgsino-couplings to the first two generations of squarks is small and therefore decays into higgsino-like neutralinos or charginos are disfavoured. The gluino, chargino, and heavier neutralino will subsequently decay until a final state with $\tilde{\chi}_1^0$ is reached. This can create long decay chains known as cascade decays.

Gluinos decay through an on- or off-shell squark. If the squark is lighter than the gluino, the gluino will decay in a two body decay, $\tilde{g} \to q\tilde{q}$, whereas if the squarks are decoupled, the decay will go through an off-shell squark to either $\tilde{g} \to qq\tilde{\chi}_i^0$ or $\tilde{g} \to qq'\tilde{\chi}_i^\pm$. The squarks, neutralinos and charginos will decay as described above eventually into final states containing the LSP. This can again lead to long decay chains with many particles in the final state.

2

The LHC and the ATLAS Detector

When very energetic protons collide, the heavier particles of the Standard Model as well as the ones predicted by physics beyond the Standard Model can be produced. The Large Hadron Collider at CERN provides a large number of high-energy proton-proton and Pb-Pb collisions so the Standard Model can be studied and tested in detail and maybe hints of new physics beyond the Standard Model can be found.

Heavy particles are typically unstable and will decay to lighter particles. To study the remnants of the heavy particles, large detectors are built. The large detectors measure the particles emerging from the collisions. The analyses presented in this thesis are all based on data collected by the ATLAS detector which is one of the large detectors used to study the collisions of protons in the Large Hadron Collider.

In this chapter an overview of the Large Hadron Collider, the ATLAS detector, and their performance during operation of proton runs from 2010 to 2015 are given. Since simulations play an important role in high energy particle physics, Monte Carlo simulations, event generators, and detector simulations are presented as well.

2.1 The Large Hadron Collider

The Large Hadron Collider (LHC) [95–98] is a circular accelerator and collider situated at the border between France and Switzerland near Geneva and is operated by the international research laboratory CERN. The accelerator is located approximately 100 m under ground in the 26.7 km circular tunnel where the Large Electron Positron collider (LEP) [99] was in operation until 2000.

The LHC is designed to accelerate and collide protons at a centre-of-mass energy of $\sqrt{s} = 14$ TeV at a luminosity of 1×10^{34} cm^{-2}s^{-1}. However, due to technical problems with the superconducting magnets in 2008, it has operated with a maximum collision energy of $\sqrt{s} = 8$ TeV until 2012 with an upgrade to $\sqrt{s} = 13$ TeV in 2015. Besides proton collisions, the LHC is designed to collide Pb nuclei either with other Pb nuclei or with protons. The lead nuclei are brought to collision at an energy of 2.76 TeV/nucleon leading to a centre-of-mass energy of Pb-Pb collisions of 1.15 PeV. Since the focus of this thesis is the search for the production of supersymmetric particles in proton collisions, the remainder of this chapter will be concentrated on the proton beams of the LHC.

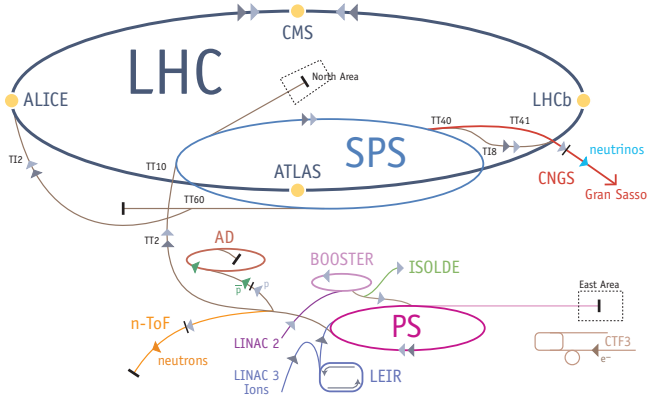

Fig. 2.1 · Illustration of the full accelerator complex at CERN. The arrows indicate the direction of particles. The protons travel from LINAC2 through the BOOSTER, PS, and SPS before arriving at the LHC. The figure is taken from Ref. [100].

The beams of protons are not directly injected into the LHC at low energy, but are first accelerated to a high energy by a set of accelerators. An illustration of the full accelerator complex at CERN can be seen in Figure 2.1.

The protons come from hydrogen atoms where the electrons are stripped off. The protons are first accelerated to an energy of 50 MeV by a linear collider, LINAC2, before they are injected into the first circular accelerator, the BOOSTER. In the BOOSTER, the proton beams are accelerated to an energy of 1.4 GeV before they are injected into the Proton Synchrotron (PS) where they are accelerated to 25 GeV. From the PS, the protons are injected into the Super Proton Synchrotron (SPS) to be accelerated to 450 GeV. The protons are then injected into the LHC for further acceleration.

Before the proton beams reach the LHC, they are ordered into bunches of protons rather than a continuous string of single protons. The design value of the number of protons per bunch is 1.15×10^{11}. There will be 2808 bunches per beam when it is fully populated. The bunches are separated by a multiple of 25 ns.

The beams of protons are held in the circular orbit of the LHC with the use of an intrinsic system of superconducting magnets. The 1232 superconducting dipole magnets provide a magnetic field of 8.33 T and bend the proton beams to follow the ring of the LHC. The beams of protons are focussed and defocussed with the use of 392 superconducting quadrupole magnets functioning as lenses. Since the LHC is not perfectly circular, a set of sextupole and quadrupole magnets are used to keep the proton beams within the beam pipe.

Magnets can only change the direction of motion of a charged particle, but they cannot increase or decrease its energy. To accelerate the protons from the injection energy of 450 GeV per beam to the design energy of 7 TeV per beam, a 400 MHz superconducting radio frequency (RF) cavity system is used. There are two RF cavity systems, one for each beam. Each system consists

of eight cavities each with a 2 MV accelerating voltage resulting in a total accelerating field of 5.5 MV/m.

The proton beams are brought to collision at four interaction points where large detectors are located to record the proton collisions. The four large detectors are the two general purpose detectors - ATLAS [101] and CMS [102] - and the two more specialised detectors: ALICE [103] and LHCb [104]. The general purpose detectors are designed to study a wide range of physics processes of the Standard Model and search for physics beyond the Standard Model such as supersymmetry. They are especially designed to search for the Higgs boson which was discovered in 2012. The two general purpose detectors are built using two different designs to ensure that eventual discoveries of physics beyond the Standard Model is cross-confirmed. The ALICE detector is designed to study Pb-Pb and Pb-p collisions where dense states of matter is created similar to the state of the Universe immediately after the Big Bang. The LHCb experiment is specialised in precise studies of physics related to b-hadrons, in particular to study possible sources of CP-violation that could explain the matter-antimatter asymmetry observed in the Universe.

In addition to the four large experiments at the LHC ring, there are three smaller experiments. The LHCf [105] experiment consists of two imaging calorimeters each located along the beam line 140 m away from the interaction point on both sides of the ATLAS detector. It is designed to study the neutral particles emitted in the very forward regions simulating the particles of cosmic rays. The TOTEM [106] experiment is dedicated to study the very forward physics of proton collisions. It is situated along the beam pipe approximately ± 500 m from the interaction point of the CMS detector. The MoEDAL [107] experiment is located at the interaction point of the LHCb detector and is designed to trap magnetic monopoles which are hypothetical particles with magnetic charge.

2.1.1 Luminosity

The probability of creating a supersymmetric particle when colliding protons is very low. The overwhelming majority of proton collisions results in low-energy scatterings of the partons within the protons and only a small fraction of the collisions results in events with a large energy transfer, i. e. high-p_{T} events. The probability of a specific processes to happen, e. g. the production of a squark or gluino, in a collision is given by the cross section $\sigma(\sqrt{s})$ which depends on the energy of the proton collision, $\sqrt{s}$, and the physics governing the processes, e. g. the mass of the particle created and its couplings. Many proton collisions are therefore needed in order to study rare processes.

The number of events per second of a given process, N, depends on the cross section of the process, σ, and the luminosity of the collisions, L:

$$N = \sigma L. \tag{2.1}$$

The luminosity depends solely on the parameters of the beams. The luminosity of a beam with a Gaussian profile is given as [98]:

$$L = \frac{N_p^2 n_b f_{\mathrm{rev}} \gamma_r}{4\pi\sigma_T} F, \tag{2.2}$$

where N_p is the number of particles in a bunch, n_b is the number of bunches in a beam, f_{rev} is the revolution frequency, γ_r is the relativistic γ-factor, σ_T is the transverse beam cross section, and F is a geometrical function accounting for the luminosity reduction due to the crossing angle at the interaction point. The design peak luminosity of the LHC is 10^{34} cm^{-2}s^{-1}. The collisions of proton bunches at the interaction points of the LHC result in fewer protons per the bunches and a diffusion of the beam. This leads to a larger transverse cross section of the beam and thereby a decrease in luminosity.

The size of a data set is given as the luminosity integrated over time:

$$\mathcal{L} = \int L \mathrm{d}t, \tag{2.3}$$

and is referred to as integrated luminosity or simply as luminosity (a nomenclature that is highly confusing). The integrated luminosity is normally given in inverse barns, $\text{b}^{-1} = 10^{24}$ cm^{-2}. A dataset is typically characterised by its integrated luminosity and the collision energy.

Due to the high number of protons in each bunch, several proton collisions can happen each time two bunches cross. The multiple proton collisions are known as pile-up. Pile-up is divided into two classes: in-time pile-up where the proton collisions seen by the experiment come from the same bunch crossing and out-of-time pile-up where proton collisions from previous bunch crossings are interfering. The luminosity depends on the in-time pile-up and can be written in terms of the number of proton interactions per bunch crossing, μ, leading to the following relation between μ and L [108]:

$$\mu = \frac{L \sigma_{\text{inel}}}{n_b f_{\text{rev}}}, \tag{2.4}$$

where σ_{inel} is the total inelastic cross section of proton collisions.

2.2 The ATLAS Detector

The ATLAS detector [101, 109, 110] is one of the general purpose detectors at the LHC. It is designed in a cylindrical shape around the interaction point and with its length of $\sim$ 40 m and radius of $\sim$ 25 m, it is the largest experiment at the LHC. The ATLAS detector is symmetric in the plane transverse to the beam direction and consists of layers of subdetectors. A sketch of a cut-away look at the ATLAS detector with all its subdetectors can be seen in Figure 2.2. The subdetector types listed from the beam pipe and out are: inner detectors where the tracks of charged particles are recorded, calorimeters used to measure the energy of electrons, photons, and strongly interacting particles, and finally the muon spectrometer, where the tracks of muons are recorded. A magnet system is installed to allow the measurement of the p_{T} of charged particles through the curvature of their tracks.

The coordinate system of ATLAS is right-handed originating from the centre of the detector at the nominal interaction point with the x-y-plane perpendicular to the direction of the beam and the z-axis in the direction of the beam line. The coordinate system is designed such that the x-axis points towards the centre of the LHC and the y-axis points upwards. Rather than using

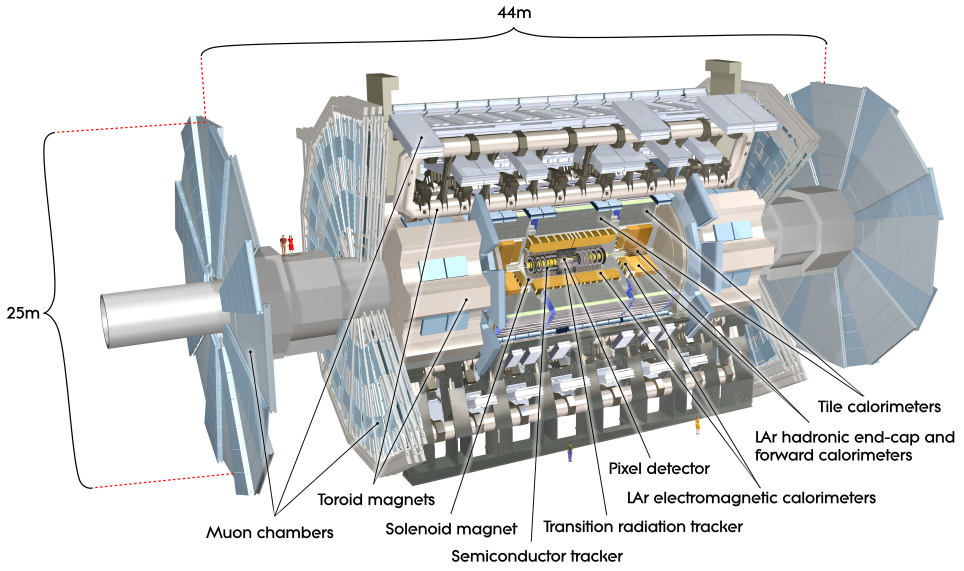

Fig. 2.2 · Illustration of a cut-away look of the full ATLAS detector with indication of subdetectors, magnet systems, and size. The figure is taken from Ref. [101].

a xyz-coordinate system, a polar coordinate system with the azimuthal angle, ϕ, and the polar angle, θ, measured from the beam line is used.

The pseudo-rapidity, η, is used often to describe the position of a particle. It is related to θ by:

$$\eta = -\ln\tan(\theta/2)\,. \tag{2.5}$$

The difference in pseudo-rapidity, $\Delta\eta$, is invariant under a boost in the z-direction and is therefore not dependent on the reference frame. The ATLAS detector can be split into two regions based on the pseudo-rapidity: the central "barrel" region at small values of $|\eta|$ ($|\eta| <\sim 1.4$) and the "end-cap" region at larger $|\eta|$-values[1]. For massive objects where the massless assumption ($E \gg m$) does not apply the rapidity ($y = \frac{1}{2}\ln[(E+p_z)/(E-p_z)]$) is used instead of the pseudo-rapidity.

A set of experimental quantities are defined in the transverse, xy-plane: the transverse energy, $E_{\mathrm{T}} = E\sin\theta$, the transverse momentum $p_{\mathrm{T}} = p\sin\theta$, and missing transverse momentum, $E_{\mathrm{T}}^{\mathrm{miss}}$, measuring the imbalance in the energy and momentum in the transverse plane. The transverse impact parameter, d_0, of a trajectory of a particle is defined as the shortest distance in the transverse plane between the trajectory and the beam axis. The longitudinal impact parameter of a trajectory, z_0, is defined as the z-position of the point of the trajectory closest to nominal beam axis, $x = 0$ and $y = 0$, or closest to the primary vertex, i. e. the position of the proton interaction with highest $\sum p_{\mathrm{T}}$.

[1] The exact values of η defining the barrel and end-cap regions depend on the subdetector in question.

Detector Component	Resolution	$\lvert\eta\rvert$ Coverage	
		Measurement	Trigger
Tracking detectors	$\sigma_{p_T}/p_T = 0.05\% \cdot p_T \oplus 1\%$	≤ 2.5	–
EM calorimetry	$\sigma_E/E = 10\%/\sqrt{E} \oplus 0.7\%$	≤ 3.2	≤ 2.5
Hadronic calorimetry:			
Barrel and end-cap	$\sigma_E/E = 50\%/\sqrt{E} \oplus 3\%$	≤ 3.2	≤ 3.2
Forward	$\sigma_E/E = 100\%/\sqrt{E} \oplus 10\%$	$3.1 \leq \lvert\eta\rvert \leq 4.9$	$3.1 \leq \lvert\eta\rvert \leq 4.9$
Muon spectrometer	$\sigma_{p_T}/p_T = 10\%$ at $p_T = 1$ TeV	≤ 2.7	≤ 2.4

Table 2.1 · The design resolution and coverage of the tracking detectors, electromagnetic calorimetry, hadronic calorimetry, and the muon spectrometer. The numbers are taken from Ref. [101].

The physics program of the ATLAS detector is rich and consists of high precision measurement of properties of the Standard Model as well as searches for new physics beyond the Standard Model. In order to fulfill the physics goals the resolution on calorimetry and tracking must be good. The design resolutions for tracking, electromagnetic calorimetry (EM), hadronic calorimetry, and the muon spectrometer are given in Table 2.1.

2.2.1 Magnet System

A charged particle moving with a velocity $\vec{v}$ in a magnetic field, $\vec{B}$, will feel the Lorentz force, $\vec{F} = q \cdot \vec{v} \times \vec{B}$. Trajectories of charged particles will thus as a consequence of the Lorentz force bend in a magnetic field depending on the p_T of the particles. The magnet system of the ATLAS detector [111] consists of two magnets: the solenoid magnet surrounding the inner tracking detectors, and the toroid magnet system integrated within the muon spectrometer.

The Solenoid Magnet

The solenoid magnet [112] located just beyond the inner tracking detectors is a super-conducting magnet. It consists of a single coil and provides a magnetic field of 2 T in the direction of the beam axis. The layout of the magnet is designed to minimise the amount of material in front of the calorimeter to ensure that the energy loss of particles traversing the magnet is kept at a minimum. Besides providing measurement of the p_T of charged particles, it also ensures that the very low energy charged particles will bend-off and never reach the calorimeter.

The Toroid Magnets

The toroid magnets [113, 114] are air-core magnets generating the magnetic field in the muon spectrometer. They are divided into barrel magnets and two end-cap magnets, one on each side of the interaction point. Each of the three magnets consists of eight coils located symmetrically around the beam axis. The magnetic field provided by the toroid magnets is approximately 0.5 T in the barrel region and 1 T in the end-cap regions. They provide a bending power[1] between

[1] The bending power of a magnet is defined as $\int \boldsymbol{B} \mathrm{d}l$, where $\boldsymbol{B}$ is the magnetic field orthogonal to the direction of flight of the muon.

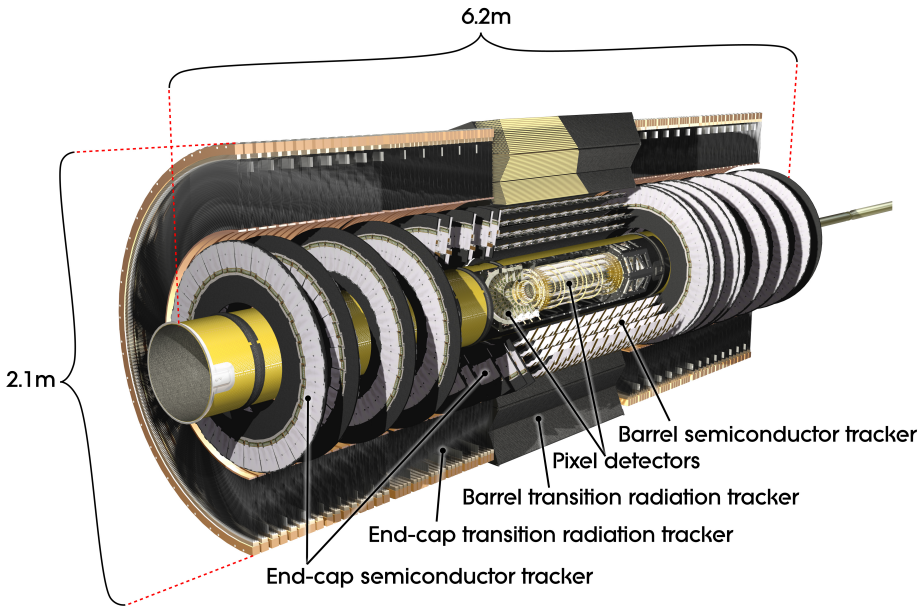

Fig. 2.3 · Illustration of a cut-away look of the inner detector system before the installation of the insertable *B*-layer. The figure is taken from Ref. [101].

1.5 Tm and 5.5 Tm in the barrel region ($|\eta| < 1.4$) and between 1 Tm and 7.5 Tm in the end-cap regions ($1.6 < |\eta| < 2.7$). In the region where the magnetic field of the barrel magnets and the end-cap magnets overlap ($1.4 < |\eta| < 1.6$), the bending power is lower.

2.2.2 Inner Detector

The inner detector (ID) [115, 116] is designed to measure the trajectories of charged particles while stopping them as little as possible. It is immersed in the magnetic field of the solenoid magnet bending the trajectory which enables measurements of the p_T of charged particles. The ID system consists of three detectors: the pixel detector, the semiconductor tracker, and finally the transition radiation tracker. During the long shutdown of the LHC in 2013 and 2014, an additional pixel layer was installed between the beam line and the old pixel detector: the insertable *B*-layer. A sketch of the ID system before the installation of the insertable *B*-layer can be seen in Figure 2.3.

The Pixel Detector

The pixel detector [117] provides the highest granularity of the inner detectors and consisted in Run-1 of 1744 silicon pixel sensors with a nominal size of 50×400 μm^2. The pixels are arranged on a structure consisting of three concentric cylinders in the barrel region with a length of 801 mm and radii of 50.5 mm, 88.5 mm, and 122.5 mm, and each end-cap region consists of three disks arranged perpendicular to the beam line with a radius of 88.8 mm $< R <$ 149.6 mm at distances

of 495 mm, 580 mm, and 650 mm away from the interaction point at $z = 0$. In total the pixel detector covers up to $|\eta| < 2.5$. The intrinsic resolution in the transverse direction (R-ϕ) is 10 μm while it is 115 μm in the longitudinal direction (z in the barrel and R in the end-cap region). Each charged particle is expected to hit 3 layers in the pixel detector.

During the long shutdown of the LHC between 2013 and 2015, the Insertable B-Layer (IBL) [118] was installed along with a new beam pipe. It is a single-layer cylindrical pixel detector located in between the beam pipe and the three-layer pixel detector at a distance of 31 mm $< R <$ 40 mm from the interaction point. It was installed to improve the reconstruction of the primary and especially secondary vertices, which will improve the ability to identify jets originating from b-quarks. Another reason for installing the IBL was to ensure that b-tagging could be performed even if the old b-layer of the Pixel detector would fail. The small distance to the interaction point will furthermore improve the precision of the impact parameters, d_0 and z_0. The pixel size if 50×250 μm^2. The intrinsic resolution is 8.5 μm in the transverse (R-ϕ) direction and 47 μm in the z direction.

The Semiconductor Tracker

The SemiConductor Tracker (SCT) [119, 120] consists of silicon sensors with strip readout. It consists of 4088 modules, 2112 modules arranged in the four concentric cylinders of the barrel region and 1976 modules arranged on nine disks on each side of the interaction point in the end-cap region. The SCT covers in total up to $|\eta| < 2.5$. Each sensor consists of 768 read-out strips with a length of 6.4 cm each separated by 80 μm from each other. In order to be able to measure the full spatial position (x, y, and z coordinate), in each layer of the detector, two sensors are glued together at an angle of 40 mrad. In the barrel region one set of the strips runs in the beam direction, while on the end-cap disks one set of the strips runs in the radial direction. The intrinsic resolution of the SCT is 17 μm in the transverse direction (R-ϕ) and 580 μm in the longitudinal direction (z in the barrel region, and R in the end-cap region). A charged particle traversing the SCT is expected to hit 4 double layers of silicon strips.

The Transition Radiation Tracker

The Transition Radiation Tracker (TRT) [121, 122] is a straw tube detector covering up to $|\eta| < 2.0$. It consists of approximately 300000 straw tubes with a diameter of 4 mm. The straw tubes are filled with a gas mixture consisting of 70% Xenon, 27% CO_2, and 3% O_2. In the barrel region the straw tubes have length of 144 cm and are arranged along the beam axis in a distance of 563 mm $< R <$ 1066 mm from the beam line. In the end-cap region, the tubes have a length of 37 cm arranged radially in wheels. The TRT provides only hits in the transverse (R-ϕ) plane with a resolution of 130 μm per straw. The many straw tubes ensure that a charged particle is expected to leave typically 36 hits in the barrel region and 22 in the end-cap regions.

Aside from the many hits which improve the measurement of the p_T of charged particles, the TRT is designed to be able to discriminate between electrons and charged hadrons, especially charged pions, exploiting transition radiation. The term transition radiation is applied to photons radiated of charged particles as they go from one medium to another. The amount of transition

radiation of a particle depends on E/m, i. e. the relativistic γ of the particle. An electron which has a mass of 0.511 MeV will therefore generate more transition radiation than a charged pion with a mass of 140 MeV. The straw tubes of the TRT are interleaved with a dielectric foil to enhance the transition radiation of charged particles.

2.2.3 Calorimeters

Calorimeters measure the energy of particles (electrons, photons, and hadronic jets) by stopping them. For muon identification, it is important that only the muons reach the muon spectrometer. Other particles must therefore not punch through the calorimeter. The depth of the calorimeter is therefore very important and must extend over many radiation lengths for electromagnetic interactions, X_0[1], or nuclear interaction lengths for strong interactions, λ[2].

There are in general two types of calorimeters: sampling calorimeters consisting of alternating layers that absorb and measure the spray of particles, and homogenous calorimeters where the entire calorimeter is made of the same material that both creates the showers and measures their energy. The calorimeters of the ATLAS detector are sampling calorimeters.

The calorimeter system of ATLAS consists of two calorimeters: one designed to measure the energy of electrons and photons (the electromagnetic calorimeter) and one designed to measure the energy of the hadronic jets (the hadronic calorimeter). A cut-away look at the calorimeter system of the ATLAS detector can be seen in Figure 2.4.

The Electromagnetic Calorimeter

The Electromagnetic Calorimeter (ECAL) [123] is a sampling calorimeter with lead as the absorbing material and liquid Argon (LAr) as the active material extending over $> 22\ X_0$ in the barrel region and $> 24\ X_0$ in the end-cap region. The barrel of the ECAL covers $|\eta| < 1.475$ and the end-cap regions cover $1.375 < |\eta| < 3.2$. The calorimeter is built of accordion-shaped modules[3] to ensure that there are no cracks in any direction of ϕ. The calorimeter consists of a presampler followed by three layers in the barrel region and two in the end-cap regions. The presampler consists of an active LAr layer and covers up to $|\eta| < 1.8$. It is used to correct the energy of the photons and electrons before they reach the actual calorimeter. The thickness of the lead varies as a function of η in order to optimise the energy resolution. The granularity depends on η and is highest in the central barrel region and coarser in some parts of the end-cap regions.The granularity of the presampler is not as fine as in the barrel as it is only used to correct the energy measurements.

The Hadronic Calorimeter

The Hadronic Calorimeter (HCAL) consists of a Tile calorimeter [124] of steel and scintillating material in the barrel ($|\eta| < 1.0$) and in the extended barrel ($0.8 < |\eta| < 1.7$), while the end-cap calorimeter is based on a copper-LAr sampling calorimeter covering $1.5 < |\eta| < 3.2$. In the Tile calorimeter in the barrel and extended barrel regions, the steel is working as the absorbing material

[1] The radiation length is defined as the mean distance where an electron looses all but $1/e$ of its original energy.
[2] The nuclear interaction length is the mean length traveled by hadron through matter before any interactions with the nuclei.
[3] Since parts of the ECAL were assembled in France, the inspiration for the accordion-shape most likely originates from a musette accordion with C-system and tremolo registers rather than a bayan accordion with B-system and casotto registers.

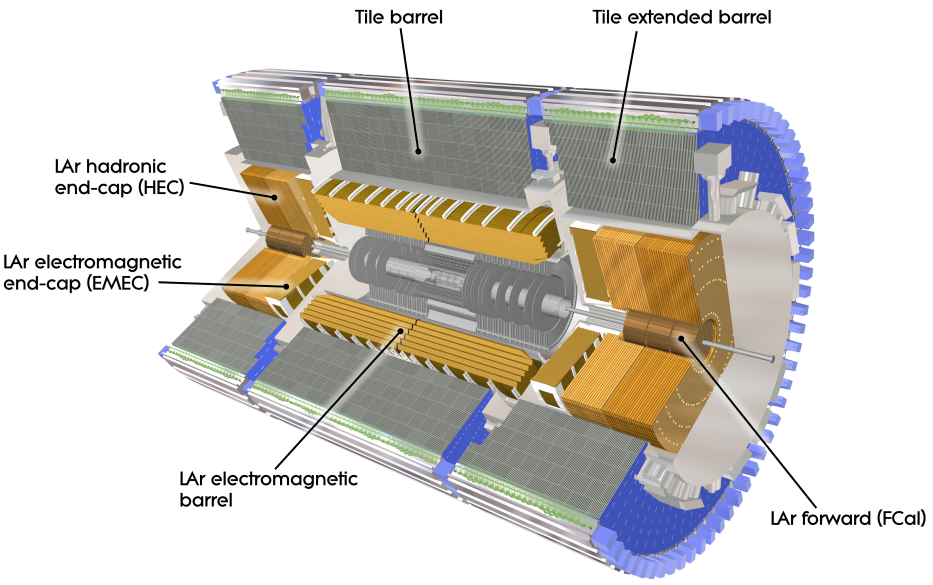

Fig. 2.4 · Illustration of a cut-away look of the calorimeter system of the ATLAS detector. The figure is taken from Ref. [101].

while the scintillators work a the active material. The Tile calorimeter consists of three layers in both the barrel and the extended barrel regions with a total depth of 9.7λ including the material in front of the Tile calorimeter. The end-cap LAr calorimeter consists of four layers arranged in wheels with a depth similar to the tile calorimeter. The granularity of the HCAL depends on the pseudo-rapidity and is finest in the Tile calorimeter and coarser in the LAr end-cap calorimeter.

The Forward Calorimeter

An additional LAr sampling calorimeter is installed at high pseudo-rapidity, the so-called Forward Calorimeter (FCAL). It is installed to provide uniformity of the coverage of the calorimeter system and to reduce non-muon radiation into the muon spectrometer. The FCAL extends over $3.1 < |\eta| < 4.9$ and consists of three layers. The first layer is mainly to measure electromagnetic showers and copper is used as the absorber material. The second and third layer are designed to stop and measure hadronic showers and the absorber material is tungsten. The FCAL is approximately 10 interaction lengths deep. The granularity of the FCAL is coarser than the other calorimeters.

2.2.4 Muon Spectrometer

The muon spectrometer [125] is the outermost subdetector system of the ATLAS detector. As muons are heavier than the electrons, they will not be stopped by the calorimeters, and unlike the tau lepton they are light enough to be treated mostly as a stable particle inside the detector.

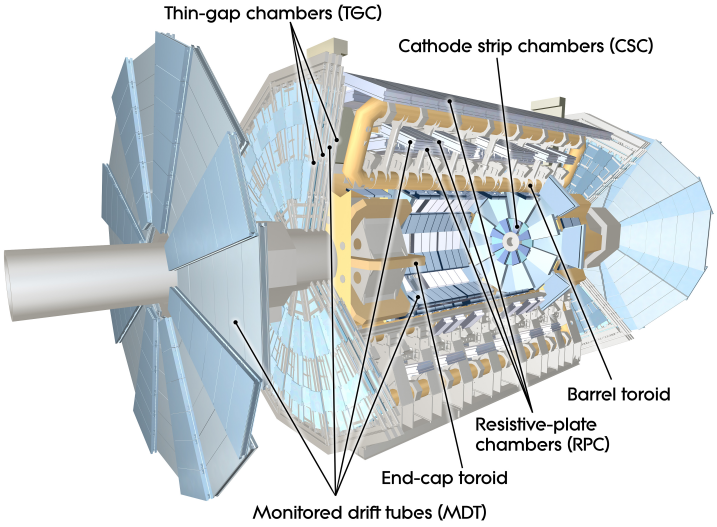

Fig. 2.5 · Illustration of a cut-away look at the muon spectrometer of the ATLAS detector. The figure is taken from Ref. [101].

The muons are therefore expected to arrive outside the calorimeter where a second set of tracking detectors, the muon spectrometer, is installed.

The muon spectrometer is built within the toroid magnets. It consists of a barrel region and end-cap regions with several wheels of muon detectors, most notably the outer large wheel giving the ATLAS detector its characteristic look. The muon spectrometer consists of different kinds of detectors. There are high-precision detectors used for measuring the p_T of the muons, and detectors with a coarser resolution used in the data-taking process (the trigger chambers). An illustration of the muon spectrometer can be seen in Figure 2.5.

Precision Chambers

The precision chambers are organised in a barrel region and an end-cap region. The barrel region consists of three layers of 16 chambers each located both inside and outside the barrel toroid magnets at a radial distance of 5 m, 7.5 m and 10 m from the interaction point. The end-cap regions are composed of four large wheels located at a distance of 7.4 m, 10.8 m, 14 m and 21.5 m from $z = 0$ on each side of the interaction point. The precision chambers cover up to $|\eta| < 2.7$. Over most of the η-range, the precision measurement of the muon tracks is performed by 1150 monitored drift tube (MDT) chambers filled with a mixture of Argon, and CO_2 and with central tungsten-rhenium wire. The MDT chambers measure only hits in the z-direction. The measurement of the ϕ-coordinate of a track is provided by the trigger chambers. In the innermost wheel covering $2.0 < |\eta| < 2.7$, 32 cathode strip chambers (CSC) are used instead of MDT chambers in order to cope with the high rate of hits. The CSCs are multi wire proportional chambers. The size of the MDT chambers increases with the distance to the interaction point. The end-cap wheels are

built of wedge-shaped chambers of two sizes in order to ensure full coverage in ϕ. The resolution of the MDT chambers is 35 μm in the z-direction, while the resolution of the CSCs is 40 μm in the radial direction and 5 mm in the transverse plane.

Trigger Chambers

A second set of muon detectors are installed to be used in the trigger system. The trigger chambers cover up to $|\eta| < 2.4$ for triggering and $|\eta| < 2.7$ for measuring the second coordinate (ϕ) of the track not measured by the MDT chambers. The trigger chambers must provide fast tracking used in the trigger decisions. The trigger chambers are composed of a barrel region covering $|\eta| < 1.05$ and an end-cap region covering $1.05 < |\eta| < 2.7$ (2.4 for triggering). The barrel region consists of three layers of modules of resistive-plate chambers (RPC) with a resolution of 10 mm in the z-direction and 10 mm in the transverse direction. The end-cap region is composed of four layers of thin-gap chambers (TGC), one located in front of the innermost precision tracking wheel and three surrounding the third MDT wheel. The resolution of the TGCs is 2-6 mm in the radial direction and 3-7 mm in the transverse plane.

2.2.5 Forward Detectors

In the very forward regions of the ATLAS detector, three detector systems are designed to study the physics at very high pseudo-rapidities. Two of the detectors, LUminosity measurement using Cerenkov Integrating Detection (LUCID) and Absolute Luminosity For ATLAS (ALFA), are designed to measure the luminosity delivered to ATLAS [126, 127] while the third detector, Zero-Degree Calorimeter (ZDC), is designed to measure the centrality of heavy-ion collisions in ATLAS [128]. The LUCID detector located at $\pm$17 m from the interaction point of ATLAS provides the main luminosity measurement for ATLAS. The ALFA detector is located at $\pm$240 m from the interaction point and consists of scintillating fibers installed in roman pots that can enter the beam pipe of the LHC and get as close as 1 mm to the beam. The ZDC is a quartz-tungsten calorimeter located $\pm$140 m away from the interaction point enabling it to measure the energy of neutral particles emitted at $|\eta| \geq 8.3$.

2.2.6 Trigger System

Every second 40 million proton bunch crossings happen in the centre of the ATLAS detector if the LHC is running with its design bunch spacing of 25 ns[1]. It is not possible to read out and save all of the collisions and it is only a very small fraction of proton collision that results in events with high-p_T or high-E_T objects such as muons, electrons, jets, taus or missing transverse momentum. A system is therefore designed to filter out the events that are found interesting containing high-p_T or high-E_T objects that should be saved. This is known as the trigger system.

Trigger System During Run-1

During 2010, 2011, and 2012, the trigger system of ATLAS consisted of three levels: Level 1 (L1), Level 2 (L2), and Event Filter (EF). Each level is more sophisticated and slower than its predecessor.

[1] The LHC ran with a 50 ns bunch spacing until 2012 resulting in a rate of 20 MHz.

The L1 trigger system is built on hardware and reduces the rate from 40 MHz to 75 kHz. The L1 trigger is based on hits in the trigger chambers in the muon spectrometer and energy deposits measured by the trigger towers in the calorimeters, L1CALO [129]. L1CALO is able to trigger separately on jets, electrons or photons, taus, and $E_{\mathrm{T}}^{\mathrm{miss}}$. The trigger decision is done by the Central Trigger Processor (CTP) based on input from the muon trigger chambers and L1CALO and uses look-up tables to see whether the trigger requirements are met. The decision of the L1 trigger to keep or reject an event is done in 2.5 μs. The L1 trigger forms Regions of Interest (RoIs) which are passed on to the L2 trigger.

The L2 trigger system is software-based and is seeded by the RoIs provided by the L1 trigger. At L2, the energy, coordinates, and type of signature (muon, jet, τ, etc.) is studied in finer detail in the RoIs reducing the rate from 75 kHz to below 6 kHz. The processing time of the L2 trigger is $\sim$ 40 ms. Both the L1 and L2 systems consist predominantly of inclusive triggers, i. e. triggering on a single high-p_{T} or high-E_{T} object in the event, and do not use information on the topology of the event, e. g. the angle between objects or the sum of p_{T} or E_{T} of selected objects.

Events that pass the L2 trigger requirements are sent on to the EF trigger system where a finer granularity of the calorimeter is used and information on tracks in the inner detector is added. Full information of the entire detector can be used in EF triggers and combined variables such as the scalar sum of p_{T} of the jets in an event can be used as the trigger element. At EF level the rate is typically reduced to 400 Hz and decisions are made in approximately 4 s.

An element in the trigger menu usually consists of a trigger object (electron, muon, tau, jet, or $E_{\mathrm{T}}^{\mathrm{miss}}$) and the threshold of the cut on the p_{T} or energy of the object in GeV as well as eventual isolation criteria. Triggers where all triggered events are saved are called un-prescaled triggers. Trigger elements with looser cuts on the p_{T} or the energy of the object will have a higher rate and are suppressed by a prescale[1] to ensure that the possible recording rate is not exceeded. The prescale values decrease with the decrease in instantaneous luminosity in ATLAS during a LHC fill to ensure that the recording rates are kept constant.

To ensure that the data recorded by the ATLAS detector is not biased, minimum bias triggers are included as well. These triggers are highly suppressed by prescales.

Trigger System During Run-2

During the shutdown of the LHC in 2013 and 2014, the trigger system underwent upgrades and changes [130]. Some of the major changes are listed here:

- The rate of the L1 triggers was increased to 100 kHz ensuring that even with increased instantaneous luminosity the trigger thresholds would not increase dramatically.
- Possibility of topological triggers at L1 (L1TOPO), i. e. triggers using combinations of kinematic information of both muon and calorimeter objects. This can be used to trigger on high-mass di-jet events targeting vector boson fusion or di-muon events with a small di-muon opening angle originating from b-hadron decays.

[1] If the prescale is 4 then every 4$^{\mathrm{th}}$ triggered event is saved.

- Upgrade of the central trigger processor to be able to handle the LITOPO decision and to double the number of parallel trigger selections.
- The L2 and EF trigger systems were merged into one, the Higher Level Trigger (HLT). The HLT relies mostly on the algorithms of the former EF trigger system.
- The HLT tracking algorithms are ready to include the new, fast, hardware-based tracking (FTK) expected to be ready for operation in 2016.
- The average rate of the HLT was increased from 400 Hz to 1 kHz.

2.3 Operational Performance of the LHC and ATLAS Experiment

The year 2012 marked the end a successful first run of the LHC (Run-1) with collision energies of $\sqrt{s} = 7$ TeV in 2010 and 2011 increasing to $\sqrt{s} = 8$ TeV in 2012. The discovery of a Higgs-like particle was announced by the ATLAS and CMS collaborations on the 4$^{\text{th}}$ of July 2012, for which the search was one of the important goals of the first run of the LHC. The LHC was shut down for maintenance in 2013 and 2014 and resumed proton collisions in 2015 at an increased collision energy of $\sqrt{s} = 13$ TeV. A summary of the beam parameters, and luminosities in the four years of LHC operation is given in Table 2.2.

During the first two years of Run-1, 2010 and 2011, the LHC ran at a collision energy of $\sqrt{s} = 7$ TeV which is half of the design collision energy. In 2010, the LHC delivered 48 pb^{-1} of which the ATLAS detector recorded 45 pb^{-1}. Between operation in 2010 and 2011 the bunch spacing was decreased from 150 ns to 50 ns, and the number of bunches per beam as well as the number of protons per beam were increased. This resulted in an increase in the peak instantaneous luminosity from 0.21×10^{33} cm^{-2}s^{-1} to 3.65×10^{33} cm^{-2}s^{-1} as well as an increase in the average number of interactions per bunch crossing. In 2011, the ATLAS detector recorded 5.08 fb^{-1} out of the total luminosity of 5.46 fb^{-1} delivered by the LHC.

The collision energy was increased to $\sqrt{s} = 8$ TeV in 2012. With the increase in number of bunches and beam intensity, the peak instantaneous luminosity reached 7.73×10^{33} cm^{-2}s^{-1} and there were 20.7 interactions per bunch crossing on average exceeding the design value of the LHC. In 2012, the LHC delivered a total integrated luminosity of 22.8 fb^{-1} of which 21.3 fb^{-1} were recorded by the ATLAS experiment. The integrated luminosity accumulated in 2011 and 2012 as well as the average number of interactions per bunch crossing are shown in Figure 2.6.

A shutdown of the LHC was scheduled for 2013 and 2014 where maintenance would be performed. Spring 2015 marked the start of the second run period of the LHC (Run-2). The collision energy was increased to $\sqrt{s} = 13$ TeV which is only 1 TeV below its design value. The number of bunches was increased and the bunch spacing reached its design value of 25 ns. In total, the LHC delivered 4.2 fb^{-1} in 2015 of which 3.9 fb^{-1} were recorded by the ATLAS experiment. The cumulative integrated luminosity and the average number of interactions per bunch crossing during the operation in 2015 are shown in Figure 2.7.

[1] There was one fill with 1854 bunches, but 1331 was the typical value.

Beam Parameters	Design	2010	2011	2012	2015
Centre-of-mass energy, $\sqrt{s}$ [TeV]	14	7	7	8	13
Peak luminosity, L [10^{33} cm^{-2}s^{-1}]	10	0.21	3.65	7.73	5.02
Integrated luminosity, delivered, $\mathcal{L}$ [fb^{-1}/y]	80-120	0.048	5.46	22.8	4.2
Integrated luminosity, recorded, $\mathcal{L}$ [fb^{-1}/y]	–	0.045	5.08	21.3	3.9
Maximum number of colliding bunches	2880	348	1331[1]	1380	2232
Maximum number of protons per bunch [10^{11}]	1.15	1.2	1.4	1.6	1.2
Minimum bunch spacing [ns]	25	150	50	50	25
Average pile-up $\langle\mu\rangle$	19.02	< 3	9.1	20.7	13.7

Table 2.2 · Design values of beam parameters and luminosities as well as the actual values during the four years of LHC operation. The design values are taken from Ref. [95] while the values from operation in the years 2010 to 2015 are taken from Ref. [131].

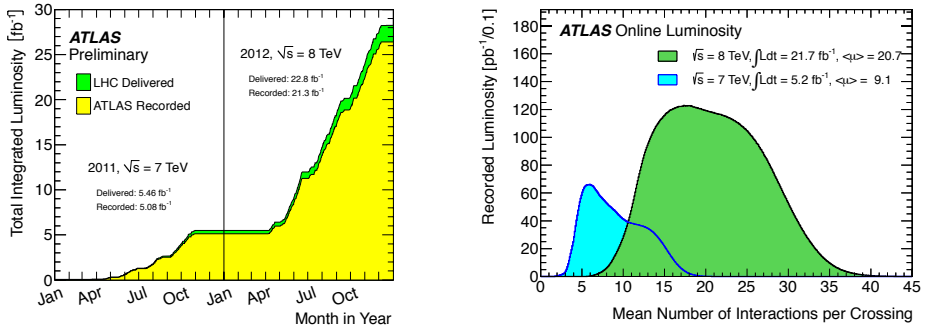

(a) (b)

Fig. 2.6 · The integrated luminosity accumulated over time delivered by the LHC (green) and recorded by ATLAS (yellow) in 2011 at $\sqrt{s} = 7$ TeV and in 2012 at $\sqrt{s} = 8$ TeV, and the mean number of interactions per bunch crossings in 2011 (cyan) and in 2012 (green) normalised to the integrated luminosity.

The data-taking period of 2016 has commenced. The collision energy is unchanged with respect to 2015. A milestone has however been reached as the peak instantaneous luminosity delivered by the LHC has reached its design value of 1×10^{34} cm^{-2}s^{-1}.

The ATLAS detector has been consistent in its recording percentage throughout Run-1 and the beginning of Run-2. In all years of LHC operation, approximately 93% of the delivered luminosity was recorded by the ATLAS experiment. With the subdetector systems recording over 95% of the time while the beams were in stable condition [132], the first run of the LHC and the beginning of the second run has proven a great success in the operation of the ATLAS experiment.

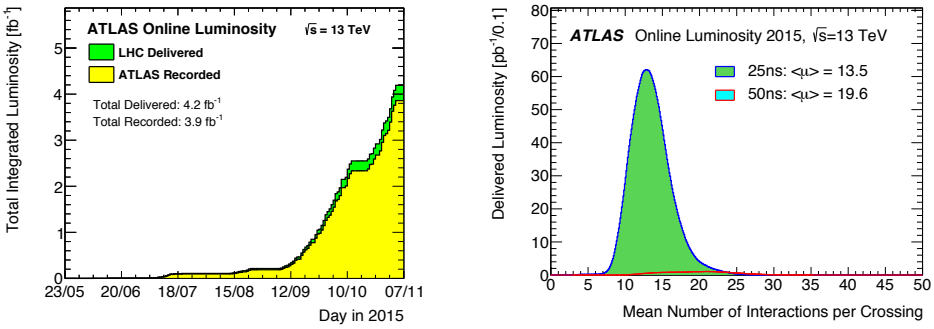

(a)

Fig. 2.7 · The integrated luminosity cumulated over time delivered by the LHC (green) and recorded by ATLAS (yellow) in 2015 at $\sqrt{s} = 13$ TeV, and the mean number of interactions per bunch crossings normalised to the integrated luminosity with a 25 ns (green) and 50 ns (cyan) bunch spacing.

2.4 Simulations

In order to compare observation to theory, one must know what to expect from theory. The Standard Model is very complex and simulations are therefore used to compare expectations to observations.

Proton-proton collisions are simulated in order to study the physics at the LHC. The simulations are done in steps: first the physics process is simulated with the event generators and afterwards the detector simulation is performed so the simulations can be compared directly to the measurements.

2.4.1 Event Generation

Collisions of protons rarely result in hard-scattering events with high-p_{T} objects in the final state. Therefore rather than simulating proton collision inclusively, sub-processes of interest are simulated, e. g. production of W or Z bosons, $t\bar{t}$-pairs or hypothetical particles such as squarks and gluinos.

The hard-scattering processes are simulated using Monte Carlo (MC) techniques where physics processes are generated using random numbers following the frequency expected from theory. The samples of the simulated hard-scattering process are then normalised to their respective cross sections so they can be compared to data.

Proton collisions are rich and very complex. Aside from the eventual hard-scattering process, the partons (quarks and gluons) radiate gluons which can either radiate off more gluons or split into quark-antiquark pairs. This is known as parton showering. Once the partons reach a certain energy, they form into clusters of particles referred to as jets, i. e. they hadronise. There are different models used for parton showering and hadronisation. The parts of the protons not participating in the hard-scattering will interact as well. This is known as the underlying event.

There are many Monte Carlo generators available for simulating proton collisions. In general they fall into two categories: general purpose generators and matrix element generators.

The general purpose generators simulate the entire proton collision including parton showering and hadronisation. The hard-scattering matrix element is typically done to leading order. The general purpose generators are limited to $2 \to 1$ and $2 \to 2$ processes and any extra particles must come from the parton showering model. Examples of general purpose generators are PYTHIA [133, 134], SHERPA [135], HERWIG [136, 137], and HERWIG++ [138].

Matrix element generators simulate only the hard-scattering and rely on interfaces with other (general purpose) generators for the parton showering process. $2 \to n$ processes are normally included and thereby a specified number of final and initial state radiation particles can be calculated at matrix element level instead of simulated through parton showering. The matrix element is either calculated to leading order like in matrix element generators as MADGRAPH [139] and ALPGEN [140] or to next-to-leading order as in matrix element generators like POWHEG-BOX [141–143] or MC@NLO [144–147].

The last ingredient needed for event generation is knowledge of the energy distributions of the partons within the proton, i. e. parton distribution functions (PDF) which were introduced in Section 1.1.5. A PDF set consists of the energy distribution of the gluons and quarks within the proton. There are many available PDF sets, for example CT10 [36] and CTEQ6L1 [37].

2.4.2 Detector Simulation

Once the event generation including the hard scattering, the decays of short-lived particles, and the showering is done, the paths of particles emerging from the collision traversing the ATLAS detector are simulated. A full simulation of the ATLAS detector is built in the GEANT4 [148] framework simulating the response of the detector as particles interact with its matter. Simulating the full ATLAS detector takes a considerable amount of computing time. Especially, the calorimeter simulation is lengthy. A parameterisation of the calorimeter exists significantly reducing the computational time of simulating particles going through the ATLAS detector. The fast simulation of the calorimeter implemented in ATLFASTII [149] is not as accurate as the full simulation as it does not use the full granularity of the calorimeter, but this is the price one must pay in order to reduce computing time.

The simulation of particles traversing the ATLAS detector is reported as hits in the subdetector systems of ATLAS. The hits are digitised afterwards to resemble the actual response of the electronics of the detector. The digitised simulation is then run through the same calibration and reconstruction algorithms used for the data.

If the exact layout of the detector is not known, samples at truth level, i. e. the results of the event generation without detector simulation, can if necessary be used for studies. To get a more realistic simulation, the energy or p_{T} of particles emerging from the simulated collision can be smeared using a Gaussian distribution with the estimated resolution of the detector as the width. This method is used in the studies of future searches for squarks and gluinos described in Chapter 7.

3 Particle Identification and Reconstruction

Particles going through the ATLAS detector are measured as hits in the subdetector systems with exception of the neutrinos that interact only through the weak force and therefore leave no hits in any subdetector system. The hits in the subdetector system must then be reconstructed as tracks of charged particles in the inner detector and muon spectrometer and clusters in the calorimeters. Every type of particle leaves a different trace in the detector allowing identification of the various particles.

In this chapter, the characteristics of particles traversing the ATLAS detector as well as the reconstruction and identification methods and their performances are presented.

3.1 Particle Characteristics

The ATLAS detector is designed such that each type of particle, i. e. quarks, gluons, electrons, muons, photons, hadronically decaying taus, and neutrinos, will leave a distinct trace. The characteristics of the particles are shown in Figure 3.1 and summarised in the following list.

Jets originate from strongly interacting particles that hadronise as they traverse the detector. They are identified by an energy deposit in the calorimeters, especially in the hadronic calorimeter, along with eventual tracks from charged particles. Jets originated from b-quarks can be identified by a secondary vertex caused by the long lifetime of the b-quark.

Photons are not electrically charged and will therefore not leave any tracks in the inner detector. However, they can convert into an electron-positron pair due to interaction with the material of the detector. Unconverted photons are identified as a shower in the electromagnetic calorimeter without any associated tracks, while converted photons are identified by deposit in the electromagnetic calorimeter matched to a displaced vertex with an electron-positron pair emerging.

Electrons will leave a shower in the electromagnetic calorimeter very similar to that of photons. Unlike photons, they are charged resulting in a track in the inner detector originating from the interaction point and pointing towards the shower in the calorimeter.

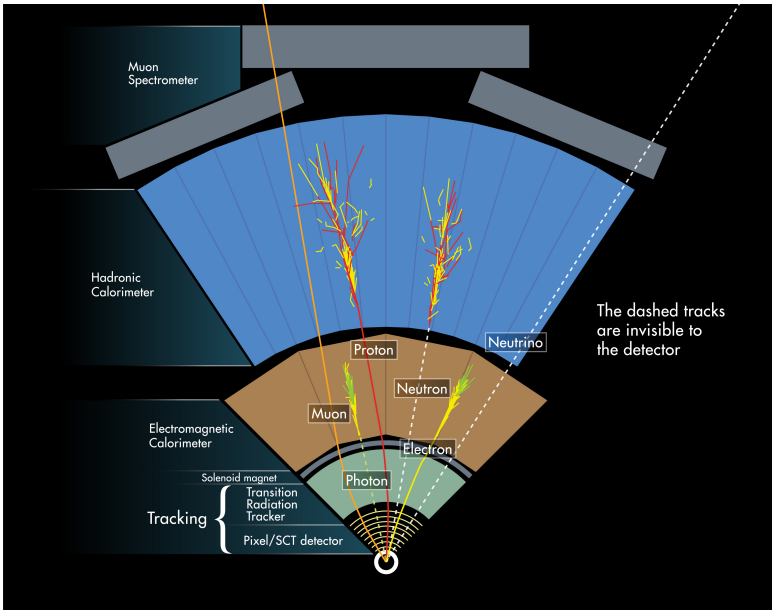

Fig. 3.1 · Illustration of particles traversing a wedge of the ATLAS detector. The characteristic traces of each particle type as the go through the detector are shown. The figure is taken from Ref. [150].

Muons have a lifetime long enough to be treated as stable particles in the detector. Due to their higher mass, they emit less bremsstrahlung than electrons. Muons are therefore not stopped by the calorimeters and will reach the muon spectrometer. They are reconstructed from tracks in the inner detector and the muon spectrometer.

Hadronically decaying taus will result in an energy deposit in the hadronic calorimeter. They can be distinguished from jets originating from quarks and gluons by the number of tracks associated to the shower in the calorimeter, the radius of the shower, and the substructure of the shower. Hadronically decaying taus will be referred to simply as taus in the remainder of this thesis.

Neutrinos interact only through the weak force and will leave the detector without a trace. They are therefore not directly measured. Their energy can be measured indirectly through a momentum imbalance in the transverse plane of the detector, the missing transverse momentum. The lightest supersymmetric neutralino will have a similar signature.

3.2 Tracks and Vertices

Charged particles leave hits in the inner detector which are combined into a track. Reconstruction of the vertex, i. e. the point from which the tracks originate, is important. Multiple pp collisions

occur at each bunch crossing and it is important to correctly assign the right tracks to the right vertex in order to understand what happened in the proton-proton interaction.

3.2.1 Track Reconstruction

Tracks are reconstructed from hits in the inner detector [151–153]. Tracks with a p_T greater than 400 MeV and with a lifetime greater than 3×10^{-11} s are considered for track reconstruction. There are two approaches to form tracks:

Inside-out tracking uses hits in the Pixel and SCT detector as the seed for the track candidate. Hits are added to the track candidate moving away from the centre of the detector. This is the baseline approach to track reconstruction in ATLAS and will be the focus of this section.

Outside-in tracking starts with hits in the TRT as the seed for the track candidate and moves towards the inner layers of the detector when extending the track candidate.

The seeds of track candidates consist of three hits in the silicon detectors, the pixel and the SCT, translated into three-dimensional space points. There are four types of combinations of space points depending on how many hits there are in each detector: three hits in either pixel detector or the SCT or one hit in one of the detectors and two hits in the other.

Tracks are reconstructed from the seeds by adding space points following the direction given by the seed moving away from the collision point. The additional points are chosen by a combinatorial Kalman Filter [154]. More than one track candidate can be formed from the same seed.

The same space point can be assigned to more than one track candidate and these ambiguities in the track reconstruction must be resolved to remove fake tracks. Tracks are assigned a score depending on their quality. There are three things that can influence the score of a track candidate: holes, outliers, and hits. Holes are space points where one would expect a hit in the detector, but none is observed. Outliers are space points assigned to the track candidate which result in a poor track fit. Both holes and outliers reduce the score. If two track candidates share a hit, then it is assigned to the track candidate with the highest score. The scores of the two track candidates are then recalculated and other ambiguities will be resolved until no more remain. The transverse impact parameter, d_0, and longitudinal impact parameter, z_0, defined in Section 2.2, are measured from the reconstructed tracks.

For Run-2 operation the track reconstruction was updated to include the newly installed extra layer of the Pixel detector, the IBL. The ambiguity solver was re-optimized for Run-2 operation, as well.

The efficiency of the track reconstruction is defined as the fraction of charged particles originating from the interaction point with a mean lifetime greater than 3×10^{-11} s and $p_T > 400$ MeV and within $|\eta| < 2.5$ matched to a reconstructed track. It is measured in a minimum bias simulation sample. Two track selections are defined when evaluating the efficiency: The `Default` or `Loose` allowing for holes in the pixel layers and with at least 7 hits in the silicon detectors, and the `Robust` or `Tight Primary` requiring at least 9 or 11 hits in the silicon detectors depending on $|\eta|$ and no holes allowed in the pixel layers.

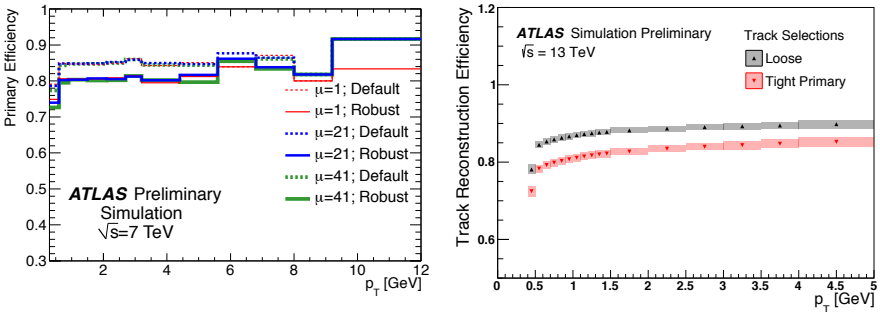

Fig. 3.2 · Track reconstruction efficiencies as a function of track p_{T} obtained from simulations with collision energies of $\sqrt{s} = 7$ TeV (a) and $\sqrt{s} = 13$ TeV (b). The efficiencies obtained from the $\sqrt{s} = 7$ TeV sample are shown with three pile-up conditions. The figures are taken from Refs. [152, 155].

The track reconstruction efficiency as a function of p_{T} of the track can be seen in Figure 3.2 at two collision energies corresponding to conditions in the 2011 and 2015 operation of the LHC. It can be seen that the reconstruction efficiency of `Robust` tracks in Figure 3.2a is similar to that of the `Tight Primary` tracks in Figure 3.2b. The effect of multiple interactions per proton bunch crossing is studied at $\sqrt{s} = 7$ TeV. The fraction of fake reconstructed tracks increases with the higher occupancy caused by increased pile-up. However, by applying the `Robust` or `Tight Primary` selection, the fraction of fake reconstructed tracks decrease and no effect of the pile-up is seen.

3.2.2 Vertex Reconstruction

Primary vertices, i. e. vertices corresponding to a proton-proton interactions, are reconstructed using a *finding-through-fitting* procedure [152, 156, 157].

Vertices are reconstructed from tracks with at least 4 hits in the SCT, 9 hits in total in the silicon trackers (pixel and SCT), and no holes in the pixel detector. They must have $p_{\mathrm{T}} > 400$ MeV, $|d_0| < 4$ mm and a resolution of the transverse and longitudinal impact parameters of $\sigma(d_0) < 5$ mm and $\sigma(z_0) < 10$ mm. For the vertex reconstruction of Run-2, additional requirements of at least 1 hit in the IBL or the first layer of the pixel detector and no more than 1 hole in the SCT are imposed.

The vertex reconstruction is performed in the following five steps:

1. A set of tracks is defined fulfilling the previously described requirements.

2. A seed position of the vertex is found based on the beam spot position.

3. The optimal position of the vertex is found with an iterative fit [158] using the set of tracks and the seed position of the vertex as input. After a fit is performed, each track is assigned

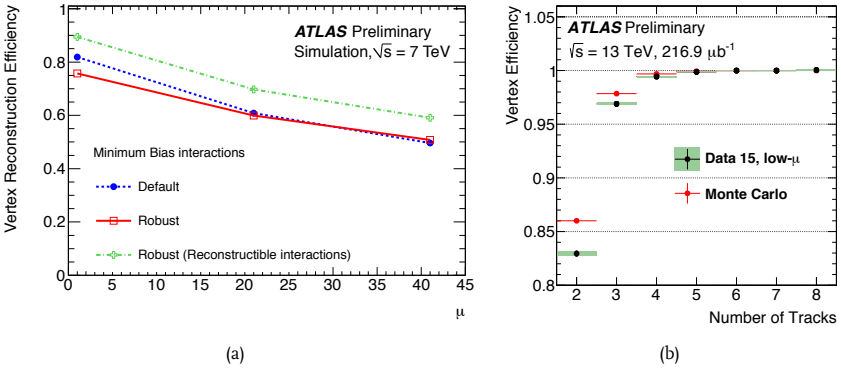

Fig. 3.3 · Vertex reconstruction efficiency as a function of number of interactions per bunch crossing at $\sqrt{s} = 7$ TeV of vertices reconstructed from `Default` tracks, `Robust` tracks, and `Robust` tracks from reconstructible interactions (a), and the vertex reconstruction efficiency as a function of tracks associated to the vertex at $\sqrt{s} = 13$ TeV of vertices reconstructed from `Robust` tracks from reconstructible interactions (b). The figures are taken from Refs. [152, 157].

a weight corresponding to the compatibility of the track with the position of the vertex. The optimal position of the vertex is re-fitted using the weighted set of tracks as input.

4. Once the position of the vertex is determined, the tracks incompatible with the reconstructed vertex are removed and can be used to find another vertex.

5. The reconstruction is performed again with the remaining tracks of the event.

The vertex reconstruction efficiency calculated as the fraction of vertices formed by at least two tracks which are matched to an interaction as a function of the number of interactions per bunch crossing in a minimum bias sample generated at $\sqrt{s} = 7$ TeV is shown in Figure 3.3a. The low efficiency of $\sim$ 80% is caused by interactions with low particle multiplicity and low-momentum tracks. If instead a vertex is required to have at least two reconstructible interactions, i. e. two particles with $p_{\mathrm{T}} > 400$ MeV and $|\eta| < 2.5$, the efficiency at low μ increases to $\sim$ 90%. The efficiency of vertex reconstruction with reconstructible interactions decreases from 90% to 60% with an increasing number of interactions per bunch crossing. The vertex reconstruction efficiency calculated for vertices with at least two tracks with $p_{\mathrm{T}} > 400$ MeV and $|\eta| < 2.5$ as a function of the number of tracks in simulation and data sample with low-μ at $\sqrt{s} = 13$ TeV are shown in Figure 3.3b. In order to have $>$ 99% efficiency, at least four tracks should be associated to the vertex.

3.3 Jets

Single strongly interacting particles cannot be observed directly. Due to colour confinement, the particles will screen off their colour charge by radiating other strongly interacting particles that will fragment and hadronise. A single quark or gluon will therefore result in a collimated spray

of hadrons. A collection of hadrons originating from a quark or a gluon or single hadrons, e. g. pions, originating from decays of unstable particles form showers in the hadronic calorimeter commonly referred to as jets. The jets are stopped in the hadronic calorimeter and their energies are measured.

The basis for calorimeter jet reconstruction are three-dimensional clusters of energy deposits in the calorimeter. The clusters are formed from topologically connected calorimeter cells using the cell-signal significance defined as the energy deposit in a cell divided by the average expected noise as input [159]. The average expected noise is estimated for each year of LHC operation as it depends on the pile-up as well as electronic noise from the calorimeter and has therefore been updated to Run-2 conditions [160].

Once the topological clusters in the calorimeter are defined, the jets can be reconstructed using a sequential recombination algorithm which combines clusters hierarchically based on the distance parameter [161]:

$$d_{ij} = \min(p_{\mathrm{T}i}^{2p}, p_{\mathrm{T}j}^{2p}) \times \frac{(y_i - y_j)^2 + (\phi_i - \phi_j)^2}{R^2}, \tag{3.1}$$

where R and p are constants of the algorithm, and $p_{\mathrm{T}i}$, y_i, and ϕ_i are the transverse momentum, rapidity, and azimuthal angle of a cluster, i. The minimal distance between two clusters, d_{ij}, is calculated and the two clusters are combined if d_{ij} is smaller than the distance from one of the clusters to the beam, $d_{iB} = p_{\mathrm{T}i}^{2p}$. If $d_{ij} > d_{iB}$ then cluster i is considered a jet, is removed from the list of clusters, and the minimal distances are re-calculated. This is done until there are no more clusters left.

The most commonly used jet reconstruction algorithm within ATLAS is the anti-k_t algorithm [161] with $R = 0.4$. The anti-k_t algorithm is characterised by the choice of $p = -1$ and orders the clusters according to inverse p_{T} which ensures that low-energy clusters are merged with high energy clusters before they merge with each other. If instead, the low energy clusters were merged with each other first, then it could lead to fake energetic jets. The anti-k_t algorithm is performed using the FastJet software package [162, 163]. After jets are reconstructed in the calorimeter, tracks are associated to them [164].

To suppress jets not originating from the primary vertex of interest, information about the tracks associated to the jet can be used. Especially the jet vertex fraction (JVF) can discriminate between jets originating from the primary vertex of interest or jets originating from other vertices [165]. The JVF of a jet is defined as the fraction of the scalar sum of the p_{T} of tracks from a chosen primary vertex compared to the total $\sum p_{\mathrm{T}}$ of the jet. Jets originating from pile-up, i. e. not the chosen primary vertex, will have a low JVF, while jets that are originating from the chosen primary vertex will have JVF = 1. Jets without any associated tracks are given a JVF-value of −1.

3.3.1 Jet Energy Calibration

The energy of topological clusters used in the jet finding algorithm is reconstructed assuming that the shower is produced through electromagnetic (EM) interactions [166]. The energy of the cells in the topological clusters is calibrated using a local cell signal weights (LCW) method that

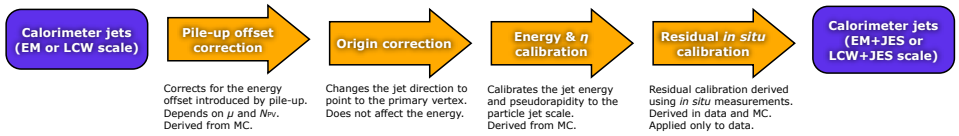

Fig. 3.4 · The jet calibration scheme used to correct the energy of the jets. The figure is taken from Ref. [166].

corrects the energy of the hadronic showers before the jets are formed. The LCW method divides showers into electromagnetic showers and hadronic showers based on the shower depth and energy density. The energy of hadronic showers is then corrected using factors obtained from Monte Carlo simulation samples of charged and neutral pions.

The jet energy scale (JES) calibration aiming at calibrating the reconstructed jet energy to the truth energy of the jet obtained in Monte Carlo samples, consists of four steps illustrated in Figure 3.4 [160, 166, 167]. It is performed on either EM or LCW corrected clusters. First the energy of the jet is corrected for effects originating from both in-time and out-of-time pile-up causing additional energy deposits in the calorimeter. The pile-up correction is derived from Monte Carlo samples. Then the origin of the jet is corrected to point to the primary vertex rather than the centre of the ATLAS detector. The origin correction does not influence the energy of the jet. Next the energy of the jets is corrected using the inverse average jet response function, $1/\mathcal{R}$, obtained from simulations:

$$1/\mathcal{R}^{\mathrm{EM(LCW)}} = E_{\mathrm{jet}}^{\mathrm{truth}}/E_{\mathrm{jet}}^{\mathrm{EM(LCW)}}, \tag{3.2}$$

where $E_{\mathrm{jet}}^{\mathrm{truth}}$ is the energy of the truth jet matched to a reconstructed jet, and $E_{\mathrm{jet}}^{\mathrm{EM(LCW)}}$ is the EM or LCW corrected energy of a reconstructed jet. The pseudo-rapidity of the jets are calibrated in a similar fashion. Finally, a data-driven residual correction is performed *in-situ* to account for differences between data and Monte Carlo simulations using the balance between the transverse momentum of a jet and well-calibrated processes such as leptonic Z decays, γ, and multijet events. The resolution of the jet energy is estimated from *in-situ* comparisons of data to Monte Carlo simulations using the balance of the transverse momentums of di-jet events [168]. The same techniques are used in jet energy scale calibration and jet energy resolution estimation during Run-1 and Run-2.

The systematic uncertainty on the jet energy scale calibration and the jet energy resolution are among the dominant experimental uncertainties in searches for squarks and gluinos in events with jets and missing transverse momentum. They are derived by systematically varying the selection criteria used in the comparisons of data to Monte Carlo and by studying the effect of alternative Monte Carlo generators used in the calibration procedure [166, 168]. The combined uncertainties of the jet energy scale and the jet energy resolution are shown in Figure 3.5. For jets with a low p_{T} of $\sim$ 20 GeV, the uncertainty on the jet energy scale is 5.5% in 2012 and 6.5% in 2015 while the uncertainty on the jet energy resolution is 2.5% in 2012 and 4% in 2015. The uncertainties on the jet energy scale and resolution decrease as a function of p_{T} until the a jet-p_{T}

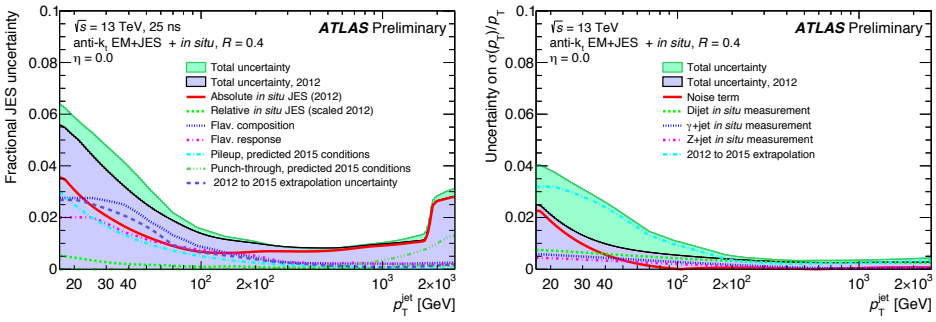

Fig. 3.5 · Fractional uncertainty as a function of the p_T of the jet of the jet energy scale (JES) (a) and jet energy resolution (JER) (b) in 2012 (light blue) and 2015 (green). The figures are taken from Refs. [160].

of 2 TeV is reached and the uncertainty on the jet energy scale increases again as there are no dedicated methods for estimating the resolution at that energy scale.

3.3.2 Flavour Tagging

Jets originating from b-quarks are of special interest as they form the dominant final state of Higgs boson and top quark decays.

The b-quark can decay either to a c-quark or to a u-quark. Both decays are suppressed by the CKM matrix resulting in a mean lifetime of a b-quark of approximately 1.5 ps. A b-quark with $p_T = 50$ GeV will therefore have a sizable mean free path length and can travel ~ 3 mm in the transverse direction before it decays. Jets originating from b-quarks (b-jets) can therefore be identified by reconstructing the displaced vertex and by studying the impact parameters of tracks; the jet can be b-tagged.

The b-tagging algorithm employed in ATLAS is based on a multivariate discriminant obtained using Boosted Decision Trees (BDTs). The inputs to the BDT are the p_T and η of the jet and the output of three basic algorithms: the impact parameter based algorithm (IP2D and IP3D) [169], the secondary vertex finder algorithm (SV) [170], and the decay chain multi-vertex algorithm (JetFitter) [171].

The IP2D and IP3D algorithms use a log-likehood ratio discriminant based on the signed impact parameters. The sign of an impact parameter is positive if the point of closest approach to the primary vertex is in front of the vertex with respect to the direction of the jet and negative if it is behind. A b-jet is expected to travel away from the primary vertex before it decays resulting in positive impact parameters. IP2D uses only the transverse impact parameter, while IP3D uses both the transverse and longitudinal impact parameters as input.

The secondary vertex algorithm aims at reconstructing displaced, secondary vertices from tracks not identified as originating from decays of long-lived particles, photon conversion or hadronic interaction with the matter of the detector.

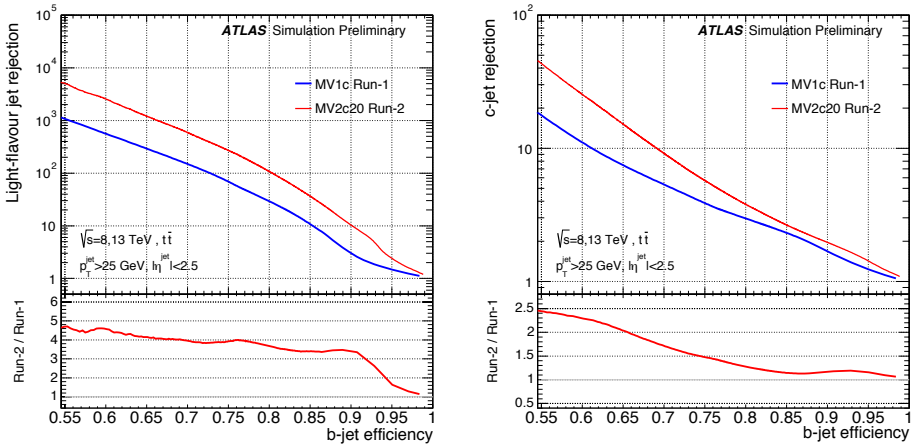

Fig. 3.6 · The b-tag efficiency versus the light-flavour jet rejection (a) and c-jet rejection (b) of the b-tagging algorithm used during Run-1 (blue) and the algorithm optimised for Run-2 (red). In the lower panel a direct comparison between the performances of MV1 and MV2C20 is shown. The figures are taken from Ref. [173].

The JetFitter algorithm distinguishes jet originating from b-quarks from jets originating from light-flavoured quarks and c-quarks by studying the topological substructure of the jet.

Precise knowledge of the position of the primary vertex is important. The precision increases with the number of associated tracks. For each bunch crossing, the primary vertex with the highest scalar $\sum p_{\mathrm{T}}^2$ is chosen for b-tagging.

During Run-1 a b-tagging algorithm, MV1 [172], was optimised to identify b-jets and reject light-flavoured and c-jets. With the installation of the IBL during the long shutdown between 2013 and 2015, the vertex resolution improved. A new b-tagging algorithm, MV2C20 [173], was optimised including a more refined track selection and the improved vertex resolution.

The performance of the b-tagging algorithms are measured in a $t\bar{t}$ sample. The b-tag efficiency versus the light-flavour and c-jets of the MV1 and MV2C20 can be seen in Figure 3.6. It is clearly seen that the Run-2 algorithm performs better than algorithm used in Run-1. This is mainly attributed to the increased vertex resolution as a result of the installation of the IBL. For a 77% b-tag efficiency, the light-flavour rejection has improved by a factor of 4 while and the rejection of c-jets has improved by 40%.

3.4 Electrons and Photons

Both electrons and photons are expected to create showers contained only in the electromagnetic calorimeter. They result in similar detector responses in the electromagnetic calorimeter. However, electrons are expected to have one track associated with an energy deposit in the calorimeter, while

photons can either be converted through interaction with the material of the detector ($\gamma \to e^+e^-$) resulting in associated tracks or unconverted where no tracks are associated to an energy deposit.

3.4.1 Electrons

Electrons in the central region of the detector ($|\eta| < 2.47$) are reconstructed from cluster seeds in the electromagnetic calorimeter [174, 175]. The calorimeter is divided into towers in $\Delta\eta \times \Delta\phi$ corresponding to its granularity with a size of 0.025×0.025. The energy deposit within a tower is summed and form the basis for identifying cluster seeds. Cluster seeds are found using a sliding window algorithm [176] with a size of 3×5 towers and a threshold transverse energy of 2.5 GeV. A cleaning is performed isolating the seed clusters. A region of interest with a size of $\Delta R = \sqrt{(\Delta\eta)^2 + (\Delta\phi)^2} = 0.3$ around the cluster is defined and tracks with $p_{\mathrm{T}} > 1$ GeV found within the region of interest are matched to the cluster. An electron candidate must have at least one track associated to the energy deposit in the cluster. If more than one track is matched with the cluster, tracks with hits in the silicon detectors have higher priority. The track with the smallest distance to the centre of the cluster is chosen. Electrons in the forward regions ($|\eta| > 2.47$) are only measured in the calorimeter and are indistinguishable from photons. They are not used in any of the analyses presented in this thesis and are therefore not discussed any further. The reconstruction efficiency of electrons in the central part of the detector is found to be at least 85%.

The energy of the electron candidate is calibrated in several steps [177]. The calibration includes calibration of the energy deposit in each of the layers of the calorimeter, Monte Carlo based response calibration of the clusters, and corrections due to variations in specific detector regions not included in the simulation. Finally, the electrons are calibrated using well-modeled $Z \to e^+e^-$ events from data and simulations. The energy calibration is validated with other processes.

Unfortunately, not all reconstructed electrons are true, prompt electrons, but rather jets passing the electron reconstruction or electrons originating from either photon conversion or heavy flavour hadron decays. A dedicated electron identification is therefore needed. The electron identification is based on variables sensitive to the longitudinal and transverse shape of the shower in the calorimeter, the properties of the tracks, and the matching of the tracks to the cluster [174, 175, 178].

During Run-1, both a sequential cut-based and multivariate likelihood-based (LH) identification were developed [174, 175], while for Run-2 only the multivariate LH identification was re-optimised [178]. Only the LH identification will be discussed further. Three LH selections are defined: Loose, Medium, and Tight. As the tightness increases, background-rejection is improved while the electron identification efficiency is lower. The Loose selection is specialised in rejecting light-flavoured jets, while in the Medium and Tight selections additional variables are included in order to reject electrons from converted photons or heavy flavour hadronic decays.

The total efficiency of detecting an electron with the ATLAS experiment is written as a product of different components [175]:

$$\epsilon_{\mathrm{total}} = \epsilon_{\mathrm{Reco}} \times \epsilon_{\mathrm{ID}} \times \epsilon_{\mathrm{Trigger}} \times \epsilon_{\mathrm{other}}, \tag{3.3}$$

where ϵ_{Reco} is the electron reconstruction efficiency, ϵ_{ID} is the identification efficiency of reconstructed electrons, $\epsilon_{\text{Trigger}}$ is the efficiency of the electron triggers with respect to reconstructed and identified electrons, and ϵ_{other} is the effect of additional requirements of the electron such as isolation criteria. The total efficiency is measured in $Z \to e^+e^-$ and $J/\Psi \to e^+e^-$ events from data and Monte Carlo simulations using a *tag-and-probe* method, where one electron is "tagged" using strict cuts and the efficiency is measured on the other, "probed" electron.

The results of the electron efficiency measurements as a function of E_{T} and η can be seen in Figure 3.7. It is seen that the efficiency varies depending on whether the electron is identified as Loose, Medium or Tight. The efficiency has increased with $\sim 2\%$ in 2015 compared to 2012. The efficiency increases with higher transverse energies resulting in an efficiency of Tight electrons with a $p_{\text{T}} > 90$ GeV of 88% in 2012 and 90% in 2015. The efficiency is almost constant as a function of η with dips where the two parts of the barrel region are joined ($\eta = 0$), at the transition from barrel to end-cap region ($\eta = \pm 1.5$), and at the most forward part of the end-cap region ($\eta = \pm 2.5$). The $\sim 5\%$ difference between data and Monte Carlo simulations is due to known mis-modeling of showers and tracks and is corrected for by applying scale factors to the simulation samples.

3.4.2 Photons

Photon reconstruction [179, 180] follows a procedure similar to the electron reconstruction. Photon reconstruction is seeded from energy deposits in clusters of cells in the electromagnetic calorimeter found with the same method used for electron reconstruction. Once the clusters are defined, tracks from the inner detector are matched to the cluster. If tracks associated to a cluster are found to originate from a conversion vertex where a photon has split into an electron-positron pair then a converted photon is reconstructed. Conversion vertices are vertices in the ID typically with two oppositely charged tracks emerging in parallel from the vertex or with a single track where energy deposited in the calorimeter is much larger than the momentum of the track. If no tracks are associated to a cluster in the calorimeter, the cluster is reconstructed as an unconverted photon. The efficiency of reconstructing prompt photons originating from the primary vertex with $E_{\text{T}} > 25$ GeV is estimated to be 96%. The remaining 4% are incorrectly identified as electrons.

The energy of the photons are measured in clusters with a size depending on whether the photon is converted or not[1]. The energy of the photon is calibrated using the same procedure used in the electron energy calibration [177].

The set of reconstructed photons consists of the prompt photons of interest, i. e. the ones originating from the primary vertex, and background photons originating from jets. The shower of prompt photons is typically narrow and contained in the electromagnetic calorimeter with limited leakage into the hadronic calorimeter. The shape of the shower in the electromagnetic calorimeter and the leakage into the hadronic calorimeter are therefore used for prompt photon identification [179]. Two sets of cut-based selections are defined: `Loose` and `Tight`. The `Loose` selection is based solely on shower shape and energy deposit in the hadronic calorimeter, while the

[1] A converted photon is expected to have a broader energy deposit due to the opening angle between the electron and the positron.

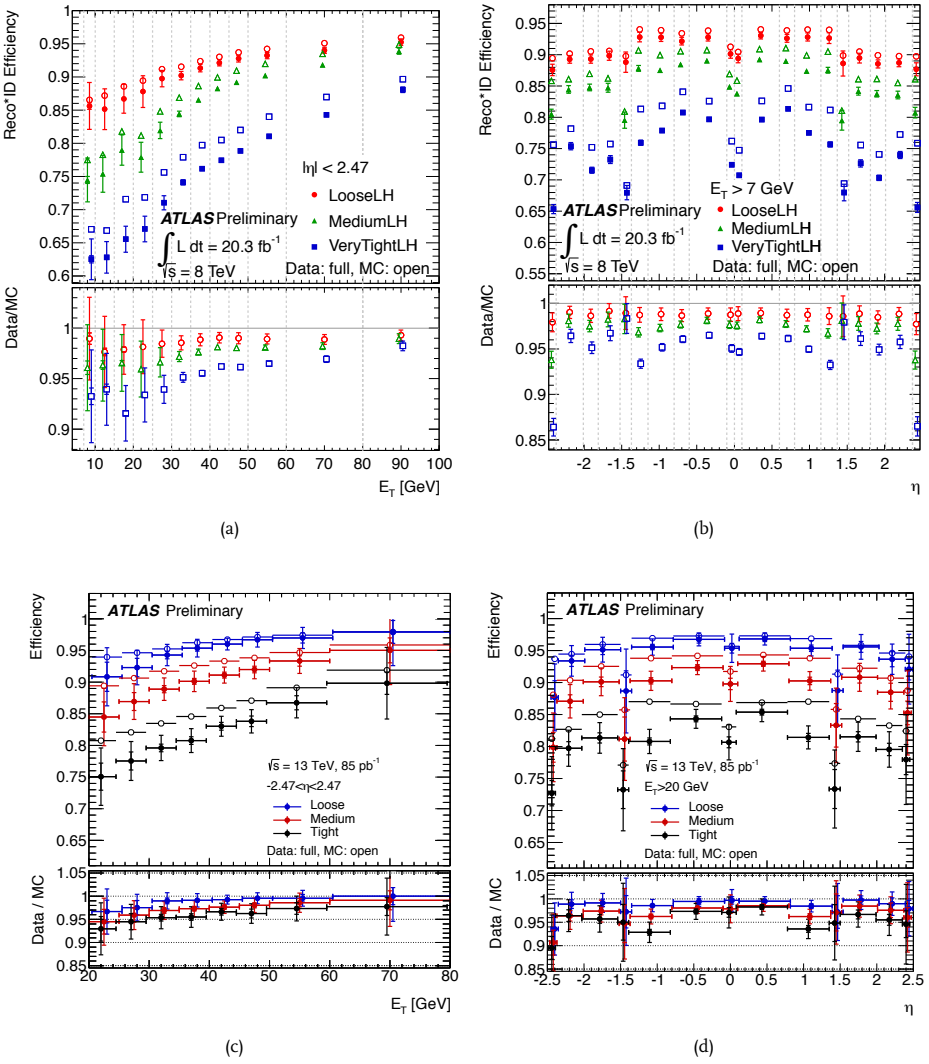

Fig. 3.7 · The electron reconstruction and identification efficiency as a function of transverse energy ((a) and (c)) and of η ((b) and (d)) using the three LH based identification selections in 2012 ((a) and (b)) and 2015 ((c) and (d)). The figures are taken from Refs. [175, 178].

`Tight` selection includes information from the first layer of the ECAL providing good rejection of neutral hadrons decaying into photons, $\pi^0 \to \gamma\gamma$. The `Loose` and `Tight` selections are optimised in seven η-bins. The identified photons must fulfill an isolation criterion: the transverse energy in a cone of size $\Delta R = 0.4$ around the identified photon, $E_{\mathrm{T}}^{\mathrm{iso}}$, must not exceed 4 GeV.

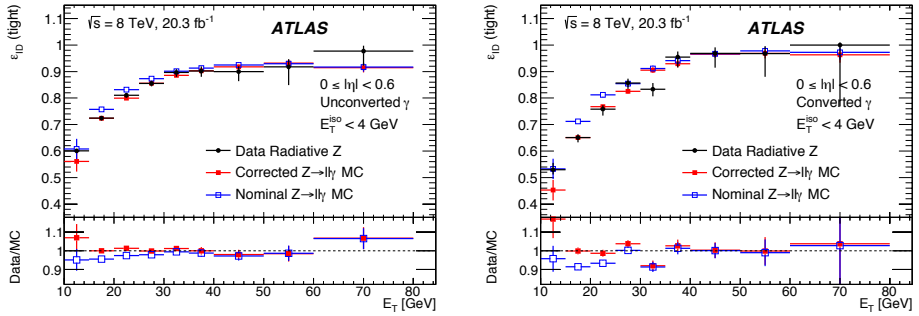

(a) (b)

Fig. 3.8 · The photon identification efficiency as a function of transverse energy of unconverted (a) and converted (b) photons within $0 \leq |\eta| \leq 0.6$ measured with uncorrected simulations (blue), simulations corrected to data (red), and data collected in 2012 (black). The figures are taken from Ref. [180].

The efficiency of the photon identification is measured as the fraction of isolated photons fulfilling the Tight identification requirements compared to the total number of isolated photons. The efficiency is obtained from three methods each optimised for a window of photon energy [179]. The efficiency was measured to be 50-65% and 45-55% for unconverted and converted photons, respectively, at $E_{\mathrm{T}} > 10$ GeV increasing to 95-100% for both converted and unconverted photons at a transverse energy larger than 100 GeV. The efficiency of the identification of converted and unconverted photons as a function of transverse energy is shown in Figure 3.8.

3.5 Muons

Muons are not stopped by the calorimeters and will reach the muon spectrometer. They are reconstructed from tracks in the inner detector (ID) and muon spectrometer (MS) [181–183]. Tracks are first reconstructed independently in the inner detector and in the muon spectrometer before they are combined into a full muon reconstruction. There are four types of reconstructions defined for muons traversing the ATLAS detector.

Combined (CB) muons are reconstructed using tracks obtained from a global fit combining the ID tracks and the MS tracks. Most muons are reconstructed using an outside-in approach where the MS tracks are extrapolated to the ID for matching. An inside-out approach seeded from ID tracks is used for complementarity.

Segment-tagged (ST) muons are reconstructed from an ID track matched to a track segment in the MS, i. e. hits in one layer of the MS are required. Segment-tagged muons have either a low-p_{T} or fall in a part of the MS with limited acceptance.

Calorimeter-tagged (CT) muons are reconstructed by matching a track in the ID to deposits in the calorimeter compatible with a minimum-ionizing particle. The CT muons have low purity,

but can regain efficiency in regions where the MS does not cover, i. e. around $\eta = 0$ where the two parts of the barrel region are joined.

Stand-alone (SA) muons (or Extrapolated (ME) muons) are reconstructed from a MS track extrapolated to the interaction point. The SA muons are targeting muons in the forward region ($2.5 < |\eta| < 2.7$) where the inner detector does not cover.

Two algorithms were developed for muon reconstruction during Run-1 [170]. Chain 1 is based on a statistical combination of ID and MS tracks, while Chain 2 is based on a global refit of the hits in the inner detector and the muon spectrometer. A third chain was defined combining the methods of Chain 1 and Chain 2. The three chains were found to show similar performance, and Chain 3 is used in the Run-2 muon reconstruction [183].

During Run-1, selection criteria on the quality of the muon track based on the minimum number of hits and maximum number of holes were applied to identify muons [182].

For Run-2, a dedicated prompt muon identification algorithm was optimised to select muons produced in the hard scattering and suppress muons formed inside hadronic jets [183]. The tracks entering the muon identification have to fulfill a set of quality cuts. The identification is based on the difference between the charge-to-momentum ratio, q/p, measured in ID and MS divided by the combined uncertainty on q/p, the difference between the p_{T} measured in ID and MS divided by the p_{T} of the combined track, and the quality of the fit of the combined track. Four identification selections are defined: `Loose`, `Medium`, `Tight`, and `High-`p_{T}. The `Medium` selection is the default for Run-2. `Loose` muon identification is optimised to recover identification efficiency in the crack region of the muon spectrometer ($|\eta| < 0.1$). The `Tight` muon selection results in higher purity, but lower signal efficiency. The `High-`p_{T} muon selection is optimised for a better momentum resolution of muons with $p_{\mathrm{T}} > 100$ GeV. The identification efficiency is measured using a $t\bar{t}$ sample is found to be above 95% for `Medium` muon identification.

The reconstruction efficiency of high-p_{T} muons is measured using a high-purity sample of $Z \to \mu^+\mu^-$ events and of low-p_{T} muons using a sample of $J/\Psi \to \mu^+\mu^-$ events with a *tag-and-probe* method in both data and simulations. The resulting efficiencies can be seen in Figure 3.9. As it can be seen, the efficiencies found in data and Monte Carlo simulations are not identical. Scale factors defined in η and p_{T}-bins are used to correct the simulation samples to the efficiencies measured in data.

The momentum and the momentum resolution of reconstructed muons in the Monte Carlo simulations are calibrated to data [182, 183]. High-purity data samples of $\Upsilon \to \mu^+\mu^-$, $J/\Psi \to \mu^+\mu^-$, and $Z \to \mu^+\mu^-$ events are used to calculate the muon momentum scale and the muon momentum resolution factors.

3.6 Taus

The tau lepton is the heaviest lepton and it decays rapidly after production due to its high mass of 1.776 GeV [12]. It is the only lepton heavy enough to decay into both leptons and hadrons. The branching fraction of taus into hadronic final states is $\sim$ 65%. The electrons or muons

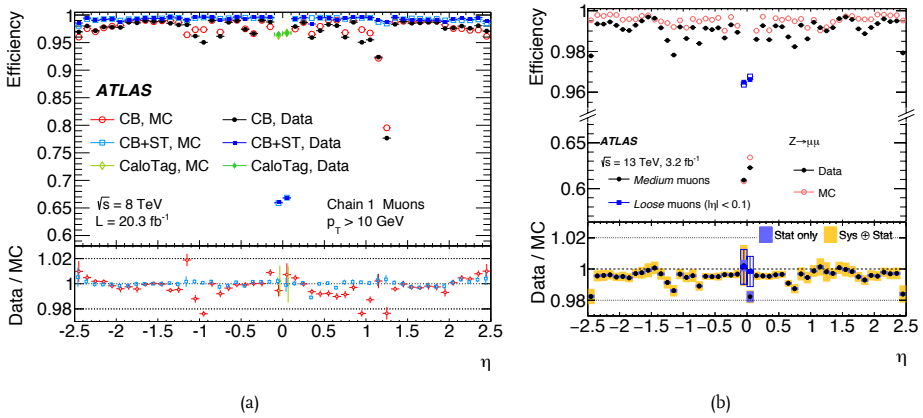

Fig. 3.9 · The muon reconstruction efficiency as a function of η obtained with data (filled) and Monte Carlo simulations (hollow) with 20.3 fb^{-1} at $\sqrt{s} = 8$ TeV collected in 2012 (a) and 3.2 fb^{-1} at $\sqrt{s} = 13$ TeV collected 2015 (b). The figures are taken from Refs. [182, 183].

originating from tau decays are almost indistinguishable from electron and muons originating from the hard scattering and are therefore reconstructed and identified as such. Hadronic tau decays are characterised by the number of prongs, i. e. the number of charged particles in the final state. The visible part of hadronically decaying taus (referred to simply as taus in the remainder of this chapter) bears great similarity to hadronic jets originating from quarks or gluons.

The basis for tau reconstruction [184, 185] is formed by LCW calibrated jets with $p_{\mathrm{T}} > 10$ GeV and falling within $|\eta| < 2.5$. In order to reduce the effect of pile-up, a tau vertex is reconstructed using all tracks with $p_{\mathrm{T}} > 1$ GeV in a region of $\Delta R < 0.2$ around the tau candidate. The tau vertex is used to estimate the direction of flight of the tau, the tracks associated to the tau, and to define the origin of the coordinate system from which the variables used in the tau identification are calculated. Tracks are associated to the tau candidate if they fulfill quality requirements, are found within $\Delta R < 0.2$ with $p_{\mathrm{T}} > 1$ GeV of the cluster in the calorimeter, and originate from the tau vertex. The majority of 1-prong taus is expected to have one associated track while the majority of 3-prong taus is expected to have three associated tracks.

Some reconstructed taus are fake originating from either electrons or jets from quarks and gluons. A dedicated tau identification is needed. Two separate identification selections are optimised to discriminate between either strongly produced jets or electrons faking 1-prong taus.

The discrimination against strongly produced jets is based on a set of variables using information of the cluster in the calorimeter and the associated tracks in the core of the reconstructed tau and in an isolation cone of $0.2 < \Delta R < 0.4$ [184, 185]. Tracks from taus are expected to be collimated and isolated and the substructure of the energy deposit of a tau in the calorimeter, e. g. the number of and the energy deposited by neutral pions, differs from that of a strongly produced jet. A multivariate discriminant is optimised using BDTs trained independently for 1-

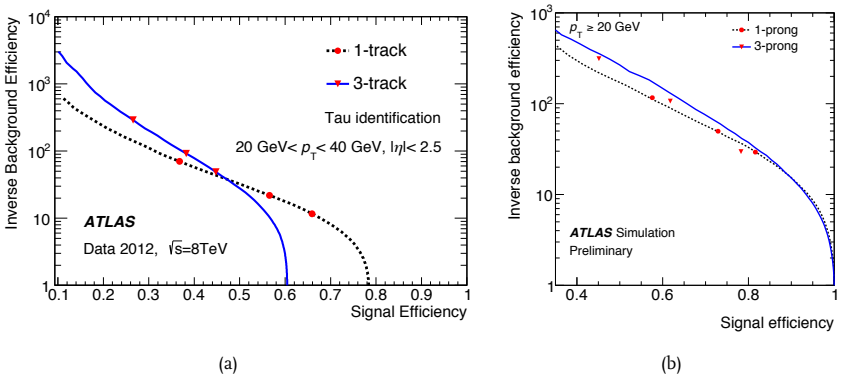

Fig. 3.10 · Signal efficiency versus inverse QCD-jet mis-tagging efficiency of the BDT discriminant optimised for identification of taus with 20 GeV $< p_T <$ 40 GeV in 2012 (a) and with $p_T >$ 15 GeV in 2015 (b). The Loose, Medium, and Tight tau identification working points are indicated with red circles (1-prong) and triangles (3-prong). The curves from 2012 show the combined reconstruction and identification efficiency while the curves from 2015 show only the identification efficiency. The figures are taken from Refs. [184, 185].

prong and 3-prong taus. Minor adjustments were done to the set of variables used in the BDT for the re-optimisation of jet discrimination in Run-2. Three working points are defined: `Loose`, `Medium`, and `Tight`. The performance of the BDT identification in 2012 and 2015 along with the three working points is shown for 1-prong and 3-prong taus in Figure 3.10. It should be noted that the efficiency from 2012 includes both reconstruction and identification efficiencies while the efficiency from 2015 only shows the efficiency of the identification. The combined reconstruction and identification efficiency in 2015 of `Loose`, `Medium`, and `Tight` taus is 45%, 55%, and 60% for 1-prong taus and 30%, 40%, and 50% for 3-prong taus.

The discriminant against strongly produced jets does not provide a good discrimination between electrons faking 1-prong taus and real taus. Another discriminant is therefore optimised to reject electrons reconstructed as taus [184, 185]. The majority of final states of true, 1-prong taus consists of neutral pions and a single charged pion. The discriminant is exploiting the different transition radiation of electrons and charged pions measured in the TRT. A working point at 95% signal efficiency is provided.

The energy deposit in the calorimeter is calibrated with the LCW method described in Section 3.3.1. An additional energy calibration is performed extracting the tau energy scale by comparing the true visible energy of the tau to the reconstructed energy using a *tag-and-probe* method in a $Z \to \tau^+\tau^-$ simulation sample [184, 185].

3.7 Missing Transverse Momentum

Particles that only interact weakly such as neutrinos or the hypothetical lightest neutralino of R-parity conserving supersymmetry will typically traverse the ATLAS detector without any interaction

thus leaving the detector without being measured directly. The transverse energy of such escaping particles can however be measured indirectly through an imbalance in the transverse momentum of identified particles.

The momentum and energy in the transverse plane prior to the collision is zero and should remain zero due to energy and momentum conservation after the collision. The calorimeter based missing transverse momentum, $E_{\mathrm{T}}^{\mathrm{miss}}$, is reconstructed from the vectorial sum of the calibrated momentum of all objects as well as a soft-term contribution [186]. The x- and y components of $E_{\mathrm{T}}^{\mathrm{miss}}$ is calculated as:

$$E_{x,y}^{\mathrm{miss}} = E_{x,y}^{\mathrm{miss},e} + E_{x,y}^{\mathrm{miss},\gamma} + E_{x,y}^{\mathrm{miss},\tau} + E_{x,y}^{\mathrm{miss,jets}} + E_{x,y}^{\mathrm{miss},\mu} + E_{x,y}^{\mathrm{miss,soft}}, \tag{3.4}$$

where each term is the negative vectorial sum of the momentum of the calibrated objects passing requirements on their p_{T}. The soft-term can be estimated both from deposits in the calorimeter and tracks. During Run-1, the soft term of the $E_{\mathrm{T}}^{\mathrm{miss}}$ was reconstructed based on topoclusters in the calorimeters not associated to any reconstructed particles [187], while the soft-term of the $E_{\mathrm{T}}^{\mathrm{miss}}$ reconstruction in Run-2 is estimated from tracks combined with information about hard objects in the calorimeter [188]. Once the x- and y-coordinates of the missing transverse momentum have been reconstructed, the total missing transverse momentum is calculated as:

$$E_{\mathrm{T}}^{\mathrm{miss}} = \sqrt{(E_x^{\mathrm{miss}})^2 + (E_y^{\mathrm{miss}})^2}. \tag{3.5}$$

Another missing transverse momentum variable can be reconstructed solely from the momentum of tracks ignoring the energy deposits in the calorimeter caused by neutral particles. The track based $E_{\mathrm{T}}^{\mathrm{miss}}$ is not used in the analyses presented in this thesis.

The missing transverse momentum is sensitive to the occurrence of multiple proton interaction per bunch crossing where tracks or objects might not be associated to the right vertex. This will lead to a mis-measurement of the missing transverse momentum.

During Run-1, the effect of pile-up coming from jets was suppressed using the jet vertex fraction discussed in Section 3.3. Any jet with $p_{\mathrm{T}} < 50$ GeV not satisfying JVF > 0 was disregarded in the $E_{\mathrm{T}}^{\mathrm{miss}}$-calculation. Two methods are defined to suppress pile-up effects on the soft-term of the $E_{\mathrm{T}}^{\mathrm{miss}}$: the soft track vertex fraction and the jet area method [187]. For Run-2, the pile-up suppression with jet vertex fraction was replaced by a jet vertex tagger (JVT) [190]. In Run-2, the soft-term calculated from tracks combined with the measurement of hard objects in the calorimeter was found to be less sensitive to pile-up than the calorimeter based soft-term used in Run-1 [188]. The agreement of $E_{\mathrm{T}}^{\mathrm{miss}}$ between data and simulation after pile-up suppression in a $W \to e\nu$ sample can be seen in Figure 3.11. The discrepancies can be explained by the lack of QCD mulitjets samples in the simulations that are expected to contribute at low values of $E_{\mathrm{T}}^{\mathrm{miss}}$.

The resolution of $E_{\mathrm{T}}^{\mathrm{miss}}$ depends on the scalar sum of the transverse energy in an event, $\sum E_{\mathrm{T}}$. It is estimated in using both events without any genuine $E_{\mathrm{T}}^{\mathrm{miss}}$ e. g. $Z \to \mu^+\mu^-$, and in events containing neutrinos, e. g. $W \to e\nu$ [187, 189]. The resolution of $E_{x,y}^{\mathrm{miss}}$ as a function of $\sum E_{\mathrm{T}}$ of various processes is shown in Figure 3.12. The resolution of $E_{\mathrm{T}}^{\mathrm{miss}}$ was very similar for all samples before pile-up suppression. The pile-up suppression decreased the $E_{\mathrm{T}}^{\mathrm{miss}}$ resolution of some of

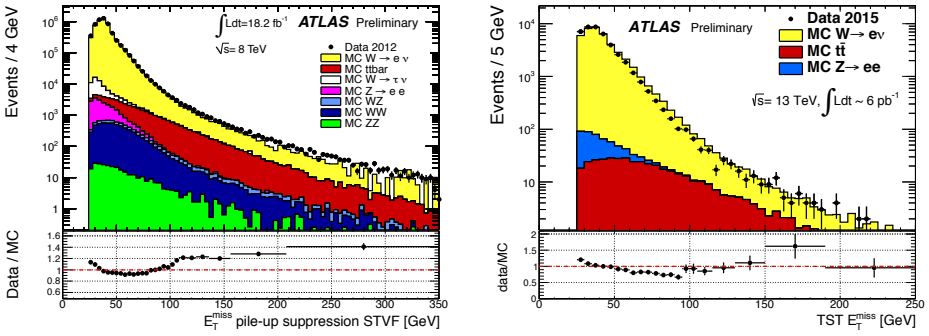

Fig. 3.11 · Distributions of $E_{\mathrm{T}}^{\mathrm{miss}}$ in a sample of $W \to e\nu$ events after pile-up suppression (STVF) with data collected in 2012 at $\sqrt{s} = 8$ TeV (a) and with the soft-term calculated from tracks (TST) with data collected in 2015 at $\sqrt{s} = 13$ TeV (b). The figures are taken from Refs. [187, 189].

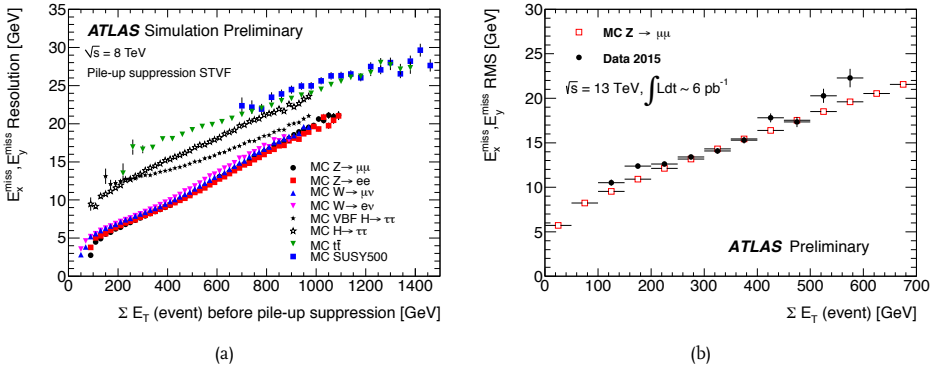

Fig. 3.12 · The resolution of the x- and y-components of $E_{\mathrm{T}}^{\mathrm{miss}}$ after pile-up suppression. The figure on the left (a) shows the resolution of several models estimated from Monte Carlo simulations (MC) in 2012. The figure on the right (b) shows the resolutions obtained with $Z \to \mu^+\mu^-$ simulations and data collected in 2015. The figures are taken from Refs. [187, 189].

the samples, but not of the samples of $t\bar{t}$-production and the supersymmetric model as shown in Figure 3.12a. As the pile-up suppression mostly affects the soft term which is not expected to contribute significantly to the missing transverse momentum the $t\bar{t}$-sample and the sample of the supersymmetric model, the $E_{\mathrm{T}}^{\mathrm{miss}}$ resolution is not affected. The expected and observed resolution of $E_{\mathrm{T}}^{\mathrm{miss}}$ in 2015 shown in Figure 3.12b are slightly higher than in 2012.

The uncertainties on the missing transverse momentum scale and resolution are influenced by the uncertainties on all the objects that enter into the calculation in Eq. 3.4. The sources of uncertainty include the energy scale and resolutions of all the hard objects as well as uncertainties

on the soft term. The uncertainties caused by the soft-term account for a $\sim 5\%$ uncertainty on both the scale and resolution of the missing transverse momentum [187].

4 Analysis Method

Many searches for supersymmetry at the LHC follow similar patterns. The goal is to select events with topologies typical for SUSY models with specific sparticles production and decay. Due to the rich event topology of the Standard Model, a background of SM processes is present in the events selected to enhance the SUSY signal. A vital task in these searches is thus a correct estimate of the SM background processes.

This chapter contains a description of the common traits in the analysis method used in inclusive searches for squarks and gluinos in events without leptons at three different collision energies, $\sqrt{s} = 8, 13$, and 14 TeV, included in this thesis.

4.1 Analysis Overview

The searches presented in this thesis are all performed in signal regions. These are kinematic regions in phase space where one expects that signal will be enhanced and background processes suppressed. Particle collisions are probabilistic in nature; searches and measurement are therefore performed on an ensemble of collisions. Typically, one looks for traits in the signal that are not present in the background. However, one can very rarely reject the entire background and there will still be background processes that can mimic the signal.

Estimating the contribution from the Standard Model background processes in signal regions is vital. The estimate of the contribution from major backgrounds is found in control regions designed to be enriched by a specific type of background. The background processes are normalised in control regions using a combined likelihood fit and the number of events coming from backgrounds in signal regions is estimated using transfer functions (TF) that transfer the estimate from control regions to signal regions. The likelihood fit is needed to correctly estimate the uncertainty on the background estimates taking into account eventual correlations of the sources of uncertainty. The robustness of the background estimate is tested in validation regions.

After the background estimate is validated, the number of observed events in the signal region is compared to the estimated number of events from background. An excess of observed events would hint to physics beyond the Standard Model and a discovery fit is performed to find the significance of the excess. If no excesses are seen, then there are no hints of physics beyond the Standard Model and an exclusion fit is performed. Both model-independent limits on the visible cross section and model-dependent limits in SUSY phase space are performed.

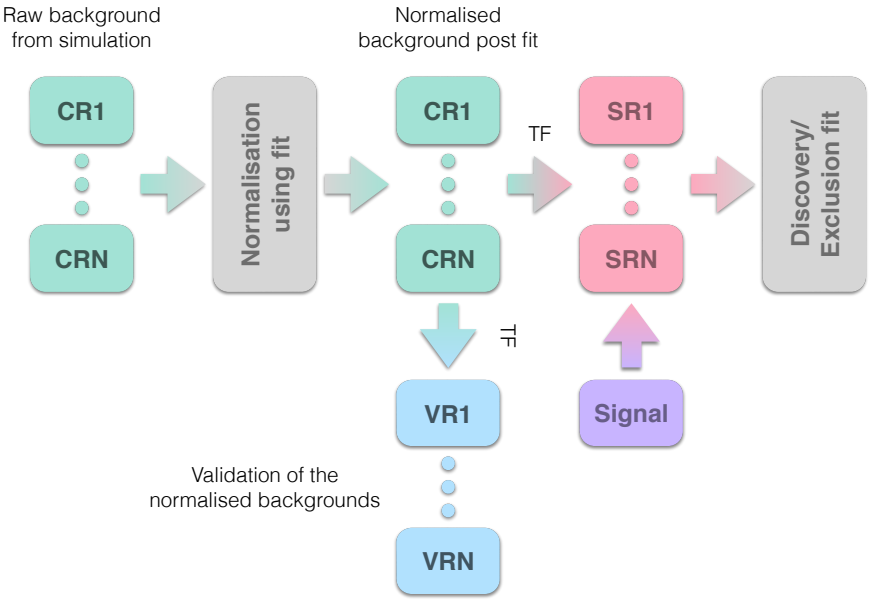

Fig. 4.1 · An overview of a SUSY analysis. Backgrounds are estimated in control regions using a normalisation factors obtained from the likelihood fit. The estimated number of background events in signal and validation regions are found through transfer functions (TF). Discovery and exclusion fits are performed after the background estimates have been validated.

All the parts of the analysis are discussed in detail in the remainder of this chapter. A schematic overview of the analysis is shown in Figure 4.1.

4.2 Signal Regions

Signal regions (SRs) are, as the name suggest, a set of event selection criteria where the contribution from SUSY signal is enhanced and the Standard Model background contribution is reduced.

The SUSY models used in searches are often simplified models with only two free parameters, which are typically the masses of SUSY particles. Combinations of values of the free parameters are simulated as each combination is in itself a specific model. The combinations form a grid in the parameter space. A schematic illustration of a parameter grid is shown in Figure 4.2. Each point corresponds to one simulated set of parameter settings in the SUSY model, e. g. the mass of the produced sparticle versus the mass of the LSP.

The event topology depends on the sparticles that are produced, how they decay and the masses of the SUSY particles. A simplified model with squark pair-production and direct decay, $\tilde{q} \rightarrow q\tilde{\chi}_1^0$, as described in Section 1.4.3, will lead to events with two jets and missing transverse momentum due to the escape of the LSP. However, the energy of the jets and the size of the missing

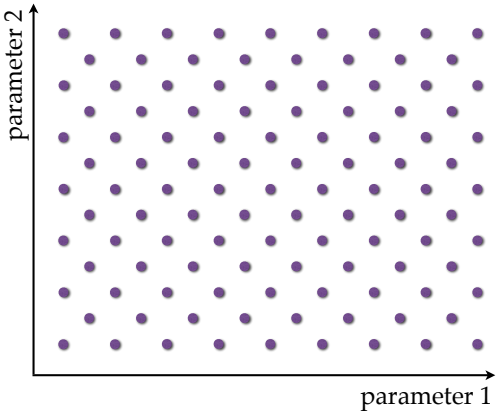

Fig. 4.2 · A sketch of a signal grid with two free parameters. The two parameters are typically the mass of the produced sparticle and the mass of the LSP.

transverse momentum depend on the mass difference of the squarks and the LSP. A longer decay chain can lead to events with many jets, leptons, and missing transverse momentum in the final state. In a single search, multiple signal regions are defined to cover the mass-parameter space of various models.

The signal regions can either be orthogonal or inclusive. Orthogonal signal regions are mutually exclusive while inclusive signal regions can have overlaps resulting in the same event entering several regions. Orthogonal signal regions have the advantage that they can all be combined into one fit for every point, whereas for the inclusive signal regions one signal region is fitted at a time. Orthogonal signal regions require a larger data-sample as each signal region must be populated to ensure the stability of the fit. This is why inclusive signal regions are chosen for the analyses presented in this thesis.

Signal regions can either be single or multiple binned. Using a single binned signal region reduces the analysis to a cut-and-count analysis not depending on the exact shape of the variables defining the signal region. A multi binned signal region depends on the shapes of one or more variables. All the analyses presented in this thesis make use of single binned signal regions.

4.2.1 Signal Sensitive Variables

A set of variables that can be used to distinguish between background and signal is used for defining the signal regions. The cuts on the various variables are varied to find the optimal signal regions. A description of the variables used in defining signal regions in the search for SUSY without leptons is provided here.

Number of jets: The number of jets expected from signal depends on the final state and therefore on the decay mode of the pair-produced sparticles. Gluino decays will in general result in a larger number of jets than squark decays.

Energy of the jets: The energy of the jets depends on the masses of the SUSY particles in the model. The energy of the jets will be small if the mass of the produced sparticle is close to the mass of the LSP - the model point is said to be compressed. A larger mass difference will lead to more energetic jets.

Missing transverse momentum: The missing transverse moment, $E_{\mathrm{T}}^{\mathrm{miss}}$, is the measure of the momentum imbalance in the transverse plane of the detector. It is used to estimate the energy of the particles that otherwise leave no trace in the detector, such as neutrinos. The lightest supersymmetric particle will only interact weakly similarly to the neutrino's interaction and will therefore leave the detector unnoticed.

$\Delta\phi_{\mathrm{min}}$(jets, $\mathbf{E}_{\mathrm{T}}^{\mathrm{miss}}$): The minimal azimuthal angle between jets and $E_{\mathrm{T}}^{\mathrm{miss}}$, $\Delta\phi_{\mathrm{min}}(\mathrm{jets}, E_{\mathrm{T}}^{\mathrm{miss}})$, is used to discriminate between signal and background originating from QCD multi-jets events. Events originating from the SUSY signal tend not to have the $E_{\mathrm{T}}^{\mathrm{miss}}$ pointing in the same direction as the jets, whereas the $E_{\mathrm{T}}^{\mathrm{miss}}$ and one of the jets will be more aligned in the QCD multijet background because of a mis-measurement of the energy of a jet.

Aplanarity: Aplanarity is an event-shape variable distinguishing spherical event topologies from planar and linear events. Standard Model particles originating from the decay of heavy particles (~ 1 TeV) tend to be collimated resulting in a more linear event shape. Aplanarity is defined as $A = \frac{3}{2}\lambda_3$, where λ_3 is the smallest eigenvalue of the sphericity tensor [191].

Effective Mass: The effective mass is a measure of the energy-"activity" in an event. It is defined as the scalar sum of the missing transverse momentum and the transverse momentum of the jets [192]:

$$m_{\mathrm{eff}} \equiv \sum_{i=1}^{n_{\mathrm{jets}}} |\vec{p}_{\mathrm{T}}^{(i)}| + E_{\mathrm{T}}^{\mathrm{miss}}, \tag{4.1}$$

where n_{jets} is the number of jets and $|\vec{p}_{\mathrm{T}}^{(i)}|$ is the size of the transverse momentum vector of the i^{th} jet. The effective mass is found to correlate well with the effective SUSY mass scale defined as [193]:

$$M_{\mathrm{SUSY}}^{\mathrm{eff}} = \left(M_{\mathrm{SUSY}} - \frac{M_{\chi}^2}{M_{\mathrm{SUSY}}} \right), \tag{4.2}$$

where M_{χ} is the mass of the lightest supersymmetric particle, and M_{SUSY} is a SUSY mass scale weighted by the individual SUSY-particle production cross section. A scatter plot of m_{eff} and $M_{\mathrm{SUSY}}^{\mathrm{eff}}$ for mSUGRA/CMSSM [61–63] is seen in Figure 4.3 with the effective mass denoted as M_{est}. The correlation is worse for the MSSM due to the larger number of free parameters.

The effective mass can either be calculated for all jets above an energy-threshold, m_{eff}(incl.), or for a specific jet multiplicity, m_{eff}(Nj).

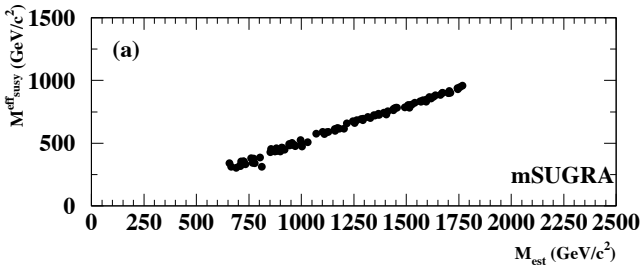

Fig. 4.3 · A scatter plot of the effective mass, M_{est}, and the effective SUSY mass scale, $M^{\text{eff}}_{\text{SUSY}}$ for mSUGRA. The figure is taken from Reference [193].

Missing transverse momentum significance: The missing transverse momentum significance is defined as $E_{\text{T}}^{\text{miss}}/\sqrt{H_{\text{T}}}$, where H_{T} is the jet-activity in an event ($H_{\text{T}} = \sum_{i=1}^{n_{\text{jets}}} |\vec{p}_{\text{T}}^{(i)}|$). The $E_{\text{T}}^{\text{miss}}$-significance is a measure of the size of the missing transverse momentum compared to the resolution of the hadronic energy in the event quantified by $\sqrt{H_{\text{T}}}$. The missing transverse momentum significance can be used to distinguish events with real $E_{\text{T}}^{\text{miss}}$ (high value of $E_{\text{T}}^{\text{miss}}/\sqrt{H_{\text{T}}}$) from events with fake $E_{\text{T}}^{\text{miss}}$ (low value of $E_{\text{T}}^{\text{miss}}/\sqrt{H_{\text{T}}}$). Especially the signal from SUSY models with direct squark decays is enhanced by a lower cut on this variable.

$E_{\text{T}}^{\text{miss}}/m_{\text{eff}}$(Nj): The fraction of m_{eff}(Nj) represented by $E_{\text{T}}^{\text{miss}}$ is greater for some signal models than the SM background. Especially signal models containing pair-production of high-mass gluinos have a high $E_{\text{T}}^{\text{miss}}/m_{\text{eff}}$(Nj)-value.

Other variables such as the *razor* variables [194], stransverse mass (m_{T2}) [195], con-transverse mass (m_{CT}) [196], and α_T [197], have also been studied. They were found not to give a significant improvement in separation between signal and background in the analyses presented in this thesis and are therefore not used in the definitions of signal regions.

4.2.2 Optimisation Strategies

Signal regions can be optimised following two strategies. The SRs are either optimised for the best discovery potential or they are optimised to set the strongest exclusion limits. The different optimisations will lead to different event selections as signal regions optimised for discovery potential tend to have harder cuts than signal regions optimised for exclusion. In this section, the two strategies will be introduced.

Optimising for Discovery Potential

Obviously, when searching for physics beyond the Standard Model such as supersymmetry, a discovery is the ultimate goal. Signal regions are therefore optimised for the greatest discovery potential the first time a dataset is studied.

Studying the discovery potential is equivalent to studying the rejection of the background-only (null) hypothesis, H_0, where the number of events coming from Standard Model processes alone

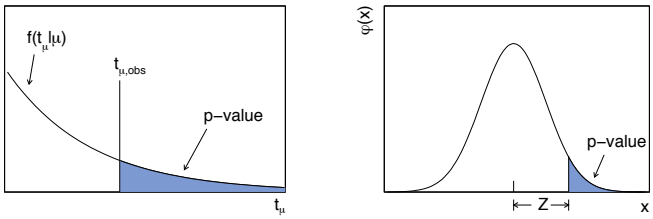

Fig. 4.4 · Relation between p-value and significance when observing $t_{\mu,\text{obs}}$. The figure is taken from Reference [198].

is compatible with the observed number of events. Let $f(x|H_0)$ be the probability density function of the number of events x given the background only hypothesis. When observing a number of events different from the expected, there is a possibility that it is a fluctuation. The compatibility of an observation, x_{obs}, with the expected outcome from the hypothesis can be quantified by the p-value. The p-value measures the probability of measuring x_{obs} or something more extreme under a hypothesis, H_μ. The p-value of the background-only hypothesis is defined as

$$p_0 = \int_{x_{\text{obs}}}^{\infty} f(x|H_0)dx, \tag{4.3}$$

if large values of x corresponds to poor compatibility. A low p-value is interpreted as a bad agreement between the hypothesis and the observation, whereas a high-value is corresponding to a good agreement. To decide whether a hypothesis is in agreement with observation or not a lower limit on the p-value, α, is chosen, so that the observation is in a critical region given the hypothesis if $p \leq \alpha$.

The p-value can be translated into a significance of the fluctuation, Z, defined as the number of standard deviations corresponding to the p-value. It is given as

$$Z = \Phi^{-1}(1-p), \tag{4.4}$$

where Φ is the cumulative distribution of a gaussian distribution. The relation between the p-value and the significance, Z, is shown in Figure 4.4. The evidence of physics beyond the Standard Model is by convention defined to be at $Z \geq 3$ corresponding to a 3σ deviation, whereas an observation or discovery is defined by $Z \geq 5$ corresponding to a p-value of 2.87×10^{-7}.

When optimising signal regions for discovery potential, the goal is to reject the background-only hypothesis given an observation of both background and signal. Assume that after a selection we expect b events on average from the background-only hypothesis, H_0, and s events on average from the signal. The significance of the observation of $x_{\text{obs}} = s + b$ events with the expected number of events b is calculated using Equation 4.4.

Combinations of the variables described in Section 4.2.1 and cut-values are varied and the significance on each choice of cuts is calculated for all signal points in the SUSY signal grid. A signal region is chosen to cover a group of signal points representing a specific region of the parameter space, e. g. the mass difference between the produced SUSY particle and the LSP.

Optimising for Best Exclusion

If a dataset has been studied with signal regions optimised for best discovery reach and the yields in the signal regions are compatible with the Standard Model-only hypothesis, then the signal regions can be re-optimised to gain better exclusion limits.

The statistical test to evaluate the exclusion power is different from the significance used to evaluate discovery potential. Instead of rejecting the background-only hypothesis, H_0, given an observation of the expected number of signal and background events, the goal has switched to rejecting the hypothesis of the presence of both signal and background, H_1, given an observation equal to the expected number of background events.

There is an uncertainty related to any measurement. Even if the number of observed events is identical to the number of events expected from the background-only hypothesis there is room for a signal as long as it is small enough to be covered by the uncertainties on the measurement. This places an upper limit on the size of the signal.

In order not to place too strong limits and reject hypotheses to which there are no real sensitivity, when for example a fluctuation in data results in fewer observed events than expected from the background hypothesis, the CL_s-method [199] is used. The measure, CL_s, is defined as

$$\mathrm{CL}_s = \frac{p_1}{1 - p_0}, \tag{4.5}$$

where p_0 is the p-value of the background-only hypothesis, H_0, given in Eq. 4.3, and p_1 is the p-value of the signal hypothesis, H_1, given by:

$$p_1 = \int_{x_{\mathrm{obs}}}^{\infty} f(x|H_1)dx. \tag{4.6}$$

A signal model is excluded at 95% confidence level (CL) if $\mathrm{CL}_s \leq 0.05$. An upper limit can be placed on the number of signal events by varying the signal strength in the signal hypothesis until CL_s reaches 0.05. The expected excluded number of signal events for a certain integrated luminosity can be interpreted as an expected excluded cross section, $\sigma^{\mathrm{expected}}_{\mathrm{excluded}}$.

When optimising signal regions for best exclusion power, the best signal region is found by minimising the ratio

$$\lambda = \frac{\sigma^{\mathrm{expected}}_{\mathrm{excluded}}}{\sigma_{\mathrm{nominal}}}, \tag{4.7}$$

where $\sigma_{\mathrm{nominal}}$ is the nominal cross section of the tested SUSY model. Again combinations of the variables described in Section 4.2.1 and cut-values are explored in all points in the parameter-space and λ is calculated for each combination in each point. The combinations resulting in the lowest value of λ for a larger part of the parameter space are chosen as the signal regions with the greatest exclusion power.

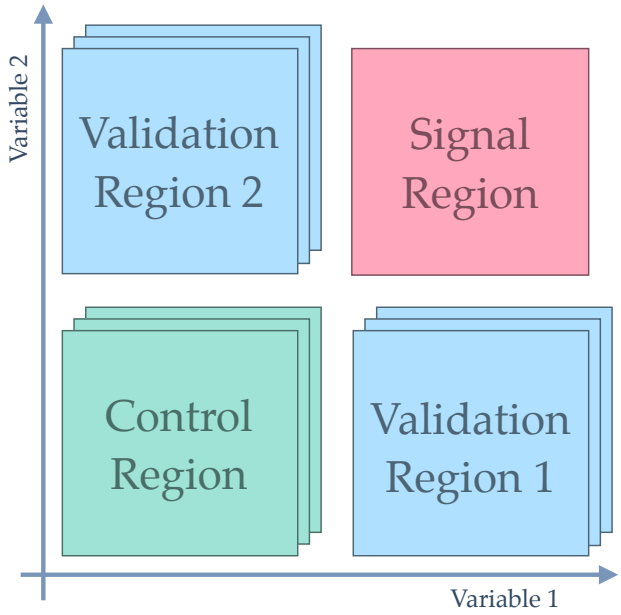

Fig. 4.5 · A sketch of a signal region with multiple control and validation regions. The signal region is defined by cuts on variable 1 and 2. Both cuts are reverted to define the control regions, while only one is reverted to define the validation regions.

4.3 Background Estimation

A vital part in searches for physics beyond the Standard Model is a reliable estimate of the Standard Model background processes. Three methods are used in the background estimation - simulation only, semi data-driven, and completely data-driven.

The smallest backgrounds are estimated using Monte Carlo simulations alone, while the major backgrounds are estimated using either completely or semi data-driven methods. Both data-driven methods make use of control regions.

4.3.1 Control Regions and Transfer Factors

Control regions (CR) are kinematic regions of phase space orthogonal to the signal regions, i. e. no event is present in both signal and control regions. Control regions are chosen to be as kinematically close to the signal regions as possible. This is typically done by inverting one or two of the signal region cuts as illustrated by the sketch in Figure 4.5. A control region is designed to be enriched in one of the Standard Model background processes. One signal region can have multiple control regions for different background processes. Control regions belonging to the same signal region are orthogonal.

The number of background events in a signal region is estimated using transfer functions from the control region to the signal region. It is assumed that for a given Standard Model background process the ratio of the number of events in the signal region and the number of events in the control region is the same for the simulated (expected) events as for the events observed in data:

$$\frac{N_{\mathrm{SR}}^{\mathrm{obs,process}}}{N_{\mathrm{CR}}^{\mathrm{obs,process}}} = \frac{N_{\mathrm{SR}}^{\mathrm{exp,process}}}{N_{\mathrm{CR}}^{\mathrm{exp,process}}}, \tag{4.8}$$

where $N_{\mathrm{X}}^{\mathrm{obs/exp,process}}$ is the observed/expected number events in region X of a specific background process. The transfer function ($\mathrm{TF}_{\mathrm{CR}\to\mathrm{SR}}$) of a control region is found from this assumption by re-arranging the terms

$$N_{\mathrm{SR}}^{\mathrm{est,process}} = N_{\mathrm{CR}}^{\mathrm{obs,process}} \times \frac{N_{\mathrm{SR}}^{\mathrm{exp,process}}}{N_{\mathrm{CR}}^{\mathrm{exp,process}}} = N_{\mathrm{CR}}^{\mathrm{obs,process}} \times \mathrm{TF}_{\mathrm{CR}\to\mathrm{SR}}, \tag{4.9}$$

where $N_{\mathrm{SR}}^{\mathrm{est,process}}$ is the estimated number of events in the signal region arising from a specific background process. There will be a transfer function for each control region estimating one specific background process. This procedure allows for the simulation to not get the individual event count in the various regions correct, but assumes that the ratio of the yield in the control region to the yield in the signal region is correct in the simulation. This assumption is validated in the validation regions.

Rather than using transfer functions in the background, Eq. 4.9 is re-ordered to show the normalisation of the background process in the control region:

$$N_{\mathrm{SR}}^{\mathrm{est,process}} = N_{\mathrm{SR}}^{\mathrm{exp,process}} \times \frac{N_{\mathrm{CR}}^{\mathrm{obs,process}}}{N_{\mathrm{CR}}^{\mathrm{exp,process}}} = N_{\mathrm{SR}}^{\mathrm{exp,process}} \times \mu_{\mathrm{process}}. \tag{4.10}$$

The normalisation factor, μ_{process}, provides information on how correctly the simulation predicts the observed event yield of a given process. If $\mu \approx 1$, the expected number of events agree well with the number of events observed in data. The normalisation factor is used in the background fit.

A control region for a specific process will still contain events arising from other background processes. This cross-contamination needs to be taken into account in the background fit to the control regions.

By ensuring that the events in the control regions are kinematically close to the events that enter into the signal, some uncertainties will cancel in the transfer functions reducing the total uncertainty on the background estimation.

The expected number of events of a background process in both signal and control regions is calculated from simulations in a semi data-driven technique for background estimation. For a completely data-driven background estimation, the input for the expected number of events of a background process is based on a sample obtained using data-driven techniques. This is especially important in order to estimate the multijet background since the cross section is large

and simulations are known not to describe the process well. The data-driven multijet background template is obtained using the jet smearing method where an event with low $E_{\mathrm{T}}^{\mathrm{miss}}$ is selected and the energy of the jets are smeared to obtained fake $E_{\mathrm{T}}^{\mathrm{miss}}$. This is described in detail in Section 5.6.2.

When performing an analysis, the signal regions are blinded, i. e. the data in the signal region is not studied, until the background estimates are validated and found reliable.

4.3.2 Validation Regions

In order to test the robustness of the estimate of the Standard Model backgrounds in the signal regions, the background estimation techniques both from simulation and data are validated in dedicated validation regions (VR).

The validation regions are defined by reverting one of the two or more cuts that were used to define the control regions based on the signal region selection. A sketch of the definition of validation regions is shown in Figure 4.5, where either the cut on variable 1 or variable 2 is reverted to define two validation regions.

The background estimates are validated by computing the transfer functions from the control regions into the validation regions similarly to the transfer functions calculated for signal regions. The total estimated number of events in a validation region is found by adding the estimates of all the processes

$$N_{\mathrm{VR}}^{\mathrm{est}} = \sum_{\mathrm{processes}} N_{\mathrm{CR}}^{\mathrm{obs,process}} \times \frac{N_{\mathrm{VR}}^{\mathrm{exp,process}}}{N_{\mathrm{CR}}^{\mathrm{exp,process}}}. \tag{4.11}$$

It is tested that a negligible amount of events originating from the signal enter into the validation regions.

If a big disagreement between the expected and observed number of events is found in a validation region, the signal regions are not unblinded and further studies are done to understand the origin of the disagreement. Only when the observed number of events in all validation regions are found to agree with expectation, the signal regions are unblinded and it is seen whether physics beyond the Standard Model has been discovered.

4.4 Statistical Procedure

The ultimate goal of a SUSY analysis is to discover physics beyond the Standard Model. To do that a method to quantify the significance of an eventual excess is needed. If no excesses are observed, the results of a SUSY analysis are upper limits on visible production cross sections of physics beyond the Standard Model and exclusions of specific SUSY models.

In total there are three types of fits relevant for a search for supersymmetry:

Background-only fit: The background only fit is done to estimate the number of events in signal regions arising from Standard Model processes. The background-only fit uses a profile likelihood function.

Discovery fit: In case an excess is observed, the discovery fit will determine the significance of the excess over the Standard Model background. The discovery fit uses a profile log-likehood ratio.

Exclusion fit: If no excesses are found, the result of the analysis will be reported as upper limits on the visible signal cross section of physics beyond the Standard Model obtained through an exclusion fit. The exclusion fit uses a profile log-likehood ratio.

All three types of fits are built on similar likelihood-functions.

The fits are performed using the Histfitter package [200] relying on Histfactory [201] which is a tool in the RooStats/RooFit frameworks [202, 203] based on ROOT [204, 205]. A thorough description of the statistical procedure is given in Reference [206].

4.4.1 Likelihood Function

The likelihood function is defined for each signal region and is a product of Poisson distributions of both the signal region and the corresponding control regions and probability density functions constraining the systematic uncertainties:

$$L\left(\boldsymbol{n}|\boldsymbol{\mu},\boldsymbol{s},\boldsymbol{b},\boldsymbol{\theta}\right) = \prod_{i\in[\mathrm{SR,CRs}]} P_i\left(n_i|\lambda_i\left(\boldsymbol{\mu},\boldsymbol{s},\boldsymbol{b},\boldsymbol{\theta}\right)\right) \prod_{j\in[\mathrm{SU}]} G(\theta_j^0,\theta_j), \tag{4.12}$$

where n_i is the observed number of events in region i, λ_i is the expected number of events in region i, and SU is the collection of sources of systematic uncertainties. $G(\theta_j^0,\theta_j)$ are Gaussian distributions constraining each systematic, θ_j, with a mean of 0 and a width of 1. The effect of the systematic uncertainties on the expected number of events is described by functions included in λ_i. The fit is performed by a maximum likelihood method. Due to technicalities, the negative logarithm of the likelihood function is minimised.

The expected number of events in a region, i, is given by:

$$\lambda_i\left(\boldsymbol{\mu},s_i,\boldsymbol{b},\boldsymbol{\theta}\right) = \mu_s\cdot s_i(\boldsymbol{\theta}) + \sum_j \mu_j\cdot b_{j,i}(\boldsymbol{\theta}), \tag{4.13}$$

where j is the sum over all the background processes, and $s_i(\boldsymbol{\theta})$ and $b_{j,i}(\boldsymbol{\theta})$ are the expected number of signal and background events, respectively, in region i taken from simulation including the effect of the systematic uncertainty. μ_s is the signal strength with $\mu_s = 1$ corresponding to the un-normalised, expected yield of the signal. μ_j is the normalisation of background process j obtained from the control region fit. For background processes estimated solely from simulation, the normalisation factor, μ_j, is one.

The expected number of background events from process j in region i, $b_{j,i}(\boldsymbol{\theta})$, included in Equation 4.13 takes into account the effect of the systematic uncertainties, $\boldsymbol{\theta}$. The expected number of background events of a given process in region R can be written as:

$$b_{\mathrm{process},R} = N_R^{\mathrm{MC,process}} \times \left(1 + \sum_k \Delta_{\mathrm{process},R;k}\theta_k\right), \tag{4.14}$$

where $\Delta_{\text{process},R;k}$ is the size of the systematic uncertainty. It is defined likewise for the expected number of signal events, $s_i(\boldsymbol{\theta})$.

The sources of systematic uncertainties include uncertainties coming from the resolution of the detector, uncertainties on the modeling in the simulation used for the background samples, and the uncertainties arising from the limited statistics of the simulation samples.

4.4.2 Background-only Fit

The background-only fit is used to get an estimate of the number of events expected from Standard Model processes in the signal regions. It is done by maximising the likelihood function defined in Equation 4.12 through normalisation of the backgrounds in the control regions using the normalisation factors μ_{process} introduced in Equations 4.12 and 4.13 as free parameters. The Poisson distribution describing the signal region is not included in the likelihood function for this fit and it is assumed that no signal enter any of the control regions, i. e.the signal strength, μ_s, is zero. The fit is performed simultaneously in all control regions to take into account the cross-contaminations of the different backgrounds in the various control regions. The input for the fit is the number of observed events in each control region and the expected number of events of each background process in each region.

After the fit is performed and the optimal normalisation factors are found, one for each background estimated through a semi or completely data-driven technique, the expected number of events from backgrounds in signal and validation regions are estimated using Equation 4.14.

4.4.3 Discovery Potential and Best Exclusion

Once the background is estimated in the control regions, it is time to test whether any physics beyond the Standard Model has shown itself or the result of the analysis is an upper limit on the number of signal events that can enter the signal region.

A discovery fit is performed in each signal region to test the agreement of the observed number of events with a background only-hypothesis, it is thus assumed that there is no signal, i. e. $\mu_s = 0$. If no excess is observed, an exclusion fit is performed assuming $\mu_s \neq 0$. For both discovery and exclusion fit, the signal region is included in the likelihood function defined in Equation 4.12. For the model-independent fit, it is assumed that there is no signal contamination in the control regions.

The test statistics used in estimating the discovery potential or the limits, is constructed from a log-likelihood ratio:

$$\Lambda(\mu_s) = -2\ln\left[\frac{L(\boldsymbol{n}, \boldsymbol{\theta}^0|\mu_s, \hat{\hat{\boldsymbol{b}}}, \hat{\hat{\boldsymbol{\theta}}})}{L(\boldsymbol{n}, \boldsymbol{\theta}^0|\hat{\mu}_s, \hat{\boldsymbol{b}}, \hat{\boldsymbol{\theta}})}\right], \tag{4.15}$$

where the single-hatted symbols maximise the likelihood and the double-hatted symbols are the best fitted values given a specific signal strength μ_s. If the best fitted value of the signal strength, $\hat{\mu}_s$, is found to be negative it is put to zero, $\hat{\mu}_s = 0$.

If a test of discovery is performed, it is assumed that the existence of physics beyond the Standard Model will lead to an increase in the observed events in the signal regions. Fewer events than what is expected from the backgrounds will lead to a negative signal strength which is regarded as unphysical. The test statistics for a discovery is therefore defined as

$$q_0 = \begin{cases} \Lambda(0) & \text{if } \hat{\mu}_s \geq 0, \\ 0 & \text{if } \hat{\mu}_s < 0. \end{cases} \tag{4.16}$$

The discovery test is a test of the agreement of the background-only hypothesis with the observed excess, the signal strength is therefore zero.

If instead a hypothesis for physics beyond the Standard Model with signal strength $\mu_s \neq 0$ is tested for exclusion, the test statistics is defined as

$$q_\mu = \begin{cases} \Lambda(\mu_s) & \text{if } \hat{\mu}_s \leq \mu_s, \\ 0 & \text{if } \hat{\mu}_s > \mu_s. \end{cases} \tag{4.17}$$

The test statistics is defined such that it is not possible to exclude a model with smaller signal strength than the best fitted value, $\hat{\mu}_s$.

There is a difference in the definition of the test statistics designed for discovery and exclusion: the test statistics for discovery disfavours a downward fluctuation of the data whereas the test statistics for exclusion disfavours an upward fluctuation in data.

The (in-)compatibility of the observation with the hypothesis is quantified by the p-value already discussed in Section 4.2.2

$$p_\mu = \int_{q_{\mu,\text{obs}}}^{\infty} f(q_\mu|\mu) dq_\mu, \tag{4.18}$$

where $f(q_\mu|\mu)$ is the probability density function of the test statistic, q_μ, given a signal strength, μ. In most cases, no simple analytical function of $f(q_\mu|\mu)$ exists. The probability density function can either be approximated with an asymptotic function, an Asimov dataset [198], if many events are observed or through toy simulations if a signal region is populated by few events (≤ 20). Both methods are used when setting upper limits.

For a discovery fit, p_0 is calculated and thereafter translated into a significance, Z, using Equation 4.4. As mentioned earlier, the convention in high energy physics is that there is evidence at $Z \geq 3$ and discovery at $Z \geq 5$.

In order not to set too strong limits due to fewer observed events than expected from background-only, the p_1-value is not used for exclusion. Instead the CL_s-method [199], introduced in Section 4.2.2 and defined in Equation 4.5, is used. A signal hypothesis is excluded at 95% confidence level if $\text{CL}_s < 0.05$. For upper limits on the visible cross section, the signal strength is varied until condition for exclusion ($\text{CL}_s < 0.05$) is met. CL_s is a conservative estimator, i. e. CL_s over-covers. CL_s can only be used for exclusions and not for discoveries or measurements as it is not a real probability.

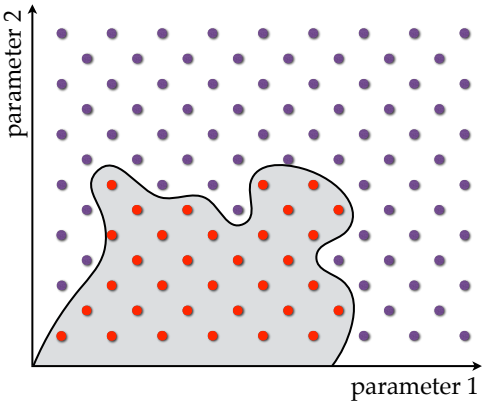

Fig. 4.6 · A sketch of a model-dependent exclusion limit. The red dots are excluded at 95% confidence level, the purple dots are not excluded. The grey area is the excluded part of the parameter space.

4.4.4 Model-dependent Limits

Aside from the model-independent upper limit per signal region on the visible cross section for physics beyond the Standard Model, model-dependent limits are set on the parameter space of specific models of supersymmetry or other beyond the Standard Model theories.

The exclusion fit performed for model-dependent limits takes into account eventual leakage of signal into the control regions from simulation. Before the observed number of events in a signal region is included in the fit, the expected limit is found by calculating CL_s in each parameter point for each signal region from simulation. The signal region yielding the lowest expected CL_s-value is chosen to form the best expected limit and the same signal region is used for that parameter point when finding the observed limit. This ensures that there is no bias of a downward fluctuation in the observed number of events in a signal region. After the best signal region for each parameter point is determined, the CL_s-value is calculated. A point is excluded if $CL_s < 0.05$. If that requirement is not fulfilled, the point cannot be excluded. The excluded area of the parameter space is found by triangular interpolation between the points. Figure 4.6 illustrates how an excluded area in a SUSY parameter space typically looks. The red points are excluded and the grey area is the entire excluded region obtained through triangulation.

Even more interesting than the exclusion limit on the simplified models are the upper limits on the cross section calculated per point. :

$$N = \sigma_{\text{tot}} \times \mathcal{L}_{\text{int}} \times \epsilon, \tag{4.19}$$

where σ_{tot} is the sparticle production cross section, and ϵ is the reconstruction efficiency times acceptance of the point. The upper limit on the number of signal events in a signal region obtained using the model-independent exclusion fit can be used to place an upper limit on the production cross section.

Upper limits on simplified models can furthermore be interpreted in larger SUSY models [207]. This is done by decomposing the larger model into a set of sparticle productions and decays that is described using simplified models. The expected number of events in a given signal region of a larger SUSY model decomposed into simplified models will then be:

$$N = \sigma_{\text{tot}} \times \mathcal{L}_{\text{int}} \times \left(\sum_{i \in [\text{SM}]} \epsilon_i \times P_i \times \mathcal{B}r_i \right), \tag{4.20}$$

where i is the sum over simplified models (SM) into which the SUSY model has been decomposed, ϵ_i is the reconstruction efficiency times acceptance of the simplified model in the given signal region, P_i the production fraction of the simplified model compared to the total cross section, and $\mathcal{B}r_i$ is the branching fraction in the larger SUSY model of the decay included in the simplified model.

5

Searching for Squarks and Gluinos at $\sqrt{s} = 8$ TeV

In this chapter a search for supersymmetry in events with jets and missing transverse momentum at $\sqrt{s} = 8$ TeV using $\int L\mathrm{d}t = 20\ \mathrm{fb}^{-1}$ data collected by the ATLAS experiment is presented. This analysis is very powerful in the search for R-parity conserving SUSY models with light first and second generation squarks as well as light gluinos all producing final states containing jets and $E_{\mathrm{T}}^{\mathrm{miss}}$. The emphasis in this chapter is on the search for left-handed squark-pair production in a phenomenological MSSM (pMSSM) model and optimising signal regions for this specific SUSY scenario. Limits on other SUSY models sensitive to this final state are presented as well.

The analysis is built on the method described in Chapter 4 using one-binned signal regions. For each signal region a set of control and validation regions is defined.

The search for supersymmetry in events with jets and missing transverse momentum is published in Ref. [1] and the updated analysis with new signal regions optimised for a pMSSM model with left-handed squark-pair production is published in Ref. [2].

5.1 SUSY Models

Three sets of SUSY models are considered in this chapter: simplified models with squark and gluino production and decay, a R-parity conserving MSUGRA/CMSSM model, and a pMSSM model with left-handed squark-pair production. Descriptions of the simplified models and the MSUGRA/CMSSM model are given in this section as well as a more extensive review of the pMSSM model with left-handed squark-pair production.

5.1.1 Simplified Models

The concept of simplified models was introduced in Section 1.4.3. Two sets of simplified models are studied in this analysis: simplified models with direct decays of squarks and gluinos, and simplified models with a one-step decays of squarks and gluinos through $\tilde{\chi}_1^{\pm}$.

Sketches of the production and decay of squarks and gluinos in models with direct decays, $\tilde{q} \to q\tilde{\chi}_1^0$ or $\tilde{g} \to q\bar{q}\tilde{\chi}_1^0$, are shown in Figure 5.1. $\tilde{\chi}_1^0$ is assumed to be the lightest supersymmetric particle (LSP). Three models with different production of sparticles are considered, $\tilde{q}\tilde{q}$, $\tilde{q}\tilde{g}$, and

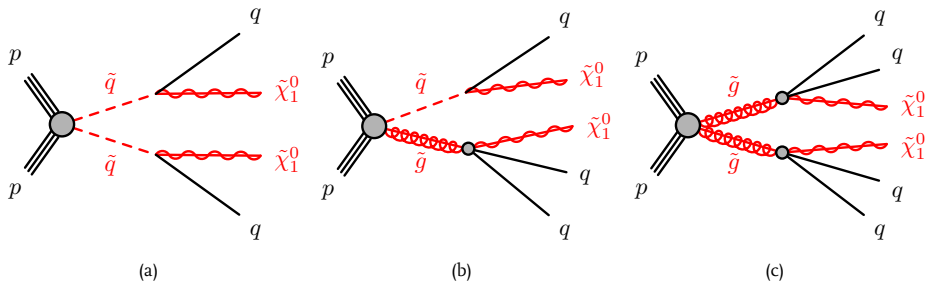

Fig. 5.1 · Sketch of squark-pair (a), squark-gluino (b), and gluino-pair (c) production with direct decays into final states with quarks and two $\tilde{\chi}_1^0$.

$\tilde{g}\tilde{g}$, leading to final states containing two $\tilde{\chi}_1^0$ and two, three, and four quarks, respectively. The free parameters in the simplified models with direct decays are the mass of the squark or the gluino and the mass of $\tilde{\chi}_1^0$. In the model with $\tilde{q}\tilde{g}$-production, the mass of the squark is a little bit lower than the mass of the gluino, $m_{\tilde{q}} = 0.96 \times m_{\tilde{g}}$ motivated by studies of compressed supersymmetry where the mass difference between sparticles is small [208, 209]. The mass of $\tilde{\chi}_1^0$ is bound to be smaller than the mass of the squark or gluino since the squark and gluino decays would not be possible, and $\tilde{\chi}_1^0$ would not be the LSP.

Two models with one-step decays are considered, squark-pair production and gluino-pair production. The one-step decays go through a intermediate chargino, $\tilde{q} \to q'\tilde{\chi}_1^\pm \to q'W^\pm\tilde{\chi}_1^0$ or $\tilde{g} \to \bar{q}q'\tilde{\chi}_1^\pm \to \bar{q}q'W^\pm\tilde{\chi}_1^0$, leading to final states containing quarks, $\tilde{\chi}_1^0$, and the decay product of W bosons. Sketches of the production and one-step decays of squarks and gluinos are shown in Figure 5.2. There are two sets of free parameters in these models: either both the mass of the squark or the gluino and the mass of $\tilde{\chi}_1^0$ are varied and $m_{\tilde{\chi}_1^\pm}$ is fixed to $m_{\tilde{\chi}_1^\pm} = (m_{\tilde{q},\tilde{g}} + m_{\tilde{\chi}_1^0})/2$ or the mass of the squark or the gluino and the relation $x = [m_{\tilde{\chi}_1^\pm} - m_{\tilde{\chi}_1^0}]/[m_{\tilde{q}/\tilde{g}} - m_{\tilde{\chi}_1^0}]$ are varied and mass of the LSP is fixed to $m_{\tilde{\chi}_1^0} = 60$ GeV.

In the simplified models with $\tilde{q}\tilde{q}$ production, the gluino is assumed to be beyond the reach of production at the LHC, i. e. decoupled ($m_{\tilde{g}} = 4.5$ TeV), while in model with $\tilde{g}\tilde{g}$ production, the squarks are assumed to be decoupled ($m_{\tilde{q}} = 4.5$ TeV).

The cross sections of all the simplified models are calculated at NLO+NLL using NLLFAST [210–214]. In the models with squark-pair production, the cross sections are calculated assuming the first two generations of squarks to be mass degenerate. By scaling the cross section by 1/8, the sensitivity to models with only one light squark can be studied.

5.1.2 MSUGRA/CMSSM

MSUGRA/CMSSM models have as described in Section 1.4.3 five free parameters, m_0, $m_{1/2}$, $\tan\beta$, A_0, and the sign of μ. In the model used in this analysis R-parity is assumed to be conserved. The values of m_0, and $m_{1/2}$ are varied freely while the values of the remaining parameters are fixed: $\tan\beta = 30$, $A_0 = -2m_0$, and $\mu > 0$. The values are chosen such that the lightest Higgs

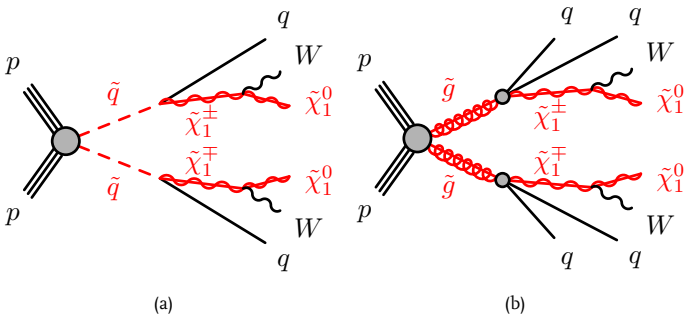

Fig. 5.2 · Sketch of squark-pair (a) and gluino-pair (b) production with one-step decays through $\tilde{\chi}_1^{\pm}$ into final states with quarks, W bosons, and two $\tilde{\chi}_1^0$.

boson will have a mass of $\sim$ 125 GeV in agreement with the observation by the ATLAS and CMS experiments.

The masses of the sparticles at the TeV-scale are calculated from the parameters using SUSY-HIT [215] interfaced with SOFTSUSY [216] and the branching fractions of the decays of sparticles are calculated using SUSY-HIT [215] interfaced with SDECAY [217]. The masses of all the sparticles, both sfermions and bosinos, depend on the value of $m_{1/2}$ whereas it is mostly the masses of the sfermions that are sensitive to the value of m_0. For high values of $m_{1/2}$ and low values of m_0, squark-pair production is the dominant production mode. If instead the values of m_0 are high, the masses of the squarks will increase and production of gauginos will dominate. The dominant decay mode of squarks and gluinos are direct decays, $\tilde{q} \to q\tilde{\chi}_1^0$ and $\tilde{g} \to q\bar{q}\tilde{\chi}_1^0$, though other decays are possible as well.

The production cross sections of the various sparticles are calculated using PROSPINO [218]. Each process is weighted by the corresponding cross section.

5.1.3 A pMSSM Model with Left-handed Squark-pair Production

The third supersymmetric model studied in this chapter is a pMSSM model where $\tilde{q}_L$-pairs are produced and immediately decay through many different decay chains. Left-handed squark-pair production is chosen to allow for one-step decays through $\tilde{\chi}_1^{\pm}$ and $\tilde{\chi}_2^0$ which are both wino-like and do therefore not couple to right-handed squarks. The set of pMSSM models is as described in Section 1.4.3 a subset of the MSSM reducing the set of free parameters from 105 to 19.

The parameters are chosen such that the right-handed sfermions and the third generation squarks are decoupled and thus only left-handed squarks of the first two generations can be produced. The gluino mass is fixed at $\sim$ 2.2 TeV through the parameter M_3, while the chargino and neutrinalino masses as well as the higgsino mixing are left to vary by varying M_1, M_2, and μ. The ratio of the Higgs vacuum expectation values ($\tan\beta$), the mass of the pseudoscalar Higgs boson (m_A), and the trilinear couplings (A_b, A_t, and A_τ) are fixed. The parameters are chosen such that the lightest Higgs boson, h_0, has a mass of $\sim$ 125 GeV which is in agreement with the

Parameter	Value
$m_{\tilde{q}_L}$	[250 GeV - 1550 GeV]
$m_{\tilde{u}_R} = m_{\tilde{d}_R} = m_{\tilde{l}_L} = m_{\tilde{e}_R}$	5 TeV
$m_{\tilde{Q}_L} = m_{\tilde{t}_R} = m_{\tilde{b}_R} = m_{\tilde{L}_L} = m_{\tilde{\tau}_R}$	5 TeV
M_1	[1 GeV – 1200 GeV]
M_2	[100 GeV – 1500 GeV]
M_3	2 TeV
μ	[950 GeV – 2700 GeV]
$\tan\beta$	4
m_A	2 TeV
A_t	4.5 TeV
A_b	0 GeV
A_τ	0 GeV

Table 5.1 · The pMSSM parameter values for the $\tilde{q}_L$-pair production.

measured mass of the recently discovered Higgs boson. Furthermore, the lightest Higgs boson is expected to have branching fractions identical to those of the Standard Model Higgs boson. A summary of the parameters and their values is given in Table 5.1.

The pMSSM parameter describing the mass of the left-handed squarks is varied in steps of 100 GeV from 250 GeV to 1550 GeV. Two different parameter scans of the bino and wino mass parameters, M_1 and M_2, are studied. One scan where the bino mass parameter is fixed to $M_1 = 60$ GeV, and the wino mass is varied independently in steps of 100 GeV. In the other parameter scan, both M_1 and M_2 are varied, however they are constrained by the relation $M_2 = \left[M_1 + m_{\tilde{q}_L}\right]/2$.

The masses of the SUSY particles are heavily correlated with the pMSSM parameters. The mass spectrum is calculated using SUSY-HIT [215] interfaced with SOFTSUSY [216]. The masses of the left-handed squarks are $\sim$ 400 GeV larger than the pMSSM parameter $m_{\tilde{q}_L}$ as is seen from the comparison in Figure 5.3. The mixing of bino, wino, and higgsino fields form the massive gauginos. The mass of the lightest neutralino, $m_{\tilde{\chi}_1^0}$, is almost identical to the pMSSM parameter M_1 thus making the LSP bino-like. The mass of the chargino, $m_{\tilde{\chi}_1^\pm}$, and second lightest neutralino, $m_{\tilde{\chi}_2^0}$, are both close in value to M_2 and therefore mostly wino. The heavier chargino and neutralinos have masses close to the μ-parameter. The correlation of the gaugino masses with the pMSSM parameters show that there is very little mixing of the bino, wino, and higgsino fields. The mass of the gluino is $\sim$ 2.2 TeV compared to the pMSSM parameter $M_3 = 2$ TeV.

Cross Section of Left-handed Squark-pair Production

As only the left-handed squarks are light enough to be produced, the main production will happen in a t-channel diagram by exchange of a gluino resulting in a dominant production of $\tilde{q}_L\tilde{q}_L$ or

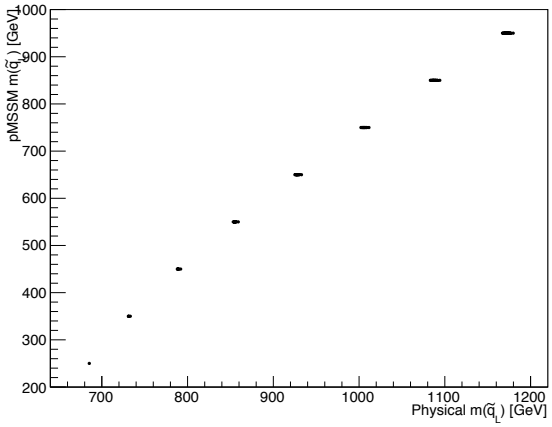

Fig. 5.3 · Correlation of the pMSSM parameter $m_{\tilde{q}_L}$ and the physical mass of a left-handed squark in the pMSSM model considered.

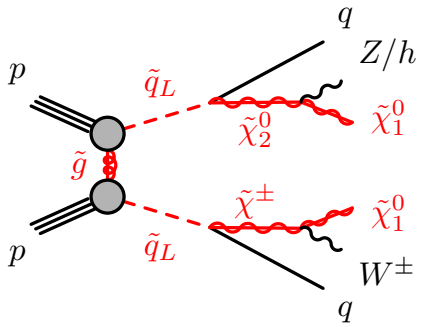

Fig. 5.4 · Sketch of $\tilde{q}_L$-pair production through exchange of a gluino. The two decays shown are the dominant decays of left-handed squarks in the pMSSM parameter scan.

$\bar{\tilde{q}}_L\bar{\tilde{q}}_L$ pairs compared to $\tilde{q}_L\bar{\tilde{q}}_L$-pair production. In Figure 5.4, the production of left-handed squarks through a t-channel is shown together with the two dominant decay modes of $\tilde{q}_L$.

If the gluino mass is changed, the cross section changes as well, but the kinematics of the events remain the same. This is checked by generating samples of $\tilde{q}_L$-pair production with three gluino masses, $m_{\tilde{g}} = 1.6$ TeV, 2.2 TeV, and 3.0 TeV. The kinematics of events generated with different gluino masses are compared. The comparison of distributions produced with different gluino masses in four variables is shown in Figure 5.5. It is seen that the shape of the distributions are comparable, differing only due to statistical fluctuations. By simply rescaling the sample of $\tilde{q}_L$-pair production generated with a gluino mass of 2.2 TeV to the cross section of $\tilde{q}_L$-pair production with a different gluino mass, it is possible to study the sensitivity of a model with another gluino mass.

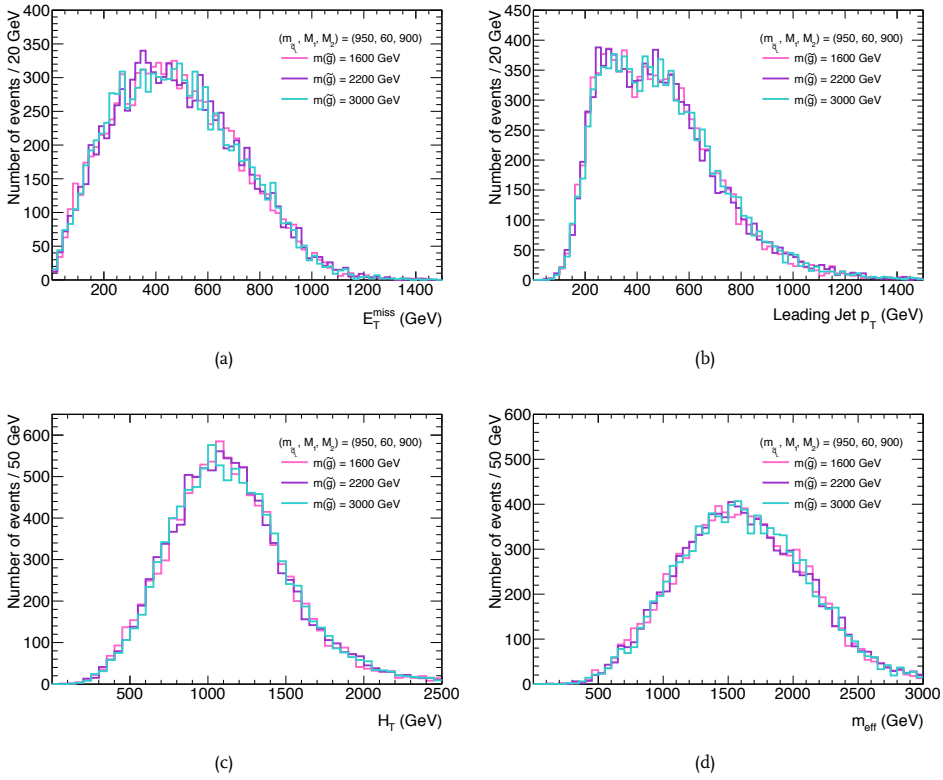

Fig. 5.5 · Distributions of E_T^{miss}(a), p_T of the leading jet (b), H_T (c), and m_{eff} (d) of $\tilde{q}_L$-pair production with different gluino mass, $m_{\tilde{g}} = 1.6$ TeV, 2.2 TeV, and 3.0 TeV. The samples are created at truth level.

The cross sections are calculated using PROSPINO [218]. Due to a technicality, the cross section cannot be computed for left-handed squarks alone. Instead the cross section is calculated assuming the masses of the left-handed and right-handed squarks are degenerate and low. To obtain the final cross section for production of only left-handed squarks, the cross section of the sum of left- and right-handed squark-pair production is divided by 2.

Decays of Left-handed Squarks

There are several decay modes of the left-handed squarks available in this pMSSM model. The branching fractions and decay modes depend on the pMSSM parameters. However, most of the parameter combinations studied here have very similar branching fractions of $\tilde{q}_L$. All the branching fractions are calculated using SUSYHIT [215] interfaced with SDECAY [217].

The most frequent decay of $\tilde{q}_L$ is into $\tilde{\chi}_1^{\pm}$ and a quark, $\tilde{q}_L \to q'\tilde{\chi}_1^{\pm}$, with a branching fraction of $\sim$ 65%. Another dominating decay mode of $\tilde{q}_L$ is into a quark and $\tilde{\chi}_2^0$, $\tilde{q}_L \to q\tilde{\chi}_2^0$ with a branching fraction of $\sim$ 33%. The left-handed squark can decay directly to a quark and an LSP, $\tilde{\chi}_1^0$,

pMSSM Parameters	$m_{\tilde{q}_L} = 950$ GeV $M_1 = 400$ GeV $M_2 = 675$ GeV	$m_{\tilde{q}_L} = 1350$ GeV $M_1 = 60$ GeV $M_2 = 700$ GeV
Squark Decays		
$\tilde{q}_L \to q\tilde{\chi}_1^0$	2.1%	2.0%
$\tilde{q}_L \to q\tilde{\chi}_2^0$	32.6%	32.6%
$\tilde{q}_L \to q'\tilde{\chi}_1^\pm$	65.2%	65.4%
Chargino Decays		
$\tilde{\chi}_1^\pm \to W^\pm\tilde{\chi}_1^0$	100%	100%
Neutralino Decays		
$\tilde{\chi}_2^0 \to Z\tilde{\chi}_1^0$	6.7%	34.2%
$\tilde{\chi}_2^0 \to h\tilde{\chi}_1^0$	93.3%	65.8%

Table 5.2 · Branching fractions of left-handed squarks, $\tilde{\chi}_1^\pm$, and $\tilde{\chi}_2^0$ for two choices of pMSSM parameters. The branching fractions are calculated using SUSYHIT [215].

as well, but the branching fraction of this decay is not very large ($\sim 2\%$). The branching fractions of left-handed squarks for two choices of pMSSM parameters are shown in Table 5.2.

The gauginos, $\tilde{\chi}_1^\pm$ and $\tilde{\chi}_2^0$, are unstable and will decay immediately. The chargino, $\tilde{\chi}_1^\pm$, will only decay into a $W^\pm$ boson and $\tilde{\chi}_1^0$ with a 100% branching fraction. The second neutralino, $\tilde{\chi}_2^0$, can decay into a $\tilde{\chi}_1^0$ and either a Z boson or a Higgs boson. The decay of $\tilde{\chi}_2^0$ into a h-boson is favoured with a branching fraction of at least $\sim 65\%$, however the branching fractions of the $\tilde{\chi}_2^0$ decays depend on the pMSSM parameter. In Table 5.2, the decay modes and branching fractions of $\tilde{\chi}_1^\pm$ and $\tilde{\chi}_2^0$ are shown for two sets of pMSSM parameters.

The final state produced by the decay of left-handed squarks contains jets originating from quarks, $E_{\mathrm{T}}^{\mathrm{miss}}$ originating from $\tilde{\chi}_1^0$, and the decay products of $W^\pm$, Z, and h. Since the branching fractions of $W^\pm$, Z, and h into quarks are dominant, it is expected that an analysis with events containing jets and $E_{\mathrm{T}}^{\mathrm{miss}}$, but no leptons will be sensitive to this model.

5.2 Standard Model Background Processes

There are several Standard Model processes that can mimic our signal which is characterised by jets and $E_{\mathrm{T}}^{\mathrm{miss}}$. Some of the backgrounds arise from mis-identification of particles or imprecise measurement of their energy, while other backgrounds truly have a final state identical to that of the signal.

There are five Standard Model backgrounds expected to contribute when selecting events with $E_{\mathrm{T}}^{\mathrm{miss}}$, jets and no leptons: $t\bar{t}$+(EW) and single-top, Z/γ^*+jets, $W^\pm$+jets, diboson production, and multijet events from the strong interaction.

5.2.1 Top Background

If a (anti-)top-quark decays leptonically, $t \to b\ell\bar{\nu}_\ell$, and the lepton is mis-identified as a jet or the lepton is not reconstructed as it can be outside the acceptance of the detector, it will lead to events seemingly containing jets and true $E_{\mathrm{T}}^{\mathrm{miss}}$ from the ν_ℓ, i. e. a final state similar to the one of the signal. Another possibility is that the (anti-)top-quark decays to a hadronically decaying tau which is very similar to a jet. A hadronic decay of a top quark $t \to bq\bar{q}'$, will not lead to real $E_{\mathrm{T}}^{\mathrm{miss}}$ in the event. Fake $E_{\mathrm{T}}^{\mathrm{miss}}$ in hadronic top decays can occur when the energy of a jet is mis-measured. Furthermore, top quarks can be produced together with a Z or $W^{\pm}$-boson whose decays can lead to final states identical to the one chosen for the analysis. Top quarks produced in association with a Higgs boson are assumed to be a negligible background.

Top quarks can either be produced in top-antitop pairs or as a single top quark. A single top quark can be produced through a s-channel diagram, a t-channel diagram or in association with a $W^{\pm}$ boson.

5.2.2 Electroweak Background

The electroweak background processes relevant for this analysis are Z/γ^*+jets, $W^{\pm}$+jets, and diboson production.

Z/γ^*+jets

One of the largest backgrounds is $Z(\to \nu\nu)$+jets as this process produces a final state identical to the one expected from signal. $Z/\gamma^*(\to \ell\ell)$+jets is a minor background since it doesn't contain any true $E_{\mathrm{T}}^{\mathrm{miss}}$ and both leptons need to fail identification. $Z/\gamma^* \to \tau\tau$ with hadronically decaying taus is a background as well, however the branching fraction for that process is much lower than $Z \to \nu\nu$.

$W^{\pm}$+jets

The main background contribution from $W^{\pm}$+ jets arise from decay into hadronic taus or leptons. The leptonic decay will only enter our selection if the lepton is mis-identified as a jet. A $W^{\pm}$-boson decaying into a tau that subsequently decays into hadrons will create a final state very similar to the signal selection.

Diboson

Diboson production (ZZ, WW, WZ, $W\gamma$, $Z\gamma$) can produce a final state similar to the one chosen for the analysis. If a Z decays into neutrinos and a $W^{\pm}$ or Z decays hadronically, the final state will contain both jets and true $E_{\mathrm{T}}^{\mathrm{miss}}$ from the neutrinos. Another way of producing a final state containing jets and $E_{\mathrm{T}}^{\mathrm{miss}}$ is when a $W^{\pm}$ decays leptonically, but the lepton is not identified.

5.2.3 Multijet Background

The multijet background accounts for jets produced through the strong interaction. This process has a high cross section, but does not contain any real $E_{\mathrm{T}}^{\mathrm{miss}}$. Multijet events can only have a sizeable missing transverse momentum if either a jet is lost in a crack region of the detector or

if the energy of a jet is not measured correctly. The main source of fake $E_{\mathrm{T}}^{\mathrm{miss}}$ arises from the second possibility, a mis-measurement of the energy of a jet.

b quarks produced in the proton-proton collision can decay semileptonically into final states containing a lepton and a neutrino which is a source of real $E_{\mathrm{T}}^{\mathrm{miss}}$. If the lepton is mis-identified as a jet or falls outside the acceptance of the detector, then the final state will be with jets, $E_{\mathrm{T}}^{\mathrm{miss}}$, and no leptons which is identical to the final state of the signal.

The multijet background is the only background process estimated solely from data-driven techniques as discussed in section 5.6.2.

5.3 Data set and Simulation Samples

A summary of the data set and the generators for the various simulation samples is given in this section.

5.3.1 Data set

The data sample consists of proton-proton collisions at an energy of $\sqrt{s} = 8$ TeV collected by the ATLAS experiment in 2012. The total integrated luminosity of the sample is 21.7 fb^{-1} reduced to 20.3 fb^{-1} after requiring that the entire dataset passed the data quality cuts posed by the Good Run List (GRL). The GRL is a collection of runs during which all the subdetectors of ATLAS have been working properly. This analysis relies on many different physics objects (electrons, muons, photons, jets, and $E_{\mathrm{T}}^{\mathrm{miss}}$) and all subsystems must therefore provide data of a good quality. The uncertainty of the total integrated luminosity has been estimated to $\pm 2.8\%$ following the prescription found in Ref. [219]. The average number of proton interactions per bunch crossing was 20.7.

5.3.2 Simulation Samples

Simulation samples are used to estimate the number of expected events of both Standard Model backgrounds and signal models. The samples are simulated productions and decays of certain particles in pp-collisions at $\sqrt{s} = 8$ TeV normalised to their production cross section.

Signal Samples

All the samples of simplified models described in Section 5.1.1 are generated with MADGRAPH-5.0 [139] matched to PYTHIA-6.426 [133] with a parton distribution set (PDF) set from CTEQ6L1 [37]. The detector simulation is done using the ATLAS fast simulation, ATLFASTII [149].

The MSUGRA/CMSSM samples of the model introduced in Section 5.1.2 are simulated using HERWIG++ [138] and CTEQ6L1 [37] as the PDF set. The response of the detector is simulated using a full simulation of the ATLAS detector described in GEANT4 [148].

The signal sample of the pMSSM model with $\tilde{q}_L$-pair production as described in Section 5.1.3 are generated with HERWIG++ [138], and a PDF set from CTEQ6L1 [37]. The detector response is simulated using ATLFASTII [149].

Background Samples

All the Standard Model background processes, except for the multijet background, are estimated either partly or completely from simulations. For the main Standard Model backgrounds, the effect of the choice of the baseline generator is studied by comparing the baseline sample to a sample simulated using an alternative generator. The comparison of the baseline and alternative sample is used as part of the estimate of the theoretical uncertainty of a background process. A summary of both baseline and alternative generators, their order of α_s and level of soft gluon resummation in cross section calculation, generator tune, and parton distribution function set used for background sample production is listed in Table 5.3. The background samples are all generated using GEANT4 for detector simulation.

$t\bar{t}$-pairs and single-t Samples

The $t\bar{t}$-sample is generated with a top mass of 172.5 GeV using POWHEG interfaced with PYTHIA6 for fragmentation and hadronisation using PERUGIA2011C tunes for the parameters and the NLO PDF set CT10. The $t\bar{t}$-sample is reweighted in bins of p_{T} due to differences between data and simulation of differential cross sections observed at $\sqrt{s} = 7$ TeV [235, 236].The alternative $t\bar{t}$-sample is generated with MC@NLO interfaced with HERWIG.

The samples of single-t production in s-channel and Wt are generated using MC@NLO interfaced with HERWIG with CT10 as the PDF set. Samples of single-t production in the t-channel are generated using ACERMC interfaced with PYTHIA6 and CTEQ6L1 as the PDF set. No alternative samples are used for these processes.

Samples of $t\bar{t}$-pair production in association with production of a Z or a W boson are generated with MADGRAPH interfaced with PYTHIA6 and using CTEQ6L1 as the PDF set.

Z/γ^*+jets, $W^{\pm}$+jets, and γ+jets

The Z+jets, $W^{\pm}$+jets, and γ^*+jets samples are simulated using SHERPA and CT10 as the PDF set. The alternative samples used to study the effect of the generator choice are generated with ALPGEN interfaced with HERWIG and using the CTEQ6L1 PDF set.

γ+jets is not a background. However, a control region containing γ+jets events is used to estimate the contribution from Z+jets in signal regions.

Diboson

The diboson samples are generated using SHERPA with CT10 as the PDF set. There are no alternative samples defined for these background processes.

Pile-up Reweighting

Several proton collisions happen simultaneously when two bunches of protons collide in the LHC. The multiple collisions per bunch crossing are known as pile-up. It is important to include pile-up in the simulation samples as it affects the reconstruction efficiencies.

Process	Generator + frag./had.	Cross section order in α_s	Tune	PDF set
W+jets	SHERPA-1.4.0 [135]	NNLO [220]	SHERPA default	CT10 [36]
W+jets($\star$)	ALPGEN-2.14 [140] + HERWIG-6.520 [136, 137]	NNLO [220]	AUET2B [221]	CTEQ6L1 [37]
Z/γ^*+jets	SHERPA-1.4.0 [135]	NNLO [220]	SHERPA default	CT10 [36]
Z/γ^*+jets($\star$)	ALPGEN-2.14 [140] + HERWIG-6.520 [136, 137]	NNLO [220]	AUET2B [221]	CTEQ6L1 [37]
γ+jets	SHERPA-1.4.0 [135]	LO	SHERPA default	CT10 [36]
γ+jets($\star$)	ALPGEN-2.14 [140] + HERWIG-6.520 [136, 137]	LO	AUET2B [221]	CTEQ6L1 [37]
$t\bar{t}$	POWHEG-BOX-1.0 [141–143]	NNLO+	PERUGIA2011C	CT10 [36]
	+ PYTHIA-6.426 [133]	NNLL [222, 223]	[224, 225]	
$t\bar{t}$($\star$)	MC@NLO-4.03 [144–147]	NNLO+	AUET2B [221]	CT10 [36]
	+ HERWIG-6.520 [136, 137]	NNLL [222, 223]		
Single top				
t-channel	ACERMC-38 [226]	NNLO+	AUET2B [221]	CTEQ6L1 [37]
	+ PYTHIA-6.426 [133]	NNLL [227]		
s-channel, Wt	MC@NLO-4.03 [144–147]	NNLO+	AUET2B [221]	CT10 [36]
	+ HERWIG-6.520 [136, 137]	NNLL [228, 229]		
$t\bar{t}$+EW boson	MADGRAPH-5.0 [139]	NLO [230–232]	AUET2B [221]	CTEQ6L1 [37]
	+ PYTHIA-6.426 [133]			
Dibosons				
WW, WZ, ZZ, $W\gamma$, and $Z\gamma$	SHERPA-1.4.0 [135]	NLO [233, 234]	SHERPA default	CT10 [36]

Table 5.3 · Simulation samples of the Standard Model background processes considered in the analysis. Generators, hard scattering cross section calculation order in α_s (Leading Order (LO), Next-to-Leading Order (NLO), Next-to-Next-to-Leading Order (NNLO)) and the level of soft gluon resummation (Next-to-Next-to-Leading Log (NNLL)), the tune used for the generation, and the parton distribution function (PDF) set are stated. Samples denoted with a **($\star$)** are used to estimate the uncertainties originating from the choice of generator. The LO cross section of the γ+jets sample is taken directly from the generator.

Events in the simulation samples are overlaid with minimum bias events to emulate multiple proton collisions per bunch crossing. The minimum bias events are generated with PYTHIA8 [134], the AM2 tune [237] and a leading order PDF set, MSTW2008LO [34]. The simulation samples are produced with a certain distribution of the average number of proton collisions per bunch crossing, $\langle\mu\rangle$, ranging from $\langle\mu\rangle = 0$ to $\langle\mu\rangle = 40$. However, the samples are produced prior to data taking when the exact distribution of $\langle\mu\rangle$ is not known precisely. The samples are therefore reweighted to emulate the exact pile-up conditions of the dataset.

The effect of the pile-up is expected to be small in the analysis. Only events with very highly energetic objects are selected and the effect of pile-up is thereby suppressed.

5.4 Object Definition

Before defining the cuts that will be used to define signal, control and validation regions, it is important to define the objects (jets, electrons, muons, etc.) that will be used when optimising the selection criteria. Objects are reconstructed using the methods described in Chapter 3. Two different selections of electrons and muons are defined, a signal object used in the event selection for control regions and a baseline object with looser cuts used for removal of overlapping objects and vetoed in the signal region selection. A summary of the cuts used in the object definition is given in Table 5.4.

Jets are reconstructed using the anti-k_t-algorithm [161] with a distance parameter $R = 0.4$. The jets used in the removal of overlapping objects are required to have $p_{\mathrm{T}} > 20$ GeV and to lie within $|\eta| < 4.5$. The jets entering in the signal region selection have higher cuts on p_{T}.

b-jets are identified using the MV1 b-tagging algorithm based on neural networks [172] at a 70% efficiency of finding b-quarks in a simulated $t\bar{t}$ sample and rejecting more than 99% jets originating from lighter quarks. The identified b-jets are required to have $p_{\mathrm{T}} > 40$ GeV and lie within $|\eta| < 2.5$.

Electrons are reconstructed using tracks and calorimeter clusters [174]. Two selection criteria are used for electrons, signal and baseline. Baseline electrons are required to have $p_{\mathrm{T}} > 10$ GeV, lie with $|\eta| < 2.47$, and fulfill the `Medium` electron identification criterion. The signal electrons have tighter cuts: $p_{\mathrm{T}} > 25$ GeV, fulfill `Tight` electron identification criterion, restrictions on the longitudinal and transverse impact parameters with respect to the primary vertex, and must be isolated, i. e. the transverse momentum arising from tracks around the electron in a cone of $\Delta R = \sqrt{(\Delta\eta)^2 + (\Delta\phi)^2} = 0.2$ must be less than 10% of the p_{T} of the electron.

Muons are reconstructed using combination of tracks in the inner detector systems and hits in the muon spectrometer [181]. The baseline muons must have $p_{\mathrm{T}} > 10$ GeV and be within $|\eta| < 2.4$. Signal muons have tighter requirements: $p_{\mathrm{T}} > 25$ GeV, cuts on the transverse and longitudinal impact parameters with respect to the primary vertex, and the transverse momentum of tracks in a cone of $\Delta R = 0.2$ around the muon must be less than 1.8 GeV.

Jets		Signal
Acceptance		$p_{\mathrm{T}} > 20$ GeV and $\lvert\eta\rvert < 4.5$
b-jets		Signal
Tagged		b-tagged
Acceptance		$p_{\mathrm{T}} > 40$ GeV and $\lvert\eta\rvert < 2.5$
Electrons	Baseline	Signal
Acceptance	$p_{\mathrm{T}} > 10$ GeV and $\lvert\eta\rvert < 2.47$	$p_{\mathrm{T}} > 25$ GeV and $\lvert\eta\rvert < 2.47$
Quality	`Medium`	`Tight`
Isolation	-	$p_{\mathrm{T}}^{\mathrm{cone},\Delta R=0.2} / p_{\mathrm{T}} < 0.10$
Primary vertex	-	$\lvert d_0^{\mathrm{PV}}\rvert < 1$ mm, $\lvert z_0^{\mathrm{PV}}\rvert < 2$ mm
Muons	Baseline	Signal
Acceptance	$p_{\mathrm{T}} > 10$ GeV and $\lvert\eta\rvert < 2.4$	$p_{\mathrm{T}} > 25$ GeV and $\lvert\eta\rvert < 2.4$
Isolation	-	$\sum p_{\mathrm{T}}^{\mathrm{cone},\Delta R=0.2} < 1.8$ GeV
Primary vertex	-	$\lvert d_0^{\mathrm{PV}}\rvert < 1$ mm, $\lvert z_0^{\mathrm{PV}}\rvert < 0.2$ mm
Taus		Signal
Acceptance		$p_{\mathrm{T}} > 20$ GeV and $\lvert\eta\rvert < 2.47$
Photons	Baseline	Signal
Acceptance	$p_{\mathrm{T}} > 130$ GeV, $\lvert\eta\rvert < 1.37$ and $1.52 < \lvert\eta\rvert < 2.47$	$p_{\mathrm{T}} > 130$ GeV, $\lvert\eta\rvert < 1.37$ and $1.52 < \lvert\eta\rvert < 2.47$
Quality	`Loose`	`Tight`
Isolation	-	$E_{\mathrm{T}}^{\mathrm{calo},\Delta R=0.4} < 4$ GeV

Table 5.4 · The cuts used to define jets, b-jets, electrons, muons, taus, and photons. The electrons, muons, and photons have two sets of cuts, a baseline and a signal cut. The jets, b-jets, and taus only have one set of cuts.

Taus are not directly used in the analysis as they do not appear in any signal or control region cuts. They are, however, used in creating validation regions cross-checking the W+jets and Top background estimates. Taus are identified using a p_{T}-correlated track counting algorithm described in Ref. [184]. Taus are required to have 1 or 3 tracks, and $p_{\mathrm{T}} > 20$ GeV. Tau candidates overlapping with electrons or b-jets within $\Delta R < 0.2$ are discarded. If there are more than one tau candidate, the one with the highest p_{T} is chosen.

Photons are used in control regions to estimate the Z+jets background. Photon candidates must pass the following cuts: `Tight` identification [179], $p_{\mathrm{T}} > 130$ GeV, $\lvert\eta\rvert < 1.37$ or $1.52 < \lvert\eta\rvert < 2.47$. They must be isolated such that the transverse energy in the calorimeter

corrected for noise and pile-up and not coming from the photon candidate is less than 4 GeV in a cone of $\Delta R = 0.4$ around the photon candidate.

5.4.1 Overlap Removal

The same signal in the detector can occasionally be reconstructed and identified as different objects such as electrons, muons, and jets. To resolve these conflicts overlapping objects within a cone are removed until only one remains.

The overlap removal is performed on baseline objects defined in Table 5.4 in the following order:

1. If a jet and an electron are found within a cone of $\Delta R < 0.2$, the object is taken as an electron and the jet is removed.
2. If a jet and a muon are found within $\Delta R < 0.4$, the object is assumed to be a jet and the muon is removed.
3. If a jet and an electron are found within $0.2 < \Delta R < 0.4$, the object is treated as a jet and the electron is removed.

In the control region containing photons used to estimate the Z+jets background, overlap removal between jets and photons is applied. If a jet and a photon are found within $\Delta R < 0.2$, the object is treated as a photon and the jet is discarded.

5.5 Signal Regions

Once the objects in the events are defined, the cuts defining the signal regions can be optimised. The signal regions are described by a set of cuts optimised for rejecting background and enhancing signal and thus optimised for discovering or excluding supersymmetry.

The cuts defining the signal regions are divided into two sets: Preselection cuts that are common for all signal regions, and the signal region selection describing the final optimisation based on three variables.

5.5.1 Event Preselection

The event preselection is a set of cuts common for all the signal regions. They include trigger, lepton veto, $E_{\mathrm{T}}^{\mathrm{miss}}$, jet p_{T}, and cuts used to reject the multijet background.

Trigger

The trigger used for the signal regions is `EF_j80_a4tchad_xe100_tclcw_veryloose` which is unprescaled while applying the lowest cuts on both $E_{\mathrm{T}}^{\mathrm{miss}}$ and the p_{T} of the leading jet. The event filter level trigger is seeded by the L2 chain `L2_j75_c4cchad_xe55` seeded in turn by `L1_J50_XE40`.

A combined $E_{\mathrm{T}}^{\mathrm{miss}}$ and leading jet-p_{T}trigger is chosen since a single trigger on either $E_{\mathrm{T}}^{\mathrm{miss}}$ or the p_{T} of the leading jet would lead to a much tighter cut on the triggered element.

`EF_j80_a4tchad_xe100_tclcw_veryloose` has an online cut on $E_{\mathrm{T}}^{\mathrm{miss}}$ of 100 GeV and on the p_{T} of the leading jet of 80 GeV. The online energies are not calibrated and the reconstructed $E_{\mathrm{T}}^{\mathrm{miss}}$

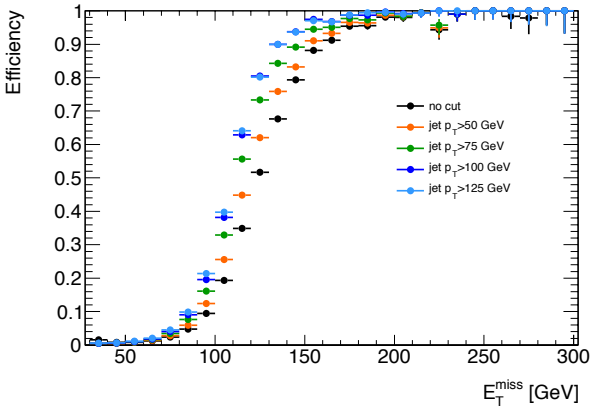

Fig. 5.6 · The efficiency of `EF_j80_a4tchad_xe100_tclcw_veryloose` as a function of offline $E_{\mathrm{T}}^{\mathrm{miss}}$ with five cuts on the p_{T} of the leading jet ($p_{\mathrm{T}}^{\mathrm{jet}} > 0$ GeV, 50 GeV, 75 GeV, 100 GeV, 125 GeV).

and p_{T} of the leading jet are higher. The trigger is therefore not fully efficient offline by simply applying the online cuts.

In Figure 5.6, the efficiency of `EF_j80_a4tchad_xe100_tclcw_veryloose` is shown as a function of $E_{\mathrm{T}}^{\mathrm{miss}}$ for five cuts on the p_{T} of the leading jet. The efficiency of the trigger depends on both $E_{\mathrm{T}}^{\mathrm{miss}}$ and the p_{T} of the leading jet since the trigger is a combined $E_{\mathrm{T}}^{\mathrm{miss}}$ and jet trigger. It is seen that the trigger is fully efficient ($> 95\%$) when the p_{T} of the leading jet is above 125 GeV and the $E_{\mathrm{T}}^{\mathrm{miss}}$ is larger than 160 GeV.

Event Cleaning

Fake missing transverse momentum not arising from proton-proton collisions can appear in the detector. There are three sources of such types of events: non-collision backgrounds such as cosmic rays or detector noise, problematic parts of the calorimeter where the energy is not measured properly, or fake muons. These events are rejected by a set of cuts.

Non-collision Background

Events contaminated by non-collision backgrounds arise either from noise in the calorimeter, a collision between a proton and a gas molecule in the beam pipe, or from highly energetic muons originating from cosmic rays or the beam halo.

A cut on the number of tracks associated to the primary vertex to be at least 4 is placed to reject events caused by cosmic rays.

To reject non-collision background events caused by noise in the calorimeter a requirement on the calorimeter performance must be satisfied or the event is rejected. This cut rejects data taken at a time around a noise-burst in the LAr or tile calorimeters causing detector activity similar to the events that would be included by the signal selection.

Data corruption in the tile calorimeter can lead to cells or clusters with large negative energy, eventually causing fake missing transverse momentum. Events with clusters or cells with large negative energy are vetoed.

Jets can be reconstructed from energy deposits in the calorimeter caused by non-collision background. Any event containing a jet with $p_{\mathrm{T}} > 20$ GeV and failing the "Looser" requirement described in Ref. [238] is vetoed in order to reject events with jets not originating from the proton collisions. To further reduce the number of such events, two sets of cuts on the fraction of the p_{T} of the associated tracks to the total energy of the jet, f_{ch}, and the fraction of the energy deposited in the electromagnetic calorimeter, f_{em}, are applied to the jet with the highest p_{T}: ($f_{\mathrm{ch}} < 0.02$ and $|\eta| < 2.0$) or ($f_{\mathrm{ch}} < 0.05$ and $f_{\mathrm{em}} > 0.9$ and $|\eta| < 2.0$). Events where the leading jet fulfills these requirements are vetoed. Events where a one of the two most energetic jet is reconstructed from an out-of-time energy deposit in the calorimeter are vetoed as well. This is done by placing a cut on the energy-weighted cell time, $|\langle t \rangle|$, which must be smaller than 4 ns.

Two cells in the tile calorimeter were found to be "hot", i. e. they were showing energy deposits even when there were no particles. Non-collision events caused by the first "hot" cell located at ($\eta = -0.15, \phi = 2.7$) were vetoed if a jet was pointing towards the region of the "hot" cell and had a big fraction of its energy deposit in the second layer of the tile calorimeter. To reject non-collision events caused by the second "hot" cell located at ($\eta = -0.1, \phi = 2.3$), events where one of the leading jets were in the region of the "hot" cell and satisfied requirements on their charged energy fraction and electromagnetic energy fraction, $f_{\mathrm{ch}} < 0.3$ and $f_{\mathrm{em}} < 0.25$, were vetoed.

The number of events originating from non-collision backgrounds after the cuts are applied, is estimated to be 0.4 in the signal regions with the loosest cuts, and negligible in signal regions with tighter cuts.

Dead Regions in the Calorimeter

A small fraction (2%) of the cells in the tile calorimeter was found to be dead by the end of Run-1 in December 2012. Dead cells can lead to a mis-measurement of the missing transverse momentum if a jet is pointing in the direction of the dead region. The energy of a jet pointing towards a dead region in the calorimeter can be estimated using shower shape information from simulations and the energy of the neighbouring cells. The fraction of the correction of the p_{T} of a jet obtained by this method is called $B_{\mathrm{jet}}^{\mathrm{corr}}$.

Events where a jet with $p_{\mathrm{T}} > 40$ GeV and $B_{\mathrm{jet}}^{\mathrm{corr}} > 5\%$ is pointing to a dead region in the tile calorimeter and the azimuthal angle between the jet and $E_{\mathrm{T}}^{\mathrm{miss}}$, $\Delta\phi(\mathrm{jet}, E_{\mathrm{T}}^{\mathrm{miss}})$, is smaller than 0.3 are vetoed. The effect of this cut on the efficiency of the SUSY signal is estimated from simulation to be $< 1\%$ and is taken into account in the final fit.

Fake Muons

Reconstructed muons not originating from the proton collisions, referred to as "fake muons", can cause large fake missing transverse momentum. To reject events with fake muons, two cuts are applied. Any event containing a baseline muon before overlap removal as described in Section 5.4 fulfilling $\sigma(q/p)/|q/p| > 0.2$ where q and p are the charge and momentum of the

muon, respectively, is rejected. If a fake muon is causing a mis-measurement of $E_{\mathrm{T}}^{\mathrm{miss}}$, then the $E_{\mathrm{T}}^{\mathrm{miss}}$ formed by the muon contribution alone, $(E_{\mathrm{T}}^{\mathrm{miss}})^{\mathrm{Muon}}$, will dominate the total $E_{\mathrm{T}}^{\mathrm{miss}}$. A cut is therefore posed on $(E_{\mathrm{T}}^{\mathrm{miss}})^{\mathrm{Muon}}/E_{\mathrm{T}}^{\mathrm{miss}} \times \cos\Delta\phi((E_{\mathrm{T}}^{\mathrm{miss}})^{\mathrm{Muon}}, E_{\mathrm{T}}^{\mathrm{miss}}) > 0.5$, and events fulfilling this requirement are rejected.

Lepton Veto

As this analysis targets SUSY models with jets and $E_{\mathrm{T}}^{\mathrm{miss}}$ in the final state, a veto on events containing electrons and muons is applied. Events where a baseline electron or muon as defined in Table 5.4 is present after overlap removal will be rejected.

$E_{\mathrm{T}}^{\mathrm{miss}}$ and p_{T} of the Jets

Requirements on $E_{\mathrm{T}}^{\mathrm{miss}}$ and the p_{T} of the leading jet are placed by the trigger. In order for the trigger to be fully efficient the $E_{\mathrm{T}}^{\mathrm{miss}}$ must be larger than 160 GeV, and the p_{T} of the leading jet larger than 130 GeV.

To avoid jets coming from other vertices, i. e. originating from simultaneous pile-up collisions, only jets with p_{T} greater than 40 GeV are considered in the construction of kinematical variables. In most signal regions a cut of $p_{\mathrm{T}}^{\mathrm{jet}} > 60$ GeV is used when counting the number of jets (one signal region uses jets with p_{T} greater than 40 GeV in calculating the jet multiplicity).

Multijet Background Rejection

Missing transverse momentum in multijet background events is mostly due to mis-measurement of the energy of a jet. The direction of the $E_{\mathrm{T}}^{\mathrm{miss}}$ is therefore expected to be close to the direction of the jet whose energy has not been measured correctly.

A cut on the minimal azimuthal angle between $E_{\mathrm{T}}^{\mathrm{miss}}$ and jets, $\Delta\phi(\mathrm{jet}, E_{\mathrm{T}}^{\mathrm{miss}})_{\mathrm{min}}$, is therefore applied. A tight cut is applied for signal regions selecting events with at least 2 or 3 jets of $\Delta\phi(\mathrm{jet}, E_{\mathrm{T}}^{\mathrm{miss}})_{\mathrm{min}} > 0.4$ for the 2 or 3 leading jets, respectively, such that if any of the selected jets are closer in $\Delta\phi$ than 0.4 to the direction of the $E_{\mathrm{T}}^{\mathrm{miss}}$, the event is rejected. Signal regions requiring a higher jet multiplicity have in addition a cut on $\Delta\phi(\mathrm{jet}, E_{\mathrm{T}}^{\mathrm{miss}})_{\mathrm{min}} > 0.2$ applied to any jet with $p_{\mathrm{T}} > 40$ GeV apart from the three leading jets.

5.5.2 Signal Region Selection

Signal regions are optimised for different SUSY scenarios described in Section 5.1. Since no excesses were seen in earlier analyses using the same dataset [239], the signal regions were optimised for exclusion as described in Section 4.2.2. The optimal signal regions are found by varying $E_{\mathrm{T}}^{\mathrm{miss}}/\sqrt{H_{\mathrm{T}}}$ or $E_{\mathrm{T}}^{\mathrm{miss}}/m_{\mathrm{eff}}(\mathrm{Nj})$, and $m_{\mathrm{eff}}(\mathrm{incl.})$, all introduced and described in Section 4.2.1. The inclusive effective mass, $m_{\mathrm{eff}}(\mathrm{incl.})$, is calculated from all jets with $p_{\mathrm{T}} > 40$ GeV. A full fit including all the systematic uncertainties is performed in the optimisation. The sets of cuts excluding the biggest part of phase space are chosen as the signal regions.

Based on the optimisation, 17 inclusive signal regions are defined. The cuts defining the signal regions and the SUSY model for which each signal region is optimised are given in Table 5.5. The regions are characterised by their minimal jet multiplicity ranging from 2 to 6. As there are more

signal regions than jet multiplicities, the signal regions are further characterised based on the cut on m_{eff}(incl.) ranging from "very loose" (labelled "l−") to "very tight" (labelled "t+").

As mentioned, different signal regions are optimised for different SUSY models and different compression factors between the mass of the squark or gluino and the LSP. Signal regions with low jet multiplicity are, in general, optimised for direct squark decays, $\tilde{q} \to q\tilde{\chi}_1^0$, whereas signal regions with higher jet multiplicity are optimised for SUSY models with direct gluino decays, $\tilde{g} \to q\bar{q}\tilde{\chi}_1^0$, or one-step decays of squarks and gluinos.

Two signal regions, 2jW and 4jW, are optimised specifically for simplified models with one-step decays of squarks and gluinos, where the mass of $\tilde{\chi}_1^\pm$ is almost identical to the mass of the squark or gluino. When the masses of $\tilde{\chi}_1^\pm$ and the squark or the gluino are almost degenerate, the W boson will receive a high boost resulting in a small opening angle between its decay products. Signal regions targeting these models have additional cuts requiring two W-candidates inside a mass-window close to the W mass, 60 GeV $< m(W_{\text{cand}}) <$ 100 GeV, in addition to the requirements on m_{eff}(incl.) and $E_{\text{T}}^{\text{miss}}/m_{\text{eff}}$(Nj). The W-candidates are either unresolved and reconstructed from a single jet with a high mass ($W \to j$ in Table 5.5) or resolved and reconstructed from two jets with a small spatial separation between them ($W \to jj$ in Table 5.5). The 2jW signal region requires two unresolved W candidates, while 4jW requires one resolved and one unresolved W-candidate.

The product of the signal acceptance and the reconstruction efficiency for each signal region in the model for which it was optimised is shown in Figure 5.7, 5.8, and 5.9. It is seen that the signal regions are designed to target specific parts of the parameter space of the SUYS models. Especially the selection efficiency of the 2jW and 4jW regions shown in Figure 5.7d and 5.8f, respectively, are designed to target models with onestep decays through $\tilde{\chi}_1^\pm$ where the mass difference between the squark or gluino and $\tilde{\chi}_1^\pm$ is small.

5.5.3 Optimising Signal Regions for Left-handed Squark Production

Two signal regions optimised specifically for the pMSSM model described in Section 5.1.3 were added to the analysis published in Ref. [1] and included in the analysis in Ref. [2]. The two new signal regions are 4jt+ and 5jt.

As the final state of left-handed squark-pair production in most cases ($\sim$ 99%) contains one quark, the decay product of an electroweak boson and a $\tilde{\chi}_1^0$ per produced squark, many jets are expected. It was found that the signal regions placing the strongest exclusion limits before the optimisation had tight cuts on m_{eff}(incl.) and a high jet multiplicity. The strongest signal regions before the optimisation for this SUSY model were 4jt, 5j, and 6jt+ given in Table 5.5.

The new signal regions were optimised for largest exclusion reach. Only the final cuts on $E_{\text{T}}^{\text{miss}}/m_{\text{eff}}$(Nj) and m_{eff}(incl.) were varied for three jet multiplicities, $N_j \geq 4$, 5, and 6. The cut on $E_{\text{T}}^{\text{miss}}/m_{\text{eff}}$(Nj) was varied in steps of 0.05 from 0.15 to 0.40, and the cut on m_{eff}(incl.) was varied in steps of 100 GeV with a range depending on the jet multiplicity to insure coverage of all possible cuts on m_{eff}(incl.). The specific scans of the variables are shown in Table 5.6.

Four sets of cuts on jet multiplicity, $E_{\text{T}}^{\text{miss}}/m_{\text{eff}}$(Nj), and m_{eff}(incl.) were found to improve the exclusion reach on the pMSSM model with left-handed squark-pair production, two with a

	2jl	2jm	2jt	2jW	3j	4jW	4jl-	4jl
$E_{\mathrm{T}}^{\mathrm{miss}}$[GeV] >	160	160	160	160	160	160	160	160
$p_{\mathrm{T}}(j_1)$[GeV] >	130	130	130	130	130	130	130	130
$p_{\mathrm{T}}(j_2)$[GeV] >	60	60	60	60	60	60	60	60
$p_{\mathrm{T}}(j_3)$[GeV] >	-	-	-	-	60	40	60	60
$p_{\mathrm{T}}(j_4)$[GeV] >	-	-	-	-	-	40	60	60
$\Delta\phi(j_{1,2,(3)}, E_{\mathrm{T}}^{\mathrm{miss}})_{\mathrm{min}}$ >	0.4	0.4	0.4	0.4	0.4	0.4	0.4	0.4
$\Delta\phi(j_{>3}, E_{\mathrm{T}}^{\mathrm{miss}})_{\mathrm{min}}$ >	-	-	-	-	-	0.2	0.2	0.2
W candidates	-	-	-	$2(W \to j)$	-	$(W \to j)+$ $(W \to jj)$	-	-
$E_{\mathrm{T}}^{\mathrm{miss}}/\sqrt{H_{\mathrm{T}}}$[GeV$^{1/2}$] >	8	15	15	-	-	-	10	10
$E_{\mathrm{T}}^{\mathrm{miss}}/m_{\mathrm{eff}}$(Nj) >	-	-	-	0.25	0.30	0.35	-	-
m_{eff}(incl.)[GeV] >	800	1200	1600	1800	2200	1100	700	1000
Optimised for	$\tilde{q}\tilde{q}$ direct	$\tilde{q}\tilde{q}$ direct	$\tilde{q}\tilde{q}$ direct	$\tilde{g}\tilde{g}$ one-step	$\tilde{q}\tilde{g}$ direct	$\tilde{q}\tilde{q}$ one-step	$\tilde{q}\tilde{q}$ direct	$\tilde{q}\tilde{q}$ direct

	4jm	4jt	4jt+	5j	5jt	6jl	6jm	6jt	6jt+
$E_{\mathrm{T}}^{\mathrm{miss}}$[GeV] >	160	160	160	160	160	160	160	160	160
$p_{\mathrm{T}}(j_1)$[GeV] >	130	130	130	130	130	130	130	130	130
$p_{\mathrm{T}}(j_2)$[GeV] >	60	60	60	60	60	60	60	60	60
$p_{\mathrm{T}}(j_3)$[GeV] >	60	60	60	60	60	60	60	60	60
$p_{\mathrm{T}}(j_4)$[GeV] >	60	60	60	60	60	60	60	60	60
$p_{\mathrm{T}}(j_5)$[GeV] >	-	-	-	60	60	60	60	60	60
$p_{\mathrm{T}}(j_6)$[GeV] >	-	-	-	-	-	60	60	60	60
$\Delta\phi(j_{1,2,(3)}, E_{\mathrm{T}}^{\mathrm{miss}})_{\mathrm{min}}$ >	0.4	0.4	0.4	0.4	0.4	0.4	0.4	0.4	0.4
$\Delta\phi(j_{>3}, E_{\mathrm{T}}^{\mathrm{miss}})_{\mathrm{min}}$ >	0.2	0.2	0.2	0.2	0.2	0.2	0.2	0.2	0.2
$E_{\mathrm{T}}^{\mathrm{miss}}/m_{\mathrm{eff}}$(Nj) >	0.40	0.25	0.30	0.20	0.15	0.20	0.20	0.25	0.15
m_{eff}(incl.)[GeV] >	1300	2200	2200	1200	1900	900	1200	1500	1700
Optimised for	$\tilde{q}\tilde{g}$,$\tilde{g}\tilde{g}$ direct	$\tilde{q}\tilde{g}$,$\tilde{g}\tilde{g}$ direct	$\tilde{q}_L\tilde{q}_L$ pMSSM	$\tilde{q}\tilde{q}$ one-step	$\tilde{q}_L\tilde{q}_L$ pMSSM	$\tilde{q}\tilde{q}$ one-step	$\tilde{g}\tilde{g}$ one-step	$\tilde{g}\tilde{g}$ one-step	$\tilde{g}\tilde{g}$ one-step

Table 5.5 · The cuts used to define signal regions and the models for which the signal regions were optimised. The signal regions are labelled by the minimum requirement on jet multiplicity and the tightness of the m_{eff}(incl.) cut: l− (very loose), l (loose), m(medium), t(tight) and t+ (very tight). Two signal regions optimised for events with boosted Ws, 2jW and 4jW, have additional requirements on the presence of W candidates, either unresolved ($W \to j$) or resolved ($W \to jj$).

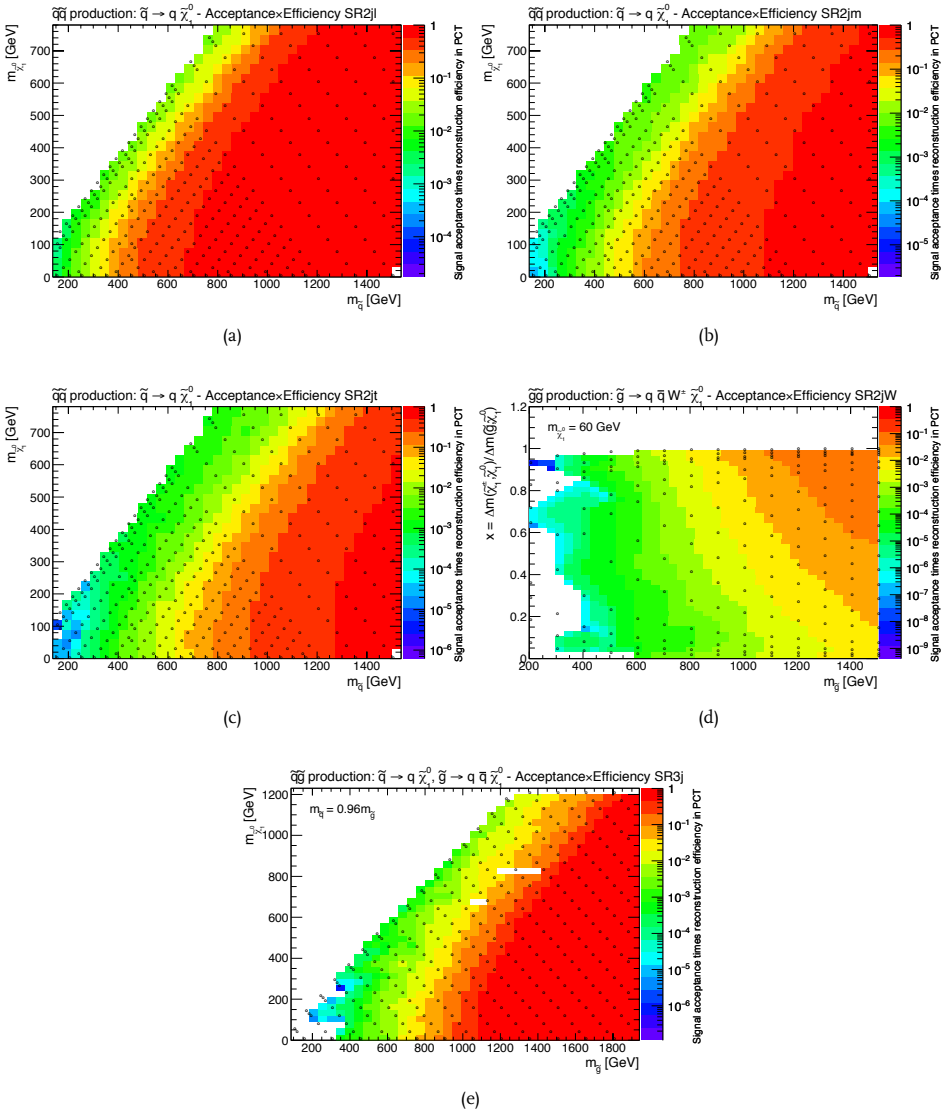

(a) (b) (c) (d) (e)

Fig. 5.7 · Product of signal acceptance and reconstruction efficiency at $\sqrt{s} = 8$ TeV for 2jl in $\tilde{q}\tilde{q}$-production with direct decay (a), 2jm in $\tilde{q}\tilde{q}$-production with direct decay (b), 2jt in $\tilde{q}\tilde{q}$-production with direct decay (c), 2jW in $\tilde{g}\,\tilde{g}$-production with onestep decay (d), and 3j in $\tilde{q}\,\tilde{g}$-production with direct decay (e). The 'o'-markers indicate the locations of the grid points used in the interpolation.

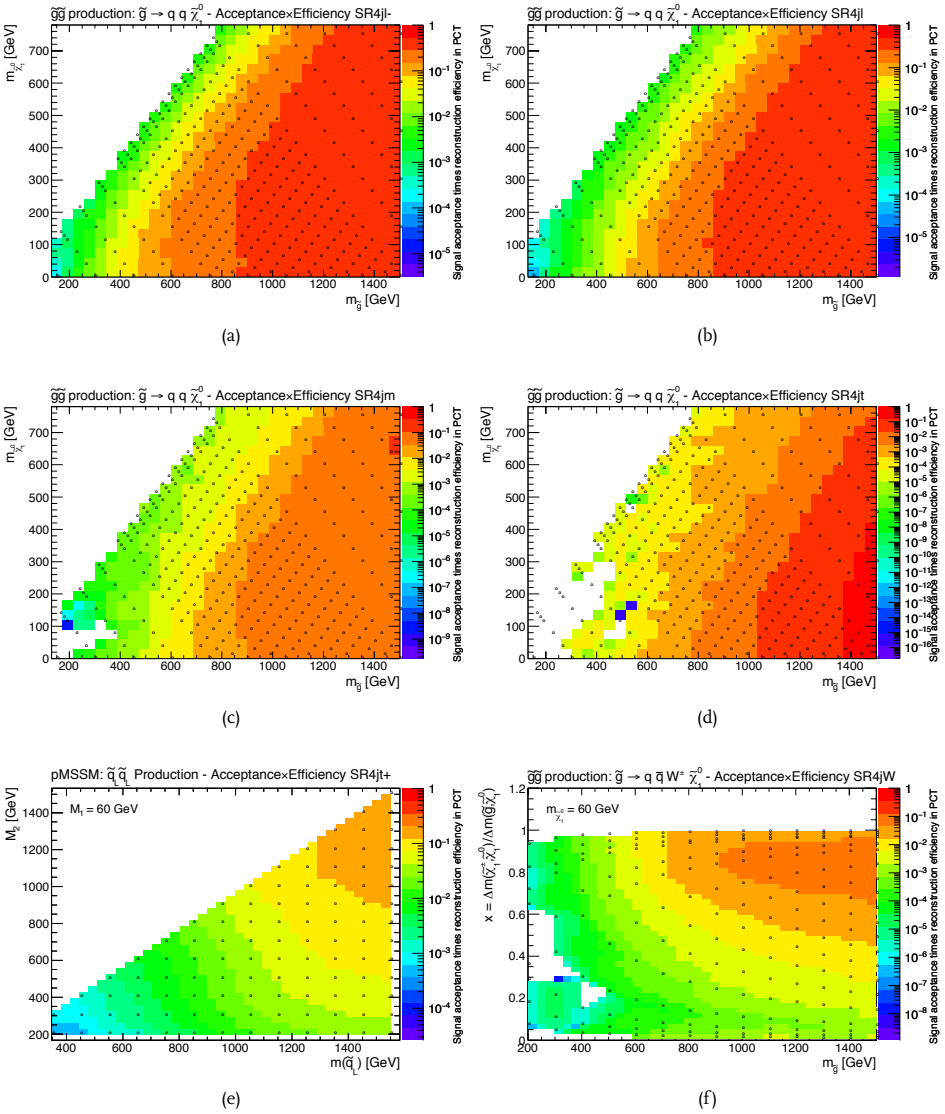

Fig. 5.8 · Product of signal acceptance and reconstruction efficiency at $\sqrt{s} = 8$ TeV for 4jl– in $\tilde{g}\tilde{g}$-production with direct decay (a), 4jl in $\tilde{g}\tilde{g}$-production with direct decay (b), 4jm in $\tilde{g}\tilde{g}$-production with direct decay (c), 4jt in $\tilde{g}\tilde{g}$-production with direct decay (d), 4jt+ in a pMSSM model with $\tilde{q}_L\tilde{q}_L$-production (e), and 4jW in $\tilde{g}\tilde{g}$-production with onestep decay (f). The 'o'-markers indicate the locations of the grid points used in the interpolation.

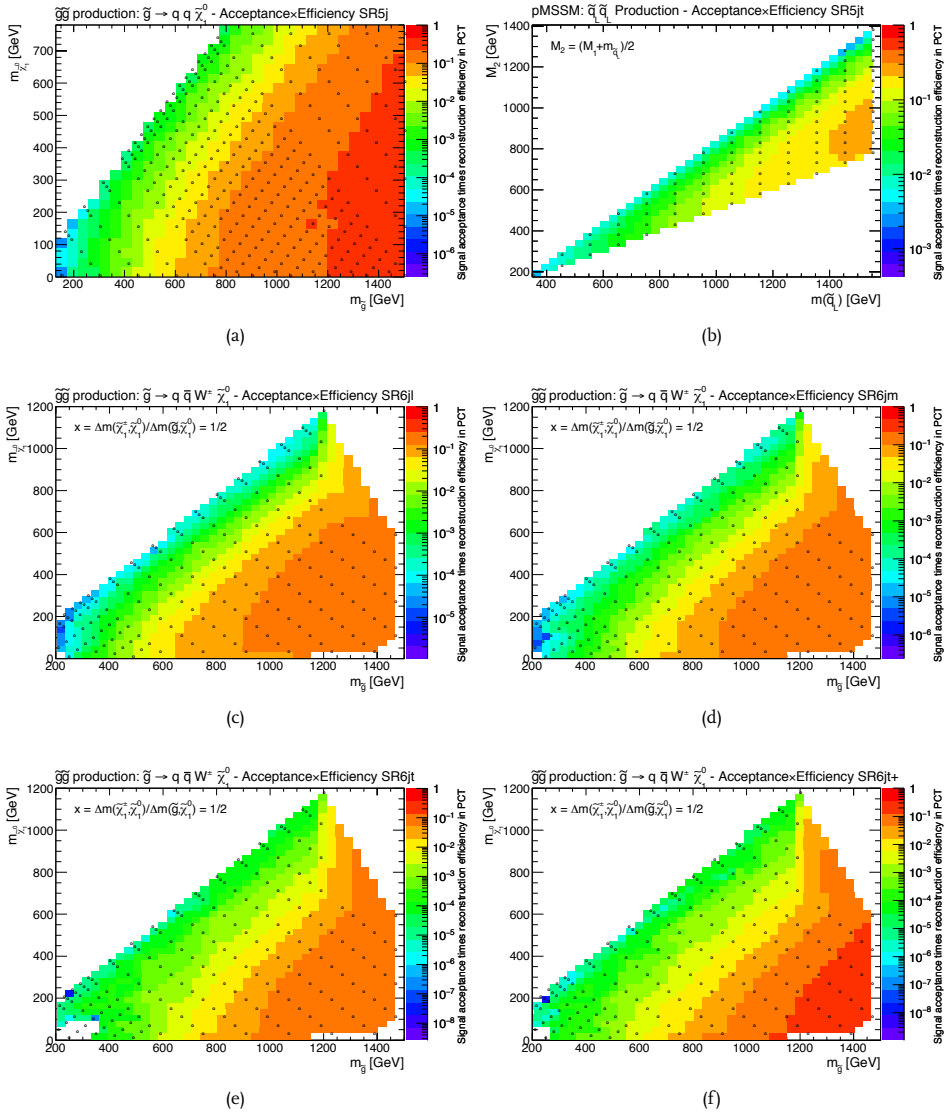

Fig. 5.9 · Product of signal acceptance and reconstruction efficiency at $\sqrt{s} = 8$ TeV for 5j in $\tilde{g}\tilde{g}$-production with direct decay (a), 5jt in a pMSSM model with $\tilde{q}_L\tilde{q}_L$-production (b), 6jl in $\tilde{g}\tilde{g}$-production with onestep decay (c), 6jm in $\tilde{g}\tilde{g}$-production with onestep decay (d), 6jt in $\tilde{g}\tilde{g}$-production with onestep decay (d), and 6jt+ in $\tilde{g}\tilde{g}$-production with onestep decay (f). The 'o'-markers indicate the locations of the grid points used in the interpolation.

Jet multiplicity	≥4 jets	≥5 jets	≥6 jets
$E_{\mathrm{T}}^{\mathrm{miss}}/m_{\mathrm{eff}}(\mathrm{Nj}) >$	[0.15 - 0.40]	[0.15 - 0.40]	[0.15 - 0.40]
$m_{\mathrm{eff}}(\mathrm{incl.}) >$	[1500 GeV- 2500 GeV]	[1200 GeV- 2300 GeV]	[1500 GeV- 2200 GeV]

Table 5.6 · Variables used in the optimisation of signal regions targeting the pMSSM model and their ranges. Three jet multiplicities (≥ 4 jets, ≥ 5 jets, and ≥ 6 jets) were studied. The cut on $E_{\mathrm{T}}^{\mathrm{miss}}/m_{\mathrm{eff}}(\mathrm{Nj})$ was varied in steps of 0.05, while the cut on $m_{\mathrm{eff}}(\mathrm{incl.})$ was varied in steps of 100 GeV.

	4jt-	4jt+	5jt	5jt+
$N_{\mathrm{jets}} \geq$	4	4	5	5
$E_{\mathrm{T}}^{\mathrm{miss}}/m_{\mathrm{eff}}(\mathrm{Nj}) >$	0.20	0.30	0.15	0.15
$m_{\mathrm{eff}}(\mathrm{incl.})[\mathrm{GeV}] >$	2200	2200	1900	2000

Table 5.7 · The four sets of cuts on the variables used in the optimisation showing the greatest improvement on the expected exclusion of production of left-handed squarks in a pMSSM model.

minimum requirement on the jet multiplicity of four and two with at least five jets. The four new signal regions were labeled 4jt−, 4jt+, 5jt, and 5jt+. Their cuts on the optimised variables can be found in Table 5.7. The two new 4-jet regions have the same $m_{\mathrm{eff}}(\mathrm{incl.})$ cuts as the already existing 4jt-region, but the cut on $E_{\mathrm{T}}^{\mathrm{miss}}/m_{\mathrm{eff}}(\mathrm{Nj})$ is decreased or increased by 0.05 for the 4jt− and 4jt+-regions, respectively. The two 5-jet regions have a lower cut on $E_{\mathrm{T}}^{\mathrm{miss}}/m_{\mathrm{eff}}(\mathrm{Nj})$ compared to the already existing 5j region, the cut on $m_{\mathrm{eff}}(\mathrm{incl.})$ is however increased to 1900 GeV and 2000 GeV for 5jt and 5jt+, respectively.

The improvement in expected sensitivity by including the new signal regions is shown in Figure 5.10. The four new signal regions are shown with dotted lines, the ones already existing in the analysis are shown with solid lines and the regions inside the contours are expected to be excluded. The expected sensitivity is shown for three gluino masses ($m_{\tilde{g}} = 1600$ GeV, 2200 GeV, and 3000 GeV) and for the two scans of M_1, M_2, and $m_{\tilde{q}_L}$ described in Section 5.1.3. Due to the lower cross section caused by a higher mass of the gluino, the expected exclusion of the SUSY phase space of the models with high gluino masses is much smaller than for models with lighter gluinos. The 4jt+-region improves the expected limit in models where $M_1 = 60$ GeV and the squark mass and M_2 are close, especially when the gluino mass is 2200 GeV. The 5jt and 5jt+-regions covers similar parts of the SUSY parameter space, except when the gluino mass is high where the 5jt outperforms 5jt+.

In order not to expand the number of signal regions too much and since there was an overlap in the expected exclusion limits between the regions, it was decided just to include the 4jt+ and 5jt-regions into the analysis as they were showing the best expected exclusion power.

The signal acceptance times the reconstruction efficiency of the 4jt+ and 5jt-regions in the pMSSM model with $\tilde{q}_L\tilde{q}_L$-production are shown in Figure 5.8e and 5.9b, respectively. As the change of gluino mass results in a change in the overall production cross section and not in

kinematics, the product of the signal acceptance and the reconstruction efficiency will be the same regardless of the gluino mass.

5.6 Background Estimation

An important task when searching for physics beyond the Standard Model is a solid estimate of the Standard Model backgrounds.

As discussed in Section 5.2, five sources of Standard Model backgrounds are considered in this analysis: W boson production in association with jets, Z boson production in association with jets, $t\bar{t}$ and single-top production, multijet events originating from strong interactions, and diboson production. The diboson production is a small background and is therefore estimated from simulation only. The remaining four sources of backgrounds are estimated using semi data-driven or fully data-driven techniques.

5.6.1 Control Regions

Control regions are used in semi data-driven and fully data-driven background estimation techniques. The background contribution in the signal regions is estimated from transfer functions as described in Section 4.3.1.

Four types of control regions are defined for each signal region designed to enhance the contribution of a single background while being as kinematically close to the signal region as possible. The four signal regions are designed to estimate the W (CRW), top (CRT), Z (CRγ), and multijet backgrounds (CRQ). They all have a cut on m_{eff}(incl.) identical to the corresponding signal region in order not to introduce extrapolation uncertainties on the shape of m_{eff}(incl.). Other cuts will differ to enhance the background process in question. The cuts defining the four control regions are given in Table 5.8.

Control Regions for W and Top Background Estimation

Events from W+jets, $t\bar{t}$-production, and single-top production are expected to enter into the signal regions mainly due to a non-reconstructed lepton (electron or muon), mis-identification of a lepton (electron or muon) as a jet or through the presence of hadronically decaying taus.

The two control regions used to estimate the W and top contribution in the signal regions, CRW and CRT, are defined by identical cuts except for requirements on the presence of or veto on b-tagged jets resulting in orthogonal control regions. The specific cuts that differ from the signal region are summarised in Table 5.8. Both sets of control regions use an inversion of the lepton-veto present in the signal region selection, i. e. the event must contain exactly one lepton.

Different triggers, compared to the one used in the signal region selection, are used for these control regions which is more efficient at filtering out the wanted events. As the events are required to contain one electron or muon, single lepton triggers are used: `EF_e24vhi_medium1` or `EF_e60_medium1` for events with and electron, and `EF_mu24i_tight` for events with a muon. The single lepton triggers reach full efficiency fast, and the offline p_{T} threshold of the electron or the muon is placed at 25 GeV.

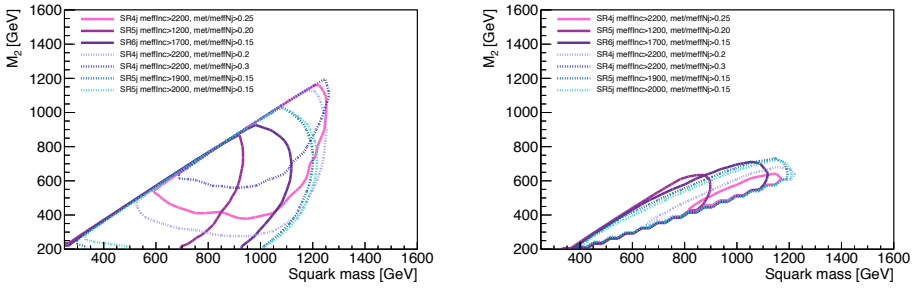

(a) $M_1 = 60$ GeV, $m_{\tilde{g}} = 1600$ GeV

(b) $M_2 = (M_1 + m_{\tilde{q}_L})/2$, $m_{\tilde{g}} = 1600$ GeV

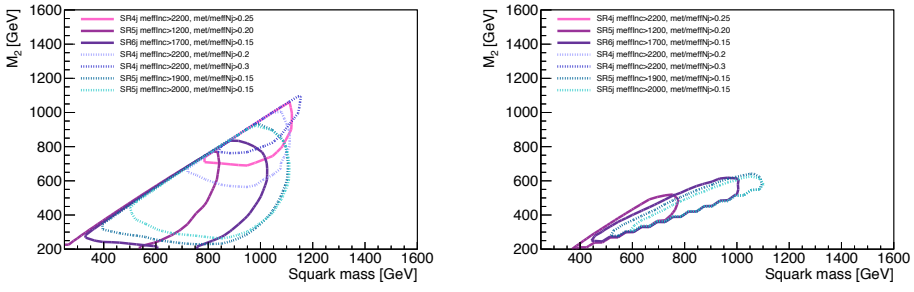

(c) $M_1 = 60$ GeV, $m_{\tilde{g}} = 2200$ GeV

(d) $M_2 = (M_1 + m_{\tilde{q}_L})/2$, $m_{\tilde{g}} = 2200$ GeV

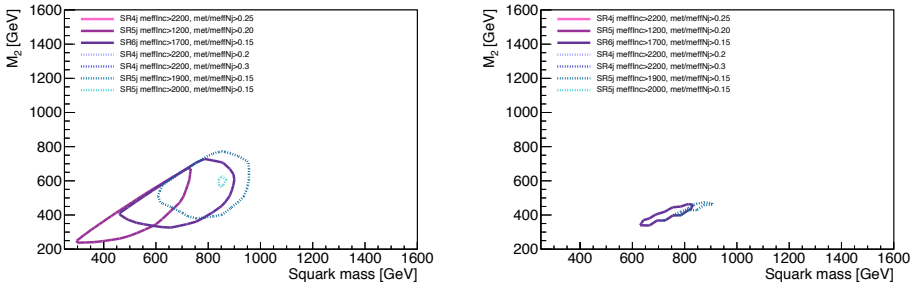

(e) $M_1 = 60$ GeV, $m_{\tilde{g}} = 3000$ GeV

(f) $M_2 = (M_1 + m_{\tilde{q}_L})/2$, $m_{\tilde{g}} = 3000$ GeV

Fig. 5.10 · Expected exclusion reach in the $m_{\tilde{q}_L}$-M_2 plane of left-handed squark-pair production using of the three strongest signal regions from Ref [1] (solid lines) and the four strongest regions found in the optimisation (dotted lines). The regions inside the contours are expected to be excluded. The exclusion is studied for three gluino masses: $m_{\tilde{g}} = 1600$ GeV (Figures (a) and (b)), $m_{\tilde{g}} = 2200$ GeV (Figures (c) and (d)), and $m_{\tilde{g}} = 3000$ GeV (Figures (e) and (f)). Two different scans of the M_1, M_2, and $m_{\tilde{q}_L}$ pMSSM parameters are used: $M_1 = 60$ GeV (Figures (a), (c), and (e)), and $M_2 = (M_1 + m_{\tilde{q}_L})/2$ (Figures (b), (d), and (f)).

	CRW	CRT	CRγ	CRQ	VRZ
Trigger	EF_e24vhi_medium1 or EF_e60_medium1/ EF_mu24i_tight	EF_e24vhi_medium1 or EF_e60_medium1/ EF_mu24i_tight	EF_g120_loose	same as SR	EF_e24vhi_medium1 or EF_e60_medium1/ EF_mu24i_tight
Extra objects	1 signal lepton (e or μ)	1 signal lepton (e or μ)	≥ 1 signal photon, no leptons	No leptons (e or μ)	Exactly 2 OS signal leptons (e or μ)
Treatment of objects	Treat lepton as jet	Treat lepton as jet	Treat photon as source of $E_{\mathrm{T}}^{\mathrm{miss}}$	No special treatment	Treat leptons as sources of $E_{\mathrm{T}}^{\mathrm{miss}}$
b-tagging	No b-tagged jets	≥ 1 b-tagged jet	No requirement	No requirement	No requirement
Transverse Mass	30 GeV $< m_{\mathrm{T}}(\ell, E_{\mathrm{T}}^{\mathrm{miss}}) <$ 100 GeV	30 GeV $< m_{\mathrm{T}}(\ell, E_{\mathrm{T}}^{\mathrm{miss}}) <$ 100 GeV	No requirement	No requirement	No requirement
Invariant Mass	No requirement	No requirement	No requirement	No requirement	66 GeV $< m(\ell\ell) <$ 116 GeV
W Candidates	Same as SR (2jW relaxed to 1 $W \to j$)	Same as SR (2jW relaxed to 1 $W \to j$)	Same as SR (2jW relaxed to 1 $W \to j$)	Same as SR (2jW relaxed to 1 $W \to j$)	Same as SR (2jW relaxed to 1 $W \to j$)
$\Delta\phi(j, E_{\mathrm{T}}^{\mathrm{miss}})_{\mathrm{min}}$	No requirement (except in 2jl)	No requirement (except in 2jl)	Same as SR	$\Delta\phi(j_{1,2,(3)}, E_{\mathrm{T}}^{\mathrm{miss}})_{\mathrm{min}} < 0.2$ and $\Delta\phi(j_{>3}, E_{\mathrm{T}}^{\mathrm{miss}})_{\mathrm{min}} < 0.1$	No requirement
$E_{\mathrm{T}}^{\mathrm{miss}}/m_{\mathrm{eff}}(\mathrm{Nj})$ or $E_{\mathrm{T}}^{\mathrm{miss}}/\sqrt{H_{\mathrm{T}}}$	No requirement (except in 2jl)	No requirement (except in 2jl)	Same as SR	$X - \Delta < E_{\mathrm{T}}^{\mathrm{miss}}/m_{\mathrm{eff}}(\mathrm{Nj}) < X$ if $E_{\mathrm{T}}^{\mathrm{miss}}/m_{\mathrm{eff}}(\mathrm{Nj}) > X$ in SR or $X - \Delta < E_{\mathrm{T}}^{\mathrm{miss}}/\sqrt{H_{\mathrm{T}}} < X$ if $E_{\mathrm{T}}^{\mathrm{miss}}/\sqrt{H_{\mathrm{T}}} > X$ in SR	No requirement
m_{eff}(incl.)[GeV]	Same as SR	Same as SR	Same as SR	Same as SR	Same as SR

Table 5.8 · Selection criteria used to define the four types of control regions and one validation region at $\sqrt{s} = 8$ TeV: CRW for estimating the W+jets background, CRT for estimating the top background, CRγ for estimating the $Z(\to \nu\nu)$+jets background, CRQ for estimating the multijet background, and VRZ for validating the estimate of the Z+jets background. Δ gives the interval of the cut on $E_{\mathrm{T}}^{\mathrm{miss}}/m_{\mathrm{eff}}(\mathrm{Nj})$ or $E_{\mathrm{T}}^{\mathrm{miss}}/\sqrt{H_{\mathrm{T}}}$ in CRQ depending on the specific signal region cut, X.

The transverse mass, m_{T}, can be used to distinguish between events containing a lepton and $E_{\mathrm{T}}^{\mathrm{miss}}$ coming from a W decay and events from another origin. The transverse mass of a lepton and $E_{\mathrm{T}}^{\mathrm{miss}}$ is given by:

$$m_T(\ell, E_{\mathrm{T}}^{\mathrm{miss}}) = \sqrt{2p_{\mathrm{T}}^{\ell} E_{\mathrm{T}}^{\mathrm{miss}} \cdot \left(1 - \cos\Delta\phi\left(\ell, E_{\mathrm{T}}^{\mathrm{miss}}\right)\right)}. \tag{5.1}$$

Since the leptons come from decays of $W^{\pm}$-bosons both in case of W background and top-background, a cut is placed on the transverse mass of the lepton and the $E_{\mathrm{T}}^{\mathrm{miss}}$ in a window around the W mass, 30 GeV $< m_{\mathrm{T}}(\ell, E_{\mathrm{T}}^{\mathrm{miss}}) <$ 100 GeV.

As the W and top backgrounds enter into the signal regions by lepton mis-identification as a jet, the signal lepton in the control region is therefore treated as jet when computing m_{eff}(incl.) and other variables.

Unlike in the signal regions, in the CRW and CRT regions no cuts on $\Delta\phi_{\mathrm{min}}$, $E_{\mathrm{T}}^{\mathrm{miss}}/m_{\mathrm{eff}}$(Nj) nor on $E_{\mathrm{T}}^{\mathrm{miss}}/\sqrt{H_{\mathrm{T}}}$ are placed. Those three cuts are mainly placed in the signal regions to reject multijet background events.

The difference between CRW and CRT lies in the requirement on b-tagged jets. As top quarks almost solely decay to a b-quark and a W boson, a requirement on an event to contain at least one b-tagged jet with $p_{\mathrm{T}} > 40$ GeV is placed in CRT. In order for the two sets of control regions to be orthogonal, i. e. no event will show up in both CRW and CRT for the same signal region, an event containing any b-tagged jets is vetoed in the CRW selection.

The observed distributions of m_{eff}(incl.) at four jet multiplicities compared to the ones expected from Standard Model processes in CRW and CRT are shown in Figures 5.11 and 5.12, respectively. The expected Standard Model background using the baseline generators given in Table 5.3 is shown as solid histograms, while the total Standard Model expectation using the alternative samples, a W+jets sample generated with ALPGEN for CRW and a Top sample generated with MC@NLO for CRT, are shown with a black, dashed line.

In CRW, it is seen especially in the high jet multiplicity regions that the expected number of W+jets from the baseline SHERPA sample is too high compared to the observed distribution, while the alternative ALPGEN sample agrees better with observation. This justifies the choice to use an alternative sample as a generator uncertainty. The SHERPA sample is generated with more events and is therefore chosen as the baseline sample. In the background-fit, the backgrounds will be normalised to the data in the control regions and an overall difference in the normalisation is therefore not a problem. The baseline POWHEG-BOX sample and the alternative MC@NLO sample used to estimate the generator uncertainty for $t\bar{t}$-production show a better agreement in CRT.

The expected purity of the control region, i. e. the fraction of the expected number of events coming from the targeted Standard Model process compared to the total number of expected events, depends on the signal region to which the control corresponds. In CRW, the purity ranges from 86% in the di-jet regions to 65% in the 6-jet regions. In CRT, the expected purity ranges from 48% in the 3-jet region to 88% in the 6-jet regions. The reason why the expected purity is lower in CRT with low jet multiplicity is that since the only difference between CRT and CRW is whether there is a b-tagged jet or not, the low jet multiplicity CRT regions are contaminated

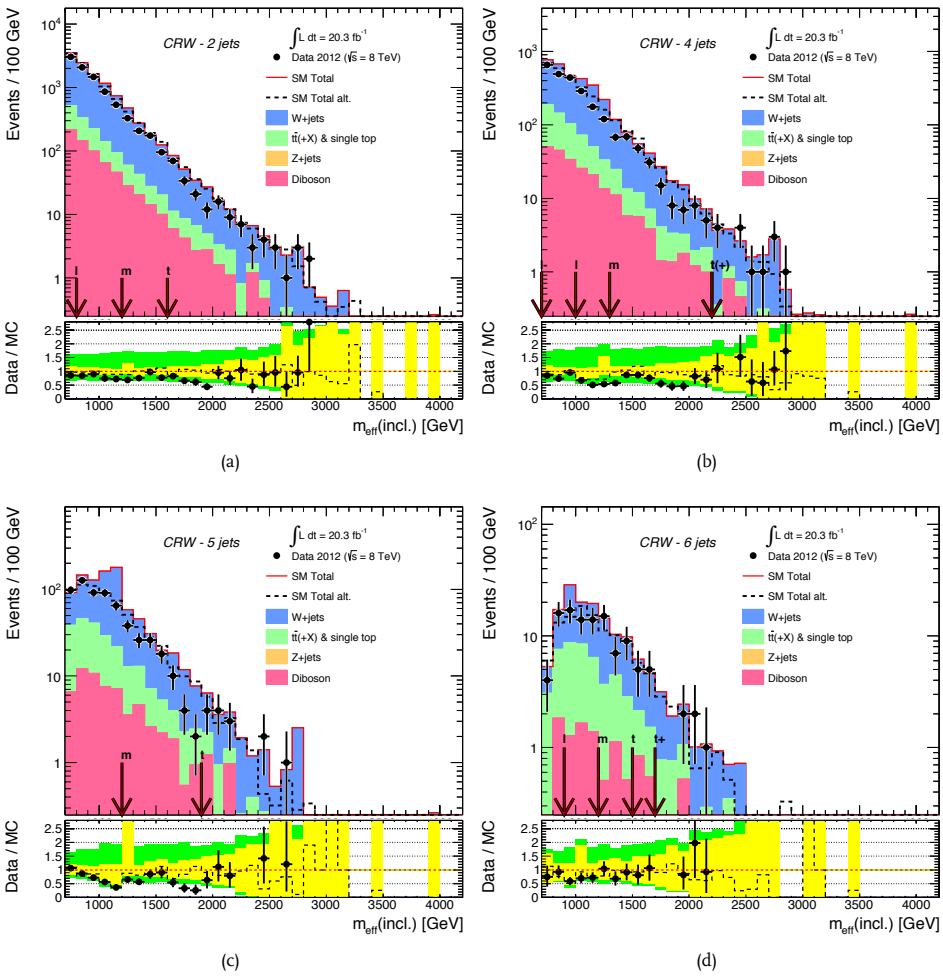

Fig. 5.11 · Observed and expected m_{eff}(incl.) distributions in 2-jet (a), 4-jet (b), 5-jet (c), and 6-jet (d) control regions of CRW at $\sqrt{s} = 8$ TeV before the final cut on m_{eff}(incl.). The histograms show the expected background from simulation normalised to the luminosity. The black dashed line in the upper panel is the expected background using an ALPGEN W+jets sample instead of the baseline W+jets sample generated with SHERPA. The red arrows indicate the specific cuts on m_{eff}(incl.) for the different jet multiplicities. The yellow error band includes the experimental uncertainties as well as the statistical uncertainties on the Monte Carlo samples. The green error band shows the total uncertainty including theory. The dashed line in the lower panel shows a comparison of the expected number of events using the baseline sample and the alternative sample.

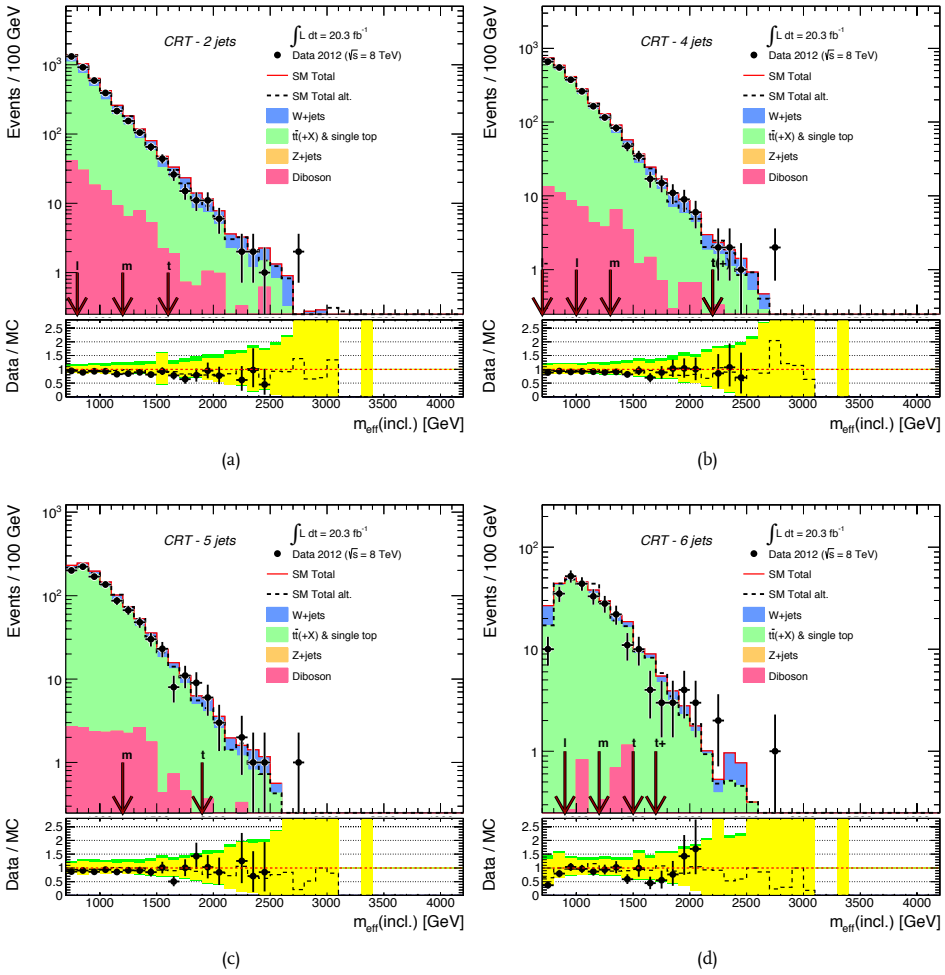

Fig. 5.12 · Observed and expected m_{eff}(incl.) distributions in 2-jet (a), 4-jet (b), 5-jet (c), and 6-jet (d) control regions of CRT at $\sqrt{s} = 8$ TeV before the final cut on m_{eff}(incl.). The histograms show the expected background from simulation normalised to the luminosity. The black dashed line in the upper panel is the expected background using an MC@NLO Top sample instead of the baseline $t\bar{t}$-sample generated with POWHEG-BOX. The red arrows indicate the specific cuts on m_{eff}(incl.) for the different jet multiplicities. The yellow error band includes the experimental uncertainties as well as the statistical uncertainties on the Monte Carlo samples. The green error band shows the total uncertainty including theory. The dashed line in the lower panel shows a comparison of the expected number of events using the baseline sample and the alternative sample.

by W+jets events. This is taken care of in the fit as all the background are fitted simultaneously over all control regions.

Control Regions for Z Background Estimation

A natural choice of control region to estimate events coming from $Z(\to \nu\nu)$+jets seems to be events containing two leptons of same flavour with opposite charge in a mass-window around the mass of the Z boson targeting the $Z(\to \ell\ell)$+jets process. These are the cuts used to define VRZ given in Table 5.8. However, a requirement of a good control region is that it is well-populated by events so the background estimate is not influenced too much by fluctuations in the data compared to expectation. Unfortunately, the statistics is too poor when requiring events with two leptons of same flavour and opposite charge along with all the additional cuts and VRZ is therefore used as a validation region instead. Instead a control region containing a high-energetic photon (CRγ) is used as it is expected to show a kinematical behavior similar to $Z(\to \nu\nu)$+jets.

Events in CRγ are triggered by a single-photon trigger, `EF_g120_loose`. The trigger reaches full efficiency within 10 GeV of the threshold, thus requiring a photon with $p_{\mathrm{T}} > 130$ GeV ensures that the trigger efficiency is $\sim 100\%$. A veto is placed on any baseline leptons just as in the signal region selection.

The photon takes the place of $Z \to \nu\nu$ which leaves the detector without a trace and is only measurable through missing transverse momentum. The photon is therefore treated as a contributor in the $E_{\mathrm{T}}^{\mathrm{miss}}$-calculation. The missing transverse momentum is thus recalculated including the p_{T} of the photon

$$\vec{E}_{\mathrm{T}}^{\mathrm{miss}}(\star) = \vec{p}_{\mathrm{T}}(\gamma) + \vec{E}_{\mathrm{T}}^{\mathrm{miss}}. \tag{5.2}$$

The $E_{\mathrm{T}}^{\mathrm{miss}}$ including the p_{T} of the photon is used to calculate m_{eff}(incl.), $E_{\mathrm{T}}^{\mathrm{miss}}(\star)/m_{\mathrm{eff}}$(Nj), $E_{\mathrm{T}}^{\mathrm{miss}}(\star)/\sqrt{H_{\mathrm{T}}}$, and $\Delta\phi(j, E_{\mathrm{T}}^{\mathrm{miss}}(\star))_{\mathrm{min}}$. The cuts on these variables calculated using $E_{\mathrm{T}}^{\mathrm{miss}}(\star)$ is identical to the cuts used in the signal regions.

The observed distributions of m_{eff}(incl.) along with the expected distribution from Standard model in CRγ before cuts on m_{eff}(incl.) and $E_{\mathrm{T}}^{\mathrm{miss}}/m_{\mathrm{eff}}$(Nj) or $E_{\mathrm{T}}^{\mathrm{miss}}/\sqrt{H_{\mathrm{T}}}$ in four jet multiplicities, di-jet, 4-jet, 5-jet, and 6-jet, are shown in Figure 5.13. The expected Standard Model distribution is shown using both the baseline SHERPA γ+jets sample (solid) and the alternative ALPGEN sample (black, dotted line). Both the SHERPA and the ALPGEN sample are scaled using the κ-factors obtained from Equation 5.4. It is seen especially in the distribution of m_{eff}(incl.) in the higher jet multiplicities, that the observed distribution is described better by the ALPGEN sample than the SHERPA sample estimating too many events. This is why a second sample is used to estimate the uncertainty coming from the choice of generator.

The purity of the CRγ depends very little on the cuts on jet multiplicity, m_{eff}(incl.) and $E_{\mathrm{T}}^{\mathrm{miss}}/m_{\mathrm{eff}}$(Nj) or $E_{\mathrm{T}}^{\mathrm{miss}}/\sqrt{H_{\mathrm{T}}}$. The CR$\gamma$ regions have in general a high purity ($\geq$ 95%) with the lowest one being 89% and the highest 97%.

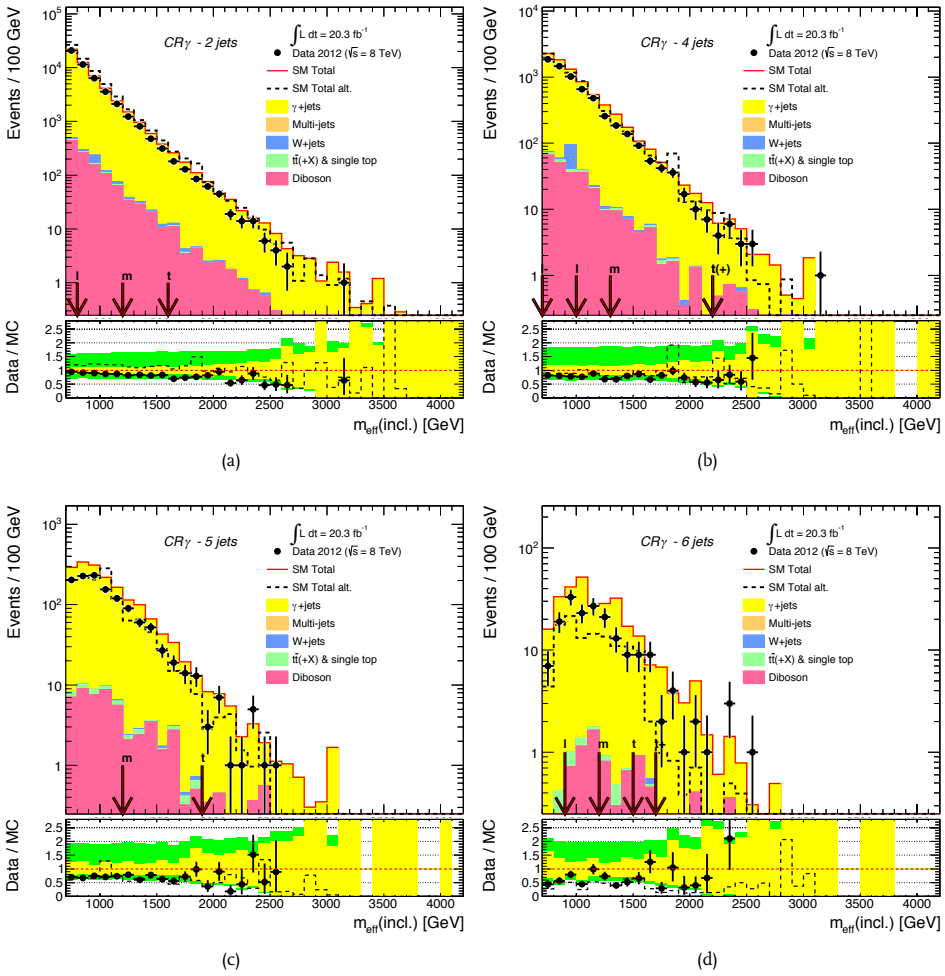

Fig. 5.13 · Observed and expected m_{eff}(incl.) distributions in 2-jet (a), 4-jet (b), 5-jet (c), and 6-jet (d) control regions of CRγ at $\sqrt{s} = 8$ TeV before the final cut on m_{eff}(incl.) and $E_{\text{T}}^{\text{miss}}/m_{\text{eff}}$(Nj) or $E_{\text{T}}^{\text{miss}}/\sqrt{H_{\text{T}}}$. The histograms show the expected background from simulation normalised to the luminosity. The black dashed line in the upper panel is the expected background using an ALPGEN γ+jets sample instead of the baseline γ+jets sample generated with SHERPA. The red arrows indicate the specific cuts on m_{eff}(incl.) for the different jet multiplicities. he yellow error band includes the experimental uncertainties as well as the statistical uncertainties on the Monte Carlo samples. The green error band shows the total uncertainty including theory. The dashed line in the lower panel shows a comparison of the expected number of events using the baseline sample and the alternative sample.

Cross Section Normalisation

The number of $Z(\to \nu\nu)$+jets events in a signal region is estimated from the normalisation of the γ+jets Monte Carlo sample to data in CRγ:

$$N_{\mathrm{SR}}^{Z\nu\nu,\mathrm{pred}} = N_{\mathrm{SR}}^{Z\nu\nu,\mathrm{MC}} \cdot \frac{N_{\mathrm{CR}\gamma}^{\gamma+\mathrm{jets,data}}}{N_{\mathrm{CR}\gamma}^{\gamma+\mathrm{jets,MC}}}. \tag{5.3}$$

However, a problem of this estimate arises by the fact that the γ+jets sample is normalised to its LO cross section, while the $Z(\to \nu\nu)$+jets sample is normalised to its NNLO cross section. The normalisation factor, $N_{\mathrm{CR}\gamma}^{\gamma+\mathrm{jets,data}}/N_{\mathrm{CR}\gamma}^{\gamma+\mathrm{jets,MC}}$ therefore reflects the precision of the cross section calculation which is not applicable to the $Z(\to \nu\nu)$+jets sample. This can be fixed by introducing a normalisation factor, κ, derived from normalising simulations to data in looser control regions containing $Z(\to \ell\ell)$+jets (CRZVL) and γ+jets (CRγVL).

CRZVL contains two leptons of same flavour and opposite electrical charge with an invariant mass in a range around the mass of the Z boson, 66 GeV $< m(\ell\ell) <$ 116 GeV and the missing transverse momentum is corrected with the p_{T} of the leptons much like VRZ. CRγVL is defined by cuts similar to those summarised in Table 5.8, however neither CRγVL nor CRZVL have any restrictions on m_{eff}(incl.), $E_{\mathrm{T}}^{\mathrm{miss}}/m_{\mathrm{eff}}$(Nj), or $E_{\mathrm{T}}^{\mathrm{miss}}/\sqrt{H_{\mathrm{T}}}$. Instead a loose cut on the corrected $E_{\mathrm{T}}^{\mathrm{miss}}$, 130 GeV $< E_{\mathrm{T}}^{\mathrm{miss}}(\star) <$ 160 GeV, is applied in both CRγVL and CRZVL.

The normalisation factor, κ, can be calculated from the observed and expected number of events in CRγVL and CRZVL as:

$$\kappa = \frac{N_{\mathrm{CR}\gamma\mathrm{VL}}^{\gamma+\mathrm{jets,data}} \cdot N_{\mathrm{CRZVL}}^{Z\ell\ell,\mathrm{MC}}}{N_{\mathrm{CR}\gamma\mathrm{VL}}^{\gamma+\mathrm{jets,MC}} \cdot N_{\mathrm{CRZVL}}^{Z\ell\ell,\mathrm{data}}}, \tag{5.4}$$

where $N_{\mathrm{CR}\gamma\mathrm{VL}}^{\gamma+\mathrm{jets,data}}$ and $N_{\mathrm{CRZVL}}^{Z\ell\ell,\mathrm{data}}$ are corrected from contamination of other background processes entering the loose control regions. The predicted number of $Z(\to \nu\nu)$+jets events in the signal region is then computed as:

$$N_{\mathrm{SR}}^{Z\nu\nu,\mathrm{pred}} = N_{\mathrm{SR}}^{Z\nu\nu,\mathrm{MC}} \cdot \frac{N_{\mathrm{CR}\gamma}^{\gamma+\mathrm{jets,data}}}{N_{\mathrm{CR}\gamma}^{\gamma+\mathrm{jets,MC}} \cdot \kappa}. \tag{5.5}$$

Ultimately, the normalisation factor used in the analysis is derived from events containing at least two jets where the number of $Z \to \ell\ell$ events is big enough and is thus not dependent on the signal region. Two γ+jets samples are used in the analysis: the baseline sample generated with SHERPA and the alternative sample generated with ALPGEN. κ differs for the two generators: $\kappa = 1.04 \pm 0.01(\mathrm{stat}) \pm 0.06(\mathrm{syst})$ for SHERPA and $\kappa = 1.40 \pm 0.03(\mathrm{stat}) \pm 0.08(\mathrm{syst})$ for ALPGEN, where the systematic uncertainties include uncertainties arising from photon and lepton selection, and background estimates. The correction factor of especially ALPGEN differs significantly from unity which would have led to an underestimation of $Z(\to \nu\nu)$+jets events if not corrected.

Control Regions for Multijet Background Estimation

The control region used to estimate multijet background (CRQ) has the same trigger requirement as the signal regions, `EF_j80_a4tchad_xe100_tclcw_veryloose`, as events containing leptons are vetoed in CRQ just as in the signal region selection.

The cuts in the signal region selection on $\Delta\phi(j, E_{\mathrm{T}}^{\mathrm{miss}})_{\mathrm{min}}$, and $E_{\mathrm{T}}^{\mathrm{miss}}/m_{\mathrm{eff}}(\mathrm{Nj})$ or $E_{\mathrm{T}}^{\mathrm{miss}}/\sqrt{H_{\mathrm{T}}}$ were placed to reject multijet events. A region with reverted cuts on these variables will therefore be ideal as a control region for selecting multijet background events. The cut on $\Delta\phi(j, E_{\mathrm{T}}^{\mathrm{miss}})_{\mathrm{min}}$ is reverted as summarised in Table 5.8. $E_{\mathrm{T}}^{\mathrm{miss}}/m_{\mathrm{eff}}(\mathrm{Nj})$ and $E_{\mathrm{T}}^{\mathrm{miss}}/\sqrt{H_{\mathrm{T}}}$ are required to lie in an interval from $X - \Delta$ to X, where X is the cut-value used in the signal region selection. There are three sizes of the interval, i. e. Δ, depending on the value of the cut, X, and the variable. The values of Δ used when a signal region places a cut on $E_{\mathrm{T}}^{\mathrm{miss}}/\sqrt{H_{\mathrm{T}}}$ is:

- $\Delta = 2\ \mathrm{GeV}^{1/2}$ when $X \leq 8\ \mathrm{GeV}^{1/2}$
- $\Delta = 4\ \mathrm{GeV}^{1/2}$ when $8 < X \leq 10\ \mathrm{GeV}^{1/2}$
- $\Delta = 6\ \mathrm{GeV}^{1/2}$ when $X > 10\ \mathrm{GeV}^{1/2}$.

When a signal region contains a cut on $E_{\mathrm{T}}^{\mathrm{miss}}/m_{\mathrm{eff}}(\mathrm{Nj})$, the values of Δ are:

- $\Delta = 0.05$ when $X \leq 0.20$
- $\Delta = 0.15$ when $0.20 < X \leq 0.40$
- $\Delta = 0.25$ when $X > 0.40$.

Since the multijet background has a high cross section and is difficult to model correctly, the template used to estimate the multijet background process is obtained by a fully data-driven technique described in Section 5.6.2.

In Figure 5.14, the observed distributions of $m_{\mathrm{eff}}(\mathrm{incl.})$ are shown together with the Standard Model predictions of CRQ before any cuts on $m_{\mathrm{eff}}(\mathrm{incl.})$ and $E_{\mathrm{T}}^{\mathrm{miss}}/m_{\mathrm{eff}}(\mathrm{Nj})$ or $E_{\mathrm{T}}^{\mathrm{miss}}/\sqrt{H_{\mathrm{T}}}$ in four jet multiplicities, di-jet, 4-jet, 5-jet, and 6-jet. The template used for the multijet contribution is obtained using the jet smearing method discussed in Section 5.6.2. In general, a good agreement between observation and expectation from the Standard Model is seen in all four jet multiplicities. There are of course deviations, but they are mostly within the statistical and systematical uncertainties. Furthermore, it should be noted that the control regions in different jet multiplicities are not orthogonal leading to a similar deviation pattern.

The expected purity of CRQ depends strongly on the cut on $E_{\mathrm{T}}^{\mathrm{miss}}/m_{\mathrm{eff}}(\mathrm{Nj})$ or $E_{\mathrm{T}}^{\mathrm{miss}}/\sqrt{H_{\mathrm{T}}}$. The purity ranges from 40% in CRQ for 4jW to 90% in CRQ for 2jl and 2jt. The cross contamination of control regions is handled by the fit where all the background contributions in all the control regions are fitted simultaneously.

5.6.2 Data-driven Multijet Estimation

The sample used to estimate the multijet background is obtained using a completely data-driven method called a jet smearing method. The jet smearing method is described in detail in Ref. [240]

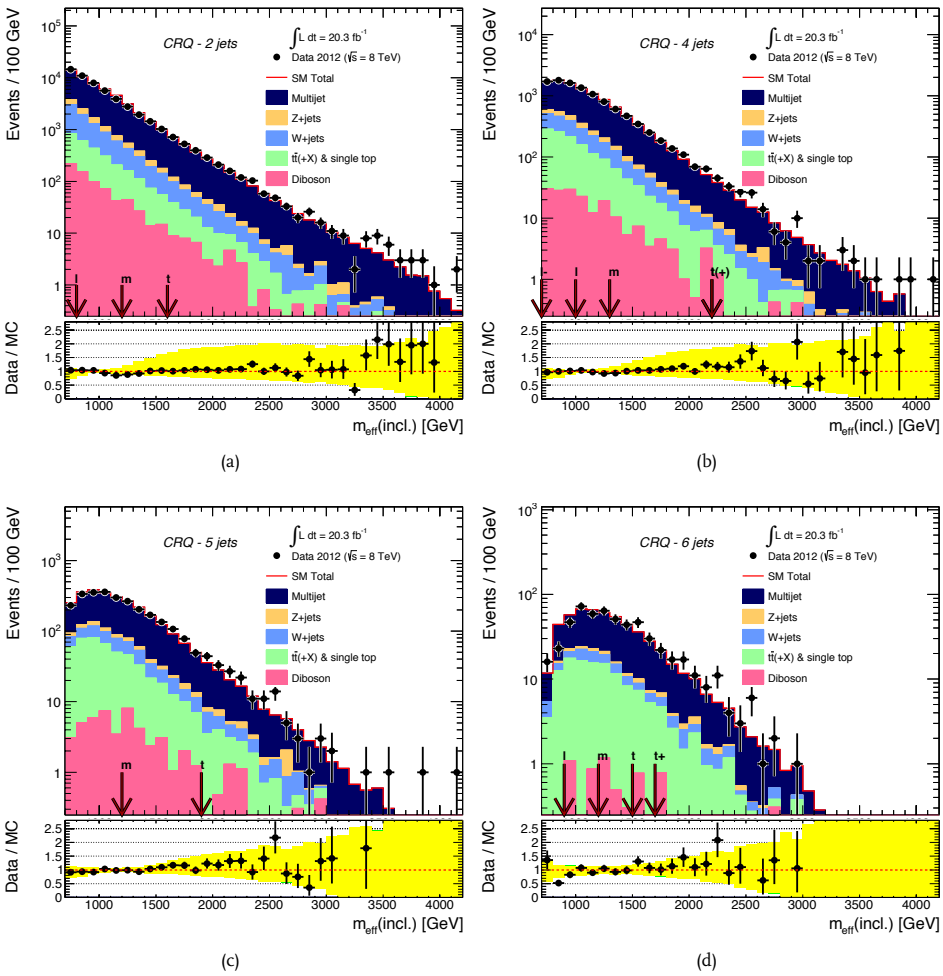

Fig. 5.14 · Observed and expected $m_{\text{eff}}(\text{incl.})$ distributions in 2-jet (a), 4-jet (b), 5-jet (c), and 6-jet (d) control regions of CRQ at $\sqrt{s} = 8$ TeV before the final cut on $m_{\text{eff}}(\text{incl.})$ and $E_{\text{T}}^{\text{miss}}/m_{\text{eff}}(\text{Nj})$ or $E_{\text{T}}^{\text{miss}}/\sqrt{H_{\text{T}}}$. The histograms show the expected background from simulation normalised to the luminosity. The red arrows indicate the specific cuts on $m_{\text{eff}}(\text{incl.})$ for the different jet multiplicities. The yellow error band includes only the uncertainties arising from the data-driven multijet estimate, and the green error band shows the total uncertainty including theory.

The main source of multijet events in the signal regions is mis-reconstruction of the energy of a jet leading to fake missing transverse momentum. To obtain a data-driven estimate of the multijet background, events containing jets, but no significant missing transverse momentum are used as seeds. The jets in the seed event are smeared using a *jet response function*, R, creating fake $E_{\text{T}}^{\text{miss}}$. The jet response function is obtained through Monte Carlo studies and modified to fit observations in data.

The seed events are triggered by one of nine single-jet triggers with p_{T} thresholds at trigger level ranging from 55 GeV to 460 GeV. An additional cut on the p_{T} of the leading jet is applied to insure that the trigger is fully efficient. The seed events must not contain high $E_{\mathrm{T}}^{\mathrm{miss}}$, and a cut on $E_{\mathrm{T}}^{\mathrm{miss}}/\sqrt{H_{\mathrm{T}}} < 0.6\ \mathrm{GeV}^{1/2}$ is therefore applied.

The jet response function is initially estimated from simulation by comparing the p_{T} of truth jets to the p_{T} of reconstructed jets matched to each other within a radius of $\Delta R = 0.1$. The p_{T} of the truth jet is taking into account the energy of electrons, muons, and neutrinos. The jets in the events must be separated by $\Delta R = 1.0$. The jet response function obtained from simulation is then:

$$R = \frac{p_{\mathrm{T}}^{\mathrm{jet}}(\mathrm{reco})}{p_{\mathrm{T}}^{\mathrm{jet}}(\mathrm{truth})}, \tag{5.6}$$

and binned in 20 GeV bins of p_{T} of the truth jet.

The jet response function obtained from simulation is modified using two methods derived from data:

1. The width of the jet response function can be widened using Gaussian smearing obtained from a di-jet analysis.

2. A correction to the low-side of the tail is performed. The lower-side of the tail corresponds to events with a significantly lower $p_{\mathrm{T}}^{\mathrm{jet}}(\mathrm{reco})$ leading to fake $E_{\mathrm{T}}^{\mathrm{miss}}$. The correction is performed using a Gaussian fit to the tail of the response function obtained from simulation and the width of the Gaussian tail is widened using a correction factor obtained from data.

The four-vectors of all the jets in the seed event are smeared using the response function obtained from both simulation and data. The smeared missing transverse momentum, $\vec{E}_{\mathrm{T}}^{\mathrm{miss}'}$, is given by:

$$\vec{E}_{\mathrm{T}}^{\mathrm{miss}'} = \vec{E}_{\mathrm{T}}^{\mathrm{miss,seed}} - \sum_i \vec{p}_{\mathrm{T}}'(j_i) + \sum_i \vec{p}_{\mathrm{T}}(j_i), \tag{5.7}$$

where the primes are denoting the smeared quantities. The $\Delta\phi(j, E_{\mathrm{T}}^{\mathrm{miss}})$ distributions can be obtained from smearing in a similar way.

The jet smearing method is validated by comparing the estimated multijet background with another sample acquired from a completely different data-driven technique, the ABCD method, exploiting the missing transverse momentum calculated from tracks only, $E_{\mathrm{T}}^{\mathrm{miss,track}}$ and $\Delta\phi(j, E_{\mathrm{T}}^{\mathrm{miss}})_{\mathrm{min}}$.

5.6.3 Validation Regions

In order to test the robustness of the background estimate from control regions, it is checked in regions orthogonal to both control regions and signal regions, the so-called validation regions. The validation regions are typically defined by inverting one of the cuts differing between the control and signal regions.

A set of 19 validation regions is defined for each signal region to test the background estimate from all the control regions as well as testing the lepton charge asymmetry and the estimate of τ background.

Validation Regions for Z Background

Two validation regions are designed to validate the estimate of the Z background coming from CRγ:

VRZ was described in Table 5.8. Two oppositely charged leptons of the same flavour with an invariant mass within a window around the mass of the Z boson are required. There are no cuts on $E_{\mathrm{T}}^{\mathrm{miss}}/m_{\mathrm{eff}}(\mathrm{Nj})$ or $E_{\mathrm{T}}^{\mathrm{miss}}/\sqrt{H_{\mathrm{T}}}$.

VRZf is very similar to VRZ. The difference is an additional cut on $E_{\mathrm{T}}^{\mathrm{miss}}/m_{\mathrm{eff}}(\mathrm{Nj})$ or $E_{\mathrm{T}}^{\mathrm{miss}}/\sqrt{H_{\mathrm{T}}}$ corresponding to the signal region cuts.

Validation Regions for W Background

There are three validation regions defined to validate the estimate of the W background based on CRW:

VRWf is very similar to CRW. Additional cuts on $\Delta\phi(j, E_{\mathrm{T}}^{\mathrm{miss}})_{\mathrm{min}}$ and $E_{\mathrm{T}}^{\mathrm{miss}}/m_{\mathrm{eff}}(\mathrm{Nj})$ or $E_{\mathrm{T}}^{\mathrm{miss}}/\sqrt{H_{\mathrm{T}}}$ are applied corresponding to the cut values of the signal region selection.

VRWM uses the same cuts as CRW, but the lepton is treated as a missing particle instead of a jet resulting in a modified $E_{\mathrm{T}}^{\mathrm{miss}}$given as $\vec{E}_{\mathrm{T}}^{\mathrm{miss}}(\star) = \vec{E}_{\mathrm{T}}^{\mathrm{miss}} + \vec{p}_{\mathrm{T}}(\ell)$.

VRWMf is similar to VRWM, but has additional cuts on $\Delta\phi(j, E_{\mathrm{T}}^{\mathrm{miss}})_{\mathrm{min}}$ and $E_{\mathrm{T}}^{\mathrm{miss}}/m_{\mathrm{eff}}(\mathrm{Nj})$ or $E_{\mathrm{T}}^{\mathrm{miss}}/\sqrt{H_{\mathrm{T}}}$ corresponding to the cut values of the signal region selection.

Validation Regions for Top Background

Four validation regions are defined to check the robustness of the top background estimate coming from CRT:

VRTf is very similar to CRT. Additional cuts on $\Delta\phi(j, E_{\mathrm{T}}^{\mathrm{miss}})_{\mathrm{min}}$ and $E_{\mathrm{T}}^{\mathrm{miss}}/m_{\mathrm{eff}}(\mathrm{Nj})$ or $E_{\mathrm{T}}^{\mathrm{miss}}/\sqrt{H_{\mathrm{T}}}$ are applied corresponding to the cut values of the signal region.

VRTM uses the same cuts as CRT, but treats the lepton as a missing particle instead of as a jet resulting in a modified $E_{\mathrm{T}}^{\mathrm{miss}}$given as $\vec{E}_{\mathrm{T}}^{\mathrm{miss}}(\star) = \vec{E}_{\mathrm{T}}^{\mathrm{miss}} + \vec{p}_{\mathrm{T}}(\ell)$.

VRTMf is similar to VRTM, but has additional cuts on $\Delta\phi(j, E_{\mathrm{T}}^{\mathrm{miss}})_{\mathrm{min}}$ and $E_{\mathrm{T}}^{\mathrm{miss}}/m_{\mathrm{eff}}(\mathrm{Nj})$ or $E_{\mathrm{T}}^{\mathrm{miss}}/\sqrt{H_{\mathrm{T}}}$ corresponding to the cut values of the signal region.

VRT2L has cuts similar to VRZ, but with a reversed cut on the invariant mass of the lepton pair, $m(\ell\ell) > 116$ GeV. Furthermore upper cuts are applied to the p_{T} of the two leptons, $p_{\mathrm{T}}(\ell_1) < 200$ GeV and $p_{\mathrm{T}}(\ell_2) < 100$ GeV, to reduce the contribution from the Z/γ^*+jets process. This validation region targets $t\bar{t}$-production with fully leptonic decay.

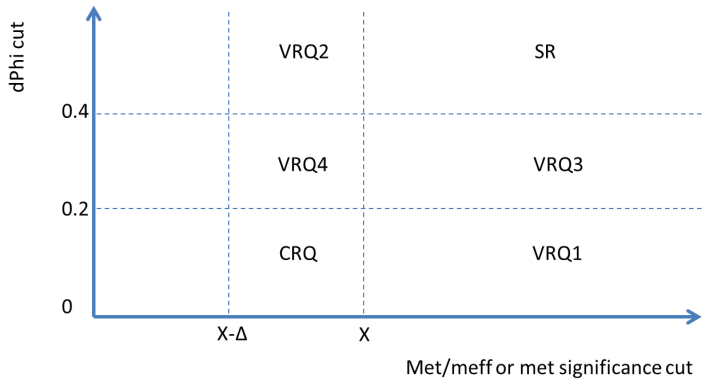

Fig. 5.15 · Illustration of cuts used to define signal regions (SR), control regions for multijet background estimation (CRQ), and validation regions used to validate the multijet background estimate (VRQ1, VRQ2, VRQ3, and VRQ4).

Validation Regions for Multijet Background

There are four validation regions designed to validate the multijet background estimate from CRQ. They are all designed by reverting the cuts on either $\Delta\phi(j, E_{\mathrm{T}}^{\mathrm{miss}})_{\mathrm{min}}$ or $E_{\mathrm{T}}^{\mathrm{miss}}/m_{\mathrm{eff}}(\mathrm{Nj})$ or $E_{\mathrm{T}}^{\mathrm{miss}}/\sqrt{H_{\mathrm{T}}}$ depending on the signal region selection.

An illustration on where the signal region, CRQ, and the validation regions are found in the $\Delta\phi(j, E_{\mathrm{T}}^{\mathrm{miss}})_{\mathrm{min}}$-$E_{\mathrm{T}}^{\mathrm{miss}}/m_{\mathrm{eff}}(\mathrm{Nj})$ (or $\Delta\phi(j, E_{\mathrm{T}}^{\mathrm{miss}})_{\mathrm{min}}$-$E_{\mathrm{T}}^{\mathrm{miss}}/\sqrt{H_{\mathrm{T}}}$) plane is shown in Figure 5.15.

The four multijet validation regions are:

VRQ1 uses all the same cut as CRQ except the cut on $E_{\mathrm{T}}^{\mathrm{miss}}/m_{\mathrm{eff}}(\mathrm{Nj})$ or $E_{\mathrm{T}}^{\mathrm{miss}}/\sqrt{H_{\mathrm{T}}}$ has the same cut value as the signal regions. This validation region is sensitive to the extrapolation in $E_{\mathrm{T}}^{\mathrm{miss}}/m_{\mathrm{eff}}(\mathrm{Nj})$ or $E_{\mathrm{T}}^{\mathrm{miss}}/\sqrt{H_{\mathrm{T}}}$ of QCD.

VRQ2 uses all the same cut as CRQ except the cut on $\Delta\phi(j, E_{\mathrm{T}}^{\mathrm{miss}})_{\mathrm{min}}$ has the same cut value as the signal regions. This validation region is sensitive to the extrapolation in $\Delta\phi(j, E_{\mathrm{T}}^{\mathrm{miss}})_{\mathrm{min}}$ of QCD.

VRQ3 is similar to VRQ1, but the cut on $\Delta\phi(j, E_{\mathrm{T}}^{\mathrm{miss}})_{\mathrm{min}}$ is changed into an intermediate cut of $0.2 < \Delta\phi(j_{1,2,(3)}, E_{\mathrm{T}}^{\mathrm{miss}})_{\mathrm{min}} < 0.4$ for all jet multiplicities and $0.1 < \Delta\phi(j_{i>3}, E_{\mathrm{T}}^{\mathrm{miss}})_{\mathrm{min}} < 0.2$ for jets with $p_{\mathrm{T}} > 40$ GeV in 4-, 5-, and 6-jet regions.

VRQ4 is similar to VRQ2, but the cut on $\Delta\phi(j, E_{\mathrm{T}}^{\mathrm{miss}})_{\mathrm{min}}$ is changed into an intermediate cut of $0.2 < \Delta\phi(j_{1,2,(3)}, E_{\mathrm{T}}^{\mathrm{miss}})_{\mathrm{min}} < 0.4$ for all jet multiplicities and $0.1 < \Delta\phi(j_{i>3}, E_{\mathrm{T}}^{\mathrm{miss}})_{\mathrm{min}} < 0.2$ for jets with $p_{\mathrm{T}} > 40$ GeV in 4-, 5-, and 6-jet regions.

Validation Regions for Testing Lepton Charge Asymmetry

A charge asymmetry of the leptons is expected from W decays, i. e. the cross sections of production of W^+ and W^- are not identical. The proton contains two u-valence quarks and a single d-valence quark and it is therefore expected that more W^+-bosons are produced than W^-.

Four validation regions are designed to test the charge asymmetry of leptons:

VRWT+ is defined by the same cuts as CRW and CRT, i. e. there is no b-tagging requirement, but only selecting events with positively charged leptons.

VRWT- is identical to VRWT+, but only selecting events with negatively charged leptons.

VRWTf+ is similar to VRWT+. Additional cuts on $\Delta\phi(j, E_{\mathrm{T}}^{\mathrm{miss}})_{\mathrm{min}}$ and $E_{\mathrm{T}}^{\mathrm{miss}}/m_{\mathrm{eff}}(\mathrm{Nj})$ or $E_{\mathrm{T}}^{\mathrm{miss}}/\sqrt{H_{\mathrm{T}}}$ are applied corresponding to the cut values of the signal region.

VRWTf- is identical to VRWTf+, but only selecting events with negatively charged leptons.

Validation Regions for τ background

There are no requirements on the presence or non-presence of tau-leptons in the signal and control regions. Therefore it is expected that there will be background contribution from W and $t\bar{t}$-decays into final states with hadronically decaying tau-leptons. Two validation regions are therefore designed to test the background estimate of W and top decaying into tau-leptons:

VRWτ has cuts identical to the signal region selection only changing the $\Delta\phi(j, E_{\mathrm{T}}^{\mathrm{miss}})_{\mathrm{min}}$ into an intermediate cut of $0.2 < \Delta\phi(j_{1,2,(3)}, E_{\mathrm{T}}^{\mathrm{miss}})_{\mathrm{min}} < 0.4$ for all jet multiplicities and $0.1 < \Delta\phi(j_{i>3}, E_{\mathrm{T}}^{\mathrm{miss}})_{\mathrm{min}} < 0.2$ for jets with $p_{\mathrm{T}} > 40$ GeV in 4-, 5-, and 6-jet regions. Furthermore there is a requirement on the event to contain at least one hadronically decaying tau-lepton and not to contain any b-tagged jets.

VRTtbarτ has all cuts identical to VRWτ except a requirement of the event to contain at least one b-tagged jet.

5.7 Systematic Uncertainties

Systematic uncertainties affect the Standard Model background expectation as well as the expected signal yield in the control, validation, and signal regions which in turn will affect the uncertainty of the excluded SUSY parameter-space. To estimate the effect of systematic uncertainties on background and signal, the sources of the uncertainties are studied and quantified to be included into the final fit.

5.7.1 Uncertainties on Background

The systematic uncertainties on the backgrounds will affect the final results through their impact on the transfer functions from control regions to signal or validation regions. The sources of the systematic uncertainties on the background are many, but can in general be divided into three categories:

Experimental uncertainties are uncertainties related to the understanding of the detector and thereby the detection of particles. The experimental uncertainty includes the uncertainties on the energy scale and resolution of the physics objects such as jets, leptons, and photons which in turn affect the calculation of $E_{\mathrm{T}}^{\mathrm{miss}}$. The estimate of the major experimental uncertainties in Chapter 3.

Theoretical uncertainties are related to the uncertainties arising from the physics modeling, e. g. the resolution and renormalisation scales, the strong coupling constant, and choice of generator used in the simulation.

Extrapolation uncertainties are uncertainties coming from the extrapolation from control regions to signal or validation regions.

The most dominant experimental uncertainties are from the jet energy scale (JES) calibration and the jet energy resolution (JER) affecting the measured p_{T} of the jets and thereby affecting the calculation of $E_{\mathrm{T}}^{\mathrm{miss}}$. The uncertainties of JES and JER are obtained by dedicated analyses [167, 241, 168] and depend on the p_{T} and η of the jets. The effect of pile-up on JES and JER is included in the JES and JER uncertainties. The resolution and the scale of the low-p_{T} terms of the $E_{\mathrm{T}}^{\mathrm{miss}}$ will also contribute to the overall uncertainty on $E_{\mathrm{T}}^{\mathrm{miss}}$. Uncertainties on b-tagging in CRW and CRT, the efficiency of photon reconstruction in CRγ, and the lepton reconstruction efficiency as well as energy scale and resolution in all control and validation regions are all included. The uncertainties on the lepton reconstruction, energy scale, and energy resolution were found to be negligible in the signal regions. An uncertainty on the luminosity measurement is accounted for as well and is found to be 2.8% [219].

The theoretical uncertainties are partly estimated by comparing the transfer functions obtained from two different Monte Carlo generators. The effect of the modeling of pile-up in the simulated events is estimated by increasing and decreasing the average number of collisions per bunch crossing by 10%. The impact of the choice of parton distribution functions was checked by a dedicated Monte Carlo study and found to be negligible. The effect of the choices of renormalisation and factorisation scales are studied by doubling and halving the nominal values. The uncertainty of the reweighting of the $t\bar{t}$-sample described in Section 5.3.2 is estimated by varying the weights depending on the p_{T} of the $t\bar{t}$ pair.

The overall uncertainty on the cross section of diboson production is estimated by comparing simulation samples generated at different factorisation and renormalisation scales and with different values of the strong coupling, α_s. It is found that an overall uncertainty of 50% covers the uncertainty in all signal regions.

The Monte Carlo samples of direct production of vector bosons, $W^{\pm}$, Z, and γ, in association with jets are affected by multiple sources of uncertainties. The minimum p_{T} used as a matching scale of the matrix element with the parton shower is increased by 10 GeV to 25 GeV in order to estimate the uncertainty arising from the matching scale choice. To further check the parton showering, the number of partons generated at matrix element level is reduced by 1 such that an extra jet must be formed from parton showering. An additional uncertainty is included for $W^{\pm}$-

Name	Characteristic Scale	Treatment	Comment
Luminosity	2.8%	Fully correlated	
MC statistics	-	Uncorrelated	All MC samples
Physics Process Modelling			
Pile-Up	$\langle\mu\rangle \times [0.9, 1.1]$	Fully correlated	All MC samples
Total cross section	Diboson (50%)	Partially correlated	Pure MC estimate
μ_R/μ_F scale variation	$\mu_{R/F} \times [0.5, 2.0]$	Per process	$W/Z/\gamma$+jets, $t\bar{t}$
Matching scale variation	$p_{\mathrm{T,min}} = [15, 25]$ GeV	Per process	$W/Z/\gamma$+jets
Number of extra partons	Decreased by one	Per process	$W/Z/\gamma$+jets
Generator comparison	ALPGEN and SHERPA	Per process	$W/Z/\gamma$+jets
W + heavy flavour	$\simeq$ 25-50%	Per process	W+jets
γ+jets κ	$\simeq$ 6%	Per process	γ+jets
Generator comparison	MC@NLO and POWHEG	Per process	$t\bar{t}$
$t\bar{t}$ diff. cross section	Vary weights	Per process	$t\bar{t}$
Multijet method (Gaus.)	$\sigma_{\mathrm{corr}} \pm 0.05$	Per process	Multijet
Multijet method (Tail)	Dependent on p_{T}	Per process	Multijet
Object Modelling			
Jet energy scale	Dependent on jet	Fully correlated	
Jet energy resolution	Dependent on jet	Fully correlated	
Soft $E_{\mathrm{T}}^{\mathrm{miss}}$ scale	5%	Fully correlated	
Soft $E_{\mathrm{T}}^{\mathrm{miss}}$ resolution	2%	Fully correlated	
Lepton efficiency	Dependent on lepton	Fully correlated	
Photon efficiency	5-7%	Fully correlated	Only in CRγ
b-tagging	Dependent on b-jet	Fully correlated	Only in CRW/CRT

Table 5.9 · The sources of the systematic uncertainties, their characteristic scale, their treatment in the fit, and eventual comments on the relevant background process of region the uncertainty.

production where events describing production in association with heavy flavour quarks (charm or bottom) are reweighted by factors ranging from 26% to 51%. This uncertainty especially affects regions with requirement on b-tagged jets. The uncertainty on the κ obtained to normalise the γ+jets simulation samples is included as well.

Uncertainties are assigned to the jet smearing method described in Section 5.6.2. The correction factors for the central Gaussian distribution and the low-energy tail obtained from fits to data are varied independently.

The extrapolation uncertainties include the statistical uncertainty on the Monte Carlo samples by a Poissonian uncertainty ($\sqrt{N_{\mathrm{MC}}}$) as well as the statistical uncertainty in the control regions.

The systematic uncertainties are treated in different ways in the fit. The treatment the systematic uncertainties can be either:

- Fully correlated across the different background processes and all regions as for example the uncertainty on the luminosity.
- Fully correlated across all regions, but independent per process, e. g. theoretical uncertainties.
- Fully uncorrelated with one parameter per bin, e. g. uncertainties arising from the limited statistics of the simulation samples.

A summary of the systematic uncertainties on the background, their characteristic size, and how they are treated in the fit, i. e. their correlation treatment, is given in Table 5.9.

5.7.2 Uncertainties on Signal

As there are uncertainties affecting the background estimate, there are uncertainties affecting the signal modeling as well. The uncertainties on signal can be divided into two groups: uncertainties affecting the total production cross section and uncertainties affecting the signal acceptance in the various regions.

The uncertainties affecting the cross section will affect the over-all normalisation of the signal in the signal regions. The cross section is calculated for each squark mass using two parton distribution function sets, CTEQ6L1 and MSTW2008LO. To estimate the uncertainty on the choice of renormalisation and factorisation scales, they are both varied by a factor of 0.5 and 2.0 and cross sections are calculated using the two PDF sets. Finally the strong coupling, α_s, is varied by a factor of 0.5 and 2.0 and the cross section is calculated using only CTEQ6L1 as the PDF set. The total uncertainty on the cross section is found by adding the contribution from the various sources in quadrature. The nominal cross section is found from two quantities defined as:

$$A = \max(\sigma_{\text{CTEQ6L1}} \cdot (1 + \Delta\sigma^{\text{up}}_{\text{CTEQ6L1}}); \sigma_{\text{MSTW2008LO}} \cdot (1 + \Delta\sigma^{\text{up}}_{\text{MSTW2008LO}})) \tag{5.8a}$$

$$B = \min(\sigma_{\text{CTEQ6L1}} \cdot (1 - \Delta\sigma^{\text{down}}_{\text{CTEQ6L1}}); \sigma_{\text{MSTW2008LO}} \cdot (1 - \Delta\sigma^{\text{down}}_{\text{MSTW2008LO}})), \tag{5.8b}$$

where σ_{PDF} is the cross section calculated with a specific PDF set, and $\Delta\sigma^{\text{up/down}}_{\text{PDF}}$ is the upward or downward error on the cross section. The nominal cross section is found by taking the average of A and B, and the symmetric error on the cross section is $\Delta\sigma/\sigma = (A - B)/(A + B)$.

Uncertainties on the acceptance of the signal arise from either detector uncertainties or uncertainties related to ISR jets. The most dominant detector uncertainties are the jet energy scale and jet energy resolution. The uncertainty on the signal acceptance coming from initial state radiation depends on the mass splitting between the produced sparticle and the LSP, $\Delta m = m_{\tilde{q}_L} - m_{\tilde{\chi}^0_1}$, as well as the jet multiplicity requirement in the signal region selection. The ISR uncertainty is parametrized as $a \cdot \exp(-\Delta m/b)$, where a is ranging from 0.1 to 0.3 and b is ranging from 123 GeV to 416 GeV depending on the jet multiplicity. The exact values of a and b are found through a fit to signal regions with a looser cut on m_{eff}(incl.) of 600 GeV.

The uncertainty on the signal acceptance is included in the systematic uncertainty of the fit when calculating the model-dependent upper limits. The uncertainty on the cross section is handled differently. The limit is obtained using the central value of the cross section. The uncertainty on the SUSY model production cross section is included by re-calculating the limits with production cross sections of $\sigma \pm \Delta\sigma$ and they are reported as separate limits.

5.8 Results

The results of the analysis are obtained using the statistical procedures described in Section 4.4. The results of the background-only fit are divided into results in validation regions presented in Section 5.8.1 and results in signal regions presented in Section 5.8.2. The results in Section 5.8.2 contain the model-independent upper limits as well. The exclusion limits on the simplified models, the MSUGRA/CMSSM model, and the pMSSM model with left-handed squark-pair production are presented in Section 5.9.

5.8.1 Validation Regions

The background estimate obtained by the background-only fit is tested in the validation regions defined in Section 5.6.3. In total 323 validation regions are tested, 19 validation regions per signal region.

The agreement between the expected and observed number of events is quantified by calculating the pull for each validation region. The pull is defined as $(n_{\text{obs}} - n_{\text{pred}})/\sigma_{\text{tot}}$, where n_{obs} is the observed number of events, n_{pred} is the number of events predicted by the fit, and σ_{tot} is the total uncertainty. The total uncertainty is calculated as $\sigma_{\text{tot}} = \sigma_{\text{stat}} \otimes \Delta n_{\text{pred}}$, where Δn_{pred} is the uncertainty coming from the fit, and σ_{stat} is the standard deviation of a Poisson distribution centered around n_{pred}. The pull is thus a measure of how many standard deviations the observed number of events differ from the prediction by the fit.

In Figure 5.16, the pulls of all the validation regions are shown. Most of the validation regions have a pull lying within 1.5σ and thus a good agreement between observation and prediction is seen. However, a few regions have pulls greater than 2σ and one region even greater then 3σ. It should be noted that the validation regions are not mutually exclusive and a combination of the pulls is not straight forward.

In VRZf of the 5j signal region, an excess over the prediction of $\sim 2.4\sigma$ is observed. The number of observed events is 13 while the number of expected events after the fit is 6.1 ± 1.3. The expected number of events from Monte Carlo simulations prior to the fit is 8.8. The reduction of the expected number of events after the fit is caused by the scaling of the Z background by a factor of 0.59 obtained in CRγ. The excess is thus believed to be caused by a combination of an upward fluctuation of data over expectation and the scaling of the Z background. A similar effect is seen in VRZ of the 4jW-region.

The biggest excess in any of the validation regions is a 3.2σ excess in VRQ3 of the 3j-region. The number of observed events is 6 while the prediction coming from the fit is 1.2 ± 0.5. The distributions of $E_{\text{T}}^{\text{miss}}/m_{\text{eff}}(3j)$, $\Delta\phi(j_i, E_{\text{T}}^{\text{miss}})_{\text{min}}$, and the number of b-jets suggested that the

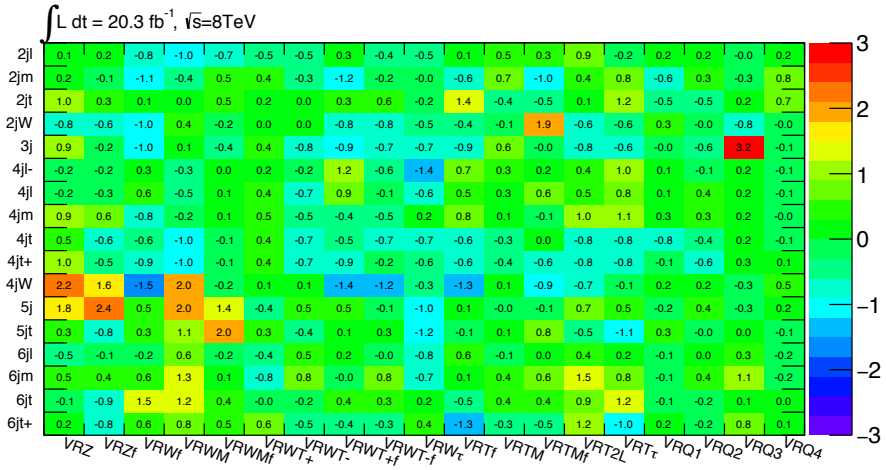

Fig. 5.16 · Pulls of all the validation regions. The pulls are calculated including the uncertainty arising from the fit as well as a standard deviation of a Poisson distribution centered around the number of events predicted by the fit.

origin of the excess does not come from multijet events or from $t\bar{t}$. Due to the very low expected and observed number of events, this region is very sensitive to fluctuations in data and it is believed to be the cause of the excess.

After accounting for the larger excesses in the validation regions, it was found that the background estimate coming from the background-only fit was reliable and the signal regions could be studied.

5.8.2 Signal Regions

Distributions of the m_{eff}(incl.) of all the signal regions before the background fit and prior to the final cut on m_{eff}(incl.) are shown in Figures 5.17, 5.18, and 5.19. The expected Standard Model distributions are obtained from Monte Carlo samples normalised with their cross sections to the integrated luminosity (except the multijet background that is obtained using the jet-smearing method discussed in Section 5.6.2). The distributions are overlaid by signal models used for the optimisation of the various signal regions to illustrate where and how an eventual signal would show up. The yellow and green uncertainty bands correspond to detector and theoretical systematic uncertainties, respectively.

In general, the observed number of events lies within the error of the expected. However, there are systematic trends in the m_{eff}(incl.) distributions that become clearer at high values of m_{eff}(incl.). This is the reason why the analysis does not rely solely on estimates from Monte Carlo simulations for the background yields, but instead utilises fits to the yields in control regions to estimate the Standard Model background. By fitting in the control regions the systematic discrepancies between observation and expectation are taken into account.

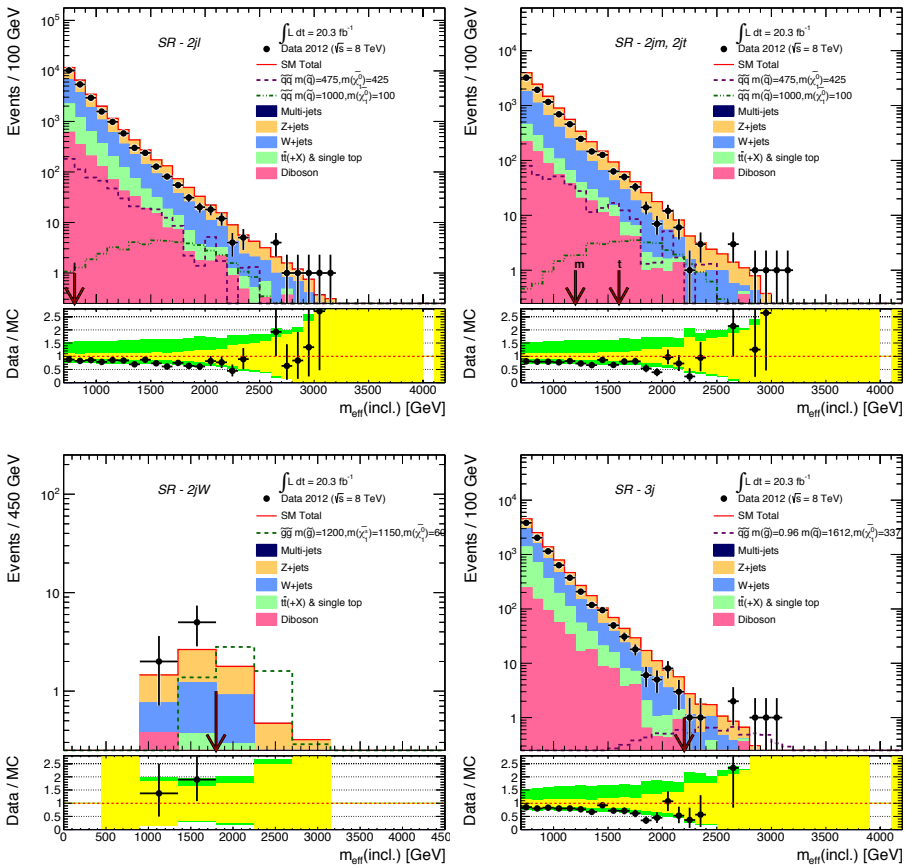

Fig. 5.17 · Observed m_{eff}(incl.) distributions in signal regions at $\sqrt{s} = 8$ TeV: 2jl (top left), 2jm and 2jt (top right), 2jW (bottom left), and 3j (bottom right) before the final cut on m_{eff}(incl.). The histograms show the expected background distribution prior to the fit obtained only from simulation and normalised to the luminosity. SUSY models with parameters given in GeVare shown for comparison. The red arrows indicate the specific cuts on m_{eff}(incl.). In the lower panel, the yellow error band includes experimental uncertainties as well as MC statistical uncertainties, and the green error band shows the total uncertainty including theory uncertainties.

The observed and expected event yields and their uncertainties in each signal region are shown in Figure 5.20. In most signal regions the expected and observed number of events agree within the uncertainties.

The normalisation factors of the simulations to the data in the control regions as defined in Eq/ 4.10 of the top, Z+jets, W+jets, and multijet background obtained by the fit are shown in Figure 5.21. The normalisation factors of the top background are flat and close to one indicating that the Monte Carlo samples describe the top contribution well. The normalisation factors of Z+jets are generally smaller than 1 and show a distinct pattern of decreasing with increasing

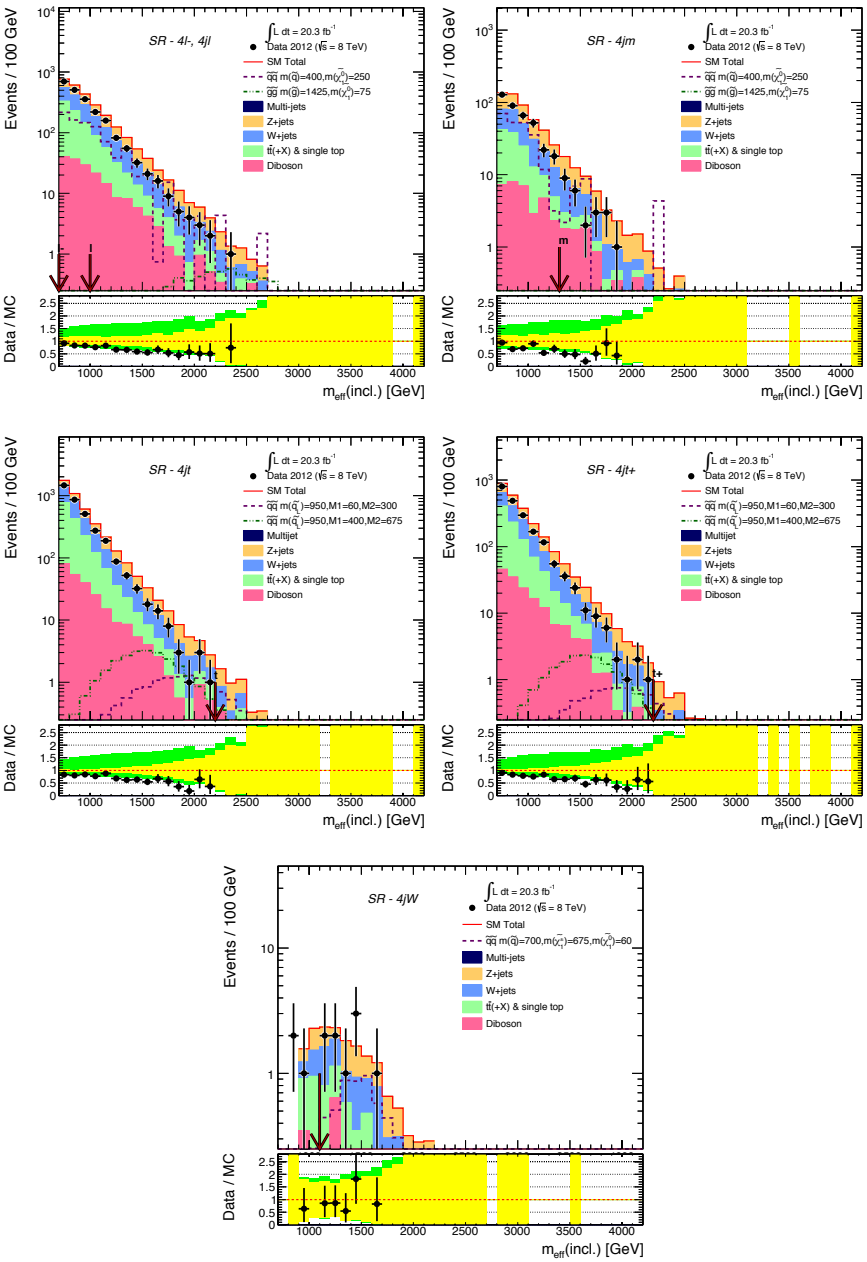

Fig. 5.18 · Observed m_{eff}(incl.) distributions in signal regions at $\sqrt{s} = 8$ TeV: 4jl– and 4jl (top left), 4jm (top right), 4jt (middle left), 4jt+ (middle right), and 4jW (bottom) before the final cut on m_{eff}(incl.). The histograms show the expected background distribution prior to the fit obtained only from simulation and normalised to the luminosity. SUSY models with parameters given in GeVare shown for comparison. The red arrows indicate the specific cuts on m_{eff}(incl.). In the lower panel, the yellow error band includes experimental uncertainties as well as MC statistical uncertainties, and the green error band shows the total uncertainty including theory uncertainties.

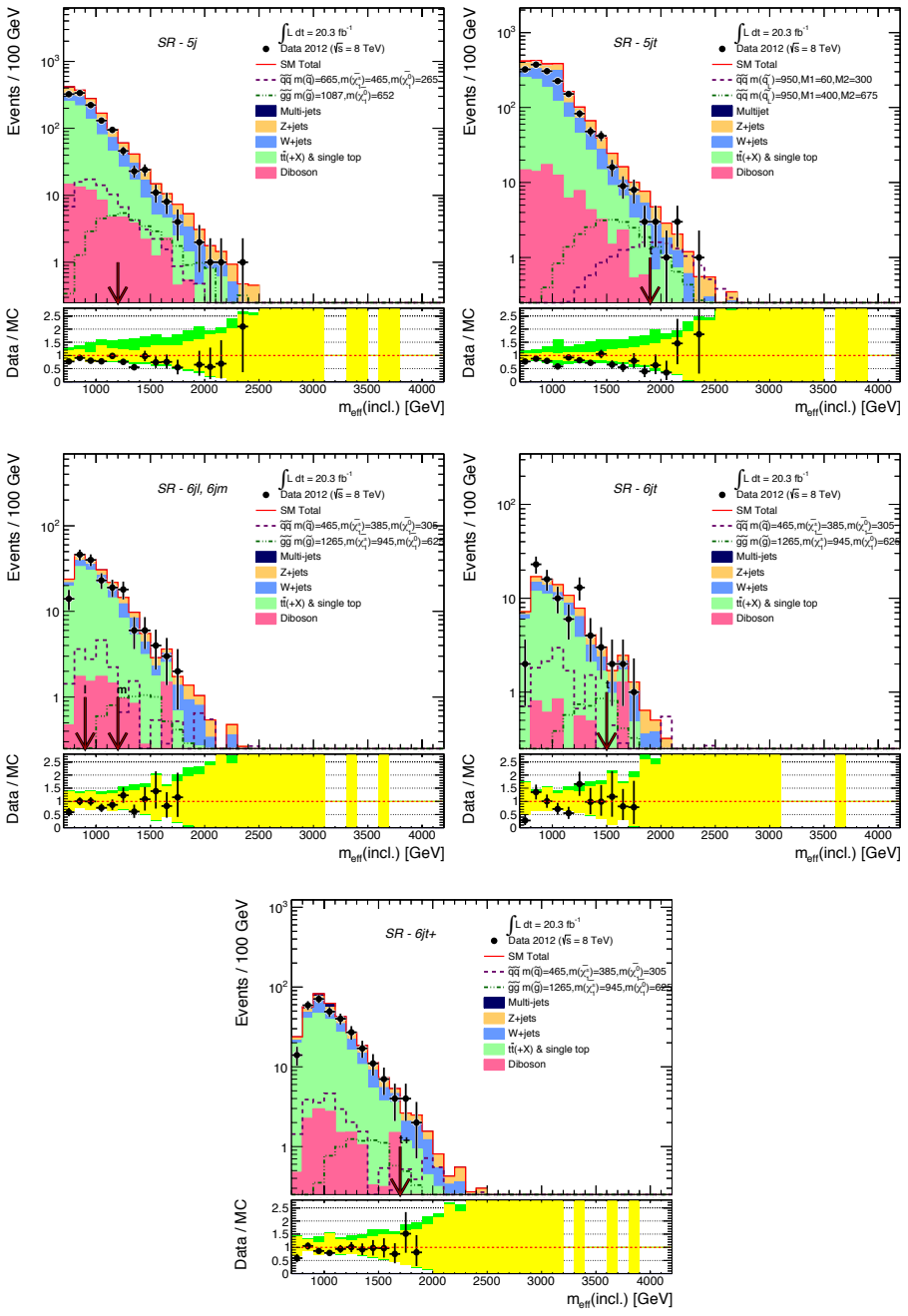

Fig. 5.19 · Observed m_{eff}(incl.) distributions in signal regions at $\sqrt{s} = 8$ TeV: 5j (top left), 5jt (top right), 6jl and 6jm (middle left), 6jt (middle right), and 6jt+ (bottom) before the final cut on m_{eff}(incl.). The histograms show the expected background distribution prior to the fit obtained only from simulation and normalised to the luminosity. SUSY models with parameters given in GeVare shown for comparison. The red arrows indicate the specific cuts on m_{eff}(incl.). In the lower panel, the yellow error band includes experimental uncertainties as well as MC statistical uncertainties, and the green error band shows the total uncertainty including theory uncertainties.

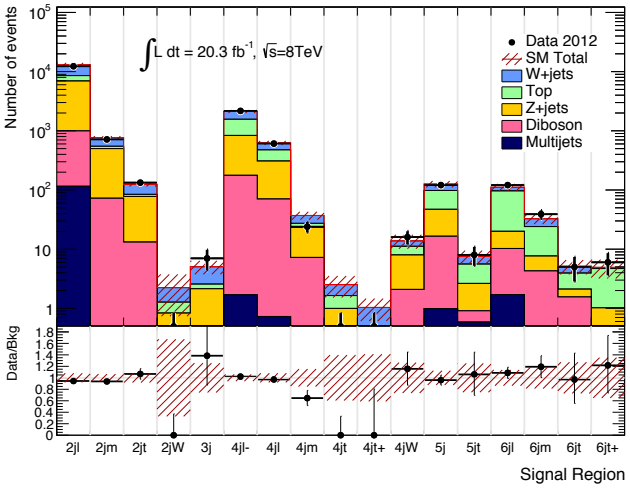

Fig. 5.20 · Comparison of observed and expected event yields after the fit as a function of the signal regions at $\sqrt{s} = 8$ TeV. In signal region 2jW, 4jt, and 4jt+ no events are observed.

jet multiplicity and tightness of the m_{eff}(incl.) cut. This is in agreement with the discussion in Section 5.6.1 on the harder jet multiplicity and thereby m_{eff}(incl.) spectrum of the SHERPA sample compared to observations in CRγ. The W+jets normalisation factors show a behavior similar to the transfer factors of Z+jets, but less distinct. The smeared data used to estimate the multijet background do not correspond to a specific luminosity. Prior to the fit, preliminary normalisation factors are obtained by simply normalising the pseudo-data from the jet-smearing method in CRQ for each signal region. The preliminary normalisation factors are applied before the fit and the final normalisation factors are fitted to take into account the cross-contamination of other background processes.

A comparison between the number of observed events in each signal region and the expected background yields both before and after the fit is given in Table 5.10. The model-independent limits on the visible cross section, the expected and observed upper limits on the visible number of signal events at 95% confidence level, and the p_0-value of the background-only hypothesis are given in Table 5.10 as well. The p-value is truncated at 0.5 such that signal regions with fewer observed events than expected will lead to a p-value of 0.5 and a corresponding Gaussian standard deviation of zero. The model-independent limits are calculated using both toy simulations and an asymptotic formula obtained from an Asimov dataset[1] [198]. The observed number of events is in general in good agreement with the estimated background yield obtained by the fit in all signal regions and with the biggest deviation being $Z = 0.7$ in SR3j no significant excesses are observed.

[1] An Asimov dataset is an artificial dataset which is generated with the expected count, but without statistical fluctuations. In that way it is representative for a large ensemble of pseudo-experiments.

Signal Region	SR2jl	SR2jm	SR2jt	SR2jW	SR3j	SR4jl-	SR4jl	SR4jm
				MC expected events				
Diboson	879	72	13	0.41	0.36	175	70	7.2
Z/γ^*+jets	6709	552	103	1.2	5.5	885	333	30
W+jets	5472	303	59	0.82	3.1	832	284	16
$t\bar{t}$(+EW) + single-t	1807	54	9.0	0.14	0.85	764	167	4.0
				Fitted background events				
Diboson	900 ± 400	70 ± 40	13 ± 6	0.41 ± 0.21	0.36 ± 0.18	180 ± 90	70 ± 34	7 ± 4
Z/γ^*+jets	5900 ± 900	430 ± 40	65 ± 8	0.4 ± 0.4	1.7 ± 1.0	660 ± 60	238 ± 28	16 ± 4
W+jets	4500 ± 600	216 ± 26	40 ± 6	1.0 ± 1.0	2.5 ± 0.9	560 ± 80	151 ± 28	10 ± 4
$t\bar{t}$(+EW) + single-t	1620 ± 320	47 ± 8	6.5 ± 2.2	$0.4^{+0.8}_{-0.4}$	$0.4^{+0.5}_{-0.4}$	730 ± 50	167 ± 18	4 ± 2
Multi-jets	115^{+140}_{-115}	$0.4^{+1.40}_{-0.4}$	$0.1^{+0.4}_{-0.1}$	0.03 ± 0.03	$0.03^{+0.06}_{-0.03}$	$1.7^{+4.0}_{-1.7}$	$0.7^{+1.6}_{-0.7}$	–
Total bkg	13000 ± 1000	760 ± 50	125 ± 10	2.3 ± 1.4	5.0 ± 1.2	2120 ± 110	630 ± 50	37 ± 6
Observed	12315	715	133	0	7	2169	608	24
$\langle\epsilon\sigma\rangle^{95}_{\text{obs}}$ [fb]	60	4.3	1.9	0.16	0.40	13	4.5	0.52
$\langle\epsilon\sigma\rangle^{95}_{\text{obs}}$ [fb] (⋆)	62	4.0	1.8	0.12	0.40	13	4.3	0.45
S^{95}_{obs}	1200	90	38	3.2	8.2	270	91	10
S^{95}_{obs} (⋆)	1300	80	37	2.5	8.1	270	87	9
S^{95}_{exp}	1700^{+600}_{-500}	110^{+40}_{-30}	32^{+11}_{-10}	$4.0^{+1.7}_{-0.7}$	$6.4^{+2.9}_{-1.3}$	240^{+90}_{-70}	103^{+34}_{-29}	16^{+6}_{-4}
S^{95}_{exp} (⋆)	1600^{+600}_{-400}	110^{+40}_{-30}	31^{+12}_{-8}	$4.1^{+2.4}_{-1.4}$	$6.3^{+3.2}_{-2.0}$	240^{+90}_{-70}	97^{+35}_{-25}	15^{+6}_{-4}
p_0 (Z)	0.50 (0.0)	0.49 (0.0)	0.29 (0.5)	0.50 (0.0)	0.24 (0.7)	0.35 (0.4)	0.50 (0.0)	0.50 (0.0)

Signal Region	SR4jt	SR4jt+	SR4jW	SR5j	SR5jt	SR6jl	SR6jm	SR6jt	SR6jt+
				MC expected events					
Diboson	0.34	–	2.1	16	0.32	9	4	1.6	0.21
Z/γ^*+jets	2.9	2.1	11	51	5	18	7	1.8	2.1
W+jets	1.2	0.75	6.1	54	5	26	12	2.1	3.4
$t\bar{t}$(+EW) + single-t	0.6	0.37	31	52	2.9	80	19	2.2	3.4
				Fitted background events					
Diboson	0.34 ± 0.17	–	2.1 ± 1.0	16 ± 8	0.32 ± 0.16	9 ± 4	4 ± 2	1.6 ± 0.8	0.2 ± 0.1
Z/γ^*+jets	$0.7^{+0.8}_{-0.7}$	$0.10^{+0.17}_{-0.10}$	5.9 ± 2.1	31 ± 8	1.7 ± 0.9	9 ± 4	3 ± 2	0.6 ± 0.6	$0.6^{+0.80}_{-0.6}$
W+jets	0.9 ± 0.4	0.6 ± 0.3	2.7 ± 1.6	28 ± 8	2.0 ± 1.5	15 ± 7	9 ± 5	1.2 ± 0.9	$0.3^{+1.2}_{-0.3}$
$t\bar{t}$(+EW) + single-t	0.6 ± 0.6	0.4 ± 0.3	3.2 ± 3.1	51 ± 9	3.0 ± 1.8	76 ± 7	16 ± 4	1.8 ± 0.6	3.7 ± 1.7
Multi-jets	–	–	–	$1.0^{+2.6}_{-1.0}$	$0.6^{+0.7}_{-0.6}$	$1.7^{+3.0}_{-1.7}$	$0.4^{+0.8}_{-0.4}$	$0.01^{+0.03}_{-0.01}$	$0.3^{+0.4}_{-0.3}$
Total bkg	2.5 ± 1.0	1.0 ± 0.4	14 ± 4	126 ± 13	8 ± 2	111 ± 11	33 ± 6	5.2 ± 1.4	4.9 ± 1.6
Observed	0	0	16	121	8	121	39	5	6
$\langle\epsilon\sigma\rangle^{95}_{\text{obs}}$ [fb]	0.15	0.17	0.68	1.7	0.40	1.9	1.2	0.32	0.39
$\langle\epsilon\sigma\rangle^{95}_{\text{obs}}$ [fb] (⋆)	0.12	0.12	0.63	1.6	0.38	1.8	1.1	0.30	0.36
S^{95}_{obs}	3.1	3.4	14	35	8.2	39	25	6.6	7.9
S^{95}_{obs} (⋆)	2.5	2.3	13	32	7.8	37	22	6.1	7.3
S^{95}_{exp}	$4.0^{+1.8}_{-0.9}$	$3.5^{+1.3}_{-0.5}$	11^{+5}_{-3}	37^{+13}_{-10}	$7.5^{+3.1}_{-2.0}$	31^{+12}_{-6}	20^{+6}_{-4}	$6.2^{+2.6}_{-1.3}$	$6.6^{+2.6}_{-1.6}$
S^{95}_{exp} (⋆)	$4.0^{+2.4}_{-1.4}$	$3.3^{+2.1}_{-1.2}$	11^{+5}_{-3}	35^{+13}_{-10}	$7.4^{+3.6}_{-2.3}$	30^{+12}_{-8}	18^{+7}_{-5}	$6.3^{+3.1}_{-2.0}$	$6.4^{+3.2}_{-2.0}$
p_0 (Z)	0.50 (0.0)	0.50 (0.0)	0.34 (0.4)	0.50 (0.0)	0.35 (0.4)	0.27 (0.6)	0.25 (0.7)	0.50 (0.0)	0.36 (0.4)

Table 5.10 · Numbers of events observed in the signal regions compared with background expectations obtained both from pure simulation and from the background-only fit at $\sqrt{s} = 8$ TeV. Empty cells correspond to estimates lower than 0.01. The p-values give the probabilities of the observations and the estimated backgrounds being consistent. The p-values are bounded to 0.5 and the gaussian sigmas (Z) equivalent to the p-values are given in the parentheses. The 95% confidence level upper limits on the visible cross section ($\langle\epsilon\sigma\rangle^{95}_{\text{obs}}$), the visible number of signal events (S^{95}_{obs}) and the number of signal events (S^{95}_{exp}) given the expected number of background events are shown obtained from both toy simulations and the asymptotic formula marked with (⋆).

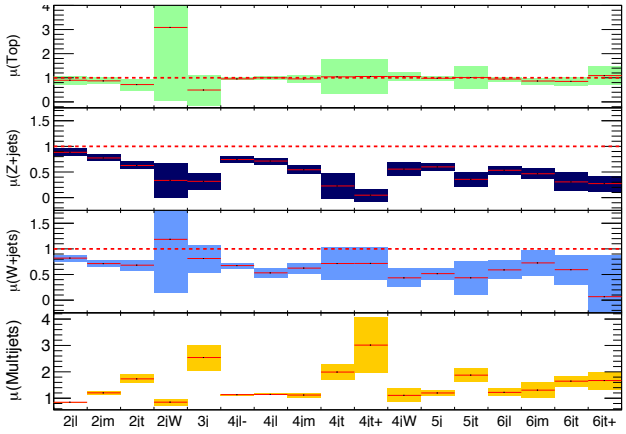

Fig. 5.21 · Normalisation factors for the four major backgrounds, μ(Top), $\mu(Z+\text{jets})$, $\mu(W+\text{jets})$, and μ(Multijets), obtained from the background-only fit at $\sqrt{s} = 8$ TeV as a function of the signal regions. The normalistion factors for the multijet background are corrections to the preliminary normalisation to pseudo-data and should therefore not be compared to unity.

Effect of the Systematic Uncertainties

The systematic uncertainties described in Section 5.7 all contribute to the total uncertainty on the estimated number of background events from the fit. The different sources of uncertainties contribute with different strength to the total uncertainty. A breakdown of the systematic uncertainties and their fractional contribution to the total uncertainty is given in Table 5.11. The total uncertainty on the estimated number of background events is ranging from 61% in the 2jW-region to 7% in the 2jm-region.

Some of the major contributions to the total uncertainty in all signal regions are the uncertainties on the normalisation factors, μ_X. The uncertainties on the normalisation factors cover both statistical uncertainties in the control regions and uncertainties related to the specific background, e. g. uncertainties on b-tagging in CRW and CRT and the $\gamma+$jets normalisation factor, κ. The uncertainties on the transfer factors are dominated by different uncertainties depending on the tightness of the signal region. In the tighter signal regions, the uncertainties on μ_X are dominated by the low statistics in the control regions while they are dominated by other source of uncertainties in the looser signal regions.

The diboson background is not estimated using a specific control region, but instead through simulation studies resulting in a conservative uncertainty of 50%. The uncertainty is applied on the diboson contribution in the signal and control regions. This leads to a large contribution to the total uncertainty in most signal regions. The flat uncertainty on the diboson background feeds into the uncertainties on the normalisation factors as well and thereby has a bigger effect.

The theory uncertainties on the $Z+$jets, $W+$jets, and Top background cover the comparison of two different generators. The comparison of the $Z+$jets samples generated with SHERPA and

Channel	2jl	2jm	2jt	2jW	3j	4jl-	4jl	4jm
Total bkg	13000	760	125	2.2	5.1	2120	630	37
Total bkg unc.	1000	50	10	1.5	1.3	120	50	6
$\Delta\mu_{\text{Multi-jets}}$	1.3	0.02	0.1	–	0.1	0.05	0.02	–
$\Delta\mu_{\text{Top}}$	310	7	2.2	0.4	0.5	40	14	0.6
$\Delta\mu_{\text{W+jets}}$	400	19	6	0.9	0.8	50	25	1.6
$\Delta\mu_{\text{Z+jets}}$	500	40	7	0.4	0.9	60	22	2.6
MC statistics	130	6	2.1	0.34	0.35	18	6	1.3
Jet/MET	140	8	0.7	0.27	0.24	40	7	0.15
Leptons	80	2.5	0.6	0.04	0.06	20	5	0.27
Theory Z+jets	800	5	4	0.03	0.29	0.16	18	2.4
Theory W+jets	270	10	1.4	0.1	0.35	33	7	2.3
Theory Top	13	1.8	0.11	0.9	0.05	29	12	1.6
Theory Diboson	400	40	6	0.2	0.18	90	34	4
Theory scales unc.	90	4	0.7	0.11	0.12	23	7	0.4
Multijets method	140	1.4	0.4	0.04	0.06	4	1.6	–
Other	30	0.5	0.4	0.25	0.02	2.0	3.1	0.2

Channel	4jt	4jt+	4jW	5j	5jt	6jl	6jm	6jt	6jt+
Total bkg	2.5	1.0	14	126	7.6	111	33	5.2	4.9
Total bkg unc.	1.0	0.4	4	16	1.9	15	6	1.4	1.7
$\Delta\mu_{\text{Multi-jets}}$	–	–	–	0.09	0.08	0.21	0.1	–	0.05
$\Delta\mu_{\text{Top}}$	0.5	0.27	0.5	5	1.4	7	2.7	0.4	1.3
$\Delta\mu_{\text{W+jets}}$	0.4	0.24	1.1	6	1.5	5	3.0	0.6	0.9
$\Delta\mu_{\text{Z+jets}}$	0.7	0.17	1.4	4	0.7	1.6	0.8	0.33	0.32
MC statistics	0.26	0.1	0.7	2.8	0.4	2.8	1.5	0.7	0.4
Jet/MET	0.06	0.06	0.6	4	0.23	6	1.2	0.5	0.29
Leptons	0.08	0.04	0.06	1.8	0.21	1.8	0.7	0.05	0.32
Theory Z+jets	0.4	0.06	1.3	7	0.5	3.0	2.0	0.5	0.7
Theory W+jets	0.07	0.23	0.9	2.2	0.18	1.7	2.8	0.4	0.07
Theory Top	0.4	0.19	2.8	5	0.6	2.7	4	0.08	0.5
Theory Diboson	0.17	–	1.0	8	0.16	4	1.9	0.8	0.1
Theory scales unc.	0.13	0.022	0.12	2.5	0.022	1.1	0.8	0.11	0.6
Multijets method	–	–	–	2.6	0.7	2.9	0.8	0.032	0.4
Other	0.05	0.04	0.12	0.15	0.04	2.2	0.7	0.1	0.04

Table 5.11 · Breakdown of the dominant systematic uncertainties on the background estimates at $\sqrt{s} = 8$ TeV. The individual uncertainties can be correlated, and do not necessarily add up quadratically to the total background uncertainty. Uncertainties on the normalisation factors, $\Delta\mu$, include both the statistical uncertainties in the control region and the systematic uncertainties entering a specific control region. The pink bar shows the fraction of the uncertainty on the total event yield. The purple bar shows the fraction of the specific systematic uncertainty compared to the total uncertainty.

ALPGEN is one of the major contributions to the total uncertainty in many signal regions. This is expected since Z+jets is a dominating background in many signal regions. In signal regions requiring W-candidates, the contribution from the theoretical uncertainty on the top background is larger than in the other regions since the top background is more dominant in those regions. The contribution to the total uncertainty coming from varying the scales of the Monte Carlo sample generation as well as the uncertainties coming from the data-driven method for estimating the multijet background are minor in most signal regions with the largest contributions in the 6jt+-region.

The contribution from the uncertainty arising from the finite size of the Monte Carlo samples is as expected more dominant in the signal regions with tighter cuts.

The experimental uncertainties such as the resolution and scale of $E_{\mathrm{T}}^{\mathrm{miss}}$, JER, JES, lepton identification, are in most signal regions minor compared to the theoretical uncertainties and the uncertainties on the transfer factors.

5.9 Model-dependent Limits

Since no significant excesses were found in any of the signal regions, exclusion limits on the SUSY models described in Section 5.1 are studied. The limits are found using the method described in Section 4.4.4.

5.9.1 Limits on Simplified Models

The limits at 95% confidence level (CL.) on simplified models with direct decays are shown in Figure 5.22 together with the limit at $\sqrt{s} = 7$ TeV obtained by the ATLAS experiment [240] where it is available. The areas within the solid red contours are excluded. The strongest signal region is shown in each point of the SUSY parameter spaces.

Figure 5.22a shows the limit on squark-pair production with the first two generations of squarks being light (8 degenerate $\tilde{q}$s), and with only a single squark being light (1 non-degenerate $\tilde{q}$). It is seen that for a high $m_{\tilde{q}}$, the strongest signal region is 2jt, while at high mass-compression ($\Delta(m_{\tilde{q}}, m_{\tilde{\chi}_1^0})$ is small), the strongest signal region is 2jm. Along the limit at $m_{\tilde{\chi}_1^0} \sim 400$ GeV and $m_{\tilde{q}} \sim$ 500-700 GeV, 4jl takes over as the strongest signal region. The limit of $m_{\tilde{q}}$ when the LSP is massless reaches 910 GeV when 8 squarks are degenerate, and 470 GeV when there is only one light squark. The limit on $m_{\tilde{\chi}_1^0}$ flattens at $\sim$ 380 GeV and decreases only slightly with increasing $m_{\tilde{q}}$.

The limit on squark-gluino production is seen in Figure 5.22b. The strongest signal region at high $m_{\tilde{g}}$ is 3j, while 2jt and 4jm take over as the mass difference between $m_{\tilde{g}}$ and $m_{\tilde{\chi}_1^0}$ decreases. At high mass-compression, 2jm is the strongest signal region. The limit on the mass of the gluino in this model reaches 1575 GeV when the LSP is massless, while the limit on the mass of the LSP reaches a plateau at 750 GeV until $m_{\tilde{g}}$ reaches 1200 GeV.

The limit on the simplified model with gluino-pair production and direct decay is shown in Figure 5.22c. The strongest signal region at high mass-compression is 2jm. At lower mass-compression, 5j and 6jt+ take over. When $\tilde{\chi}_1^0$ is massless, 4jt is the strongest region. The bump in

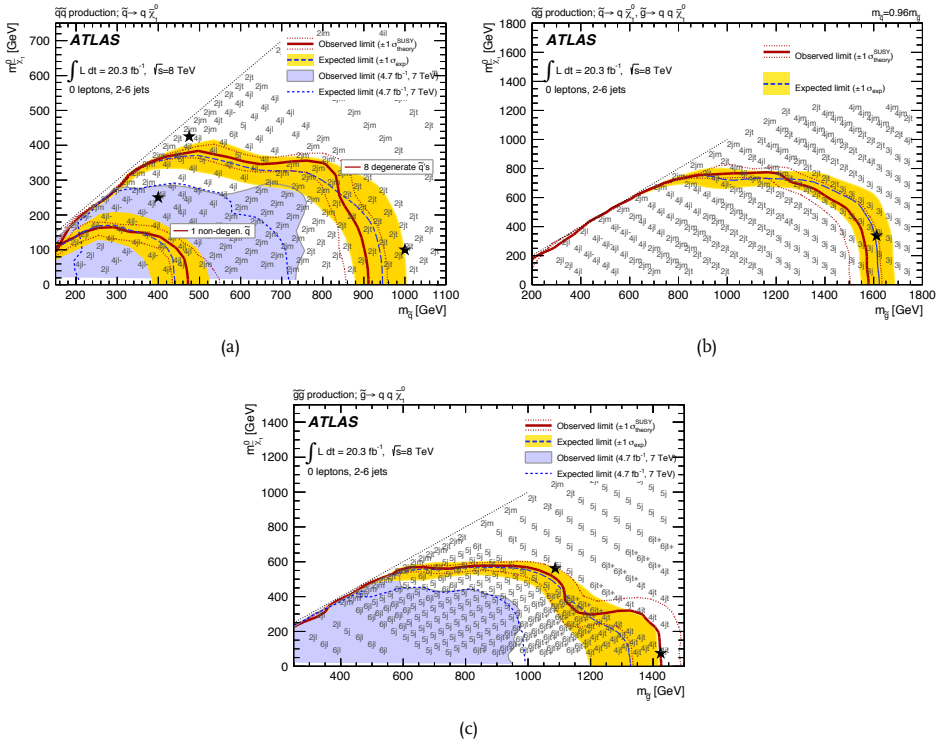

Fig. 5.22 · Expected (blue) and observed (red) exclusion limits at 95% CL on simplified models of $\tilde{q}\tilde{q}$ (a), $\tilde{q}\tilde{g}$ (b), and $\tilde{g}\tilde{g}$ (c) production with direct decays in the plane of $m_{\tilde{q},\tilde{g}}$ and $m_{\tilde{\chi}_1^0}$ at $\sqrt{s} = 8$ TeV. The strongest signal region in each point is shown. The shaded blue area shows the limit at $\sqrt{s} = 7$ TeV [240] where it is available. The yellow band indicates the 1σ uncertainty on the limit arising from the experimental, and background-only theoretical uncertainties. The dashed red lines indicate the 1σ uncertainty on the signal cross section. The limit of $\tilde{q}\tilde{q}$ production is shown both with 8 degenerate, light squarks, and with 1 non-degenerate, light squark.

the observed limit compared to the expected limit at high $m_{\tilde{g}}$ is caused by the 0 observed events in the 4jt signal region. The limit on $m_{\tilde{g}}$ reaches 1425 GeV when $\tilde{\chi}_1^0$ is massless. The limit on $m_{\tilde{\chi}_1^0}$ is 550 GeV when $m_{\tilde{g}}$ is in the range from 600 GeV to 1050 GeV.

In general, it is seen in Figure 5.22 that the limits along the low mass-splitting ($m_{\tilde{q},\tilde{g}} \sim m_{\tilde{\chi}_1^0}$) are not as strong as the limits at a higher mass-splitting. This is because this compressed area of the parameter space is especially hard to discover or exclude. The low difference of the masses results in low energy of the jets and low $E_{\mathrm{T}}^{\mathrm{miss}}$, making it very hard to distinguish the signal from the overwhelming Standard Model background.

The observed and expected limits at 95% CL. on simplified models of squark-pair and gluino-pair production with one-step decays are shown in Figure 5.23 together with the observed limit

obtained with the data collected at $\sqrt{s} = 7$ TeV [240]. In each signal point, the strongest signal region is shown.

Two different scans are done in both models with $\tilde{q}\tilde{q}$ and $\tilde{g}\tilde{g}$ production as described in Section 5.1.1. The limits of squark- and gluino-pair production where $m_{\tilde{\chi}_1^0}$ is constant are shown in Figure 5.23a and 5.23b, respectively. It is seen that when $x \approx 1$, i. e. when $m_{\tilde{\chi}_1^\pm} \approx m_{\tilde{q},\tilde{q}}$, the strongest regions are the regions targeting boosted W bosons, 2jW and 4jW, designed to be specifically sensitive to this mass scenario. The limit on the mass of the squark mass reaches 760 GeV when $x = 0.5$-0.8, while the limit on the gluino mass reaches 1325 GeV when $x \approx 1$. The limit on the squark mass decreases at other values of x with a minimum at $x = 0.2$ of 520 GeV. The limit on $m_{\tilde{g}}$ reaches a minimum at $x = 0.1$ of 1100 GeV. The limit on the mass of the squark and on the mass of the gluino reaches 750 GeV and 1300 GeV, respectively, when $m_{\tilde{\chi}_1^0} \approx 50$ GeV in the simplified model with the parameter scan where the mass of $\tilde{\chi}_1^\pm$ is fixed to $m_{\tilde{\chi}_1^\pm} = (m_{\tilde{q},\tilde{g}} + m_{\tilde{\chi}_1^0})/2$. Along the diagonal, the limit on the LSP mass reaches 340 GeV and 550 GeV in the $\tilde{q}\tilde{q}$ and $\tilde{g}\tilde{g}$ model, respectively. There are no points generated at a gluino mass of 200 GeV in the scan with $x = 0.5$ and it does therefore appear not to be excluded. The point is however excluded by the 7 TeV analysis.

The analysis is not sensitive to some of the signal points at low squark masses ($m_{\tilde{q}} \sim 200$ GeV) and at $x \sim 0.3$-0.8 in the model where $m_{\tilde{\chi}_1^0} = 60$ GeV causing the kinks in the limit that can be seen in Figure 5.23a. A similar effect is seen in the shaded blue area which shows the limit obtained using data collected at $\sqrt{s} = 7$ TeV.

It seen that the limits at $\sqrt{s} = 8$ TeV on the simplified models have expanded considerably compared to the limits obtained at $\sqrt{s} = 7$ TeV with up to a $\sim$ 500 GeV gain in the $\tilde{g}\tilde{g}$-model with direct decay.

5.9.2 Limits on MSUGRA/CMSSM

The expected and observed limits at 95% CL. of the MSUGRA/CMSSM model described in Section 5.1.2 with $\tan\beta = 30$, $A_0 = -2m_0$, and $\mu > 0$ are shown in Figure 5.24. The green area in the plot indicates the part of the m_0-$m_{1/2}$ parameter space where the stau, $\tilde{\tau}$, is the LSP. If the LSP is a candidate for Dark Matter it cannot be electrically charged, unlike the stau. This area is therefore excluded. Masses of the lightest Higgs boson, the squarks, and the gluinos are indicated by magenta and grey dashed lines.

The limit on $m_{1/2}$ is strongest for low value of m_0 where it reaches 810 GeV. Squarks and gluinos with equal masses are excluded up to 1650 GeV. The analysis has no sensitivity when $m_0 > 2000$ GeV and $m_{1/2} > 500$ GeV corresponding to gluino masses between 1200 GeV and 1400 GeV and squark masses of 2200 GeV.

5.9.3 Limits on Left-handed Squark-pair Production

The limits on left-handed squark pair production in the pMSSM model are shown in Figures 5.25 and 5.26. They are presented in the parameter planes of $m_{\tilde{q}}$ and $m_{\tilde{\chi}_1^\pm/\tilde{\chi}_2^0}$ or $m_{\tilde{q}}$ and $m_{\tilde{\chi}_1^0}$ depending on the scan on M_1 and M_2 for three gluino masses . The strongest signal region, i. e. the

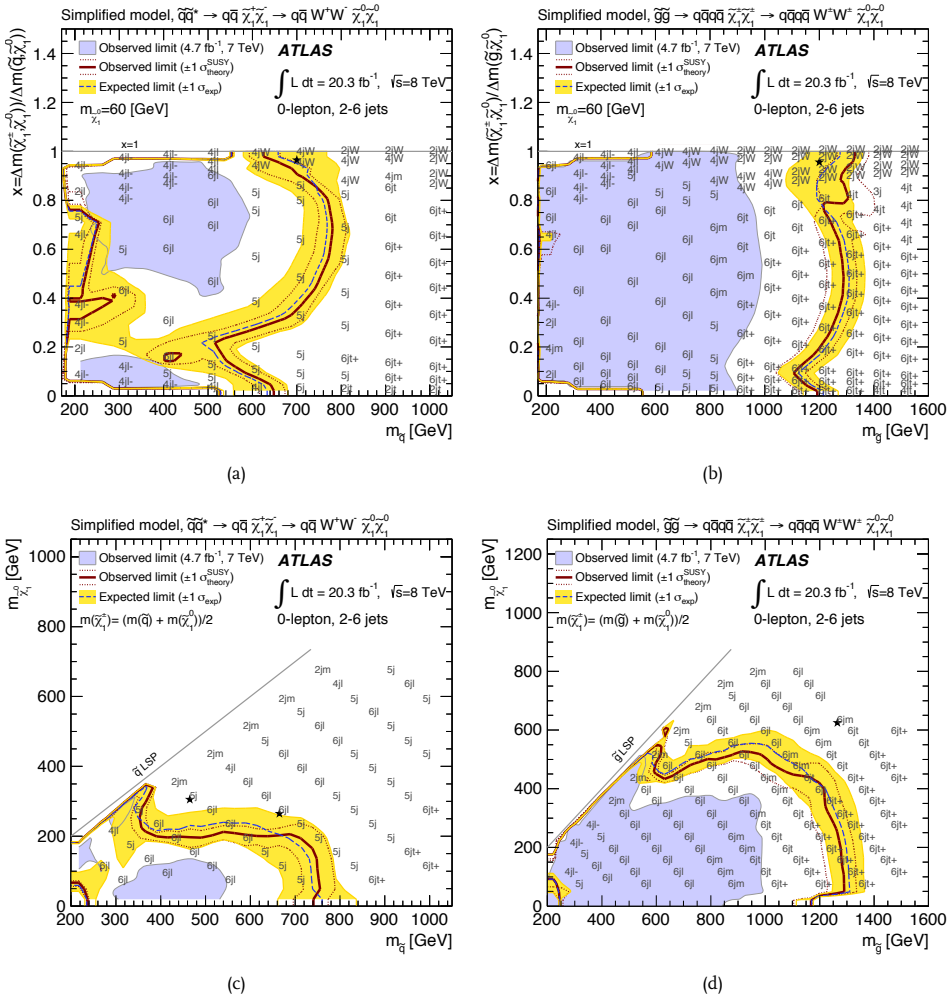

Fig. 5.23 · Expected (blue) and observed (red) exclusion limits at 95% CL on simplified models of $\tilde{q}\tilde{q}$ ((a) and (c)), and $\tilde{g}\tilde{g}$ ((b) and (d)) production with one-step decays at $\sqrt{s} = 8$ TeV. The limits are shown either in the $m_{\tilde{q},\tilde{g}}$-$m_{\tilde{\chi}_1^0}$-plane (when $m_{\tilde{\chi}_1^\pm} = (m_{\tilde{q},\tilde{g}} + m_{\tilde{\chi}_1^0})/2$) or in the $m_{\tilde{q},\tilde{g}}$-x-plane where $x = \Delta m(\tilde{\chi}_1^\pm;\tilde{\chi}_1^0)/\Delta m([\tilde{q},\tilde{g}];\tilde{\chi}_1^0)$ (when $m_{\tilde{\chi}_1^0} = 60$ GeV). The strongest signal region in each point is shown. The shaded blue areas show the limit at $\sqrt{s} = 7$ TeV [240]. The yellow band indicates the 1σ uncertainty on the limit arising from the experimental, and background-only theoretical uncertainties. The dashed red lines indicate the 1σ uncertainty on the signal cross section.

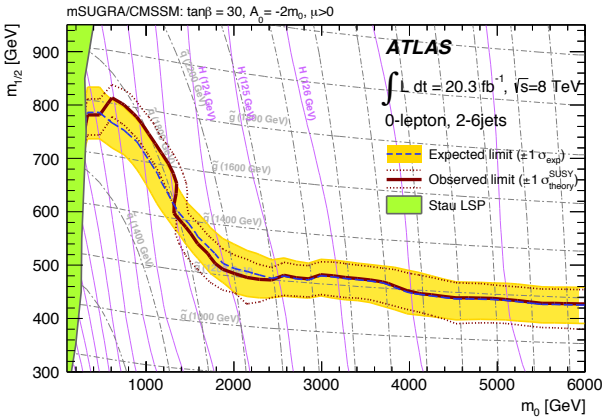

Fig. 5.24 · Expected (blue) and observed (red) exclusion limits at 95% CL. of an MSUGRA/CMSSM model with $\tan\beta = 30$, $A_0 = -2m_0$, and $\mu > 0$ presented in the m_0-$m_{1/2}$-plane. The green area indicates the part of parameter space, where the LSP is a stau ($\tilde{\tau}$). Mass-lines of gluino and squarks are shown by dashed, light blue lines, while the mass-lines of the lightest Higgs boson are shown in magenta. The yellow band indicate the 1σ uncertainty on the limit arising from the experimental, and background-only theoretical uncertainties. The dashed red lines indicate the 1σ uncertainty on the signal cross section.

signal region with the lowest CL_s-value, in each point of the parameter space is shown as well as the excluded cross section times branching fraction.

In general, it is seen that the strongest signal regions have high jet multiplicities ($n_{\text{jet}} \geq 4$) and tight cuts on m_{eff}(incl.). The signal regions that were added to the analysis to increase the exclusion reach for this specific model, 4jt+ and 5jt, are among the strongest signal regions along the limits. The two signal regions designed to be sensitive to events with high compression of the mass of $\tilde{\chi}_1^{\pm}$ or $\tilde{\chi}_2^0$ as well as boosted W bosons, 2jW and 4jW, do not show up, as the mass compression is not high enough in any of the signal points. In points where 4jt or 4jt+ are the strongest signal regions, the observed limit is stronger than the expected due to fewer observed events than expected.

The upper limit on the production cross section decreases with increasing squark mass. The excluded cross section does not depend strongly on the gluino mass which is seen by comparing the upper limits for given squark mass and $\tilde{\chi}_1^0$ or $\tilde{\chi}_2^0/\tilde{\chi}_1^{\pm}$ mass. It is not surprising as the change of gluino mass results in a change in the production cross section. The strongest signal region will therefore most likely remain the same independent of the gluino mass. The product of the signal acceptance and the reconstruction efficiency in the signal regions does not depend on the mass of the gluino either. This results in the excluded cross section being more or less the same regardless of gluino mass.

Figure 5.25a and 5.26a show the limits with a gluino mass of 1.6 TeV in the two parameter scans where either $M_1 = 60$ GeV and M_2 is varied independently or both M_1 and M_2 are varied, but restricted to $M_2 = (M_1 + m_{\tilde{q}_L})/2$. The exclusion limit reaches a squark mass of 1500 GeV

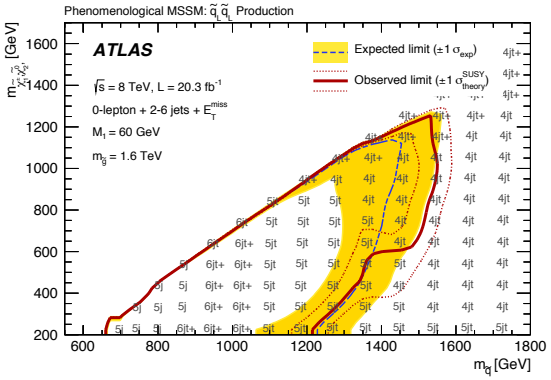

(a)

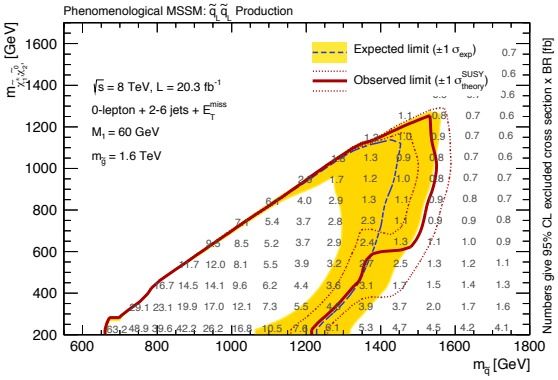

(b)

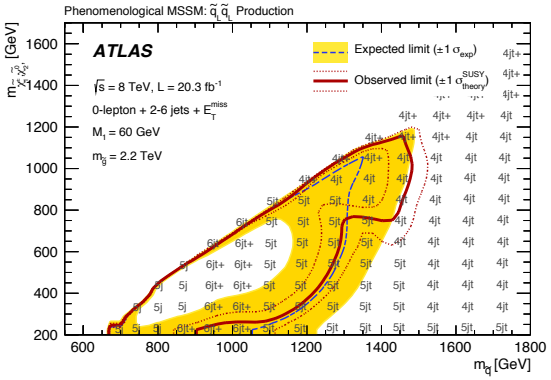

(c)

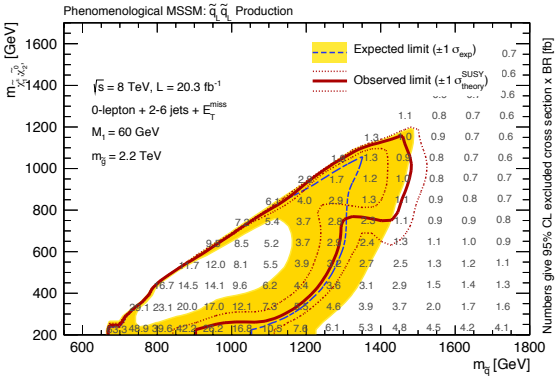

(d)

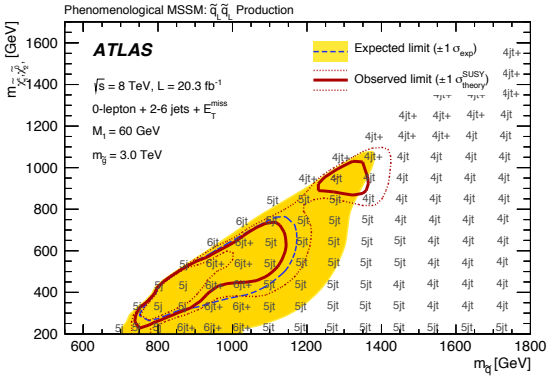

(e)

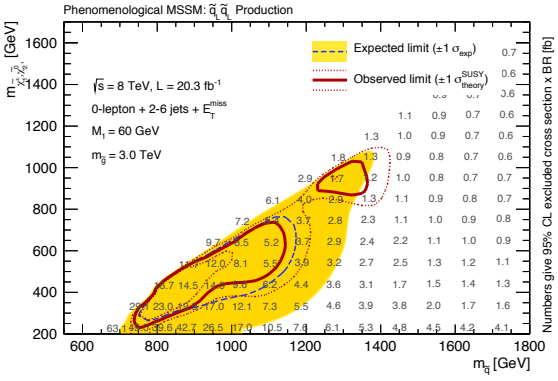

(f)

Fig. 5.25 · Expected (blue) and observed (red) exclusion limits at 95% CL on a pMSSM model with left-handed squark-pair production where $M_1 = 60$ GeV. The exclusion limits are shown with three gluino masses: $m_{\tilde{g}} = 1600$ GeV ((a) and (b)), $m_{\tilde{g}} = 2200$ GeV ((c) and (d)), and $m_{\tilde{g}} = 3000$ GeV ((e) and (f)). The limits are shown in the $m_{\tilde{q}}$-$m_{\tilde{\chi}_1^\pm,\tilde{\chi}_2^0}$-plane. The limits are shown with the strongest signal region in each point ((a), (d), and (e)) and with the upper limit on the cross section per point ((b), (d), and (f)). The yellow band indicates the 1σ uncertainty on the limit arising from the experimental, and background-only theoretical uncertainties. The dashed red lines indicate the 1σ uncertainty on the signal cross section.

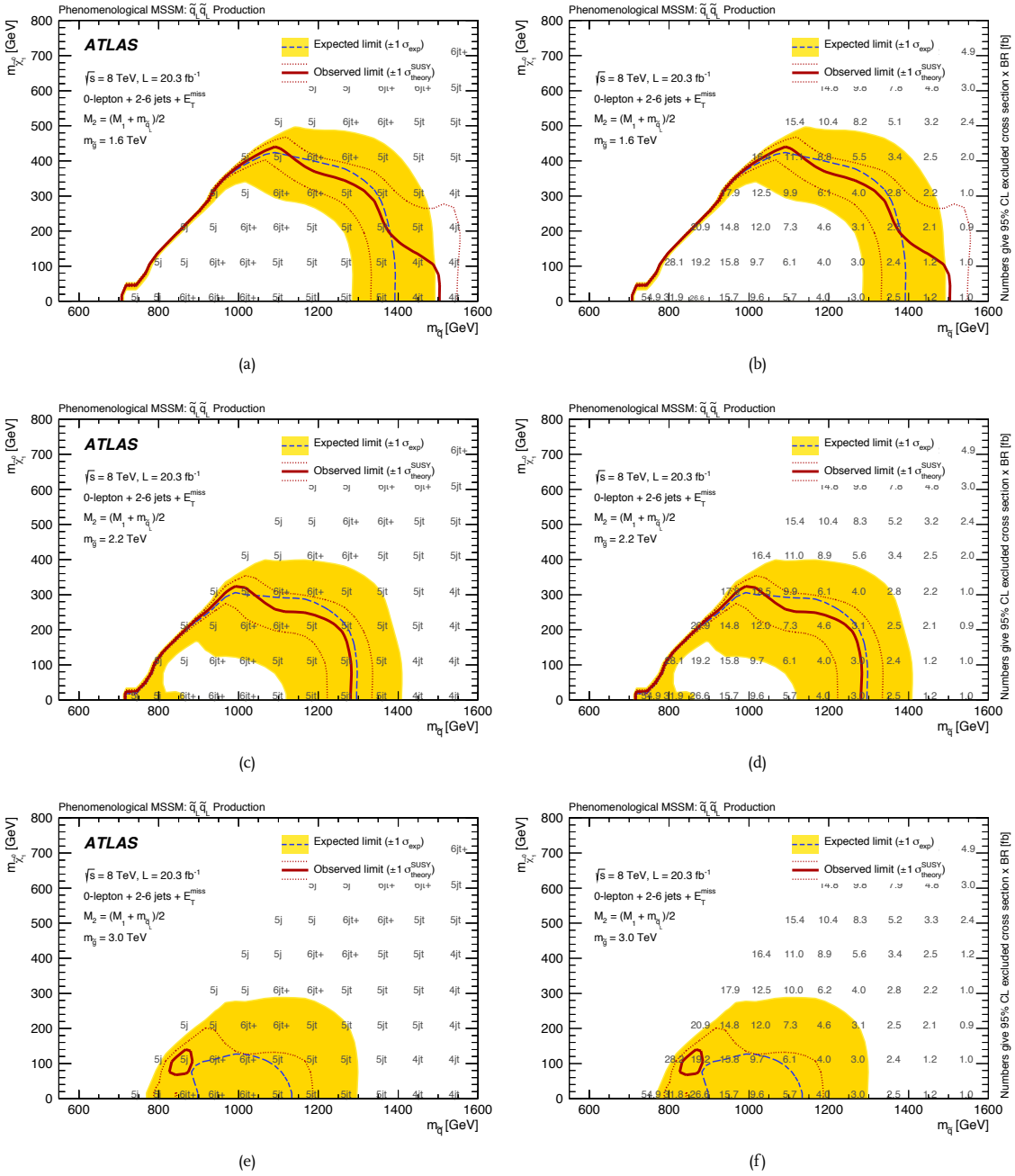

Fig. 5.26 · Expected (blue) and observed (red) exclusion limits at 95% CL on a pMSSM model with left-handed squark-pair production where $M_2 = (M_1 + m_{\tilde{q}_L})/2$. The exclusion limits are shown with three gluino masses: $m_{\tilde{g}} = 1600$ GeV ((a) and (b)), $m_{\tilde{g}} = 2200$ GeV ((c) and (d)), and $m_{\tilde{g}} = 3000$ GeV ((e) and (f)). The limits are shown in the $m_{\tilde{q}}$-$m_{\tilde{\chi}_1^0}$-plane. The limits are shown with the strongest signal region in each point ((a), (d), and (e)) and with the upper limit on the cross section per point ((b), (d), and (f)). The yellow band indicates the 1σ uncertainty on the limit arising from the experimental, and background-only theoretical uncertainties. The dashed red lines indicate the 1σ uncertainty on the signal cross section.

either for high values or $m(\tilde{\chi}_1^{\pm}/\tilde{\chi}_2^0)$ or low values of $m(\tilde{\chi}_1^0)$ depending on the parameter scan. Masses of $\tilde{\chi}_1^{\pm}$ or $\tilde{\chi}_2^0$ ranging from 600 GeV to 1250 GeV are excluded when the mass of the squark is 1500 GeV in the scan where $M_1 = 60$ GeV. The limit on $m_{\tilde{\chi}_1^0}$ reaches 450 GeV when the mass of the squarks is 1100 GeV. As expected, the limits decrease with increasing gluino mass reflecting the effect of the gluino mass on the production cross section as discussed in Section 5.1.3. This is seen most clearly in Figure 5.25e and 5.26e showing very limited exclusion power.

5.10 Outlook

In this chapter a search for supersymmetry in events with many jets, missing transverse momentum, and without any leptons (e, μ) is presented. It is shown that it is sensitive to both "complex" as well as simplified SUSY Models containing squark and gluino production. Limits in simplified models with direct and one-step decays of squarks and gluinos, a MSUGRA/CMSSM model, and a pMSSM model with left-handed squark-pair production were shown. To conclude this chapter, a few possibilities of improving the sensitivity of the models included in the analysis, especially the pMSSM model, will be presented.

A more precise estimate of the backgrounds in the signal region would lead to a higher sensitivity to all models. If the uncertainty could be decreased, it would therefore mean a gain in exclusion power. The dominant systematic uncertainties in most signal regions are the theory uncertainty on the diboson background and the uncertainties related to the Z+jets estimate. As discussed earlier, the uncertainty on the diboson background is a very conservative upper estimate not related to any observation in control regions. If instead the diboson background could be estimated from a control region, the uncertainty would most likely decrease compared to the current, conservative estimate. The uncertainties related to the Z+jets background estimate arise partly from lack of statistics and partly from the normalisation factor, κ, used to normalise the LO γ+jets cross section to the NNLO cross section of Z+jets. An alternative control region for estimating the Z+jets background could be the VRZ validation region, but due to low statistics in that region it was not found suitable as a control region.

The final state of the simplified models with one-step decays contain the decay-products of a W boson. Since the branching fraction of a W boson into a lepton and a neutrino is $\sim 1/9$ per lepton species, an analysis selecting events with an electron or a muon will be sensitive to this model as well. Such an analysis selecting events with an electron or a muon has been published by ATLAS [242]. Furthermore, an analysis selecting events with electrons or muons will be orthogonal to the analysis presented in this chapter and the two analyses could be statistically combined with a joint profile likelihood function taking into account the correlation on some of the systematic uncertainties. This has been done for several SUSY models where both analyses had published their limits [2]. The increase in sensitivity of the simplified models with one-step decays compared to the reach of each analysis separately can be seen in Figure 5.27.

The pMSSM model with left-handed squarks has a final-state similar to the simplified models with one-step decay. A combination of the 0- and 1-lepton analyses could have been performed on this model as well, but due to time constraints it was not included in the combinations.

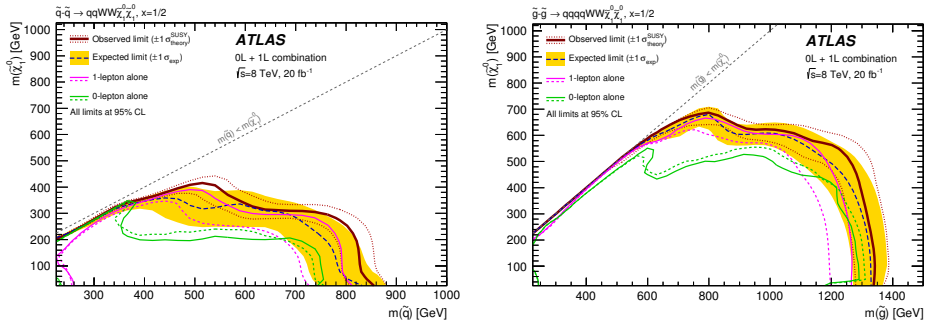

(a) (b)

Fig. 5.27 · Expected (blue) and observed (red) exclusion limits at 95% CL on simplified models of $\tilde{q}\tilde{q}$ (a), and $\tilde{g}\tilde{g}$ (b) production with one-step decays obtained by a statistical combination of the 0- and 1-lepton analyses. The limits are presented in the $m_{\tilde{q},\tilde{g}}$-$m_{\tilde{\chi}_1^0}$-plane with $m_{\tilde{\chi}_1^\pm} = (m_{\tilde{q},\tilde{g}} + m_{\tilde{\chi}_1^0})/2$. The green and magenta lines indicate the reach of each analysis separately. The yellow band indicates the 1σ uncertainty on the limit arising from the experimental, and background-only theoretical uncertainties. The dashed red lines indicate the 1σ uncertainty on the signal cross section. The Figure is taken from Ref. [2].

Another possible way of improving the sensitivity to the pMSSM model, could be to select events with hadronically decaying bosons much like the selection of the boosted W bosons in the 2jW and 4jW signal regions. By making requirements on the invariant mass of jet pairs in mass-windows around the boson masses, events with bosons can be selected. Since the vast majority of the squarks in this SUSY model decay into final states with bosons, selecting events with bosons will likely increase the sensitivity.

The mSUGRA/CMSSM model with $\tan\beta = 30$, $A_0 = -2m_0$, and $\mu > 0$ is a "complex" SUSY model with production of many different sparticles and many available decay chains for each type of sparticle. A wide range of analyses targeting different final states will therefore be sensitive to this model. In Figure 5.28, the expected and observed limits are presented of all the analyses published by ATLAS that are sensitive to this model. The best limit is found in a similar fashion to how the limits are obtained with multiple signal regions: a simple or-ing of the expected sensitivity of the analyses is performed choosing the strongest one in each point. It is seen that at low values of m_0, the statistical combination of the 0- and 1-lepton analyses places the strongest expected limit. At values of $m_0 > 2000$ GeV, an analyses selecting events with 0 or 1 lepton and multiple b-jets takes over as the strongest analysis. This is because at higher values of m_0, the stop ($\tilde{t}$) is expected to be lighter and an analyses selecting b-jets will therefore be more sensitive.

The mSUGRA/CMSSM models was a very popular model framework in the searches for supersymmetry at the LHC. It is appealing because of its low number of free parameters. However, with the non-observation of any excesses in data, the limits get stronger and stronger making mSUGRA/CMSSM a less likely SUSY scenario. This does not imply that supersymmetry no longer poses an appealing set of models that could potentially solve theoretical concerns in the Standard

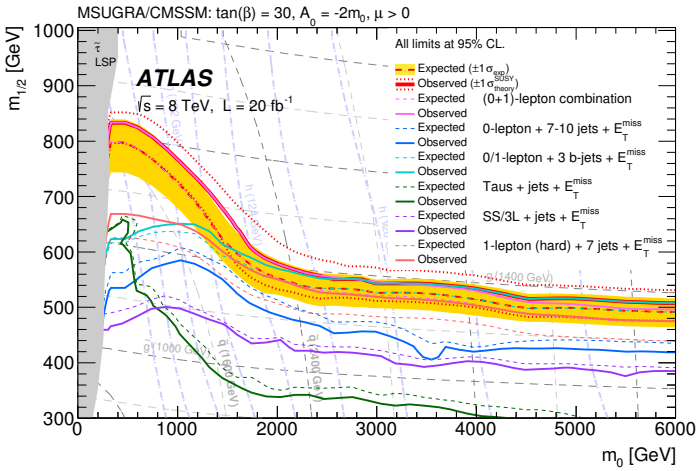

Fig. 5.28 · Best expected (red, dashed) and observed (red, solid) exclusion limits at 95% CL. of all ATLAS analyses placing limits on the MSUGRA/CMSSM model with $\tan\beta = 30$, $A_0 = -2m_0$, and $\mu > 0$ presented in the m_0-$m_{1/2}$-plane. The expected (dashed) and observed (solid) limits of the individual analyses are shown in various colours. The 0- and 1-lepton analyses are shown in combination. The grey area indicates the part of parameter space, where the LSP is a stau ($\tilde{\tau}$). Mass-lines of gluino and squarks are shown by dashed, grey lines, while the mass-lines of the lightest Higgs boson are shown in light blue. The yellow band indicates the 1σ uncertainty on the limit arising from the experimental, and background-only theoretical uncertainties. The dashed red lines indicate the 1σ uncertainty on the signal cross section. The figure is taken from Ref. [2].

Model. This only means that supersymmetry is probably not present in its simpler forms such as the MSUGRA/CMSSM model presented in this chapter.

The largest improvement in sensitivity to all the models would obviously be if the production cross section of squarks and gluinos could increase leading to a larger expected signal yield. Since the squarks and gluinos considered in this analysis are heavy (≈ 1 TeV), an increase in the energy of the proton collisions would lead to a large increase in the cross section. This is of course a very technical collider improvement beyond the scope of the ATLAS detector, but with the restart of the LHC in 2015 and the increase in collision energy from 8 TeV to 13 TeV, a new part of the SUSY phase space is open for exploration.

6

Searching for Squarks and Gluinos at $\sqrt{s} = 13$ TeV

The Large Hadron Collider was shut down in December 2012 after having delivered beams for a few years at a collision energy of $\sqrt{s} = 7$ and 8 TeV. The planned shutdown lasted for two years where repairs, checks, and updates were performed on both experiments and collider. In the Spring of 2015, the LHC turned on again with an increased collision energy of $\sqrt{s} = 13$ TeV compared to the collision energy in 2012 of $\sqrt{s} = 8$ TeV.

An increase in collision energy opens a new door to a yet un-explored energy at High Energy Physics colliders, where the Standard Model will be tested and physics beyond the Standard Model might show its face.

Previous searches for squarks and gluinos place limits on squark and gluino masses of 910 GeV and 1425 GeV, respectively, in simplified models with direct decay. In the search for supersymmetry presented in this chapter, the masses of the sparticles are therefore high ($\sim$ 800 - 1400 GeV) in most of the models used in optimising the signal regions. An increase in collision energy will result in an increase of the heavy sparticle production cross section as well as an increase in the production cross section of the Standard Model background processes.

In this chapter a search for simplified models of squark and gluino production in events with jets and missing transverse momentum performed on the 3.2 fb^{-1} of proton-proton collisions at $\sqrt{s} = 13$ TeV collected by the ATLAS experiment in 2015 is presented. The selection and method of the analysis presented in this chapter is in many ways very similar to the analysis presented in Chapter 5. The work presented in this chapter has been published in Ref. [3].

6.1 Squark and Gluino Production at $\sqrt{s} = 13$ TeV

The search for squarks and gluinos at $\sqrt{s} = 8$ TeV presented in Chapter 5 placed limits beyond 1 TeV on the masses of squarks and gluinos in simplified models. The production cross section of particles with masses greater than 1 TeV increases with an increase of the collision energy, thereby increasing the sensitivity of such heavy particles.

As the energy of the protons increases, the parton distribution functions change resulting in an increase in the probability of a hard scattering at high energies to occur. This can be seen by

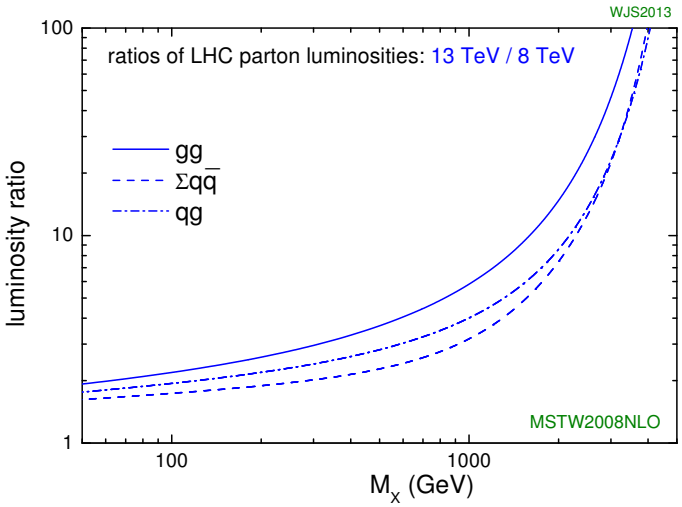

Fig. 6.1 · The parton luminosity ratios of proton-proton collisions at $\sqrt{s} = 13$ TeV compared to $\sqrt{s} = 8$ TeV as a function of the energy of the hard scattering, M_X, using gluon-gluon (solid), quark-antiquark (dashed), and quark-gluon (dash-dotted) PDFs from MSTW2008NLO [34]. The Figure is taken from Ref. [243].

comparing the parton luminosity as a function of the energy of the hard collision, M_X, at two energies. The parton luminosity is related to the probability of the occurrence of a hard scattering in the interaction of two partons, e. g. two gluons, a quark and an antiquark, or a quark and a gluon, and is thus related to the parton distribution functions. In Figure 6.1, the ratios of the parton luminosity at $\sqrt{s} = 8$ TeV and $\sqrt{s} = 13$ TeV of gg, $\sum q\bar{q}$, and qg are shown and it can be seen that they increase rapidly with higher M_X. The increase in the parton luminosity of gluon-gluon interaction is the largest. This is expected as the parton distribution function of the gluon increases more than the ones of the quarks and anti-quarks.

In Figure 6.2, the production cross section of squark-antisquark (6.2a) and gluino pairs (6.2b) calculated at two collision energies, $\sqrt{s} = 8$ TeV (blue) and $\sqrt{s} = 13$ TeV (pink), are shown. The cross sections of squark-pair production are calculated assuming that the gluinos are decoupled, and the cross section of gluino-pair production is calculated assuming the squarks to be decoupled. All cross sections are calculated at (NLL+NLO) using NLLFAST [210–214], except the cross sections of squark-pair production at $\sqrt{s} = 8$ TeV that are calculated at next-to-leading order with PROSPINO [218].

By comparing the production cross sections of squark- and gluino-pairs at $\sqrt{s} = 8$ TeV and $\sqrt{s} = 13$ TeV, it is seen that it increases by factors ranging from ~ 10 at low $m_{\tilde{q}/\tilde{g}}$ to ~ 1000 at higher masses. As squarks and gluinos are produced from gluon-pairs or quark-(anti)quark pairs, the increase in cross section is simply explained by the increase in the parton luminosity

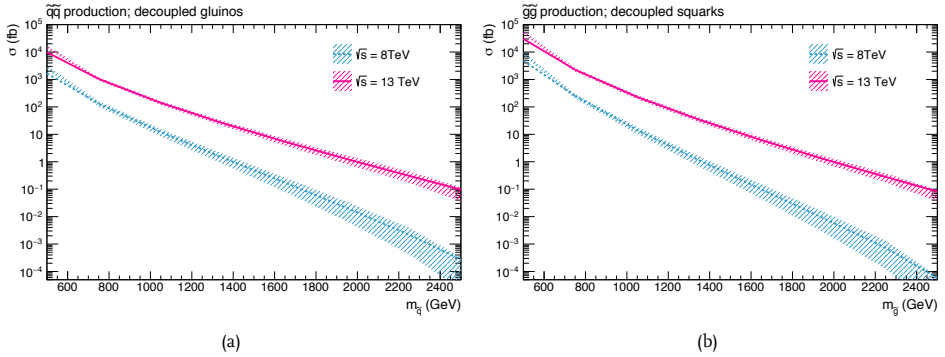

Fig. 6.2 · Cross sections of squark-pair production (a) and gluino-pair production (b) calculated at $\sqrt{s} = 8$ TeV (blue) and $\sqrt{s} = 13$ TeV (pink). The cross sections are calculated using NLLFAST [210–214] and PROSPINO [218].

illustrated in Figure 6.1. A higher production cross section will lead to a higher possibility of producing squarks and gluinos if they exist and they are not too heavy to be produced. This will lead to larger discovery reach even with a smaller dataset than the dataset of 20.3 fb^{-1} used in the analysis at $\sqrt{s} = 8$ TeV.

6.1.1 Simplified Models

Since this search for supersymmetry is performed on the very first data collected at $\sqrt{s} = 13$ TeV, only a limited number of models of squark and gluino production and decays are used in this optimisation and to study the discovery reach or eventual model-dependent limits.

Sketches of the sparticle pairs and their decays in the three simplified models studied in this chapter, are shown in Figure 6.3. The three models are squark-pair production with direct decay ($\tilde{q} \to q\tilde{\chi}_1^0$), gluino-pair production with direct decay ($\tilde{g} \to q\bar{q}\tilde{\chi}_1^0$), and gluino-pair production with one-step decay through a chargino ($\tilde{g} \to q\bar{q}'\tilde{\chi}_1^\pm \to q\bar{q}'W^\pm\tilde{\chi}_1^0$). The models are almost identical to the simplified models studied in the analysis performed with data collected at $\sqrt{s} = 8$ TeV that are introduced in Section 5.1.1. The only difference between the simplified models studied in this analysis compared to the ones studied in the previous analysis is an increase in the mass of the decoupled particles from 4.5 TeV to 45 TeV.

In the models with direct decays, the two free parameters are the mass of the squark or gluino and the mass of the LSP. In the gluino-pair production model with one-step decay, the free parameters are the mass of the gluino and the mass of the LSP while the mass of the chargino is fixed to $m_{\tilde{\chi}_1^\pm} = (m_{\tilde{g}} + m_{\tilde{\chi}_1^0})/2$.

6.2 Standard Model Backgrounds at $\sqrt{s} = 13$ TeV

Since the analysis in this chapter is selecting final states with jets and $E_{\mathrm{T}}^{\mathrm{miss}}$ similar to the analysis presented in Chapter 5, the Standard Model background processes remain the same.

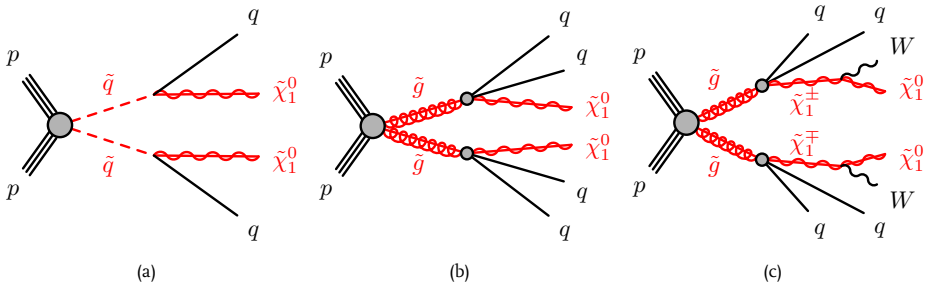

Fig. 6.3 · Sketch of squark-pair (a), and gluino-pair (b) production with direct decays into final states with quarks and two $\tilde{\chi}_1^0$, and gluino-pair (c) production with onestep decays through $\tilde{\chi}_1^\pm$ into final states with quark, two $\tilde{\chi}_1^0$, and decay products of W bosons.

The dominant backgrounds in the signal regions in the analysis performed with data collected at $\sqrt{s} = 8$ TeV described in Chapter 5 were W+jets, Z+jets, top ($t\bar{t}$ and single-t), and diboson. The contributions from the multijet background in the signal regions were minor compared to the other background processes.

Just as the cross section of sparticle production increases with increasing collision energy, the cross sections of the various Standard Model background processes increase as well. The cross sections at $\sqrt{s} = 8$ TeV and $\sqrt{s} = 13$ TeV of the dominant backgrounds are given in Table 6.1. The cross sections of $Z \to \ell^+\ell^-$, and $W^\pm \to \ell^\pm\nu_\ell$ are calculated at NNLO [220], and the cross sections of WW, WZ, and ZZ are calculated to NLO [233, 234]. The values of the boson and diboson cross sections are taken from Ref. [244]. The cross section of $t\bar{t}$ production is calculated at NNLL+NNLO [222, 223], and the single-t cross sections are calculated at NLO precision [245, 246].

To compare the cross sections at the two collision energies, the ratio is given in Table 6.1 as well. It is seen that in general the cross section of the Standard Model background processes increase by a factor 2-3 when the collision energy is raised from 8 TeV to 13 TeV. The smallest increase is seen in the cross section of $W \to \ell\nu_\ell$ with a factor of 1.66 and the largest in the cross section of $t\bar{t}$-production with a factor of 3.29. $t\bar{t}$-pairs can be produced from parton interactions of both gluon pairs and quark-antiquark pairs, while W bosons are produced at leading order from quark-antiquark pairs. As it was seen in Figure 6.1, the parton luminosity ratio of gluon-gluon interactions increases more when the energy of the collisions is increased than that quark-antiquark parton luminosity ratio. Furthermore, the mass of a $t\bar{t}$-pair is larger than the mass of the W boson which leads to an even larger increase in production cross section since the parton luminosity ratio increases with the energy of the hard scattering.

In general the cross sections of the Standard Model background processes are much larger than the production cross section of squarks and gluinos. The cross sections of squarks and gluinos at $\sqrt{s} = 8$ TeV and $\sqrt{s} = 13$ TeV are in the range from 10^{-4} fb to 1 pb and from 10^{-1} fb to 10 pb, respectively, depending on the mass of the squark or gluino. This should be compared to the cross section of the Standard Model processes that are in general of the order 10-10000 pb.

Process	$\sigma(\sqrt{s} = 8\ \text{TeV})$ [pb]	$\sigma(\sqrt{s} = 13\ \text{TeV})$ [pb]	$\sigma(13\ \text{TeV})/\sigma(8\ \text{TeV})$
$Z \to \ell^+\ell^-$	1128 ± 56	1914 ± 96	1.70 ± 0.12
$W^\pm \to \ell^\pm \nu_\ell$	12087 ± 640	20080 ± 1004	1.66 ± 0.12
$t\bar{t}$ ($m_t = 172.5$ GeV)	$252.9^{+13.3}_{-14.5}$	$831.8^{+40.3}_{-45.7}$	$3.29^{+0.24}_{-0.26}$
single-t (t-channel)	$84.69^{+3.76}_{-3.23}$	$217.0^{+9.0}_{-7.7}$	$2.56^{+0.16}_{-0.13}$
single-t (s-channel)	$5.24^{+0.22}_{-0.20}$	$10.32^{+0.40}_{-0.36}$	$1.97^{+0.11}_{-0.10}$
single-t (Wt-channel)	22.37 ± 1.52	71.7 ± 3.8	3.21 ± 0.28
WW	54.71 ± 2.74	106.8 ± 5.3	1.95 ± 0.14
WZ ($M_Z > 12$ GeV)	33.31 ± 2.33	65.14 ± 4.56	1.95 ± 0.19
ZZ ($M_Z > 12$ GeV)	11.17 ± 0.56	21.04 ± 1.1	1.89 ± 0.13

Table 6.1 · Production cross sections in pb of the dominant Standard Model background processes at $\sqrt{s} = 8$ TeV and $\sqrt{s} = 13$ TeV as well as the ratio of the cross sections at the two energies, $\sigma(13\ \text{TeV})/\sigma(8\ \text{TeV})$.

However, with the increase in collision energy the cross sections of squark and gluino production increase with a factor of 10 to 1000 compared to the largest increase in cross section of the backgrounds of 3.3. An increase in collision energy from 8 TeV to 13 TeV will thus improve the signal-to-background ratio dramatically leading to a largely increased discovery reach.

6.3 Data and Simulation Samples

A description of the dataset and the generators used for simulating signal and background samples are given in this section.

6.3.1 Data Sample

The dataset used in the analysis consists of 3.2 fb^{-1} of proton-proton collisions at a collision energy of $\sqrt{s} = 13$ TeV with a 25ns bunch spacing collected by the ATLAS experiment in 2015. Events are required to pass a Good Run List (GRL) where all sub-detectors of the ATLAS detector were in good condition and functioning well ensuring high quality data. Many proton-proton interactions can happen for each bunch crossing. The average number of proton-proton interactions per bunch crossing in the dataset was $\langle\mu\rangle = 14$. The uncertainty on the luminosity is estimated to be 5% obtained by a method similar to the one described in Ref. [219].

6.3.2 Simulation Samples

Simulation samples are used in estimating both Standard Model backgrounds and the signal yields of the models described in Section 6.1.1.

Signal Samples

The signal samples of the simplified models described in Section 6.1.1 are all generated at matrix element level with MG5_aMC@NLO-2.2.2 [247] interfaced with PYTHIA-8.168 [133, 134] for parton showering and with NNPDF2.3LO [248] as the parton distribution function set. The detector simulation is done with a fast simulation of the ATLAS calorimeter [149] while the rest of the ATLAS detector response [249] is simulated with GEANT4 [148].

In total 85 samples of $\tilde{q}\tilde{q}$-production with direct decay, 122 samples of $\tilde{g}\tilde{g}$-production with direct decay, and 133 samples of $\tilde{g}\tilde{g}$-production with onestep decay through $\tilde{\chi}_1^{\pm}$ were generated with various masses of the squark or gluino and $\tilde{\chi}_1^0$. The cross sections of all the samples were calculated to NLO in α_s with re-summation of soft gluon emission to NLL accuracy [210–214]

Background Samples

All the Standard Model backgrounds are estimated using simulation samples, including the multijet background arising from pure QCD interactions. The multijet background is thus estimated with a semi-data-driven technique as apposed to the fully data-driven technique used in the previous analysis described in Section 5.6.2. The detector simulation is done with a full simulation of the ATLAS detector [249] using GEANT4 [148].

A summary of the generators used for event generation and parton showering, the order in the strong coupling, α_s, of the cross section calculation and eventual precision in re-summation of soft gluon emission, the Monte Carlo generator tune, and the PDF set for each background sample are given in Table 6.2. Detailed descriptions of the generator settings used for simulating the background samples can be found in Refs. [250–253]

W+jets, Z+jets, γ+jets

Two samples are generated for the W+jets, and Z+jets processes using SHERPA with a PDF set from CT10 as baseline and MG5_aMC@NLO interfaced with PYTHIA and a NNPDF PDF set. There is only one γ+jets sample and it is generated with SHERPA and a PDF set from CT10. A more detailed description of the generator settings can be found in Ref. [250].

Top

Two samples are generated to simulated $t\bar{t}$-production: a baseline sample simulated using POWHEG-BOX, and an alternative sample generated with aMC@NLO. Both samples are generated with a PDF from CT10. In the analysis performed on data collected at $\sqrt{s} = 8$ TeV, the $t\bar{t}$-samples were reweighted to fit the observed differential cross section [235, 236]. There is no longer a need for the reweighing the $t\bar{t}$ samples since the generators have been tuned to fit data.

The single-t samples are divided into three channels: t-channel, s-channel, and Wt-channel. The t-channel sample is generated with POWHEG-BOX interfaced with PYTHIA and a four-flavour PDF set from CT10, CT10F, is used. The s- and Wt-channel samples are both generated with POWHEG-BOX and a PDF set from CT10. There are no alternative samples for these processes.

Process	Generator + frag./had.	Cross section order in α_s	Tune	PDF set
W+jets	SHERPA-2.1.1 [135]	NNLO [254, 255]	SHERPA default	CT10 [36]
W+jets($\star$)	MG5_aMC@NLO-2.2.2 [247] + PYTHIA-8.168 [133, 134]	NNLO [254, 255]	A14 [256]	NNPDF2.3LO [248]
Z/γ^*+jets	SHERPA-2.1.1 [135]	NNLO [254, 255]	SHERPA default	CT10 [36]
Z/γ^*+jets($\star$)	MG5_aMC@NLO-2.2.2 [247] + PYTHIA-8.168 [133, 134]	NNLO [254, 255]	A14 [256]	NNPDF2.3LO [248]
γ+jets	SHERPA-2.1.1 [135]	LO	SHERPA default	CT10 [36]
$t\bar{t}$	POWHEG-BOX-2.0 [141–143] + PYTHIA-6.426 [133]	NNLO+ NNLL [222, 223]	Perugia2012 [225]	CT10 [36]
$t\bar{t}$($\star$)	aMC@NLO-2.2.1 [144–147] + HERWIG++-2.7.1 [138]	NNLO+ NNLL [222, 223]	UEEE5 [257]	CT10 [36]
Single top				
t-channel	POWHEG-BOX-1.0 [141–143] + PYTHIA-6.426 [133]	NLO [245, 246]	Perugia2012 [225]	CT10F4 [36]
s-channel	POWHEG-BOX-2.0 [141–143] + PYTHIA-6.426 [133]	NLO [245, 246]	Perugia2012 [225]	CT10 [36]
Wt-channel	POWHEG-BOX-2.0 [141–143] + PYTHIA-6.426 [133]	NNLO+ NNLL [229, 227]	Perugia2012 [225]	CT10 [36]
$t\bar{t}$+EW boson	MG5_aMC@NLO-2.2.2 [247] + PYTHIA-8.168 [133, 134]	NLO [230, 232]	A14 [256]	NNPDF2.3LO [248]
Dibosons				
WW, WZ, ZZ,	SHERPA-2.1.1 [135]	NLO [233, 234]	SHERPA default	CT10 [36]
Multijet	PYTHIA-8.168 [133, 134]	LO	A14 [256]	NNPDF2.3LO [248]

Table 6.2 · Simulation samples of the Standard Model background processes considered in the analysis. Generators, hard scattering cross section calculation order in α_s (Leading Order (LO), Next-to-Leading Order (NLO), Next-to-Next-to-Leading Order (NNLO), and Next-to-Next-to-Leading Log (NNLL)), the tune used for the generation, and the parton distribution function (PDF) set are stated. Samples denoted with a **($\star$)** are used to estimate the uncertainties originating from the choice of generator. The LO cross section of the γ+jets and multijet samples are taken directly from the generator.

The $t\bar{t}+W$, $t\bar{t}+Z$, and $t\bar{t}+WW$ samples are all generated with MG5_aMC@NLO interfaced with PYTHIA. The NNPDF2.3LO parton distribution function set is used.

More information on the generator settings for the $t\bar{t}$, single-top, and $t\bar{t}$+EW production can be found in Refs. [251] and [252].

Diboson

The WW, WZ, and ZZ samples are all generated using SHERPA and a parton distribution set from CT10 is used. No alternative samples are used in this analysis for any of the diboson samples. More information on the generator settings can be found in Ref. [253].

Multijet

The multijet sample is generated with PYTHIA and a PDF set from NNPDF2.3LO [248]. The cross section is taken directly from the generator at leading order in α_s.

Pile-up Simulation

The multiple proton-proton interactions per bunch crossing (pile-up) are simulated by overlaying events with soft QCD processes generated with PYTHIA-8.168 [133, 134]. Due to technicalities, the simulation samples of signal and background are not reweighted to fit the pile-up profile of the data. It was found not to affect the result of the analysis and could therefore safely be omitted.

6.4 Object Definition

Before defining the set of cuts used in the signal region selection, the physics objects such as jets and leptons must be defined.

Two set of cuts, baseline and signal, are defined for muons, electrons, and photons. The baseline electrons and muons are used in the removal of overlapping objects and to veto leptons in the signal regions. The signal electrons and muons are used in selecting events in the $W+$jets and top control regions. The baseline photons are used in resolving overlapping objects, while the signal photons are used in selecting events for the $\gamma+$jets control region used for estimating the $Z+$jets background.

A summary of the cuts used to define the objects are given in Table 6.3. Here follows a short description on the difference between selection criteria of objects in the analysis performed at $\sqrt{s} = 8$ TeV compared to object definition updated for the analysis presented in this chapter:

Jets are reconstructed using the same algorithm as in the precious analysis. The only difference in the object definition of the analysis presented in this chapter with respect to the object definition of the previous analysis is that the jets are required to be more central ($|\eta| < 2.8$ compared to $|\eta| < 4.5$)

b-jets are tagged using a b-tagging algorithm re-optimised for Run-2 operation, MV2C20 [173]. The b-tag efficiency is increased to 77% compared to 70% in the Run-1 analysis. The cut on the p_{T} of a b-jet is increased to 50 GeV.

Electrons are reconstructed using the same technique in Run-1 and Run-2. The identification and isolation criteria have been updated for Run-2 while the requirements on p_{T} and $|\eta|$ have remained the same. Baseline electron must fulfill a `Loose` identification requirement [178] while signal electrons must fulfill a `Tight` identification requirement and the `GradientLoose` isolation requirements [183].

Jets		Signal
Acceptance		$p_{\mathrm{T}} > 20$ GeV and $\lvert\eta\rvert < 2.8$
b-jets		Signal
Tagged		b-tagged
Acceptance		$p_{\mathrm{T}} > 50$ GeV and $\lvert\eta\rvert < 2.5$
Electrons	Baseline	Signal
Acceptance	$p_{\mathrm{T}} > 10$ GeV and $\lvert\eta\rvert < 2.47$	$p_{\mathrm{T}} > 25$ GeV and $\lvert\eta\rvert < 2.47$
Quality	`Loose`	`Tight`
Isolation	-	`GradientLoose`
Primary vertex	-	$\lvert d_0^{\mathrm{PV}}\rvert/\sigma(d_0^{\mathrm{PV}}) < 5$, $\lvert z_0^{\mathrm{PV}}\rvert < 0.5$ mm
Muons	Baseline	Signal
Acceptance	$p_{\mathrm{T}} > 10$ GeV and $\lvert\eta\rvert < 2.7$	$p_{\mathrm{T}} > 25$ GeV and $\lvert\eta\rvert < 2.4$
Quality	`Medium`	`Medium`
Isolation	-	`GradientLoose`
Primary vertex	-	$\lvert d_0^{\mathrm{PV}}\rvert/\sigma(d_0^{\mathrm{PV}}) < 3$, $\lvert z_0^{\mathrm{PV}}\rvert < 0.5$ mm
Photons	Baseline	Signal
Acceptance	$p_{\mathrm{T}} > 25$ GeV and $\lvert\eta\rvert < 2.37$	$p_{\mathrm{T}} > 130$ GeV and $\lvert\eta\rvert < 2.37$
Quality	`Loose`	`Tight`
Isolation	-	$E_{\mathrm{T}}^{\mathrm{calo},\Delta R=0.2} < 0.65 \times p_{\mathrm{T}}$, $p_{\mathrm{T}}^{\mathrm{track},\Delta R=0.2}/p_{\mathrm{T}} < 0.05$

Table 6.3 · The cuts used to define jets, b-jets, electrons, muons, and photons. The electrons, muons, and photons have two sets of cuts, a baseline and a signal cut. The jets and b-jets have one set of cuts.

Muons used in the analysis presented in this chapter must fulfill the `Medium` identification requirement [183] unlike the muons used in the previous analysis. The cut on $|\eta|$ of the baseline muon has been loosened to 2.7 compared to 2.4. The isolation criteria has been updated to the `GradientLoose` isolation requirement [183] and the primary vertex requirement is changed as well.

Photons are reconstructed and identified using the same techniques in both analyses [179]. The baseline photons are used in overlap removal in this analysis and the cut on their p_{T} is therefore loosened to $p_{\mathrm{T}} > 20$ GeV compared to 130 GeV in the previous analysis.The isolation criteria are updated to include isolation in both the calorimeter and in the inner detector.

Taus are not used in any of the selections of the analysis presented in this chapter.

6.4.1 Overlap Removal

As different objects can occasionally be reconstructed from the same detector responses, overlap removal is performed to solve the conflicts of overlapping objects. The overlap of objects can both be caused by mis-reconstruction and due to muons and electrons in the jets. The procedure for overlap removal in this analysis is similar to the one described in Section 5.4.1, however additional overlap removal in regions were photons are selected is applied.

Most overlap removal criteria are based on the distance between two objects in the η-ϕ-plane given by $\Delta R = \sqrt{(\Delta\eta)^2 + (\Delta\phi)^2}$. In regions where photons are selected, e. g. CRγ, additional overlap removal is performed resolving overlaps containing photons. The overlap removal marked with ($\star$) in the following list are only applied in regions where photons are selected. The overlap removal between jets, leptons (electrons or muons), and photons are done in the following steps:

1. If a baseline electron and a baseline muon are sharing tracks in the inner detector, then the object is reconstructed as a muon and the electron is rejected.

2. ($\star$) If a baseline photon and a baseline electron are found within a cone of $\Delta R < 0.4$, the object is taken as an electron and the photon is removed.

3. ($\star$) If a baseline photon and a baseline muon are found within a cone of $\Delta R < 0.4$, the object is treated as a muon and the photon is ignored.

4. If a baseline electron and a jet are found within a cone of $\Delta R < 0.2$, the object is treated as an electron and the overlapping jet is removed.

5. If a baseline electron and a jet are found within $0.2 < \Delta R < 0.4$, the object is interpreted as a jet, and the electron is ignored.

6. If a baseline muon and a jet are found within $\Delta R < 0.4$, then the object is treated as a jet and the overlapping muon is ignored.

7. ($\star$) If a baseline photon and a jet are found within a cone of $\Delta R < 0.4$, the object is treated as a photon and the jet is removed.

6.5 Signal Regions

The signal regions are very similar in the choice of variables and cuts to the ones used in the analysis performed on the dataset collected at $\sqrt{s} = 8$ TeV and described in Section 5.5.

All the signal regions have a common preselection. After the preselection, the final event selection of each signal region is found by an optimisation. Each signal region is optimised for a different combination of the free parameters in the simplified models discussed in Section 6.1.1. The signal regions are all optimised to cover the largest area of discovery potential following the method described in Section 4.2.2.

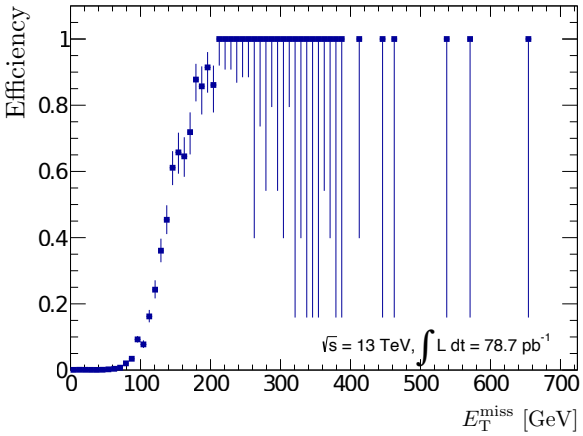

Fig. 6.4 · Efficiency of the missing transverse momentum trigger `HLT_xe70` measured in a dataset collected at $\sqrt{s} = 13$ TeV corresponding to an integrated luminosity of 78.7 pb^{-1}.

6.5.1 Event Preselection

The event preselection is common to all signal regions. It includes trigger, event cleaning, cuts on $E_{\mathrm{T}}^{\mathrm{miss}}$ and the p_{T} of the leading jet, veto on leptons, and cuts used to reject multijet background.

Trigger

In Run 2, the trigger system of ATLAS consists of two layers, a hardware trigger, L1, and a higher level software trigger, HLT. The dataset is collected using a missing transverse momentum trigger, `HLT_xe70`, with a cut on $E_{\mathrm{T}}^{\mathrm{miss}}$ at 70 GeV at trigger level.

The missing transverse momentum used by the trigger is not fully calibrated. A tighter cut than 70 GeV is therefore needed to ensure that the trigger is fully efficient. The efficiency of the trigger is studied as a function of the offline calibrated $E_{\mathrm{T}}^{\mathrm{miss}}$ in Figure 6.4. It is seen from the turn-on curve that the trigger is fully efficient when the offline $E_{\mathrm{T}}^{\mathrm{miss}}$ is larger than 200 GeV.

Event Cleaning

The event cleaning covers cuts used to reject events where the detector response is not coming solely from proton-proton collisions, but is contaminated by cosmic rays, discharges in the detector, beam remnants, and objects pointing to problematic detector regions.

Non-collision Background

The leading primary vertex, i. e. the vertex of the bunch crossing with the highest p_{T} tracks, is required to have at least 2 tracks associated to it with $p_{\mathrm{T}} > 400$ MeV to reduce non-collision background.

Events containing jets with $p_{\mathrm{T}} > 20$ GeV satisfying the "BadLoose" requirement [258] or one of the two highest-p_{T} jets with $p_{\mathrm{T}} > 100$ GeV satisfying the "BadTight" requirement [258]

are rejected. The "BadLoose" and "BadTight" cleaning requirements contain cuts on the energy fraction of the jet deposited in the forward hadronic calorimeter, the fraction of the energy of the jet deposited in the electromagnetic calorimeter, the size of the negative energy, the fraction of the p_{T} of the tracks to the total energy of the jet, and the maximal fraction of an energy deposit in a single layer of the calorimeter. These variables are found to be good at discriminating between real jets and jets reconstructed from noise bursts in the calorimeter that are expected to have a large energy deposit in a single layer of the calorimeter and not have many associated tracks.

A jet out of time with a collision is typically caused by non-collision background. Events with a jet "time" (the energy average of the cell time) of the two highest-p_{T} jets larger than 4 ns are rejected.

Problematic Regions in the Calorimeter

Two dead regions have been found in the Tile Calorimeter. They are situated at ($0 < \eta < 0.9$ and $0.8 < \phi < 1.0$) and ($-1.6 < \eta < -0.9$ and $1.9 < \phi < 2.1$). Events where a jet pointing to the dead region fulfills $p_{\mathrm{T}} > 50$ GeV and $\Delta\phi(\text{jet}, E_{\mathrm{T}}^{\mathrm{miss}}) < 0.3$ are rejected in the signal region selection and the event selection of control region used for the multijet background estimate. The loss of events in the Monte Carlo simulation and data samples due to the dead Tile veto is negligible ($< 0.1\%$).

Fake Muons

The origin of fake muons is discussed in Section 5.5.1. Events with fake muons are rejected by implying cuts on events containing muons not originating from the primary vertex, i. e. a muon with $|z_0^{\mathrm{PV}}| > 1$ mm or $|d_0^{\mathrm{PV}}| > 0.2$ mm, after the overlap removal. Fake muons are expected to lead to large fake missing transverse momentum dominated by the contribution from muons. Events fulfilling $(E_{\mathrm{T}}^{\mathrm{miss}})^{\mathrm{Muon}}/E_{\mathrm{T}}^{\mathrm{miss}} \times \cos\Delta\phi((E_{\mathrm{T}}^{\mathrm{miss}})^{\mathrm{Muon}}, E_{\mathrm{T}}^{\mathrm{miss}}) > 0.5$ are therefore rejected. To further reduce the number of events containing fake muons, any event containing a muon with an uncertainty on $1/p$ larger than 20% is rejected.

$E_{\mathrm{T}}^{\mathrm{miss}}$ and Jet p_{T} Requirements

The minimum requirement on the missing transverse momentum is motivated by the trigger threshold. In order for the trigger to be fully efficient, the missing transverse momentum must be larger than 200 GeV.

All events in the signal regions must contain at least two jets. The p_{T} of the most energetic jet must be larger than 200 GeV, while p_{T} of the subleading jet must be larger than 50 GeV.

Lepton Veto

The analysis described in this chapter is selecting events with jets and missing transverse momentum, and without leptons. A veto on events with any baseline muons or electrons after overlap removal is therefore placed.

	$\tilde{q}\tilde{q}$ **Large** $\Delta m(m_{\tilde{q}}, m_{\tilde{\chi}_1^0})$	$\tilde{g}\tilde{g}$ **Large** $\Delta m(m_{\tilde{q}}, m_{\tilde{\chi}_1^0})$	$\tilde{q}\tilde{q}$, $\tilde{g}\tilde{g}$ **Small** $\Delta m(m_{\tilde{q}}, m_{\tilde{\chi}_1^0})$
$n_{\text{jets}} \geq$	2	4, 5, 6	2, 3, 4
$E_{\text{T}}^{\text{miss}}$[GeV] >	200	200	200, 250, 300
$p_{\text{T}}(j_1)$[GeV] >	200	200	200, 250, 300
$p_{\text{T}}(j_2)$[GeV] >	50, 100, 200	50, 100, 200	50, 100, 150, 200
$p_{\text{T}}(j_3)$[GeV] >	-	50, 100, 150	50, 100, 150
$p_{\text{T}}(j_4)$[GeV] >	-	50, 100	50, 100
$p_{\text{T}}(j_{5,6})$[GeV] >	-	50	-
$\Delta\phi(j_{1,2,(3)}, E_{\text{T}}^{\text{miss}})_{\text{min}}$ >	0.4, 0.8, 1.2	0.4	0.4, 0.6, 0.8
$\Delta\phi(j_{>3}, E_{\text{T}}^{\text{miss}})_{\text{min}}$ >	-	0.2	0.0, 0.2
Aplanarity	0.00, 0.02, 0.04	0.00, 0.02, 0.04	-
$E_{\text{T}}^{\text{miss}}/\sqrt{H_{\text{T}}}$[GeV$^{1/2}$] >	8, 15, 20	-	8, 12, 15, 20, 25
$E_{\text{T}}^{\text{miss}}/m_{\text{eff}}$(Nj) >	-	0.20, 0.25, 0.30	0.15, 0.20, ..., 0.40
m_{eff}(incl.)[GeV] >	800, 1200, ..., 2800	800, 1200, ..., 2800	1200, 1400, ..., 2000

Table 6.4 · The variables and cut ranges used in the optimisation of signal regions. Three scans were done studying the discovery reach of different models with different mass-splittings: $\tilde{q}\tilde{q}$-production with large $\Delta m(m_{\tilde{q}}, m_{\tilde{\chi}_1^0})$, $\tilde{g}\tilde{g}$-production with large $\Delta m(m_{\tilde{q}}, m_{\tilde{\chi}_1^0})$ with both direct and one-step decays, and $\tilde{q}\tilde{q}$- and $\tilde{g}\tilde{g}$-production with a small $\Delta m(m_{\tilde{q}}, m_{\tilde{\chi}_1^0})$.

Mutljet Rejection

The missing transverse momentum in multijet background events is not real $E_{\text{T}}^{\text{miss}}$, but originates from a mis-reconstruction of the energy of jets. This will typically cause the $E_{\text{T}}^{\text{miss}}$ to point in the direction of the jet with the mis-measured energy. A cut on the minimal azimuthal angle between the $E_{\text{T}}^{\text{miss}}$ and the jets, $\Delta\phi(j, E_{\text{T}}^{\text{miss}})_{\text{min}}$, is therefore introduced. In signal regions where the minimal jet multiplicity is two a requirement that $\Delta\phi(j_{1,2}, E_{\text{T}}^{\text{miss}})_{\text{min}}$ must be larger than 0.4 is placed. In signal regions with higher jet multiplicities a cut on $\Delta\phi(j_{1,2,3}, E_{\text{T}}^{\text{miss}})_{\text{min}}$ of 0.4 and on $\Delta\phi(j_{>3}, E_{\text{T}}^{\text{miss}})_{\text{min}}$ of all other jets with $p_{\text{T}} > 50$ GeV of 0.2 is introduced.

6.5.2 Signal Region Selection

The final signal region selection is found by optimising the values of the cuts on several variables in order to find the event selection covering the largest discovery potential in the parameter space of the simplified models. This is done by calculating the discovery significance at 3σ calculated from the expected number events of SUSY signal and Standard model backgrounds, and the uncertainty on the expected number of background events.

The optimisation was done with three different scans of the values of the cuts on the variables introduced in Section 4.2.1. The three scans were done studying the discovery reach in three different scenarios: $\tilde{q}\tilde{q}$-production with a large $\Delta m(m_{\tilde{q}}, m_{\tilde{\chi}_1^0})$, $\tilde{g}\tilde{g}$-production with a large

	2jl	2jm	2jt	4jt	5j	6jm	6jt
$E_{\mathrm{T}}^{\mathrm{miss}}$[GeV] >	200	200	200	200	200	200	200
$p_{\mathrm{T}}(j_1)$[GeV] >	200	300	200	200	200	200	200
$p_{\mathrm{T}}(j_2)$[GeV] >	200	50	200	100	100	100	100
$p_{\mathrm{T}}(j_3)$[GeV] >	-	-	-	100	100	100	100
$p_{\mathrm{T}}(j_4)$[GeV] >	-	-	-	100	100	100	100
$p_{\mathrm{T}}(j_5)$[GeV] >	-	-	-	-	50	50	50
$p_{\mathrm{T}}(j_6)$[GeV] >	-	-	-	-	-	50	50
$\Delta\phi(j_{1,2,(3)}, E_{\mathrm{T}}^{\mathrm{miss}})_{\mathrm{min}}$ >	0.8	0.4	0.8	0.4	0.4	0.4	0.4
$\Delta\phi(j_{>3}, E_{\mathrm{T}}^{\mathrm{miss}})_{\mathrm{min}}$ >	-	-	-	0.2	0.2	0.2	0.2
Aplanarity >	-	-	-	0.04	0.04	0.04	0.04
$E_{\mathrm{T}}^{\mathrm{miss}}/\sqrt{H_{\mathrm{T}}}$[GeV$^{1/2}$] >	15	15	20	-	-	-	-
$E_{\mathrm{T}}^{\mathrm{miss}}/m_{\mathrm{eff}}$(Nj) >	-	-	-	0.20	0.25	0.25	0.20
m_{eff}(incl.)[GeV] >	1200	1600	2000	2200	1600	1600	2000
Optimised for	$\tilde{q}\tilde{q}$ direct	$\tilde{q}\tilde{q}$,$\tilde{g}\tilde{g}$ direct	$\tilde{q}\tilde{q}$ direct	$\tilde{g}\tilde{g}$ direct	$\tilde{g}\tilde{g}$ direct	$\tilde{g}\tilde{g}$ one-step	$\tilde{g}\tilde{g}$ one-step

Table 6.5 · The cuts used to define signal regions and the models for which the signal regions were optimised. The signal regions are labelled by the minimum requirement on jet multiplicity and the tightness of the m_{eff}(incl.) cut: l (loose), m(medium), and t(tight).

$\Delta m(m_{\tilde{g}}, m_{\tilde{\chi}_1^0})$ with both direct and one-step decays, and $\tilde{q}\tilde{q}$- and $\tilde{g}\tilde{g}$-production with a small $\Delta m(m_{\tilde{q},\tilde{g}}, m_{\tilde{\chi}_1^0})$. The variables and the values of the cuts for the three different scans are given in Table 6.4. In the scan studying the discovery reach for compressed scenarios (small $\Delta m(m_{\tilde{q},\tilde{g}}, m_{\tilde{\chi}_1^0})$), either a cut on $E_{\mathrm{T}}^{\mathrm{miss}}/\sqrt{H_{\mathrm{T}}}$ or on $E_{\mathrm{T}}^{\mathrm{miss}}/m_{\mathrm{eff}}$(Nj) were imposed. For each combination of the cuts in Table 6.4, a fit is performed in a set of mass-points and the discovery significance was calculated to find the optimal combination of the cut-values.

To keep the analysis as simple as possible and to avoid a large look-elsewhere effect[1] in case of an excess, it was decided to keep the number of signal regions at a minimum. Seven signal regions were therefore defined based on the optimisation. The cuts defining the event selection of the signal regions as well as the simplified model for which the various signal regions are optimised are given in Table 6.5. The signal regions are labeled by their jet-multiplicity. Since there can be more than one signal region per jet-multiplicity, the signal regions are labeled with the tightness of the cut on m_{eff}(incl.) as well.

Two of the di-jet regions, 2jl and 2jt, are optimised for squark-pair production with direct decay. The last di-jet region, 2jm, is optimised for a compressed mass scenario where $m_{\tilde{q},\tilde{g}} \approx m_{\tilde{\chi}_1^0}$. The tighter cut on the p_{T} of the leading jet of 300 GeV is targeting a jet originating from initial state radiation. The 4jt-region is optimised for $\tilde{g}\tilde{g}$-production with direct decay and a large mass-splitting between $m_{\tilde{g}}$ and $m_{\tilde{\chi}_1^0}$, while the 5j-region is targeting a medium mass-splitting. The

[1] The look-elsewhere effect is used when estimating a global significance of an excess in a signal region. It takes into account the probability of observing an excess given the number of regions that has been studied. For example, it is expected on average to find a 3σ local significance if 1000 exclusive signal regions have been studied.

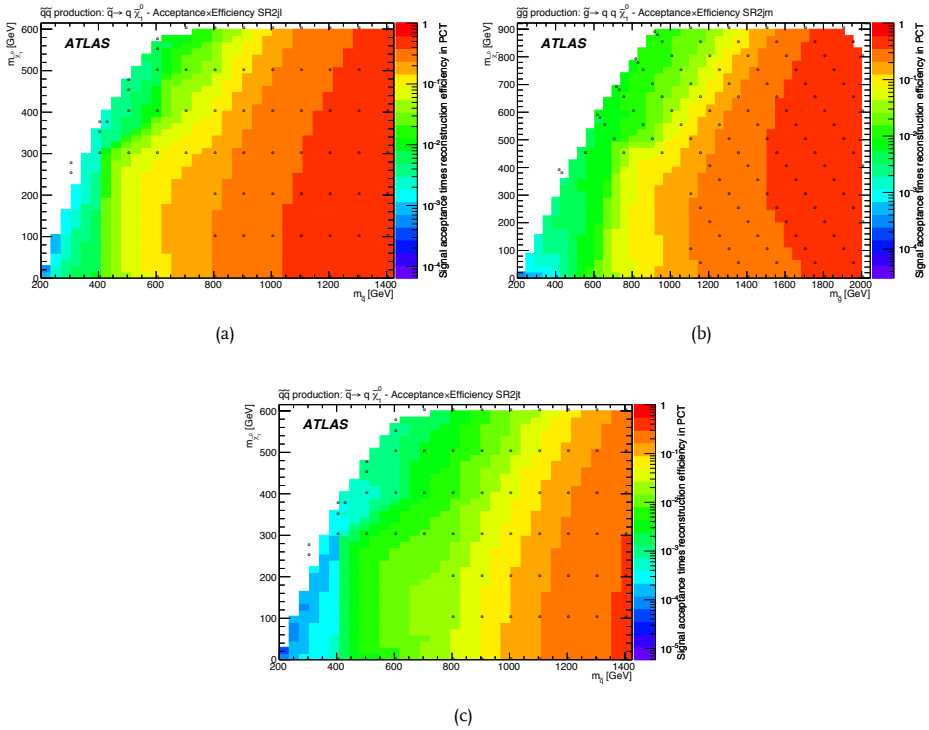

Fig. 6.5 · Product of signal acceptance and reconstruction efficiency at $\sqrt{s} = 13$ TeV for 2jl in $\tilde{q}\tilde{q}$-production with direct decay (a), 2jm in $\tilde{g}\tilde{g}$-production with direct decay (b), and 2jt (c) in $\tilde{q}\tilde{q}$-production with direct decay. The 'o'-markers indicate the locations of the grid points used in the interpolation.

two 6-jet regions are optimised for different mass splittings in the simplified model with $\tilde{g}\tilde{g}$-production and one-step decay through $\tilde{\chi}_1^{\pm}$.

The acceptance×efficiency calculated on reconstructed objects, i. e. the fraction of signal events that pass the selection, of all the signal regions defined in Table 6.5 are shown in Figures 6.5 and 6.6 in the model for which they were optimised.

Not surprisingly, the signal acceptance is largest in the regions with the loosest cuts, e. g. 2jl compared to 2jt in Figure 6.5. However, with a tighter selection the background rejection will be larger as well possibly leading to a better signal-to-background ratio. A region like 2jt might therefore prove stronger than 2jl in parts of the SUSY parameter space even though the signal acceptance is smaller. In the signal region optimised for a compressed mass scenario, 2jm, the acceptance along the diagonal where $m_{\tilde{g}} \approx m_{\tilde{\chi}_1^0}$ is larger than in the other signal regions optimised for $\tilde{g}\tilde{g}$-production with direct decays, i. e. 4jt and 5j in Figures 6.6a and 6.6b, respectively. It can be seen by the acceptance of 4jt and 6jt shown in Figures 6.6a and 6.6d that the regions were optimised for selecting signal events with high gluino masses and a massless $\tilde{\chi}_1^0$,

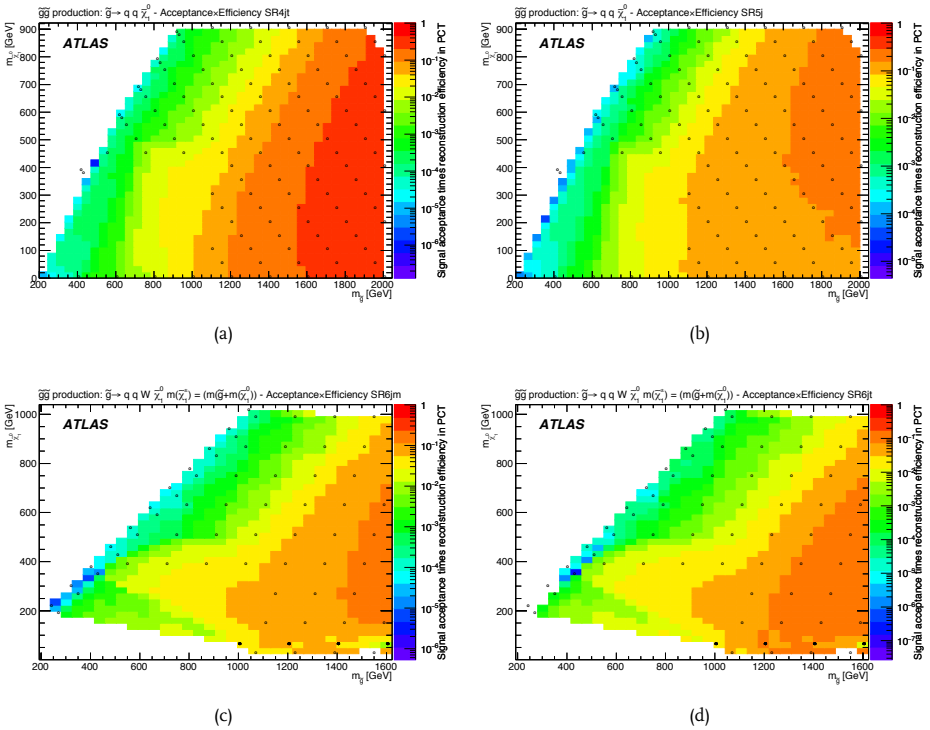

Fig. 6.6 · Product of signal acceptance and reconstruction efficiency at $\sqrt{s} = 13$ TeV for 4jt in $\tilde{g}\tilde{g}$-production with direct decay (a), 5j in $\tilde{g}\tilde{g}$-production with direct decay (b), 6jm (c) in $\tilde{q}\tilde{q}$-production with onestep decay, and 6jt (d) in $\tilde{q}\tilde{q}$-production with onestep decay. The 'o'-markers indicate the locations of the grid points used in the interpolation.

while 5j and 6jm (Figures 6.6b and 6.6c) were optimised for to select signal with smaller gluino mass and a massive $\tilde{\chi}_1^0$.

6.6 Background Estimation

The event yield and the precision of the yield of the Standard Model background processes in the signal regions is either estimated with a semi-data-driven technique using control regions to normalise the Monte Carlo simulation samples or estimated completely from simulation samples.

Four of the Standard Model background processes are estimated in control regions: $W+$jets, top backgrounds, $Z+$jets, and multijet. The diboson background is estimated completely from simulations. The multijet background is in this analysis estimated from a Monte Carlo sample normalised in a control region and not from a template obtained from a completely data-driven method as it was in the analysis performed on data collected at $\sqrt{s} = 8$ TeV.

To test the robustness of the background estimate, it is checked in validation regions where signal is not expected to be present. This is done before the signal regions are unblinded.

6.6.1 Control Regions

The control regions are designed to enhance the yield of a specific background process while being be orthogonal and as kinematically close the signal regions as possible. For each signal region a set of four control regions are defined: a control region for W+jets (CRW), a control region for the top background (CRT), a control region for Z+jets (CRγ), and a control region for the multijet background(CRQ).

Since the strategy of this analysis is very similar to the one presented in Chapter 5, the event selection of the control regions is almost identical to that used in the analysis performed with data collected at $\sqrt{s} = 8$ TeV and presented in Section 5.6.1. The only difference in the control region selections with respect to the previous analysis is a change of triggers. The focus of this section will therefore be on the distributions and purity of the control regions compared to $\sqrt{s} = 8$ TeV. The event selections with updated triggers of the four control regions and a validation region used for validating the Z+jets estimate are given in Table 6.6.

Control Region for W+jets and Top

The distributions of m_{eff}(incl.) at four jet-multiplicities of CRW and CRT are shown in Figures 6.7 and 6.8, respectively. In the m_{eff}(incl.) distributions of CRW and CRT, it is seen that there is a tendency for overestimating the number of events at high values of m_{eff}(incl.) in the 2jl region. At higher jet-multiplicities the same tendency seems to be present. A similar effect is seen in the m_{eff}(incl.) distributions of CRW in the 2-jet regions at $\sqrt{s} = 8$ TeV in Figure 5.11. The distributions of CRT at $\sqrt{s} = 8$ TeV in Figure 5.12 show deviations as well. It should be noted that the statistics in the control regions at $\sqrt{s} = 13$ TeV is small resulting in larger fluctuations.

The purity of CRW, i. e. the fraction of events in the region coming from W+jets, varies between 60% in 6jt to 75% in 2jl. The CRW-regions are mainly contaminated by events coming from the top background and diboson production. The CRT regions are mainly contaminated by events coming from W+jets and the purity of the CRT-regions is ranging from 75% in the low jet-multiplicity regions to 85% in 6jm. The purity in this analysis is comparable to the purity of the CRW- and CRT-regions in the analysis performed with data collected at $\sqrt{s} = 8$ TeV. The contamination of other backgrounds in the control regions is taken into account in the fit.

Control Region for Z+jets

The cross section of γ+jets is only available at leading order. A normalisation factor, κ, is therefore found by normalising the γ+jets sample to Z+jets in looser control regions using a technique very similar to the one at$\sqrt{s} = 8$ TeV presented Section 5.6.1. The looser control regions, CRZVL and CRγVL, are similar to VRZ and CRγ presented in Table 6.6, containing at least 2 jets, but the cuts on $\Delta\phi(j, E_{\text{T}}^{\text{miss}})_{\text{min}}$, $E_{\text{T}}^{\text{miss}}/m_{\text{eff}}$(Nj), $E_{\text{T}}^{\text{miss}}/\sqrt{H_{\text{T}}}$, and m_{eff}(incl.) are omitted. A loose cut

	CRW	CRT	CRγ	CRQ	VRZ
Trigger	HLT_e24_lhmedium_iloose or HLT_e60_lhmedium1 / HLT_mu20_iloose or HLT_mu50	HLT_e24_lhmedium_iloose or HLT_e60_lhmedium1 / HLT_mu20_iloose or HLT_mu50	HLT_g120_loose	same as SR	HLT_e24_lhmedium_iloose or HLT_e60_lhmedium1 / HLT_mu20_iloose or HLT_mu50
Extra objects	1 signal lepton (e or μ)	1 signal lepton (e or μ)	≥ 1 signal photon, no leptons	No leptons (e or μ)	Exactly 2 OS signal leptons (e or μ)
Treatment of objects	Treat lepton as jet	Treat lepton as jet	Treat photon as source of $E_{\mathrm{T}}^{\mathrm{miss}}$	No special treatment	Treat leptons as source of $E_{\mathrm{T}}^{\mathrm{miss}}$
b-tagging	No b-tagged jets	≥ 1 b-tagged jet	No requirement	No requirement	No requirement
Transverse Mass	30 GeV $< m_{\mathrm{T}}(\ell, E_{\mathrm{T}}^{\mathrm{miss}}) <$ 100 GeV	30 GeV $< m_{\mathrm{T}}(\ell, E_{\mathrm{T}}^{\mathrm{miss}}) <$ 100 GeV	No requirement	No requirement	No requirement
Invariant Mass	No requirement	No requirement	No requirement	No requirement	66 GeV $< m(\ell\ell) <$ 116 GeV
$\Delta\phi(j, E_{\mathrm{T}}^{\mathrm{miss}})_{\mathrm{min}}$	No requirement	No requirement	Same as SR	$\Delta\phi(j_{1,2,(3)}, E_{\mathrm{T}}^{\mathrm{miss}})_{\mathrm{min}} < 0.2$ and $\Delta\phi(j_{>3}, E_{\mathrm{T}}^{\mathrm{miss}})_{\mathrm{min}} < 0.1$	No requirement
Aplanarity	No requirement	No requirement	No requirement	No requirement	
$E_{\mathrm{T}}^{\mathrm{miss}}/m_{\mathrm{eff}}(\mathrm{Nj})$ or $E_{\mathrm{T}}^{\mathrm{miss}}/\sqrt{H_{\mathrm{T}}}$	No requirement	No requirement	Same as SR	$X - \Delta < E_{\mathrm{T}}^{\mathrm{miss}}/m_{\mathrm{eff}}(\mathrm{Nj}) < X$ if $E_{\mathrm{T}}^{\mathrm{miss}}/m_{\mathrm{eff}}(\mathrm{Nj}) > X$ in SR or $X - \Delta < E_{\mathrm{T}}^{\mathrm{miss}}/\sqrt{H_{\mathrm{T}}} <$ X if $E_{\mathrm{T}}^{\mathrm{miss}}/\sqrt{H_{\mathrm{T}}} > X$ in SR	No requirement
m_{eff}(incl.)[GeV]	Same as SR	Same as SR	Same as SR	Same as SR	Same as SR

Table 6.6 · Selection criteria used to define the four types of control regions and one validation region at $\sqrt{s} = 13$ TeV: CRW for estimating the W+jets background, CRT for estimating the top background, CRγ for estimating the $Z(\rightarrow \nu\nu)$+jets background, CRQ for estimating the multijet background, and VRZ for validating the estimate of the Z+jets background. Δ gives the interval of the cut on $E_{\mathrm{T}}^{\mathrm{miss}}/m_{\mathrm{eff}}(\mathrm{Nj})$ or $E_{\mathrm{T}}^{\mathrm{miss}}/\sqrt{H_{\mathrm{T}}}$ in CRQ depending on the specific signal region cut, X.

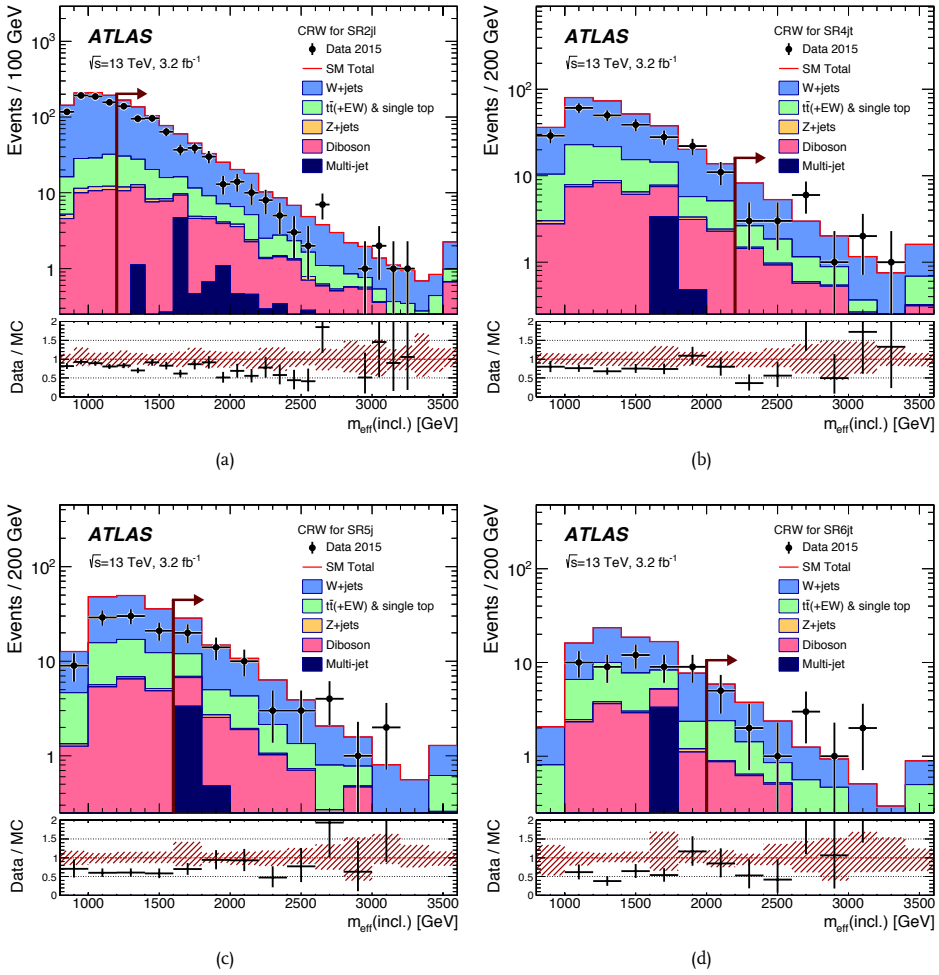

Fig. 6.7 · Observed and expected m_{eff}(incl.) distributions in 2jl (a), 4jt (b), 5j (c), and 6jt (d) regions of CRW at $\sqrt{s} = 13$ TeV before the final cut on m_{eff}(incl.). The histograms show the expected background from simulation normalised to the luminosity before the fit. The last bin includes the overflow. The red arrow indicates the cut on m_{eff}(incl.). The red hatched error band includes the combined uncertainty coming from detector uncertainties, Monte Carlo statistics, and theoretical modeling.

on the re-calculated $E_{\text{T}}^{\text{miss}}$ including the energy of the photon, 200 GeV $< E_{\text{T}}^{\text{miss}} <$ 300 GeV is applied. The normalisation factor is found to be:

$$\kappa = \frac{N_{\text{CR}\gamma\text{VL}}^{\gamma+\text{jets,data}} \cdot N_{\text{CRZVL}}^{Z\ell\ell,\text{MC}}}{N_{\text{CR}\gamma\text{VL}}^{\gamma+\text{jets,MC}} \cdot N_{\text{CRZVL}}^{Z\ell\ell,\text{data}}} = 1.5 \pm 0.1, \tag{6.1}$$

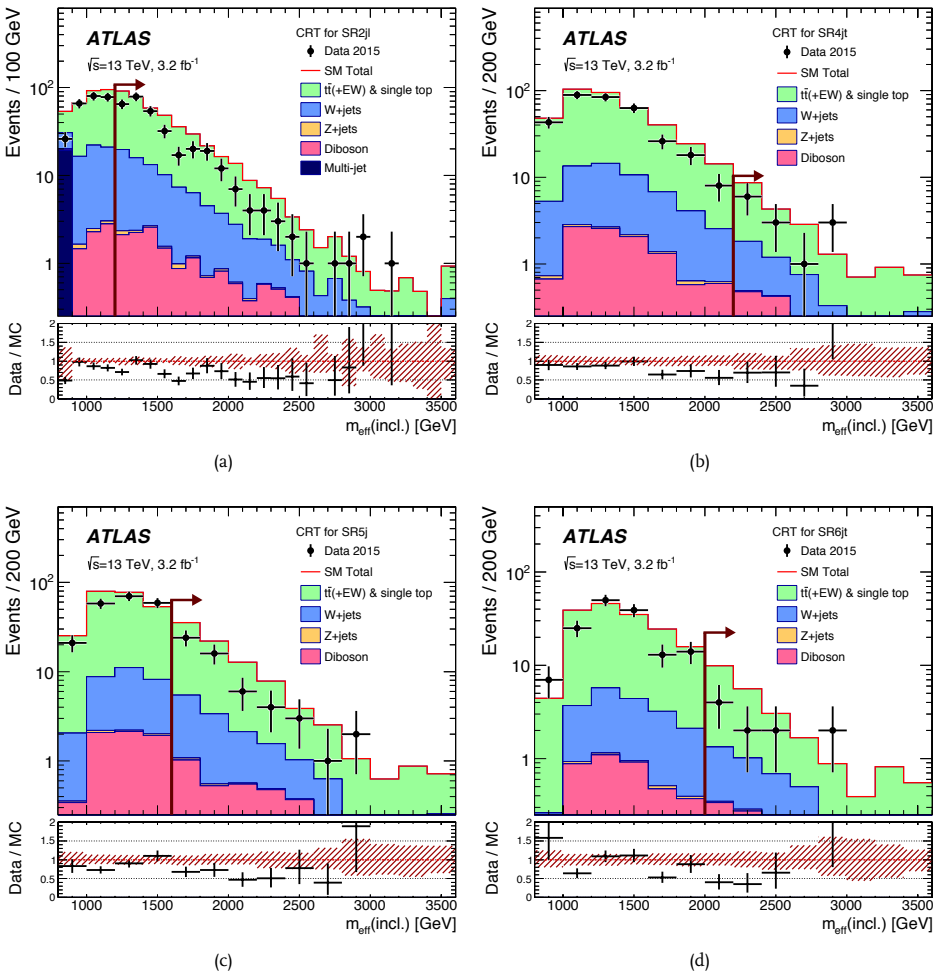

Fig. 6.8 · Observed and expected m_{eff}(incl.) distributions in 2jl (a), 4jt (b), 5j (c), and 6jt (d) regions of CRT at $\sqrt{s} = 13$ TeV before the final cut on m_{eff}(incl.). The histograms show the expected background from simulation normalised to the luminosity before the fit. The last bin includes the overflow. The red arrow indicates the cut on m_{eff}(incl.). The red hatched error band includes the combined uncertainty coming from detector uncertainties, Monte Carlo statistics, and theoretical modeling.

where $N_{\text{CR}\gamma\text{VL}}^{\gamma+\text{jets,data}}$ and $N_{\text{CRZVL}}^{Z\ell\ell,\text{data}}$ are number of events in CRγVL and CRZVL, respectively, subtracted the contribution from other backgrounds, and $N_{\text{CR}\gamma\text{VL}}^{\gamma+\text{jets,MC}}$ and $N_{\text{CRZVL}}^{Z\ell\ell,\text{MC}}$ are the expected number of γ+jets events in CRγVL and Z+jets events in CRZVL coming from simulation. The same normalisation factor is applied in all CRγ regions. In the analysis performed with data collected at $\sqrt{s} = 8$ TeV, κ of the SHERPA sample had a value of $1.04 \pm 0.01(\text{stat}) \pm 0.06(\text{syst})$. The large difference in the value of κ between this analysis and the previous one can have several

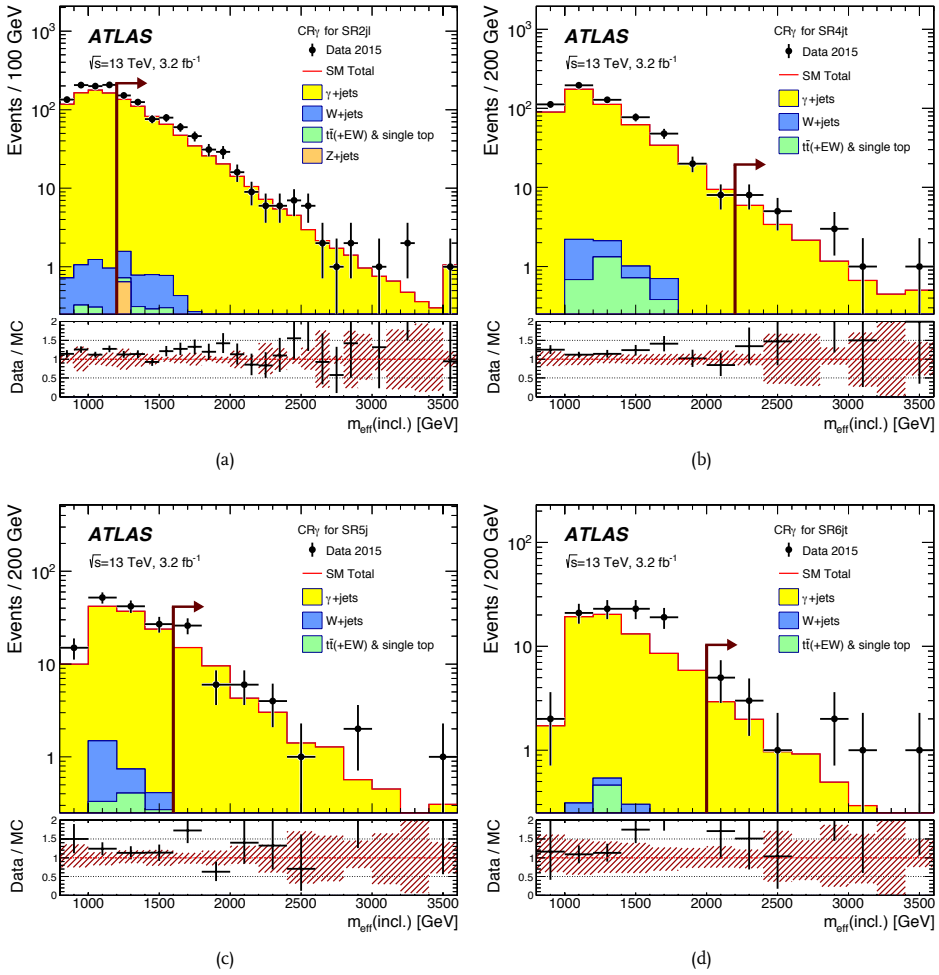

Fig. 6.9 · Observed and expected m_{eff}(incl.) distributions in 2jl (a), 4jt (b), 5j (c), and 6jt (d) regions of CRγ at $\sqrt{s} = 13$ TeV before the final cut on m_{eff}(incl.). The histograms show the expected background from simulation normalised to the luminosity before the fit. The γ+jets sample is normalised using the κ-factor defined in Eq. 6.1. The last bin includes the overflow. The red arrow indicates the cut on m_{eff}(incl.). The red hatched error band includes the combined uncertainty coming from detector uncertainties, Monte Carlo statistics, and theoretical modeling.

causes: the selection of the loose control regions used to obtain κ is slightly different, the statistics in the looser regions is smaller in this analysis compared to the previously, and the cross section has increased due to the increase in collision energy.

The observed and expected distributions of m_{eff}(incl.) in CRγ of 2jl, 4jt, 5j, and 6jt are shown in Figure 6.9. The γ+jets sample is normalised using the κ-factor of Eq. 6.1. It is seen that the simulations in general underestimate the number of events in the entire m_{eff}(incl.)-spectrum in all

jet multiplicities. This is quite different from the m_{eff}(incl.) distributions of the analysis performed on data collected at $\sqrt{s} = 8$ TeV shown in Figure 5.13, where the expected distributions are in general over-estimating the data. In CRγ of 6jt shown in Figure 6.9d, the expected distribution in m_{eff}(incl.) ranging from 1000 GeV to 1500 GeV seems to not describe the data very well. The number of events is however low and the errors are large so nothing definite can be concluded with this amount of data.

The purity of the CRγ-regions is in general very high at a level of $\sim$ 98%-99% with very low contamination of other background processes, which is comparable to the purity of CRγ in the previous analysis.

Control Region for Multijet

The cuts on $E_{\text{T}}^{\text{miss}}/m_{\text{eff}}$(Nj) and $E_{\text{T}}^{\text{miss}}/\sqrt{H_{\text{T}}}$ are reversed compared to the signal region cuts with a lower cut at $X - \Delta$ where X is the signal region cut on the variable. The value of Δ depends on the signal region cut. There are three values of Δ: $\Delta = 6$ [GeV$^{1/2}$] in the 2-jet regions, $\Delta = 0.05$ in the 4jt and 6jt regions, and $\Delta = 0.15$ in the 5j and 6jm regions.

The observed and expected distributions of m_{eff}(incl.) in 2jl, 4jt, 5j, and 6jt selections of CRQ are shown in Figure 6.10. It is seen that the Monte Carlo simulation overestimates the data over the entire m_{eff}(incl.) range in the 2jl-region shown in Figure 6.10a. Spikes in the multijet samples are seen in regions with tighter cuts, especially in the 6jt-region in Figure 6.10d. This is caused by the limited statistics of the multijet Monte Carlo sample. If instead a data-driven method was used to obtain a multijet sample like it was in the previous analysis, the expected distribution would be more smooth.

The purities of the CRQ regions are in general high ($\sim$ 85%) with the lowest purities in the 2jt-region ($\sim$ 65%) and 6jt-region ($\sim$ 70%) which is in agreement with the purity of the CRQ regions at $\sqrt{s} = 8$ TeV. The regions are contaminated by all the other Standard Model background processes. The contamination from other processes are taken into account in the background fit.

6.6.2 Validation Regions

A set of 7 validation regions is defined per signal region. Each validation region is designed to test the estimate of a specific background and is therefore defined to be kinematically close to both the signal and the control region and enriched by that background process. The 7 validation regions are:

VRZ is used to test the estimate of the Z+jets background. This is done in a sample where $Z \to \ell\ell$ events are selected in an invariant mass-window around the Z mass. The specific set of cuts can be seen in Table 6.6.

VRW is used to test the estimate of the W+jets background. The selection is similar to CRW with additional cuts on $\Delta\phi(j, E_{\text{T}}^{\text{miss}})_{\text{min}}$, aplanarity, and $E_{\text{T}}^{\text{miss}}/m_{\text{eff}}$(Nj) or $E_{\text{T}}^{\text{miss}}/\sqrt{H_{\text{T}}}$ corresponding to the signal region selection.

VRWν is identical to VRW, but instead of treating the lepton as a jet, it is treated as a missing particle and thus as a contributor to the missing transverse momentum.

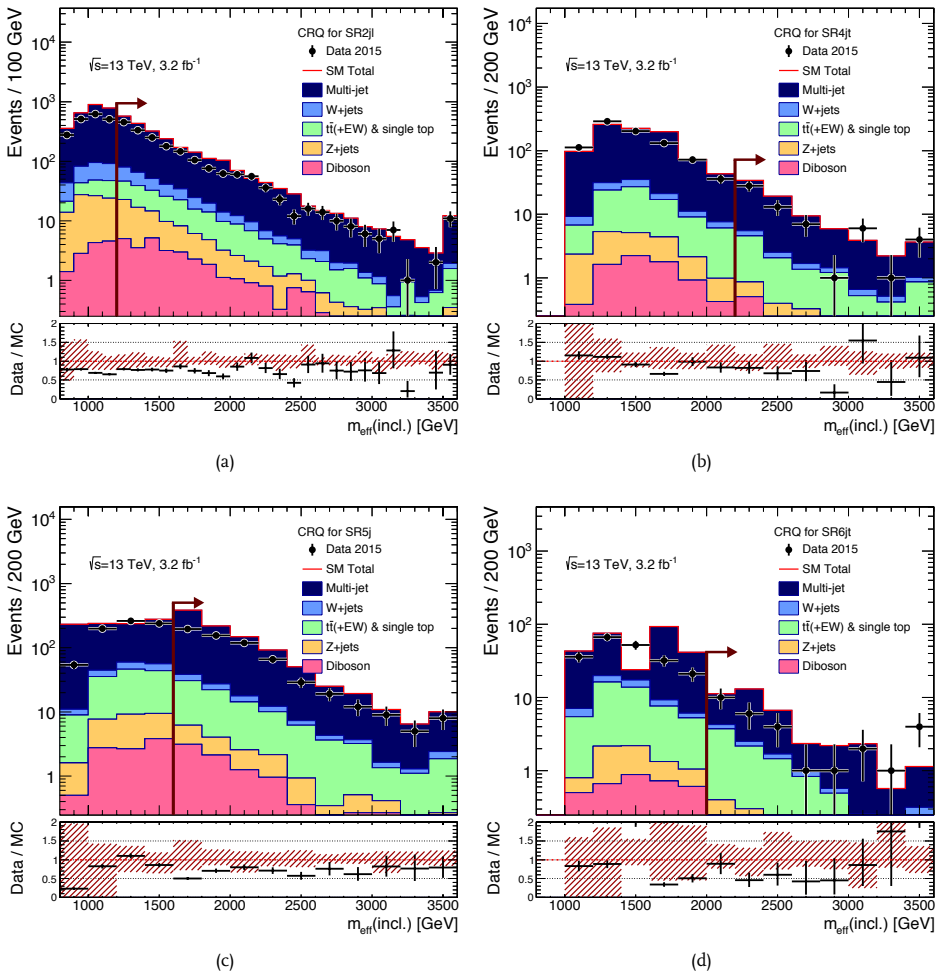

Fig. 6.10 · Observed and expected $m_{\text{eff}}(\text{incl.})$ distributions in 2jl (a), 4jt (b), 5j (c), and 6jt (d) regions of CRQ at $\sqrt{s} = 13$ TeV before the final cut on $m_{\text{eff}}(\text{incl.})$. The histograms show the expected background from simulation normalised to the luminosity before the fit. The last bin includes the overflow. The red arrow indicates the cut on $m_{\text{eff}}(\text{incl.})$. The red hatched error band includes the combined uncertainty coming from detector uncertainties, Monte Carlo statistics, and theoretical modeling.

VRT is used to test the top background estimate. The selection is similar to CRT with additional cuts on $\Delta\phi(j, E_{\text{T}}^{\text{miss}})_{\text{min}}$, aplanarity, and $E_{\text{T}}^{\text{miss}}/m_{\text{eff}}(\text{Nj})$ or $E_{\text{T}}^{\text{miss}}/\sqrt{H_{\text{T}}}$ corresponding to the signal region selection.

VRTν is identical to VRT, but instead of treating the lepton as a jet, it is treated as a missing particle and thus as a contributor to the missing transverse momentum.

VRQa is testing the multijet background estimate and especially the extrapolation in $E_{\mathrm{T}}^{\mathrm{miss}}/m_{\mathrm{eff}}(\mathrm{Nj})$ or $E_{\mathrm{T}}^{\mathrm{miss}}/\sqrt{H_{\mathrm{T}}}$ by reverting the cuts in CRQ to be identical to that of the the signal regions.

VRQb is testing the multijet background estimate and especially the extrapolation in $\Delta\phi(j, E_{\mathrm{T}}^{\mathrm{miss}})_{\mathrm{min}}$ by imposing a intermediate cut on $\Delta\phi(j, E_{\mathrm{T}}^{\mathrm{miss}})_{\mathrm{min}}$ between the CRQ cut and the signal region cut.

6.7 Systematic Uncertainties

Systematic uncertainties related to the reconstruction of objects such as jets, leptons, and $E_{\mathrm{T}}^{\mathrm{miss}}$ described in Chapter 3, as well as uncertainties related to the modeling of the physics processes in simulations the signal and background samples can affect the expected number of events of both background and signal in the control, validation, and signal regions. The sources and sizes of the uncertainties are studied and is finally included into the likelihood-fit.

6.7.1 Uncertainties on Background

The dominant experimental uncertainties are the uncertainties on the jet energy scale (JES) and jet energy resolution (JER). The sizes of the JES and JER uncertainties depend on the p_{T} and η of the jet and are obtained by separate analyses [160, 167, 241, 168]. An uncertainty on the resolution and scale of the contribution to the calculation of the missing transverse momentum from tracks not associated to any reconstructed object is included as well (referred to as "$E_{\mathrm{T}}^{\mathrm{miss}}$" in Table 6.7). Uncertainties arising from b-tagging and lepton energy scale and resolution were found to be negligible and are therefore not included. The uncertainty on luminosity of 5% is expected to have a minor effect as it will cancel out in the normalisation factors from control regions to signal and validation regions.

The uncertainties on the modeling of W+jets and Z+jets are included by comparing a sample generated with MG5_aMC@NLO to a sample generated with SHERPA. The uncertainty on the normalisation-factor of γ+jets in CRγ, κ, is found to be $\simeq 7\%$. The $t\bar{t}$-modeling is studied by a comparison of samples generated with aMC@NLO and POWHEG-BOX. To study the uncertainty related to the choice of factorisation and renormalisation scale, μ_F and μ_R, in $t\bar{t}$-production, samples are generated where μ_F and μ_R are increased and decreased by a factor of two. The choice of Monte Carlo tune used in simulation of $t\bar{t}$-events is studied by comparing samples tuned with PERUGIA2012 to samples tuned with A14. The uncertainty on the diboson background is estimated by varying the matching, factorisation, and renormalisation scales as well as the parton distribution functions set. Due to the tight selection in the signal regions and to ensure that the uncertainty is not under-estimated, a flat uncertainty of 50% is applied in all regions.

The uncertainty coming from the limited statistics of the Monte Carlo samples used in estimating the Standard Model background is $\sqrt{N_{\mathrm{MC}}}$ normalised to the full integrated luminosity of the dataset. The number of observed events in the control regions have an impact on the precision of the background estimate as well.

The systematic uncertainties can be treated in different ways in the likelihood-fit. They can either be fully correlated over all regions and all processes, correlated over all regions for each

Name	Characteristic Scale	Treatment	Comment
Luminosity	5%	Fully correlated	
MC statistics	-	Uncorrelated	All MC samples
Physics Process Modelling			
Total cross section	Diboson (50%)	Uncorrelated	Pure MC estimate
Generator comparison	MG5_aMC@NLO and SHERPA	Per process	$W/Z/\gamma$+jets
γ+jets normalisation, κ	$\simeq 7\%$	Per process	γ+jets
Generator comparison	aMC@NLO and POWHEG-BOX	Per process	$t\bar{t}$
μ_R/μ_F scale variation	$\mu_{R/F} \times [0.5, 2.0]$	Per process	$t\bar{t}$
Generator Tune	PERUGIA2012 and A14	Per Process	$t\bar{t}$
Object Modelling			
Jet energy scale	Dependent on jet	Fully correlated	
Jet energy resolution	Dependent on jet	Fully correlated	
$E_{\mathrm{T}}^{\mathrm{miss}}$		Fully correlated	

Table 6.7 · The sources of the systematic uncertainties, their characteristic scale, their treatment in the fit, and eventual comments on the relevant background process of region the uncertainty.

process, or uncorrelated. A summary of the sources of systematic uncertainties their characteristic scale, treatment in the likelihood-fit, and eventual comments is given in Table 6.7.

6.7.2 Uncertainties on Signal

Both experimental and theoretical uncertainties will affect the event yield of the simplified models of squark and gluino-production in the signal regions. These uncertainties are taken into account when the model-dependent limits are calculated.

The experimental uncertainties will affect the acceptance of the SUSY models in the different signal regions. The uncertainties on jet energy scale, jet energy resolution, and on the missing transverse momentum are included in the fit together with the uncertainties on the background.

The uncertainty on the production cross section of the SUSY signal is estimated by varying the factorisation and renormalisation scale, the PDF set, and the strong coupling and calculating the cross section for each variation. The procedure for obtaining the central value and the uncertainty is identical to the one described in Section 5.7.2. The limit is calculated using the central value of the cross section. The uncertainty on the SUSY model production cross section is included by re-calculating the limits with a cross sections of $\sigma \pm \Delta\sigma$ and they are then reported as separate limits.

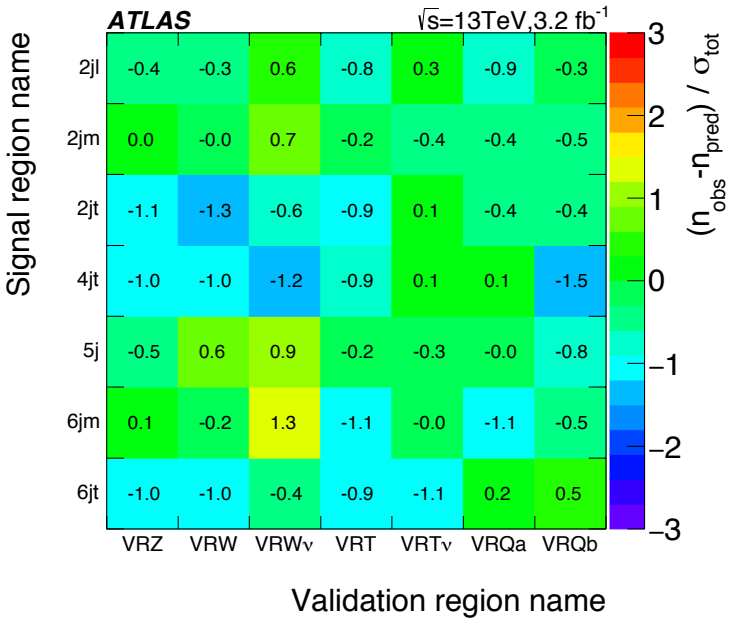

Fig. 6.11 · Pulls of all the validation regions at $\sqrt{s} = 13$ TeV. The pulls are calculated including the uncertainty arising from the fit as well as a standard deviation of a Poisson distribution centered around the number of events predicted by the fit.

6.8 Results

The results are obtained using the statistical procedure described in Section 4.4. The results of the background-only fit in the validation regions are discussed in Section 6.8.1. The result of the background fit and the model-independent upper limits on the visible cross section in the signal regions are discussed in Section 6.8.2.

6.8.1 Validation Regions

The background-only fit is tested in a set of validation regions where the Standard Model background is estimated through normalisation factors from the control regions. In total the background estimate is tested in 49 validation regions, 7 validation regions per signal region as defined in Section 6.6.2.

The pull are calculated for each validation region as described in Section 5.8.1. The calculated pulls in all the validation regions are shown in Figure 6.11. In general a good agreement between the observed and predicted number of events are seen with few pulls exceeding 1σ and no pulls exceeding 2σ. There seems to be a bias in the pull towards negative values. However, it should be noted that the signal regions and thereby the validation regions as well are not mutually exclusive and a simple combination of all the pulls is therefore not possible.

The largest pull is observed in VRQb of the 4jt-region with a value of 1.5σ. The number of events observed in that validation region is 7 while the prediction from the fit is 16.0 ± 4.8. Built on experience from the analysis performed with the dataset obtained with $\sqrt{s} = 8$ TeV, it is expected that the contribution of the multijet background in the signal regions is very small. A 1.5σ deviation in a multijet enriched region as VRQb is therefore found to be acceptable.

A good agreement between prediction and observation with pulls within a 2σ-window are seen in all validation regions. This ensures that the background estimate is robust and the signal regions can then be studied.

6.8.2 Signal Regions

Distributions of the inclusive effective mass in all signal regions before the final cut on m_{eff}(incl.) are shown in Figure 6.12 and 6.13. The expected distributions are shown before the fit and the red hashed error bars in the lower panel includes all systematic uncertainties without taking into account eventual correlations. In each signal region a signal point is shown to indicate where an eventual signal would show up and how it would look.

The agreement between the observed and expected distributions are in general within the statistical and systematic uncertainties, but there are some deviations. Especially in the m_{eff}(incl.) distributions with high jet multiplicities in Figures 6.13 similar patterns in the deviations are seen between 5j and 6jt. Since the signal regions are not mutually exclusive, an eventual excess or deficit in a bin of the m_{eff}(incl.) distribution in one signal region can be present as well in other signal regions.

The results in the one-binned signal regions after the fit are shown in Figure 6.14, where the observed number of events is compared to the expectation from the background-only fit. In the lower panel, the ratio of the observed number of events to the expected number of events is shown together with the uncertainty coming from the fit. It is seen that there are no large excesses in any of the signal regions.

The normalisation factor of a process, μ(process), obtained from the expected number of events, $N_{\text{CR}}^{\text{exp,process}}$, and the observed number of events subtracted the contribution from other processes,$N_{\text{CR}}^{\text{obs,process}}$ in a control region is given in Eq. 4.10 as:

$$\mu(\text{process}) = \frac{N_{\text{CR}}^{\text{obs,process}}}{N_{\text{CR}}^{\text{exp,process}}}. \tag{6.2}$$

The normalisation factors of the four backgrounds obtained from the background-only fit are shown for each of the signal regions in Figure 6.15. The normalisation factors of the top background, μ(Top), are all smaller than one with small errors and a central value ranging from 0.4 to 0.8. The normalisation factors of W+jets and Z+jets are in general in agreement with unity within 1σ, but with larger errors than μ(Top). The ranges of $\mu(W + \text{jets})$ and $\mu(Z + \text{jets})$ are 0.7 to 1.2 and 1.0 to 1.6, respectively. As none of the multijet background events from simulation survives the cuts of the signal regions with high jet-multiplicity ($n_{\text{jets}} \geq 4$), the normalisation factors of the multijet background are only shown in the 2-jet regions. The normalisation factors of the multijet background in the 2-jet regions are smaller than one with larger errors.

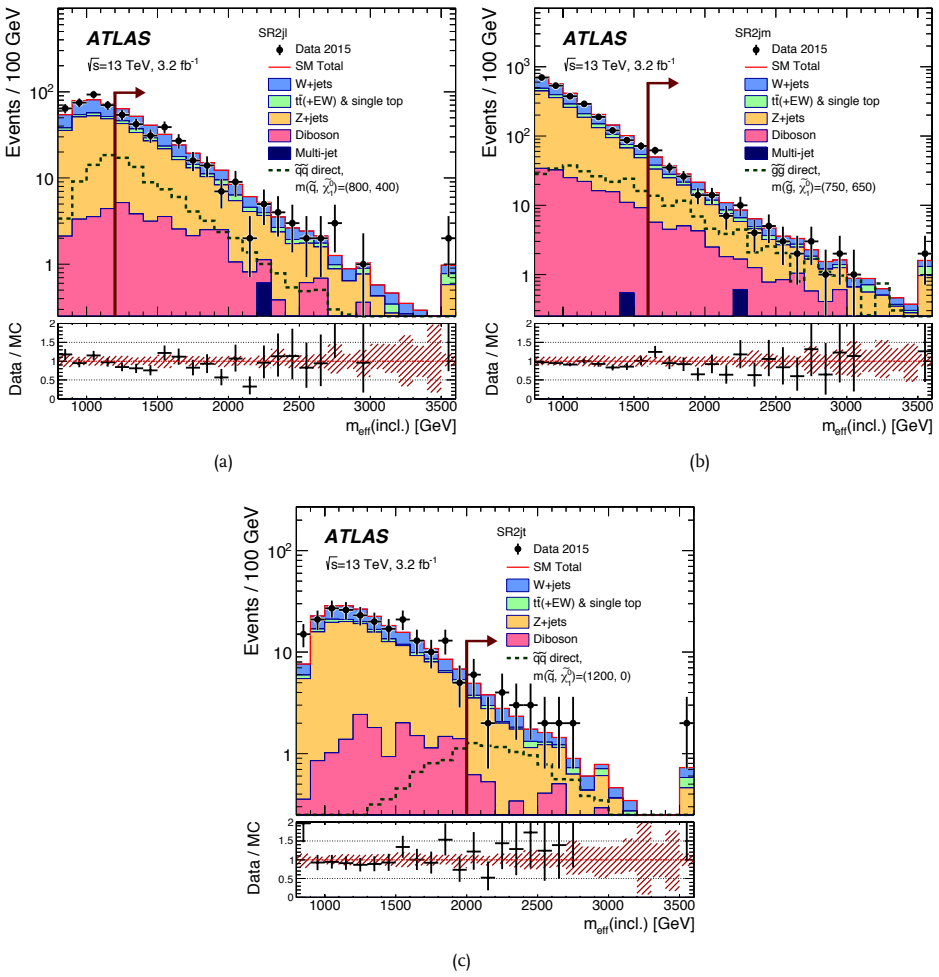

Fig. 6.12 · Observed m_{eff}(incl.) distributions in signal regions at $\sqrt{s} = 13$ TeV: 2jl (a), 2jm (b), and 2jt (c) before the final cut on m_{eff}(incl.). The histograms show the expected background distribution prior to the fit obtained only from simulation and normalised to the luminosity. SUSY models with parameters given in GeV are shown for comparison. The red arrows indicate the specific cuts on m_{eff}(incl.). In the lower panel, the red hashed error band includes experimental, MC statistical, and theoretical modeling uncertainties.

The number of background events predicted by simulation only and by the fit as well as the observed number of events in each signal region are given in Table 6.8. A good agreement between the observed number of events and the number of events predicted by the fit is seen.

Model-independent upper limits in each signal region are calculated as described in Section 4.4.3. The model-independent upper limits on the visible cross section of physics beyond the Standard Model ($\langle\epsilon\sigma\rangle^{95}_{\text{obs}}$), on the visible number of signal events (S^{95}_{obs}), and on the visible number

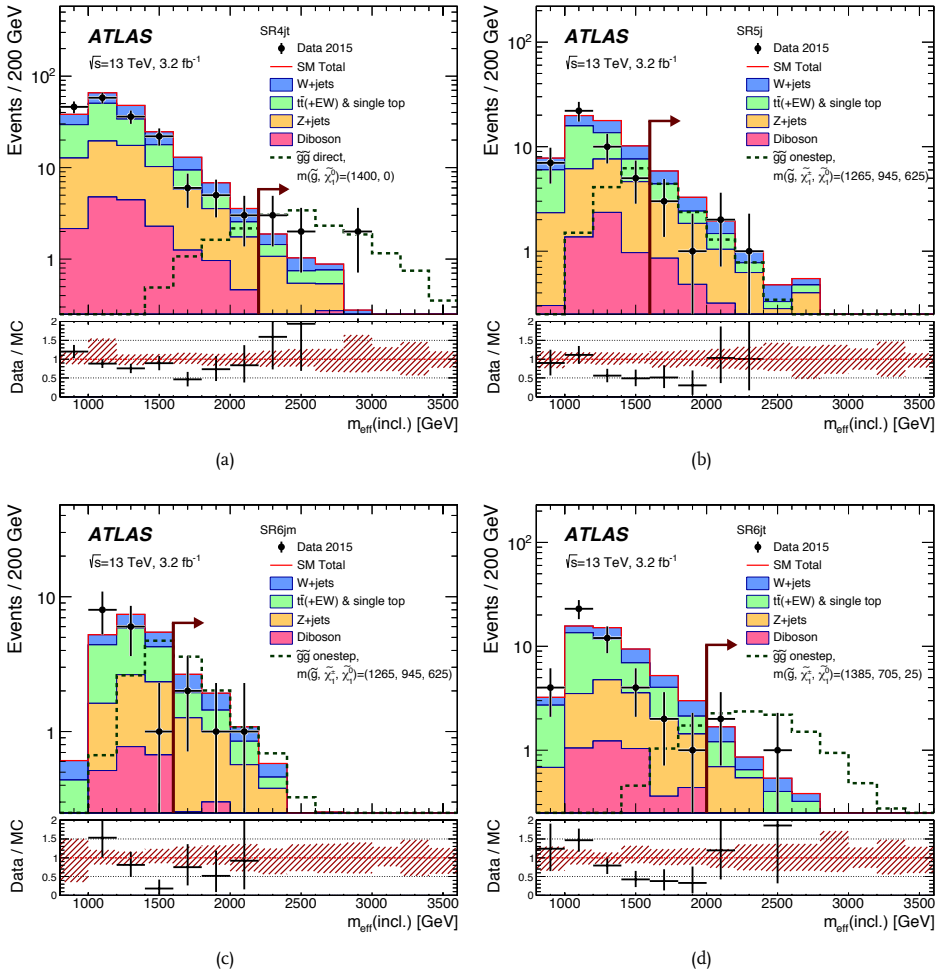

Fig. 6.13 · Observed m_{eff}(incl.) distributions in signal regions at $\sqrt{s} = 13$ TeV: 4jt (a), 5j (b), 6jm (c), and 6jt (d) before the final cut on m_{eff}(incl.). The histograms show the expected background distribution prior to the fit obtained only from simulation and normalised to the luminosity. SUSY models with parameters given in GeV are shown for comparison. The red arrows indicate the specific cuts on m_{eff}(incl.). In the lower panel, the red hashed error band includes experimental, MC statistical, and theoretical modeling uncertainties.

of signal events given the expected number of events (S^{95}_{exp}) are calculated at a 95% confidence level in each signal region and given in Table 6.8.

The probability of the (in-)compatibility of the observed number of events with the number of events estimated by the fit is quantified in Table 6.8 with the p-value as well as the number of Gaussian standard deviations corresponding to the p-value, Z. The p-value is bound from above at 0.50 corresponding to a 0σ deviation. The p-value of any region where fewer events are

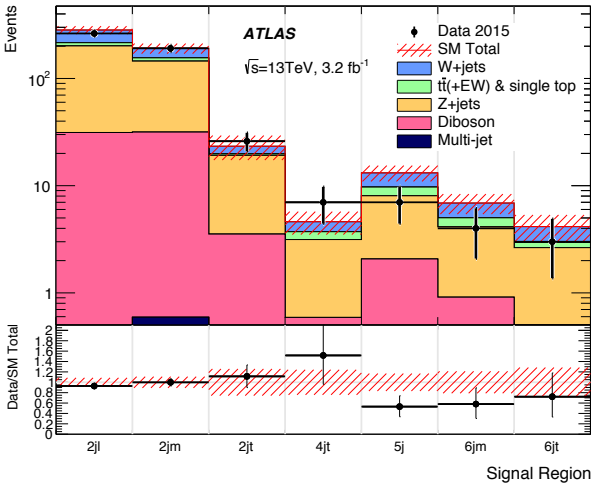

Fig. 6.14 · Comparison of observed and expected event yields after the fit as a function of the signal regions at $\sqrt{s} = 13$ TeV. The red, hashed area illustrates the uncertainty on the background estimate.

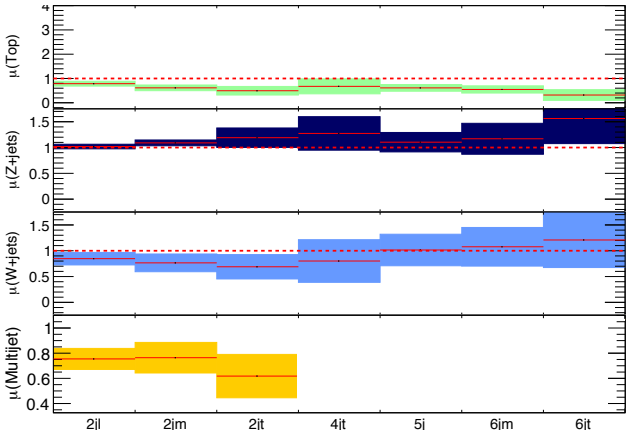

Fig. 6.15 · Normalisation factors for the four major backgrounds, μ(Top), $\mu(Z+\text{jets})$, $\mu(W+\text{jets})$, and μ(Multijets), obtained from the background-only fit as a function of the signal regions at $\sqrt{s} = 13$ TeV. Since there are no multijet events from the Monte Carlo sample in the 4jt, 5j, 6jm, and 6jt regions, the normalisation factors of multijet are not shown in those regions.

observed than expected will therefore be 0.50. It is seen that there are no large excesses in any of the signal regions. The region with the largest excess is 4jt with a p-value of 0.17 corresponding to a 0.94σ deviation.

Signal Region	2jl	2jm	2jt	4jt	5j	6jm	6jt
			MC expected events				
Diboson	31	31	3.5	0.6	2.1	0.9	0.4
Z/γ^*+jets	167	104	13	2.0	5.4	2.8	1.4
W+jets	80	46	5.0	1.1	3.4	1.7	1.0
$t\bar{t}$(+EW) + single-t	18	17	1.3	0.9	2.7	1.6	1.0
Multi-jet	0.7	0.8	0.04	–	–	–	–
			Fitted background events				
Diboson	31 ± 15	31 ± 16	3.5 ± 1.8	0.6 ± 0.3	2.1 ± 1.1	0.9 ± 0.5	0.43 ± 0.27
Z/γ^*+jets	170 ± 16	114 ± 11	16 ± 4	2.5 ± 0.9	6.0 ± 1.3	3.2 ± 1.0	2.2 ± 1.0
W+jets	68 ± 10	35 ± 9	3.5 ± 1.3	0.9 ± 0.6	3.5 ± 1.3	1.9 ± 0.9	1.2 ± 0.7
$t\bar{t}$(+EW) + single-t	14 ± 3	10 ± 3	0.7 ± 0.4	0.6 ± 0.3	1.7 ± 0.9	0.9 ± 0.5	0.32 ± 0.26
Multi-jet	0.49 ± 0.05	0.6 ± 0.4	$0.02^{+0.10}_{-0.02}$	–	–	–	–
Total bkg	283 ± 24	191 ± 21	23 ± 4	4.6 ± 1.1	13.2 ± 2.2	6.9 ± 1.5	4.2 ± 1.2
Observed	263	191	26	7	7	4	3
$\langle\epsilon\sigma\rangle^{95}_{\text{obs}}$ [fb]	16	15	5.2	2.7	1.7	1.7	1.6
S^{95}_{obs}	52	48	17	8.7	5.4	5.4	5.0
S^{95}_{exp}	53^{+22}_{-12}	48^{+16}_{-10}	$14.0^{+5.4}_{-3.9}$	$6.3^{+2.9}_{-1.7}$	$8.7^{+4.2}_{-1.9}$	$6.6^{+3.2}_{-1.5}$	$5.7^{+2.8}_{-1.5}$
p_0 (Z)	0.50 (0.00)	0.50 (0.00)	0.40 (0.26)	0.17 (0.94)	0.50 (0.00)	0.50 (0.00)	0.50 (0.00)

Table 6.8 · Numbers of events observed in the signal regions used in the analysis compared with background expectations obtained both from pure simulation and from the background-only fit at $\sqrt{s} = 13$ TeV. Empty cells (indicated by a '-') correspond to estimates smaller than 0.01. The p-values (p_0) give the probabilities of the observations being consistent with the estimated backgrounds. They are bounded above by 0.5. Between the parentheses of p-values, the number of equivalent Gaussian sigma (Z) are given. The 95% CL upper limits on the visible cross-section ($\langle\epsilon\sigma\rangle^{95}_{\text{obs}}$), the visible number of signal events (S^{95}_{obs}) and the number of signal events (S^{95}_{exp}) given the expected number of background events (and $\pm 1\sigma$ excursions on the expectation) are given as well.

Effect of the Systematic Uncertainties

The various sources of systematic uncertainties on the background estimate described in Section 6.7.1 all contribute to the total uncertainty on the estimated background yield in each signal region. The sources of uncertainty have different impacts in the various signal regions. A breakdown of the systematic uncertainties is given in Table 6.9 where the contribution from each source is given and the fraction of the source compared to the total uncertainty is illustrated by purple bars. It should be noted that some of the uncertainties might be correlated and a combination of the numbers in Table 6.9 might not result in the total uncertainty. The total uncertainty differs depending on the signal region and ranges from 8% in 2jl to 29% in 6jt.

The uncertainties on the normalisation factors, $\Delta\mu_X$, are in general main contributors to the uncertainty. The uncertainties are dominated by the statistical uncertainty in the control regions. Especially the uncertainties on the normalisation factors of Z+jets and W+jets are dominant in most regions since they are the major backgrounds. The contribution from the uncertainty on the

Channel	2jl	2jm	2jt
Total bkg	283	191	23
Total bkg unc.	24	21	4
$\Delta\mu_{\text{Z+jets}}$	7	6	2.5
$\Delta\mu_{\text{W+jets}}$	10	8	1.2
$\Delta\mu_{\text{Top}}$	1.8	2.0	0.23
$\Delta\mu_{\text{Multijets}}$	0.05	0.09	0.1
MC statistics	–	2.3	0.5
CRγ corr. factor	11	7	1.0
Theory Z+jets	8	4	2.4
Theory W+jets	2.9	2.5	0.5
Theory Top	2.1	2.1	0.28
Theory Diboson	15	15	1.0
Jet/MET	0.7	0.6	0.09

Channel	4jt	5j	6jm	6jt
Total bkg	4.6	13.2	6.9	4.2
Total bkg unc.	1.1	2.2	1.5	1.2
$\Delta\mu_{\text{Z+jets}}$	0.7	1.0	0.8	0.7
$\Delta\mu_{\text{W+jets}}$	0.5	1.1	0.7	0.5
$\Delta\mu_{\text{Top}}$	0.26	0.4	0.24	0.22
$\Delta\mu_{\text{Multijets}}$	–	–	–	–
MC statistics	0.31	0.5	0.4	0.32
CRγ corr. factor	0.17	0.4	0.21	0.15
Theory Z+jets	0.6	0.6	0.5	0.6
Theory W+jets	0.29	0.7	0.5	0.4
Theory Top	0.12	0.8	0.4	0.13
Theory Diboson	–	1.0	–	–
Jet/MET	0.1	0.4	0.21	0.19

Table 6.9 · Breakdown of the dominant systematic uncertainties on background estimates at $\sqrt{s} = 13$ TeV. The individual uncertainties can be correlated, and do not necessarily add up quadratically to the total background uncertainty. The uncertainties on the normalisation factors, $\Delta\mu_X$, are the result of the control region statistical uncertainties and the systematic uncertainties entering a specific control region. The pink bar shows the fraction of the uncertainty on the total event yield. The purple bar shows the fraction of the specific systematic uncertainty compared to the total uncertainty.

the normalisation factor of the top background becomes larger at higher jet-multiplicities where the top background is more dominant. Since very few multijet events survive into the 2-jet signal region selections, the uncertainty on the multijet background is very small in those regions and zero in the remaining regions where no multijet events survive the event selection.

The uncertainty arising from limited statistics in the Monte Carlo samples contributes the most in the signal regions with the tightest cuts where the estimated number of background events is lower, e. g. signal regions with a minimum jet-multiplicity of 4 or higher.

The normalisation of γ+jets to Z+jets as described in Section 6.6.1 results in uncertainties coming from the normalisation factor, κ. The uncertainty coming from the correction factor has

the largest contribution to the total uncertainty in 2jl and 2jm and ranges from 12.5% in 6jt to 45% in 2jl.

The theoretical uncertainties on Z+jets, W+jets, and top include the generator comparisons as well as the generator tune comparison, renormalisation and factorisation scale variation studied in the $t\bar{t}$ sample. The theoretical uncertainty on Z+jets is dominant in signal regions with high cuts on m_{eff}(incl.) such as 2jt, 4jt, and 6jt.

The theoretical uncertainty on the diboson production is estimated to be 50% in all regions based on dedicated studies of samples simulated with variations on the value of the matching, factorisation, and renormalisation scale and different PDF sets. Since it is a flat uncertainty applied in all regions, it has an impact on the normalisation factors of other background processes in the control regions and is expected to be a big contributor to the systematic uncertainty. In regions where the uncertainty on the diboson background is non-negligible, it has a large contribution to the total uncertainty. It is the dominant systematic uncertainty in 2jl and 2jm, where it accounts for 63% and 71% of the total uncertainty, respectively.

The uncertainties arising from the jet energy scale, jet energy resolution and $E_{\text{T}}^{\text{miss}}$ are combined into "Jet/$E_{\text{T}}^{\text{miss}}$" in Table 6.9. They are minor contributors to the uncertainty in all signal regions with the largest contribution to the total uncertainty in 6jt of 15%.

6.9 Limits on Simplified Models

As described in Section 6.8.2, no significant excesses were observed in any of the signal regions. The result of the analysis is therefore presented as model-dependent exclusion limits in the simplified models described in Section 6.1.1. The fit is done including the signal model contribution in the signal regions and eventual leakage of signal into control regions is taken into account as described in Section 4.4.4. The uncertainties on the signal acceptance is included in the fit.

The expected and observed exclusion limits at 95% confidence level in the simplified models with squark-pair production and gluino-pair production with direct decays and gluino-pair production with onestep decays through $\tilde{\chi}_1^{\pm}$ are presented in Figure 6.16 along with the strongest signal region with the largest sensitivity and in Figure 6.17 together with the upper limit on the production cross section in each point.

The blue, dashed line indicates the expected limit and the red, solid line the observed limit. The points lying within the area formed by the solid red line and the diagonal indicating the part of parameter space where the decays are no longer possible are excluded at 95% C.L. The yellow band includes the systematic uncertainties on the background as well as the experimental uncertainties on the signal acceptance while the dashed, red lines represent the limits calculated with the nominal sparticle production cross section $\pm 1\sigma_{\text{Theory}}^{\text{SUSY}}$. The grey areas show the limits obtained with 20.3 fb^{-1} at $\sqrt{s} = 8$ TeV [2].

The limit on a simplified model of $\tilde{q}\tilde{q}$-production with direct decays is shown in Figures 6.16a and 6.17a. It is seen that the limit obtained with the dataset of 3.2 fb^{-1} collected at $\sqrt{s} = 13$ TeV exceeds the limit based on 20.3 fb^{-1} collected at $\sqrt{s} = 8$ TeV everywhere. The limit on $m_{\tilde{q}}$ reaches 1030 GeV when $\tilde{\chi}_1^0$ is massless while the limit on $m_{\tilde{\chi}_1^0}$ reaches a plateau at 400 GeV for squark

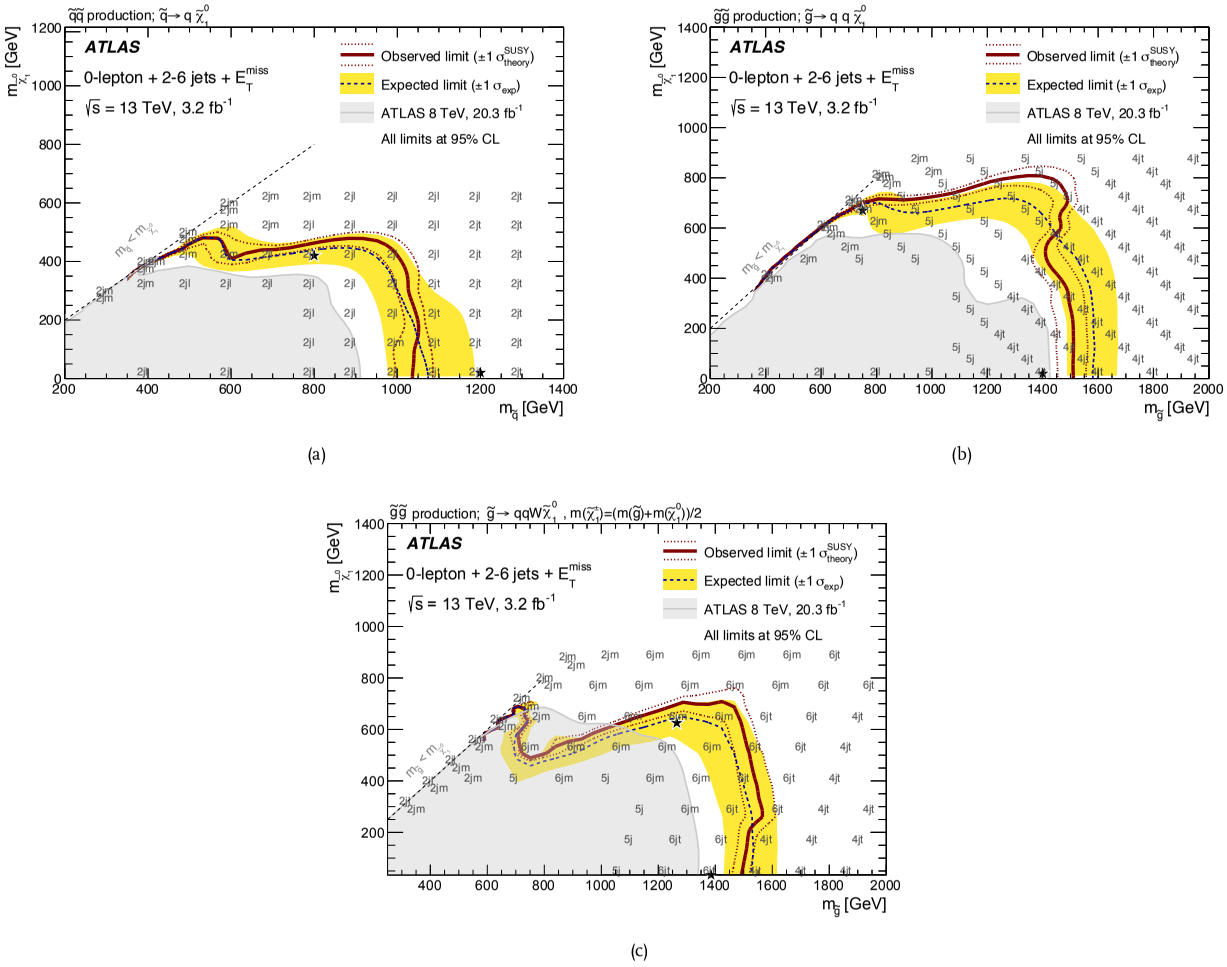

Fig. 6.16 · Expected (blue) and observed (red) exclusion limits at 95% CL on simplified models of $\tilde{q}\bar{\tilde{q}}$ (a), and $\tilde{g}\,\tilde{g}$ (b) production with direct decays, and $\tilde{g}\,\tilde{g}$ (c) production with onestep decays through $\tilde{\chi}_1^\pm$ in the plane of $m_{\tilde{q},\tilde{g}}$ and $m_{\tilde{\chi}_1^0}$ at $\sqrt{s} = 13$ TeV. The strongest signal region in each point is shown. The shaded grey area shows the limit at $\sqrt{s} = 8$ TeV [2]. The yellow bands indicate the 1σ uncertainty on the limit arising from the experimental, and background-only theoretical uncertainties. The dashed red lines indicate the 1σ uncertainty on the signal cross section.

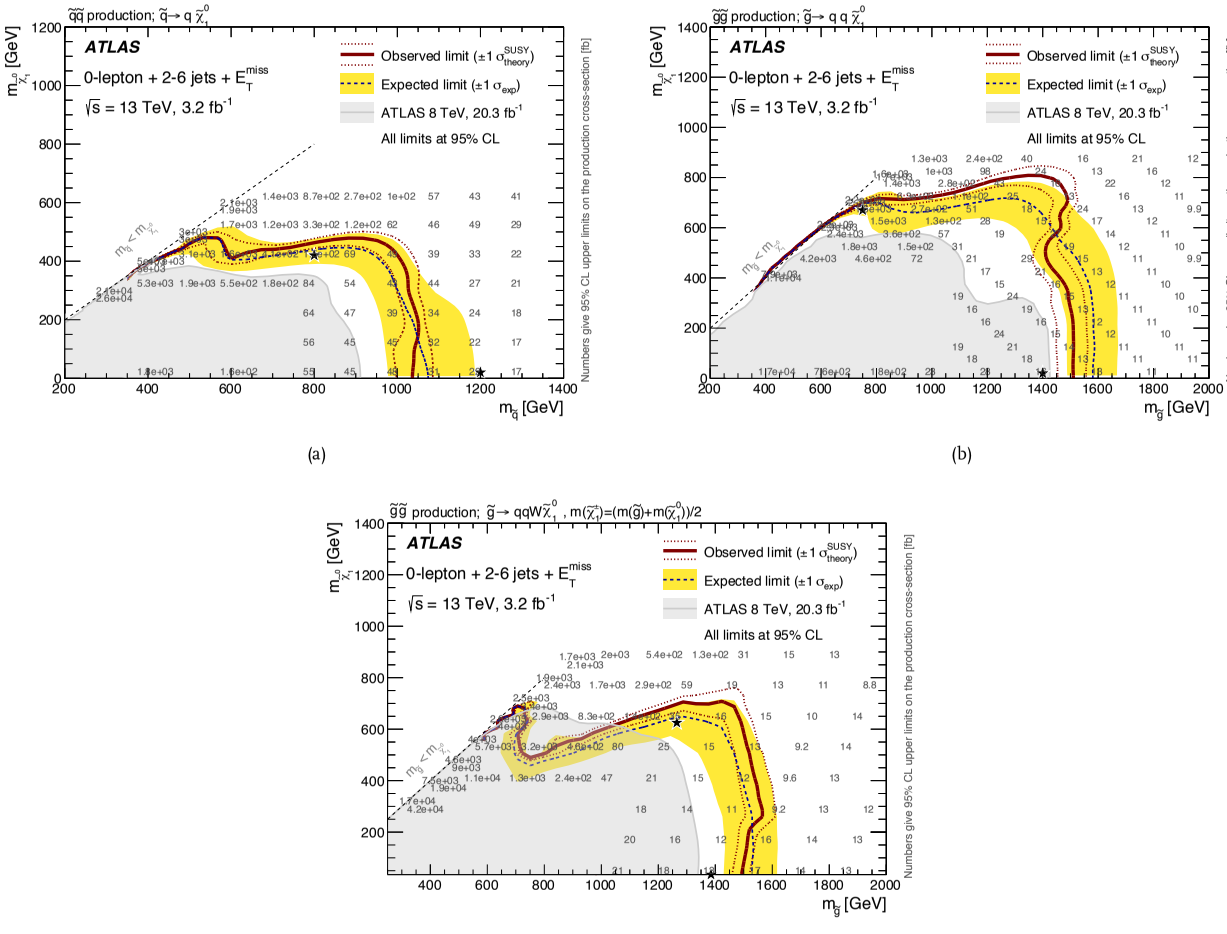

Fig. 6.17 · Expected (blue) and observed (red) exclusion limits at 95% CL on simplified models of $\tilde{q}\tilde{q}$ (a), and $\tilde{g}\tilde{g}$ (b) production with direct decays, and $\tilde{g}\tilde{g}$ (c) production with onestep decays through $\tilde{\chi}_1^{\pm}$ in the plane of $m_{\tilde{q},\tilde{g}}$ and $m_{\tilde{\chi}_1^0}$ at $\sqrt{s} = 13$ TeV. The upper limit on the production cross section at 95% C.L. of each point is shown. The shaded grey area shows the limit at $\sqrt{s} = 8$ TeV [2]. The yellow band indicates the 1σ uncertainty on the limit arising from the experimental, and background-only theoretical uncertainties. The dashed red lines indicate the 1σ uncertainty on the signal cross section.

masses in a range from 400 GeV to 1000 GeV. It is seen in Figure 6.16a that as expected, the di-jet regions are the strongest signal regions in all points. As seen in Figure 6.17a, the upper limits on the squark-pair production cross section decrease with increasing squark mass and are in general higher when $m_{\tilde{\chi}_1^0}$ is larger.

As seen in Figures 6.16b and 6.17b, the limit on gluino-pair production with direct decays obtained with the analysis presented in this chapter exceeds the previously obtained limits. The limit on the gluino mass reaches 1510 GeV when the $\tilde{\chi}_1^0$ is massless, while the limit on $m_{\tilde{\chi}_1^0}$ reaches 800 GeV when $m_{\tilde{g}}$ ranges from 1300 GeV to 1500 GeV. From Figure 6.16b it is seen that the strongest signal region is 4jt when the difference between $m_{\tilde{g}}$ and $m_{\tilde{\chi}_1^0}$ is large. The strongest region is the 5j region as the mass of $\tilde{\chi}_1^0$ increases and at high mass-compression, 2jm is the strongest signal region. It is seen that the observed limit exceeds the expected when the strongest region is 5j. This is due to fewer observed events compared to the expectation in this region. The upper limits on the cross section of $\tilde{g}\tilde{g}$-production with direct decay decrease with increasing $m_{\tilde{g}}$ as seen in Figure 6.17b and range from $\sim 10^3$-10^4 fb at gluino masses of 700-900 GeV to ~ 10 fb at higher gluino masses. In general the upper limits on the production cross section increase with increasing $m_{\tilde{\chi}_1^0}$.

The limit on a simplified model of $\tilde{g}\tilde{g}$-production with onestep decays through $\tilde{\chi}_1^\pm$ into a final state of quarks, $\tilde{\chi}_1^0$, and decay products of W bosons is presented in Figures 6.16c and 6.17c. The mass of the gluino and $\tilde{\chi}_1^0$ are free parameters while the mass of $\tilde{\chi}_1^\pm$ is fixed to $m_{\tilde{\chi}_1^\pm} = (m_{\tilde{g}} + m_{\tilde{\chi}_1^0})/2$. The limit achieved with the analysis presented in this chapter exceeds the already existing limit only when $\tilde{\chi}_1^0$ is lighter than 700 GeV and the gluino is heavy. At higher values of $m_{\tilde{\chi}_1^0}$, the already existing limit is as strong or even stronger especially in the region where $m_{\tilde{g}}$ ranges from 700 GeV to 1100 GeV. The previous limit is stronger because it was obtained from the statistical combination of the 0- and 1-lepton analyses performed on data collected at $\sqrt{s} = 8$ TeV and thereby exceeding the limits of the individual analyses. Furthermore no signal region in the analysis presented in this chapter was optimised specifically for this mass-difference scenario. The limit on the gluino mass reaches $\sim$ 1500 GeV when $m_{\tilde{\chi}_1^0}$ ranges from 50 GeV to 700 GeV. The strongest signal regions are 4jt and 6jt when $\tilde{\chi}_1^0$ is massless. At higher values of $m_{\tilde{\chi}_1^0}$, 6jm is the strongest signal region while at high mass-compression 2jm takes over. The upper limits on the cross section of $\tilde{g}\tilde{g}$-production with onestep decays are presented in Figure 6.17c. The upper limits on the cross section are highest at low values of $m_{\tilde{g}}$ and decrease with increasing mass of the gluino.

6.10 Outlook

With the first dataset collected at $\sqrt{s} = 13$ TeV with an integrated luminosity of 3.2 fb^{-1}, the limits on squark and gluino masses in simplified models have exceeded the limits obtained with the 6 times larger dataset collected at $\sqrt{s} = 8$ TeV by up to 100 GeV. The reason why the limits are stronger with the smaller dataset collected at $\sqrt{s} = 13$ TeV, is the large increase in production cross section of squarks and gluinos compared to the increase in the production cross section of

the Standard Model background processes. As it was discussed in Section 6.1, the cross sections of squark and gluino pair production increase by a factor of 10-1000 when the collision energy is increased from 8 TeV to 13 TeV while the cross section of the Standard Model processes only increases by a factor of 2-3. This leads to a larger sensitivity to squark and gluino production at $\sqrt{s} = 13$ TeV.

A more precise estimate of the Standard Model background would lead to a further increase in the sensitivity. The uncertainty on the diboson background is dominant in many of the signal regions where diboson events enter. It is estimated from dedicated systematics with various matching, factorisation, and renormalisation scales to be 50% in all signal regions. The choice of 50% for the flat uncertainty is conservative and chosen to ensure coverage in all signal regions. The uncertainty on the diboson background has an effect on the normalisation factors of the control regions as well, since diboson events are present in most control regions. If instead the diboson background was estimated from a control region, the uncertainty could be estimated individually for each signal region leading to a smaller total uncertainty on the diboson background.

The uncertainties on the normalisation factors are dominated by the statistical uncertainty in the control regions. As more data is collected, the control regions should be more populated by events. Of course the signal region selection and thereby also the control region selection will change with increasing integrated luminosity. However, it should be ensured that there is a reasonable number of events in each control region to reduce the uncertainty on the normalisation factors.

As more data is collected, the need for a fully data-driven method for multijet background estimation grows. The cross section of multijet production from strong interaction is large and it is therefore not feasible to generate samples to describe the multijet background in a larger dataset. With an increase in integrated luminosity, the uncertainty coming from the limited statistics of the multijet sample will therefore increase. If instead the multijet background was estimated from a template obtained from the jet smearing method used in the previous analysis and described in Section 5.6.2, the sample would grow with increasing luminosity and the statistical uncertainty of the sample would not increase.

Different strategies can be employed when searching for supersymmetry. In the analysis described in this chapter, it was chosen to optimise single-binned, inclusive signal regions for discovery and include as few signal regions as possible. Another strategy would be to define mutually exclusive signal regions or not to optimise signal regions for discovery, but instead study a larger number of regions.

The CMS collaboration has published two analyses searching for supersymmetry in a final state similar to the one presented in this chapter [259, 260]. The analyses are performed on a dataset consisting of 2.3 fb^{-1}. In one of the analyses (H_{T}-analysis), 72 exclusive signal regions are defined based on intervals of number of jets, number of b-jets, intervals of H_{T}, and intervals of $H_{\mathrm{T}}^{\mathrm{miss}}$. H_{T} is the scaler sum of the p_{T} of the jets, and $H_{\mathrm{T}}^{\mathrm{miss}}$ is corresponding to $E_{\mathrm{T}}^{\mathrm{miss}}$ calculated only from jets. In the other analysis (M_{T2}-analysis), 172 exclusive signal regions are defined from intervals on the number of jets, number of b-jets, H_{T}, and M_{T2}. M_{T2} is the stransverse mass which is sensitive to the mass of particles decaying into semi-invisible final states [195].

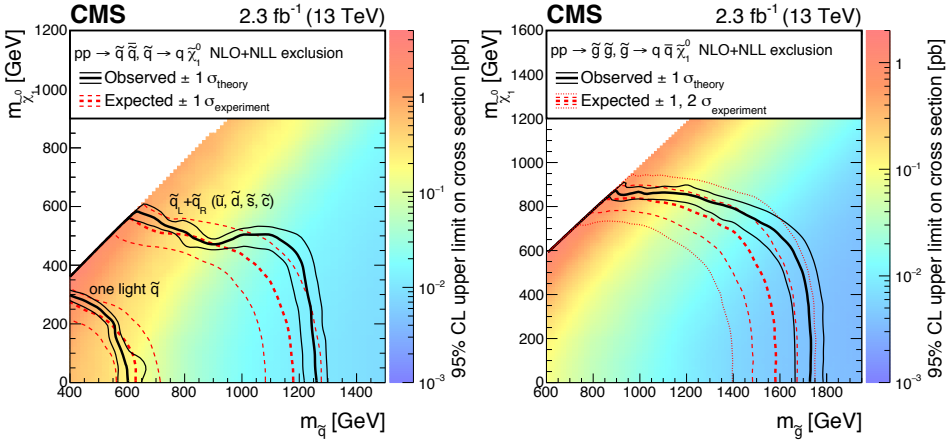

Fig. 6.18 · The expected (red) and observed (black) exclusion limits at 95% CL in simplified models of $\tilde{q}\tilde{q}$ (a), and $\tilde{g}\tilde{g}$ (b) production with direct decays as obtained from the M_{T2}-analysis published by the CMS collaboration. The limits are presented in the $m_{\tilde{q},\tilde{g}}$-$m_{\tilde{\chi}_1^0}$-plane. The limit of $\tilde{q}\tilde{q}$-production is presented with 8 mass-degenerate, light squarks and with 1 non-degenerate, light squarks. The upper limit on the production cross section at 95% C.L. are indicated on a colour scale. The Figures are taken from Ref. [260].

Of the two analyses, the strongest limits are placed by the M_{T2}-analysis. The expected and observed limits in simplified models of squark-pair and gluino-pair production with direct decays obtained by the M_{T2}-analysis using the 172 signal regions are shown in Figure 6.18.

By comparing the expected exclusion limits of the M_{T2}-analysis to the ones shown in Figure 6.17 obtained by the m_{eff}(incl.)-based analysis presented in this chapter, it is seen that even with a smaller dataset the limits placed by the M_{T2}-analysis are comparable in the gluino-model and stronger in the squark-model at high masses of gluinos or squarks. At high valuers of $m_{\tilde{\chi}_1^0}$, the M_{T2}-analysis is stronger than the m_{eff}(incl.)-based analysis in both models. It is not surprising that the M_{T2}-analysis places stronger limits than the m_{eff}(incl.)-based analysis, since the m_{eff}(incl.)-based analysis was not optimised for best exclusion, but rather for the highest discovery-potential. Furthermore it should be noted that in case an excess is seen in one of the 172 signal regions of the M_{T2}-analysis, a large look-elsewhere effect is introduced simply by the large amount of signal regions.

The sensitivity of squark and gluino production will improve with a larger dataset. The LHC has already provided 10 fb^{-1} of proton-proton collisions by Summer 2016, which will increase the discovery reach of the analysis presented in this chapter.

The sensitivity to simplified models with squark and gluino-pair production with direct decays has been studied with four integrated luminosity scenarios, 1 fb^{-1}, 2 fb^{-1}, 5 fb^{-1}, and 10 fb^{-1}, using simulation samples [261]. Signal regions with a sliding cut on m_{eff}(incl.) depending on

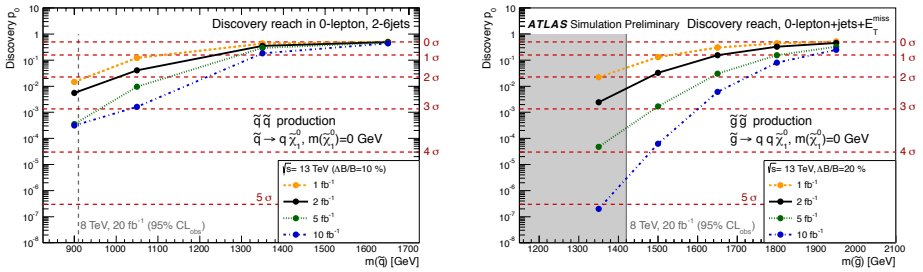

Fig. 6.19 · Discovery p_0-values at four integrated luminosities (1 fb^{-1}, 2 fb^{-1}, 5 fb^{-1}, and 10 fb^{-1}) as a function of squark mass (a) and gluino mass (b) in simplified models with direct decay. The total uncertainty on the background is assumed to be 10% in the squark model and 20% in the gluino model. The observed limit at 95% C.L. at $\sqrt{s} = 8$ TeV is overlaid for comparison.

the integrated luminosity have been optimised for largest sensitivity in the simplified models with direct decays. For each model and each luminosity scenario, a signal region is optimised. The signal regions optimised for the squark model have an event selection with at least 2 jets, $E_{\mathrm{T}}^{\mathrm{miss}}/m_{\mathrm{eff}}(\mathrm{Nj}) > 0.4$, and a cut on m_{eff}(incl.) ranging from 1600 GeV to 2000 GeV while in the signal regions optimised for the gluino model events with at least 5 jets, $E_{\mathrm{T}}^{\mathrm{miss}}/m_{\mathrm{eff}}(\mathrm{Nj}) > 0.2$, and a cut on m_{eff}(incl.) ranging from 2200 GeV to 2600 GeV are selected. In the study of the sensitivity on the squark model, an overall uncertainty of 10% on the total background is assumed, while in the gluino model the total uncertainty on the background is assumed to be 20%. This is roughly in agreement with the uncertainties observed in the signal regions in Section 6.8.2.

The expected discovery reach in the four luminosity scenarios can be seen in Figure 6.19. It is seen that the discovery reach increases significantly with an increase integrated luminosity. The expected sensitivity reach at 3σ of squark-pair production with direct decays will reach 1050 GeV with a dataset of 10 fb^{-1} which is slightly beyond the limits placed in this chapter while the expected sensitivity reach of a gluino-model with direct decay will reach 1600 GeV which is 90 GeV beyond the current limit. If no excesses are observed, the limit on squark and gluino masses will reach even higher values.

As seen, the analysis will gain sensitivity by increasing the size of the dataset. By the end of 2016, the LHC is expected to have delivered 25-30 fb^{-1}, and by 2018 the integrated luminosity should be $\mathcal{O}(100\ \mathrm{fb}^{-1})$. With a planned upgrade of the LHC a dataset of $\mathcal{O}(1000\ \mathrm{fb}^{-1})$ is expected. This will increase the discovery reach of squarks and gluinos even further.

7

Prospects of Squark and Gluino Searches at the HL-LHC

The LHC resumed proton collisions in 2015 after more than a year of scheduled shutdown. The collision energy was increased to $\sqrt{s} = 13$ TeV and by the end of 2015, a dataset of 3.2 fb^{-1} was collected by the ATLAS experiment. This is only the beginning of the data-taking period and many interesting years lie ahead in high energy physics where a considerable increase in the amount of data is expected. Already by the summer 2016, the rate of the data collection has increased resulting in a dataset with a total integrated luminosity combined with the 2015 dataset of 14 fb^{-1}.

By 2023, the LHC is expected to have delivered 300 fb^{-1} of proton-proton collisions at $\sqrt{s} = 13$ or 14 TeV. By that time, an upgrade of the LHC to the High Luminosity Large Hadron Collider (HL-LHC) is planned and proton collisions are expected to resume in 2026. The HL-LHC is expected to deliver an unprecedented amount of data corresponding to an integrated luminosity of 3000 fb^{-1} at a collision energy of $\sqrt{s} = 14$ TeV. If physics beyond the Standard Model is not discovered in the LHC dataset, it might reveal itself in the ten-fold larger dataset of the HL-LHC.

In this chapter, a sensitivity study of squark and gluino searches in final states with jets and $E_{\mathrm{T}}^{\mathrm{miss}}$ is presented. The sensitivity is studied both with the full LHC dataset of 300 fb^{-1} and the full HL-LHC dataset of 3000 fb^{-1}. The sensitivity studies are based on the strategy of the analysis described in Chapter 5 performed on a dataset of 20.3 fb^{-1} of proton collisions at $\sqrt{s} = 8$ TeV [1]. The studies presented in this chapter are publicly available in Ref. [4].

7.1 Schedule of the LHC and HL-LHC

The Large Hadron Collider has been planned for many years with the first ideas emerging in the 1980's and is expected to run for many years ahead. The schedule of the LHC operation might be subject to change in the coming years, but in this section the current schedule of the LHC and HL-LHC [262, 263] are discussed. A sketch of the planned schedule of the LHC and HL-LHC can be seen in Figure 7.1.

Protons have collided in the LHC since 2010 where the first run period of the LHC (Run-1) began with a collision energy of $\sqrt{s} = 7$ TeV. By 2012, the collision energy was increased to $\sqrt{s} = 8$ TeV and by the end of the year more than 20 fb^{-1} had been collected by the ATLAS

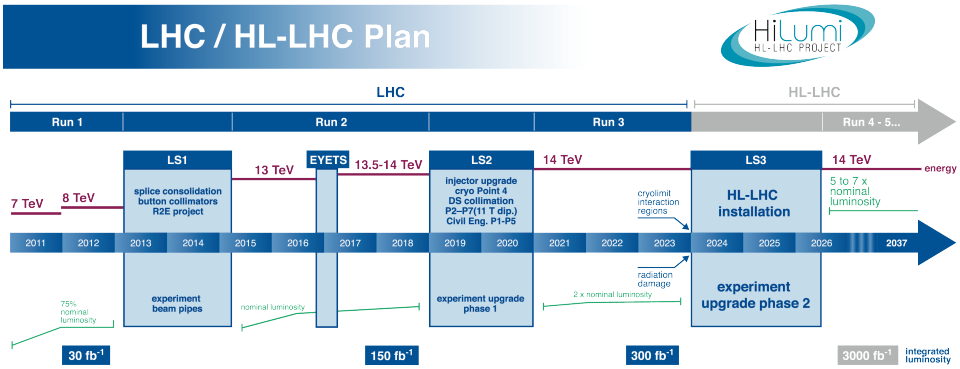

Fig. 7.1 · Planned operation schedule of the LHC and the HL-LHC. The Figure is taken from Ref. [263]

experiment marking the end of the first LHC run. The first long shutdown of the LHC (LS1) was scheduled for 2013 and 2014 where maintenance was performed on the collider to reach the design luminosity of 1×10^{34} cm^{2}s^{-1} and a beam energy close to the design value of 7 TeV per beam.

The second run period of the LHC (Run-2) began in 2015 with an increased collision energy of $\sqrt{s} = 13$ TeV. The LHC is scheduled to run at the same collision energy, but with an increasing luminosity until the end of 2016, where an extended yearly technical stop (EYETS) is expected to take place. In 2017, the LHC will resume operation potentially at a slightly increased center-of-mass energy of $\sqrt{s} = 13.5$-14 TeV and with a continual increase in luminosity until the end of 2018, where the size of the dataset of Run-2 is expected to reach ~ 150 fb^{-1}. A second long shutdown of the LHC (LS2) is planned in 2019 and 2020. During LS2, the LHC will be upgraded to reach the design beam energy of 7 TeV per proton beam and to deliver twice the design luminosity, i. e. 2×10^{34} cm^{2}s^{-1}.

After LS2, the third run period of the LHC (Run-3) is expected to commence operation in 2021 with a collision energy of $\sqrt{s} = 14$ TeV. The LHC is scheduled to run without any longer shutdowns until 2023, where the size of the dataset is expected to reach 300 fb^{-1}.

After the end of Run-3 in 2023 a long shutdown (LS3) is planned to last for 2-3 years until 2026 or 2027. During LS3, the LHC will be upgraded to the HL-LHC with an unchanged collision energy, but with an increased luminosity of $5\text{-}7 \times 10^{34}$ cm^{2}s^{-1}. The HL-LHC is foreseen to operate for 10-12 years with occasional technical shutdowns providing 250-300 fb^{-1} per year of proton collisions at $\sqrt{s} = 14$ TeV resulting in a total integrated luminosity of 3000 fb^{-1} .

7.1.1 pile-up at LHC and HL-LHC

The LHC is foreseen to be able to deliver a luminosity of 2×10^{34} cm^{2}s^{-1} during Run-3. This is expected to result in a maximum of the average pile-up ($\langle\mu\rangle$) of ~ 60 compared to $\langle\mu\rangle \sim 20$ of Run-1 and early Run-2.

With the increase of luminosity of the HL-LHC to 5-7 $\times 10^{34}$ cm^{2}s^{-1}, the average pile-up will increase as well. The average pile-up is expected to lie between 140 and 200 collisions per bunch crossing depending on the luminosity [264]. The increased pile-up will result in poorer reconstruction efficiency and resolution of physics objects. The missing transverse momentum is especially sensitive to high pile-up. This is however the cost of operating the accelerator at a higher luminosity ultimately resulting in a much larger dataset.

It was decided to use $\langle\mu\rangle = 60$ for the 300 fb^{-1} dataset of the LHC and $\langle\mu\rangle = 140$ for the 3000 fb^{-1} dataset provided by the HL-LHC to study the physics prospects of the full datasets.

7.1.2 Motivation for HL-LHC

An upgrade of the LHC to the HL-LHC is a costly procedure and the gain in precision of measurements of the Standard Model or increase in sensitivity for physics beyond the Standard Model must be convincing. The prospects of several analyses and searches have been studied aside from the sensitivity of squark and gluino searches. A short summary of some of the analyses that will benefit from the larger dataset of the HL-LHC are given here. A more detailed review of the physics prospects of the ATLAS experiment with the HL-LHC dataset is given in Refs. [265] and [266].

With the high integrated luminosity provided by the HL-LHC, the newly discovered Higgs boson can be studied in detail. The precision of the coupling strength of the Higgs boson to other particles through various decay channels and production mechanisms can increase by up to a factor of 2-3 [267]. Furthermore, the sensitivity to rare Higgs decays such as $H \to J/\psi\gamma$ [268] and $H \to Z\gamma$ [269] will increase. The self-coupling of the Higgs boson can be studied through di-Higgs production that with its low cross section will benefit from an increased dataset [270, 271]. Finally, the nature of the electroweak symmetry breaking can be studied through vector-boson scattering [272].

The sensitivity to physics beyond the Standard Model will increase as well with an increased dataset. Especially searches for electroweak supersymmetric particle production, $\tilde{\chi}^0$ and $\tilde{\chi}^{\pm}$, where the cross sections are low will benefit from a larger dataset [4].

7.2 SUSY models

The sensitivity to two simplified models are studied: squark-pair production with direct squark decays ($\tilde{q} \to q\tilde{\chi}_1^0$) and gluino-pair production with direct gluino decays ($\tilde{g} \to q\bar{q}\tilde{\chi}_1^0$). In the squark-model, both left-handed and right-handed squarks of the first two generations are assumed to be light and mass-degenerate. The free parameters of the models are the mass of the squark or gluino and the mass of $\tilde{\chi}_1^0$.

In the squark-model, two gluino-masses scenarios are studied, $m_{\tilde{g}} = 4.5$ TeV and $m_{\tilde{g}} \gg m_{\tilde{q}}$ (the gluino is decoupled). The size of the gluino mass influences the available squark-pair production mechanisms: as the gluino gets lighter, t-channel production where both $\tilde{q}\bar{\tilde{q}}$-pairs and $\tilde{q}\tilde{q}$-pairs can be produced though gluino exchange becomes more important. The t-channel production is heavily suppressed when the mass of the gluino is very high. The addition of the t-channel production mechanism changes both the kinematics of the squark-pair and the

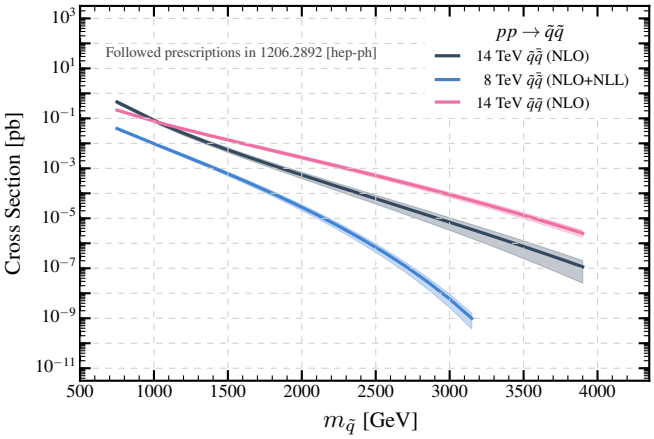

Fig. 7.2 · Cross sections of $\tilde{q}\bar{\tilde{q}}$-pair production at $\sqrt{s} = 8$ TeV with decoupled gluinos (blue) and cross sections of $\tilde{q}\bar{\tilde{q}}$-pair production (grey) and $\tilde{q}\tilde{q}$-pair production (pink) $\sqrt{s} = 14$ TeV with $m_{\tilde{g}} = 4.5$ TeV.

production cross section. The increase in the cross section when the gluino is not decoupled can be seen in Figure 7.2, where especially the $\tilde{q}\tilde{q}$ production (pink) dominates compared to the $\tilde{q}\bar{\tilde{q}}$ production cross section (grey) which is the only production available when the gluino is decoupled. In the gluino model, the squarks are assumed to be completely decoupled, i. e. $m_{\tilde{q}} \gg m_{\tilde{g}}$.

The gluino model is generated with MADGRAPH-5.0 [139] and the squark model is generated with HERWIG++-2.5.2 [138]. The samples of gluino production and squark production with decoupled gluinos were normalised to their NLO+NLL cross sections calculated using NLLFAST [210–214] while the cross sections of squark-pair production with $m_{\tilde{g}} = 4.5$ TeV were calculated with PROSPINO [218]. The samples are generated at Monte Carlo truth level and no detector simulation is performed.

7.3 Background Processes

As the sensitivity studies of the simplified models with direct decays of squarks and gluinos are targeting final states with jets and $E_{\mathrm{T}}^{\mathrm{miss}}$, identical to the final states of the analyses presented in Chapter 5 and 6, the Standard Model background processes remain the same. The background processes included in these prospect studies are $Z(\to \nu\nu)$+jets, $W(\to \ell\nu)$+jets (ℓ is e, μ or τ), $t\bar{t}(+V)$-production and diboson production. The Z+jets, W+jets, and $t\bar{t}(+V)$ background are estimated from Monte Carlo simulations. The diboson background is assumed to be 10% of the entire background in each signal region in agreement with the results of the analysis performed with $\sqrt{s} = 8$ TeV data. The multijet background was found to be of the order of $\sim 1\%$ in the analysis presented in Chapter 5 and it is therefore considered safe to ignore it in these studies.

Process	Generator	PDF set	σ [pb]	ϵ
$W(\to e\nu)$+jets	SHERPA-1.4.1	CT10	27.742	1.0
$W(\to \mu\nu)$+jets	SHERPA-1.4.1	CT10	27.742	1.0
$W(\to \tau\nu)$+jets	SHERPA-1.4.1	CT10	27.771	1.0
$Z(\to \nu\nu)$+jets	SHERPA-1.4.1	CT10	5.6657	1.0
$t\bar{t}$ (2 ℓ)	SHERPA-1.4.1	CT10	517.8	0.0116
$t\bar{t}$ (ℓ and h)	SHERPA-1.4.1	CT10	517.8	0.0179
$t\bar{t}$ (ℓ and τ_{had})	SHERPA-1.4.1	CT10	517.8	0.00815
$t\bar{t}$ (τ_ℓ and h)	SHERPA-1.4.1	CT10	517.8	0.0155
$t\bar{t}$ (τ_ℓ and τ_{had})	SHERPA-1.4.1	CT10	517.8	0.0099
$t\bar{t}$ (τ_{had} and h)	SHERPA-1.4.1	CT10	517.8	0.00936
$t\bar{t}$ (τ_{had} and τ_{had})	SHERPA-1.4.1	CT10	517.8	0.00885
$t\bar{t}$ (ℓ and τ_ℓ)	SHERPA-1.4.1	CT10	517.8	0.03058
$t\bar{t}$ (τ_ℓ and τ_ℓ)	SHERPA-1.4.1	CT10	517.8	0.00271
$t\bar{t}+W$	MADGRAPH-5.0	CTEQ6L1	0.315	1.0
$t\bar{t}+W$+jets	MADGRAPH-5.0	CTEQ6L1	0.456	1.0
$t\bar{t}+Z$	MADGRAPH-5.0	CTEQ6L1	0.358	1.0
$t\bar{t}+Z$+jets	MADGRAPH-5.0	CTEQ6L1	0.763	1.0

Table 7.1 · Monte Carlo samples used to estimate the Standard Model background. The generator, PDF, cross section and filter efficiency are given. The cross sections of $W(\to e\nu)$+jets, $W(\to \mu\nu)$+jets, $W(\to \tau\nu)$+jets, and $Z(\to \nu\nu)$+jets have been multiplied by the efficiency of cuts at generator level. The cross sections of the $t\bar{t}$ samples include the branching fraction into final states with at least one electron or muon. The filter efficiencies of the $t\bar{t}$ cross sections take into account the branching fractions and efficiency of cuts applied at generator levels. ℓ refers to electrons or muons, τ_ℓ to a leptonically decaying tau, τ_{had} to a hadronically decaying tau, and h to a hadronic jet originating from a quark.

The Z+jets, W+jets, and $t\bar{t}$ samples were all generated with SHERPA-1.4.1 [135] with a PDF set from CT10 [36]. The Z+jets and W+jets samples were generated with massive c and b quarks. MADGRAPH-5.0 [139] was used to generate the $t\bar{t}+V$ samples and CTEQ6L1 [37] was used for PDFs. All the background samples were generated at truth level without any detector simulation. The W+jets and Z+jets are normalised to cross sections calculated to NNLO precision using FEWZ [254, 255]. The cross section of $t\bar{t}$ production is calculated to NNLO accuracy [245]. A filter efficiency, ϵ, is applied to the normalisation of the $t\bar{t}$ samples taking into account the branching fractions and eventual cuts on $E_{\text{T}}^{\text{miss}}$ applied at generator level. The $t\bar{t}+V$ samples were normalised to cross sections calculated at NLO. All samples are generated to correspond to an integrated luminosity of at least 1000 fb^{-1}. A summary of the generators, PDF sets, cross sections, and filter efficiency of each process is given in Table 7.1. The quoted cross sections of $W\to\ell\nu$ and $Z\to\nu\nu$ are multiplied by the efficiency of cuts applied at generator level, $p_{\text{T}}(\ell) > 200$ GeV in the $W\to\ell\nu$ samples and $p_{\text{T}}(Z) > 280$ GeV in the $Z\to\nu\nu$ sample, explaining their very low

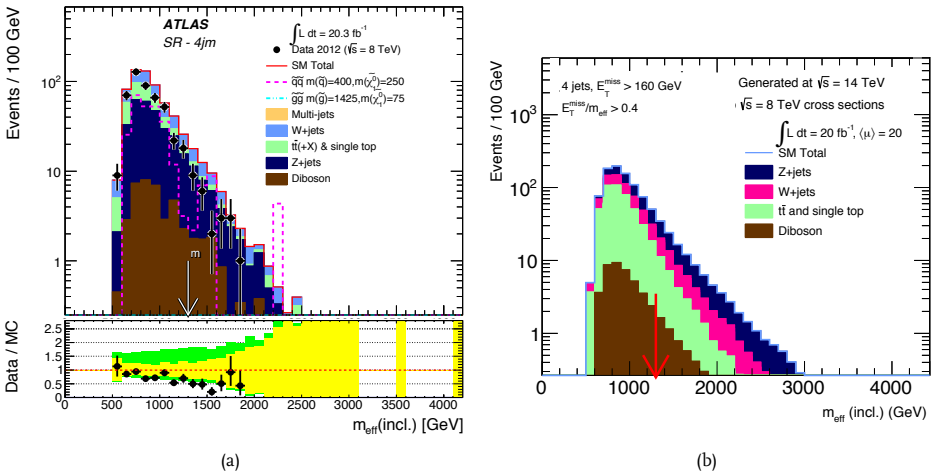

Fig. 7.3 · Distributions of m_{eff}(incl.) in a 4j signal region with samples generated at $\sqrt{s} = 8$ TeV (a) and samples generated at $\sqrt{s} = 14$ TeV normalised to production cross sections at $\sqrt{s} = 8$ TeV (b). The figure of the distribution of the $\sqrt{s} = 8$ TeV samples is taken from Ref. [1].

values. The cross sections of $t\bar{t}$ quoted in Table 7.1 is the production cross section multiplied with the branching fraction into a final state with at least one electron or muon.

To test the reliability of the background samples, distributions of m_{eff}(incl.) generated at $\sqrt{s} = 14$ TeV and normalised with the cross sections at $\sqrt{s} = 8$ TeV to an integrated luminosity of 20 fb^{-1} were compared to the ones obtained with samples generated with a collision energy of $\sqrt{s} = 8$ TeV. The distributions of m_{eff}(incl.) of the two samples in a 4j region can be seen in Figure 7.3. It is seen that the distributions agree at low values of m_{eff}(incl.), while the tail of the distribution of the 14 TeV sample is wider. This is an expected behavior due to the higher collision energy. It is concluded that the background samples generated at $\sqrt{s} = 14$ TeV are consistent with the samples generated at $\sqrt{s} = 8$ TeV and are thus reliable for this study.

7.4 Expected Detector Performance

Two major upgrades of the ATLAS detector are planned: the Phase-1 upgrade during LS2 [273] and the Phase-2 upgrade during LS3 [274]. Large parts of the ATLAS detector will be either renewed or completely changed. The exact lay-out of the ATLAS detector during HL-LHC is not yet definite.

The samples used in these studies are generated at truth level and do thus not include detector simulation. Truth samples are very unrealistic as all the information of every particle is known accurately and obviously detector resolutions are not included. Parameterisations of the expected performance of the ATLAS detector during the HL-LHC runs have been derived with dedicated studies. These parameterisations can be found in Refs. [275] and [276]. Truth particles are smeared using their respective energy resolution to ensure that the prospect studies are more realistic.

A description of the expected energy resolutions of the particles relevant for this study is given here.

7.4.1 Electrons

The energy resolution of electrons is not expected to be affected by the busier environment at a higher pile up. Two energy resolutions are defined for an energy E given in GeV depending on whether the electron is in the barrel or endcap region [275]:

$$\sigma(E) = 0.3\ \text{GeV} \oplus 0.10(\text{GeV})^{1/2} \times \sqrt{E} \oplus 0.010 \times E \qquad \text{for} \quad |\eta| < 1.4 \tag{7.1a}$$

$$\sigma(E) = 0.3\ \text{GeV} \oplus 0.15(\text{GeV})^{1/2} \times \sqrt{E} \oplus 0.015 \times E \qquad \text{for} \quad 1.4 < |\eta| < 2.47. \tag{7.1b}$$

7.4.2 Muons

The momentum resolution of the muons depends on the p_{T} of the muon measured in GeV. Separate momentum resolutions are provided for muon tracks in the inner detector (ID) and hits in the muon spectrometer (MS) [275, 276]:

$$\sigma_{\text{ID}}(p_{\text{T}}) = p_{\text{T}} \times \sqrt{a_1^2 + (a_2 \times p_{\text{T}})^2} \tag{7.2a}$$

$$\sigma_{\text{MS}}(p_{\text{T}}) = p_{\text{T}} \times \sqrt{\left(\frac{b_0}{p_{\text{T}}}\right)^2 + b_1^2 + (b_2 \times p_{\text{T}})^2}, \tag{7.2b}$$

where the p_{T} of the muon is given in GeV. The values of the a_1, a_2, b_0, b_1, and b_2 parameters depend on the η of the muon and are available in Ref. [276]. The values of a_1 and a_2 differ between the ATLAS detector before and after the Phase-2 upgrade where the tracking in the inner detector is expected to be improved.

The muon momentum resolutions in the inner detector and muon spectrometer are joined into a "combined" muon resolution (CB):

$$\sigma_{\text{CB}} = \frac{\sigma_{\text{ID}} \times \sigma_{\text{MS}}}{\sqrt{\sigma_{\text{ID}}^2 + \sigma_{\text{MS}}^2}}. \tag{7.3}$$

7.4.3 Jets

Jets are reconstructed with an anti-k_t algorithm with a radius parameter of $R = 0.4$. The fractional energy resolution of the jets is characterised by a noise parameter (N), a stochastic parameter (S), and a constant parameter (C) and is given by [275]:

$$\frac{\sigma(p_{\text{T}})}{p_{\text{T}}} = \sqrt{\frac{N^2}{p_{\text{T}}^2} + \frac{S^2}{p_{\text{T}}} + C^2}, \tag{7.4}$$

where the p_{T} of the jet is given in GeV.

The stochastic and constant terms in the fractional jet energy resolution were found to be dependent on the η of the jet, but independent of pile up. The effect of pile-up on the noise term was parameterised with a linear function depending on η of the jet:

$$N = a(\eta) + b(\eta)\mu. \tag{7.5}$$

The values of a and b as well as the stochastic parameter and constant parameter in different η-bins can be found in Ref. [275].

7.4.4 Missing Transverse Momentum

The resolution of the missing transverse momentum is sensitive to the busier environment created by higher pile up. As more collisions per bunch crossing happen, it gets more difficult to correctly identify the vertex of origin of the particles created in each collision.

The missing transverse momentum used in the smearing is calculated at truth level as the sum of the energy of all interacting, stable particles within the detector acceptance. The true missing transverse momentum is smeared in the x and y directions with a Gaussian centered around zero [276]:

$$E_{x,y}^{\text{miss}} = E_{x,y}^{\text{miss,true}} + \text{Gaussian}(0, \sigma(\mu)), \tag{7.6}$$

where the width of the Gaussian distribution, σ, depends on the average pile up, μ.

The parameterisation of the resolution of the $E_{\text{T}}^{\text{miss}}$ has been studied using three samples all generated at $\sqrt{s} = 14$ TeV, with a 25 ns spacing between the proton bunches in the beam, and with three different pile up conditions $\langle\mu\rangle = 60$, 80, and 160. The three samples are: $Z' \to t\bar{t}$ ($m(Z') = 2$ TeV), a minimum bias, and di-jets samples with various p_{T} of the jets.

The resolution of the $E_{\text{T}}^{\text{miss}}$ depends on the total transverse energy in an event, $\sum E_{\text{T}}$. The effect of pile-up on the total transverse energy, $\sum E_{\text{T}}^{\text{PU}}$, can be isolated as:

$$\sum E_{\text{T}}^{\text{PU}} = \sum E_{\text{T}} - \sum E_{\text{T}}^{\text{true}}, \tag{7.7}$$

where $\sum E_{\text{T}}^{\text{true}}$ is the total transverse energy calculated at truth level. A random number can be drawn from the distribution of $\sum E_{\text{T}}^{\text{PU}}$ to estimate the total transverse energy. The default distribution of $\sum E_{\text{T}}^{\text{PU}}$ is taken from the $Z' \to t\bar{t}$ sample. Two sources of systematic uncertainties are included in the study of the parametrization of $\sum E_{\text{T}}$: changing to an alternative sample (minimum bias), and varying the pile up noise threshold. The noise threshold is applied to suppress the effects of pile up when the clusters of energy are formed in the calorimeter.

The resolution of the missing transverse momentum in the x and y directions as a function of $\sum E_{\text{T}}$ at $\langle\mu\rangle = 60$ and $\langle\mu\rangle = 140$ are shown in Figure 7.4. The parameterisation is compared to three samples and is found to agree within the uncertainties.

7.5 Signal Regions

The signal regions are defined to optimise the discovery potential of the simplified models of squark and gluino production with direct decays.

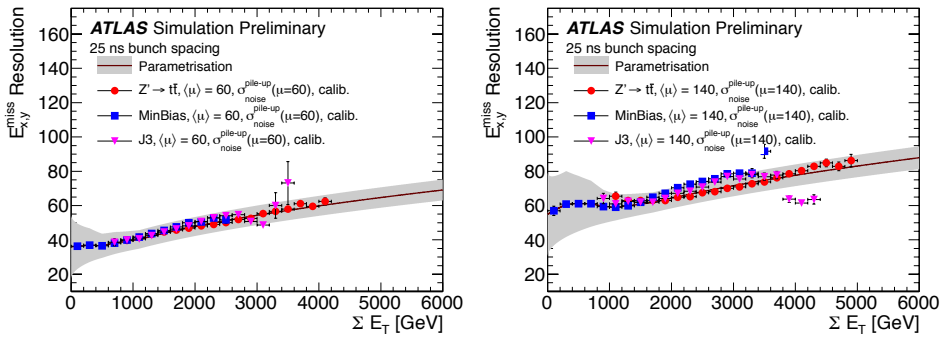

(a) (b)

Fig. 7.4 · The resolution of the x and y-components of the $E_{\mathrm{T}}^{\mathrm{miss}}$ as a function of the total transverse energy, $\sum E_{\mathrm{T}}$ obtained from different samples compared to the parameterisation at $\langle\mu\rangle = 60$ (a) and $\langle\mu\rangle = 140$ (b). J3 refers to a di-jet sample. The figure is taken from Ref. [276].

The selection of the signal regions follow three steps. A preselection at truth level is performed to reduce the computing time. Then the smearing of the objects, the object definitions and resolving conflicts of overlapping objects are performed on events that fulfill the preselection at truth level. The final signal region selection is performed on smeared objects. The final signal regions are chosen based on the sets of cuts on $E_{\mathrm{T}}^{\mathrm{miss}}/\sqrt{H_{\mathrm{T}}}$, $m_{\mathrm{eff}}(\mathrm{Nj})$, and $m_{\mathrm{eff}}(\mathrm{incl.})$ that optimise the discovery potential of the simplified models with squark and gluino production.

7.5.1 Preselection at Truth Level

To reduce the computing time required for this study a preselection is applied at truth level before any smearing is performed. Events must fulfill the following requirements in order to pass the preselection at truth level: $E_{\mathrm{T}}^{\mathrm{miss}} > 110$ GeV, the p_{T} of the leading jet must be larger than 90 GeV, and the p_{T} of the subleading jet must be larger than 40 GeV. Both jets must lie within $|\eta| < 3.6$.

Some of the events rejected by the preselection can survive the tighter cuts of the final selection when the energy of the jets and missing transverse momentum are smeared as described in Section 7.4. Especially the resolution of the $E_{\mathrm{T}}^{\mathrm{miss}}$ can increase the truth level missing transverse momentum to a value above the cut-off. The number of events rejected by the preselection that could have survived the final signal region cuts on $E_{\mathrm{T}}^{\mathrm{miss}}$ and jet p_{T} after smearing was estimated to be approximately 1%.

7.5.2 Object Definitions and Overlap Removal

After the preselection at truth level is performed to reduce the size of especially the background samples, all the objects in the events that survived are smeared using the resolutions described in Section 7.4. The object definitions of jets, electrons, and muons are based on the smeared object.

Jets with $p_{\mathrm{T}} > 20$ GeV lying within $|\eta| < 2.8$ are selected. Electrons must lie within $|\eta| < 2.47$ and have a p_{T} greater than 10 GeV, while muons must be within $|\eta| < 2.4$ and have a p_{T} greater than 10 GeV as well. The truth missing transverse momentum before smearing is calculated from the energy of the non-interacting particles such as neutrinos and the hypothetical neutralino.

Jets can be mis-identified as electrons. The probability of a truth jet at a given p_{T} to be identified falsely as an electron is assumed to be [275]:

$$\epsilon(p_{\mathrm{T}}) = 0.11 \times \exp(-0.033(\mathrm{GeV})^{-1} \times p_{\mathrm{T}}). \tag{7.8}$$

Overlap Removal

Conflicts with overlapping objects must be resolved once the objects are selected. The overlap removal is performed on jets and leptons following a set of criteria similar to those in Chapter 5.

The overlap removal criteria are based on the distance between objects in the η-ϕ-plane, $\Delta R = \sqrt{(\Delta\eta)^2 + (\Delta\phi)^2}$. Three overlap removals are applied in the following order:

1. If an electron and a jet are found within $\Delta R < 0.2$, then the object is treated as an electron and the jet is ignored.

2. If a muon and a jet are found within $\Delta R < 0.4$, then the object is treated as a jet and the muon is ignored.

3. If an electron and a jet are found within $0.2 < \Delta R < 0.4$, then the object is treated as a jet and the electron is ignored.

7.5.3 Signal Region Selection

The signal region selection is very similar to that of the signal regions defined in the analysis performed at $\sqrt{s} = 8$ TeV [1] presented in Chapter 5.

All signal regions have a common preselection before the final optimisation is performed. Cuts on $E_{\mathrm{T}}^{\mathrm{miss}}$ and the p_{T} of the most energetic jet of 160 GeV are applied with the expectation that a combined jet and $E_{\mathrm{T}}^{\mathrm{miss}}$ trigger will be used during the data taking. The signal regions are characterised by the number of jets with p_{T} greater than 60 GeV which have been shown to safely suppress jets originating from pile-up. All events containing either an electron or a muon after overlap removal are rejected. Finally cuts are applied on the azimuthal angle between the jets and the $E_{\mathrm{T}}^{\mathrm{miss}}$, $\Delta\phi(\mathrm{jet}, E_{\mathrm{T}}^{\mathrm{miss}})_{\mathrm{min}}$, in order to reject multijet background ensuring that the multijet background in the signal regions can safely be neglected.

After the preselection is applied, the signal regions are optimised by varying the values of the cuts on m_{eff}(incl.), and $E_{\mathrm{T}}^{\mathrm{miss}}/m_{\mathrm{eff}}$(Nj)or $E_{\mathrm{T}}^{\mathrm{miss}}/\sqrt{H_{\mathrm{T}}}$. The number of Standard Model background events in the signal regions is estimated purely from simulations unlike the analyses presented in Chapter 5 and 6, where the backgrounds were normalised the observed event yields in control regions. The various signal regions are optimised for discovery of either squark-pair production or gluino-pair production. Two sets of signal regions are defined: one for a total integrated luminosity of 300 fb^{-1} with an average pile-up of $\langle\mu\rangle = 60$, and one for a total integrated luminosity of 3000 fb^{-1} with an average pile-up of $\langle\mu\rangle = 140$.

Selection	Channel									
	2jl	2jm	3j	4jl	4jm	4jt	5j	6jl	6jm	6jt
$p_{\mathrm{T}}(j_1)$ [GeV] >	160									
$N_{\mathrm{jets}}(p_{\mathrm{T}} > 60\ [\mathrm{GeV}]) \geq$	2		3	4			5	6		
$E_{\mathrm{T}}^{\mathrm{miss}}$ [GeV] >	160									
$\Delta\phi(\mathrm{jet}, E_{\mathrm{T}}^{\mathrm{miss}})_{\mathrm{min}}$ >	0.4 (j_1, j_2, j_3), 0.2 (all $p_{\mathrm{T}} > 40$ GeV jets)									
	$\langle\mu\rangle = 60$, 300 fb^{-1} scenario									
$E_{\mathrm{T}}^{\mathrm{miss}}/m_{\mathrm{eff}}$ >	–	–	0.3	0.40	0.25	–	0.20	0.30	0.15	0.20
$E_{\mathrm{T}}^{\mathrm{miss}}/\sqrt{H_{\mathrm{T}}}$ [GeV$^{1/2}$] >	8	15	–	–	–	10	–	–	–	–
m_{eff} [GeV] >	3600	3100, 4300	3600, 3000	3000, 2200	3200	3400	3000	2800	3400	3400
	$\langle\mu\rangle = 140$, 3000 fb^{-1} scenario									
$E_{\mathrm{T}}^{\mathrm{miss}}/m_{\mathrm{eff}}(\mathrm{Nj})$ >	–	–	0.3	0.35	0.25	–	0.25	0.25	0.35	0.15
$E_{\mathrm{T}}^{\mathrm{miss}}/\sqrt{H_{\mathrm{T}}}$ [GeV$^{1/2}$] >	8	15	–	–	–	10	–	–	–	–
m_{eff}(incl.) [GeV] >	4500, 5000	4500, 4900	4000	4000, 3800	4000	4500	4000	3400	3500	5000
Optimised for	$\tilde{q}\tilde{q}$	$\tilde{q}\tilde{q}$	$\tilde{q}\tilde{q}$	$\tilde{q}\tilde{q}$	$\tilde{g}\tilde{g}$	$\tilde{g}\tilde{g}$	$\tilde{g}\tilde{g}$	$\tilde{g}\tilde{g}$	$\tilde{g}\tilde{g}$	$\tilde{g}\tilde{g}$

Table 7.2 · Signal region selection for an integrated luminosity of 300 fb^{-1} with $\langle\mu\rangle = 60$, and an integrated luminosity of 3000 fb^{-1} with $\langle\mu\rangle = 140$. The 2j, 3j and 4jl regions are targeting squark-pair production and some have two cuts on m_{eff}(incl.). The first is designed for scenarios where the gluino is decoupled, the other for the case in which the gluino mass is 4.5 TeV.

In total, 10 signal regions are defined for each luminosity hypothesis. A summary of the cuts defining the signal regions can be found in Table 7.2. The signal regions are classified by their jet multiplicity as well as the tightness of the cut on m_{eff}(incl.) ranging from "loose" (l) to "tight" (t). The 2-jet, 3-jet, and 4jl signal regions are optimised for discovery of squark-pair production, while the rest of the signal regions are optimised for gluino-pair production. Some of the signal regions optimised for $\tilde{q}\tilde{q}$ production have two cuts on m_{eff}(incl.): one for a model where the gluino is completely decoupled (the first value in the table), and one for a model where the mass of the gluino is 4.5 TeV (the second value in the table).

The cuts on the missing transverse momentum and the p_{T} of the leading jet are lower than the ones applied in the signal region selection of the analysis performed at $\sqrt{s} = 13$ TeV [3] presented in Chapter 6. It is very likely that the cuts are too low and that they must be increased due to higher trigger thresholds. However, the events passing the full signal region selection with tight cuts applied on m_{eff}(incl.), $E_{\mathrm{T}}^{\mathrm{miss}}/m_{\mathrm{eff}}$(Nj), and $E_{\mathrm{T}}^{\mathrm{miss}}/\sqrt{H_{\mathrm{T}}}$ will have $E_{\mathrm{T}}^{\mathrm{miss}}$ and p_{T} of the leading jet with values higher than the preselection cuts. The background and signal yields in the signal regions are therefore not expected to change dramatically with a moderate increase of the cut on the $E_{\mathrm{T}}^{\mathrm{miss}}$ and the p_{T} of the leading jet.

7.5.4 Results

Distributions of m_{eff}(incl.) in three signal regions with the two luminosity assumptions are shown in Figure 7.5. The m_{eff}(incl.) distribution of two signal points with different mass compressions, i. e. the difference between the mass of the produced squark or gluino and the $\tilde{\chi}_1^0$, are shown to illustrate where a signal would show up and how it would look. It can be seen that the m_{eff}(incl.) distribution of the signal point with large mass difference ($m_{\tilde{q},\tilde{g}} \gg m_{\tilde{\chi}_1^0}$) peaks at high values of m_{eff}(incl.), while the distribution of the signal point with small mass compression ($m_{\tilde{q},\tilde{g}} \approx m_{\tilde{\chi}_1^0}$) follows the distribution of the background and will therefore be harder to discover.

By comparing the m_{eff}(incl.) distributions normalised to an integrated luminosity of 300fb^{-1} with $\langle\mu\rangle = 60$ in Figure 7.5a, 7.5c, and 7.5e to the distributions normalised to 3000fb^{-1} with $\langle\mu\rangle = 140$ in Figure 7.5b, 7.5d, and 7.5f, it can be seen that the distributions are broader when the luminosity and pile-up are higher. This is an expected feature as especially the missing transverse momentum resolution decreases with a higher average number of interactions per bunch crossing.

The expected number of background events in each signal region at an integrated luminosity of 300 fb^{-1} and 3000 fb^{-1} are given in Table 7.3 and 7.4, respectively, along with the yield of four selected signal points. It can be seen that the dominant background in all signal regions is $Z(\to \nu\nu)$+jets with the contribution of the $t\bar{t}$ background increasing at higher jet multiplicity. A similar pattern in background composition is seen in the analyses performed with data collected at $\sqrt{s} = 8$ TeV [1] and $\sqrt{s} = 13$ TeV [3] described in Chapter 5 and 6.

7.6 Expected Sensitivity

The expected sensitivity is calculated using Z_N [277], which is a significance-like measure where the systematic uncertainty on the background is taken into account. To be classified as a discovery, the value of Z_N must be larger than 5, while to claim an exclusion at 95% CL, a one-sided interval is used and the value of Z_N must be greater than 1.64. Results on the exclusion range obtained using a dedicated 95% CL exclusion test was found to give very similar results.

It is assumed that the systematic uncertainty will not change a lot at the HL-LHC compared to the uncertainty on the background in the analysis performed at $\sqrt{s} = 8$ TeV [1]. The systematic uncertainty on the background is therefore taken to be 10% which is consistent with the uncertainty in the signal regions of the previously published analysis. Theoretical uncertainties on the sparticle production cross section is evaluated by changing the pdf set, the strong coupling constant, and the renormalisation and factorisation scales as described in Section 5.7.2. Effects of experimental uncertainties on the yield of the signal are not included.

The expected discovery and exclusion reaches are shown in the $m_{\tilde{q},\tilde{g}}$-$m_{\tilde{\chi}_1^0}$-plane in Figure 7.6. The 5σ discovery reaches are shown by black and red solid lines for the 300 fb^{-1} and 3000 fb^{-1} luminosity scenario, respectively. The exclusion reaches at 95% CL are illustrated by black and red dashed lines for the 300 fb^{-1} and 3000 fb^{-1} luminosity scenario, respectively. The blue and grey shaded areas indicate the uncertainty on the signal production cross section. In yellow, the

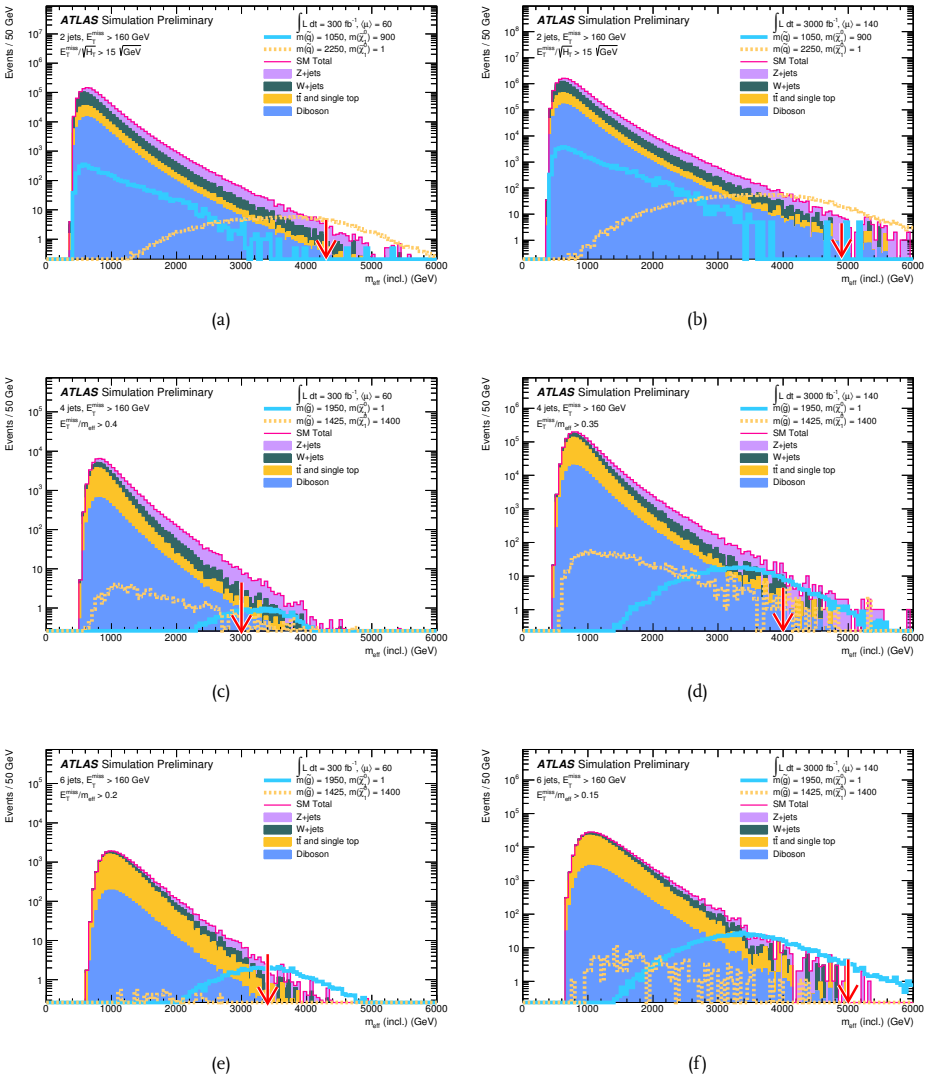

Fig. 7.5 · Distributions of m_{eff}(incl.) in three signal regions: 2jl ((a) and (b)), 4jm ((c) and (d)), and 6jt ((e) and (f)). The distributions are shown with two luminosity assumption: 300 fb^{-1} with $\langle\mu\rangle = 60$ ((a), (c), and (e)), and 3000 fb^{-1} with $\langle\mu\rangle = 140$ ((b), (d), and (f)). The red arrows indicate the cut on m_{eff}(incl.). For illustration, two signal points are shown.

Region	2jl	2jm	3j	4jl	4jm
W+jets	45 ± 4	2.7 ± 0.9	11 ± 2	12 ± 2	26 ± 3
Z+jets	104 ± 3	17 ± 1	43 ± 2	49 ± 2	76 ± 3
$t\bar{t}$	16 ± 2	1.6 ± 0.5	4.2 ± 0.8	5.1 ± 1.1	11 ± 2
Diboson	18 ± 2	2.4 ± 0.5	6.5 ± 0.9	7.3 ± 1.0	13 ± 1
Total background	183 ± 5	24 ± 2	65 ± 3	73 ± 3	126 ± 4
$m_{\tilde{g}} = 1950$ GeV $m_{\tilde{\chi}_1^0} = 1$ GeV	68.8 ± 0.6	12.5 ± 0.3	35.4 ± 0.5	18.4 ± 0.3	70.6 ± 0.7
$m_{\tilde{g}} = 1425$ GeV $m_{\tilde{\chi}_1^0} = 1400$ GeV	12.6 ± 1.2	3.7 ± 0.6	8.5 ± 1.0	7.5 ± 0.9	8.1 ± 0.9
$m_{\tilde{q}} = 1050$ GeV $m_{\tilde{\chi}_1^0} = 900$ GeV	2.5 ± 1.1	1.5 ± 0.9	2.0 ± 1.0	3.5 ± 1.3	6.4 ± 1.8
$m_{\tilde{q}} = 2250$ GeV $m_{\tilde{\chi}_1^0} = 1$ GeV	141.7 ± 0.9	60.1 ± 0.6	82.1 ± 0.7	39.2 ± 0.5	59.3 ± 0.6

Region	4jt	5j	6jl	6jm	6jt
W+jets	113 ± 6	30 ± 3	8.5 ± 1.5	6.3 ± 1.3	3.6 ± 1.0
Z+jets	111 ± 3	74 ± 3	21 ± 1	13 ± 1	10 ± 1
$t\bar{t}$	46 ± 3	19 ± 2	5.2 ± 1.1	6.0 ± 1.2	3.4 ± 0.9
Diboson	30 ± 2	14 ± 2	3.8 ± 0.8	2.8 ± 0.7	1.9 ± 0.5
Total background	300 ± 8	137 ± 5	39 ± 3	28 ± 2	19 ± 2
$m_{\tilde{g}} = 1950$ GeV $m_{\tilde{\chi}_1^0} = 1$ GeV	102.4 ± 0.8	83.4 ± 0.7	25.6 ± 0.4	44.6 ± 0.5	35.4 ± 0.5
$m_{\tilde{g}} = 1425$ GeV $m_{\tilde{\chi}_1^0} = 1400$ GeV	6.2 ± 0.8	4.7 ± 0.7	1.6 ± 0.4	1.1 ± 0.3	1.1 ± 0.3
$m_{\tilde{q}} = 1050$ GeV $m_{\tilde{\chi}_1^0} = 900$ GeV	4.0 ± 1.4	7.4 ± 1.9	3.5 ± 1.3	1.5 ± 0.9	1.5 ± 0.9
$m_{\tilde{q}} = 2250$ GeV $m_{\tilde{\chi}_1^0} = 1$ GeV	58.9 ± 0.6	28.4 ± 0.4	7.8 ± 0.2	8.0 ± 0.2	7.6 ± 0.2

Table 7.3 · Yields for the main backgrounds and selected signal points simulated with $\langle\mu\rangle = 60$, normalised to $\mathcal{L} = 300$ fb^{-1}. The signal samples of squark-pair production are normalized for the scenario with a gluino mass of 4.5 TeV.

Region	2jl	2jm	3j	4jl	4jm
W+jets	8 ± 5	5 ± 4	38 ± 10	8 ± 5	14 ± 6
Z+jets	51 ± 7	51 ± 7	185 ± 13	78 ± 8	127 ± 11
$t\bar{t}$	9 ± 4	9 ± 4	20 ± 5	7.0 ± 3.1	18 ± 6
Diboson	7.6 ± 3.1	7.2 ± 2.9	27 ± 6	10.4 ± 3.4	18 ± 5
Total background	76 ± 10	72 ± 9	269 ± 18	104 ± 11	176 ± 14
$m_{\tilde{g}} = 1950$ GeV, $m_{\tilde{\chi}_1^0} = 1$ GeV	55.8 ± 1.8	43.4 ± 1.6	163.9 ± 3.1	75.2 ± 2.1	191.0 ± 3.4
$m_{\tilde{g}} = 1425$ GeV, $m_{\tilde{\chi}_1^0} = 1400$ GeV	10.5 ± 3.3	15 ± 4	48 ± 7	19 ± 4	23 ± 5
$m_{\tilde{q}} = 1050$ GeV, $m_{\tilde{\chi}_1^0} = 900$ GeV	5 ± 5	10 ± 7	15 ± 9	10 ± 7	15 ± 9
$m_{\tilde{q}} = 2250$ GeV, $m_{\tilde{\chi}_1^0} = 1$ GeV	186 ± 3	208.2 ± 3.4	558 ± 6	254 ± 4	320 ± 4

Region	4jt	5j	6jl	6jm	6jt
W+jets	101 ± 17	14 ± 6	25 ± 8	11 ± 5	–
Z+jets	125 ± 11	65 ± 8	85 ± 9	29 ± 5	3.6 ± 1.8
$t\bar{t}$	37 ± 9	11 ± 4	17 ± 5	3.5 ± 2.1	1.4 ± 1.4
Diboson	29 ± 7	9.9 ± 3.5	14 ± 4	4.8 ± 2.6	0.6 ± 0.8
Total background	76 ± 10	72 ± 9	269 ± 18	104 ± 11	176 ± 14
$m_{\tilde{g}} = 1950$ GeV, $m_{\tilde{\chi}_1^0} = 1$ GeV	159.1 ± 3.1	152.7 ± 3.0	257 ± 4	73.4 ± 2.1	36.0 ± 1.5
$m_{\tilde{g}} = 1425$ GeV, $m_{\tilde{\chi}_1^0} = 1400$ GeV	8.4 ± 3.0	14 ± 4	7.4 ± 2.8	5.3 ± 2.4	–
$m_{\tilde{q}} = 1050$ GeV, $m_{\tilde{\chi}_1^0} = 900$ GeV	15 ± 9	10 ± 7	25 ± 11	5 ± 5	5 ± 5
$m_{\tilde{q}} = 2250$ GeV, $m_{\tilde{\chi}_1^0} = 1$ GeV	182.6 ± 3.2	136.4 ± 2.7	75.2 ± 2.0	50.9 ± 1.7	13.6 ± 0.9

Table 7.4 · Yields for the main backgrounds and selected signal points simulated with $\langle\mu\rangle = 140$, normalised to $\mathcal{L} = 3000$ fb^{-1}. The signal samples of squark-pair production are normalized for the scenario with a gluino mass of 4.5 TeV. Entries labeled as '–' indicate that no events of the samples survived the selection.

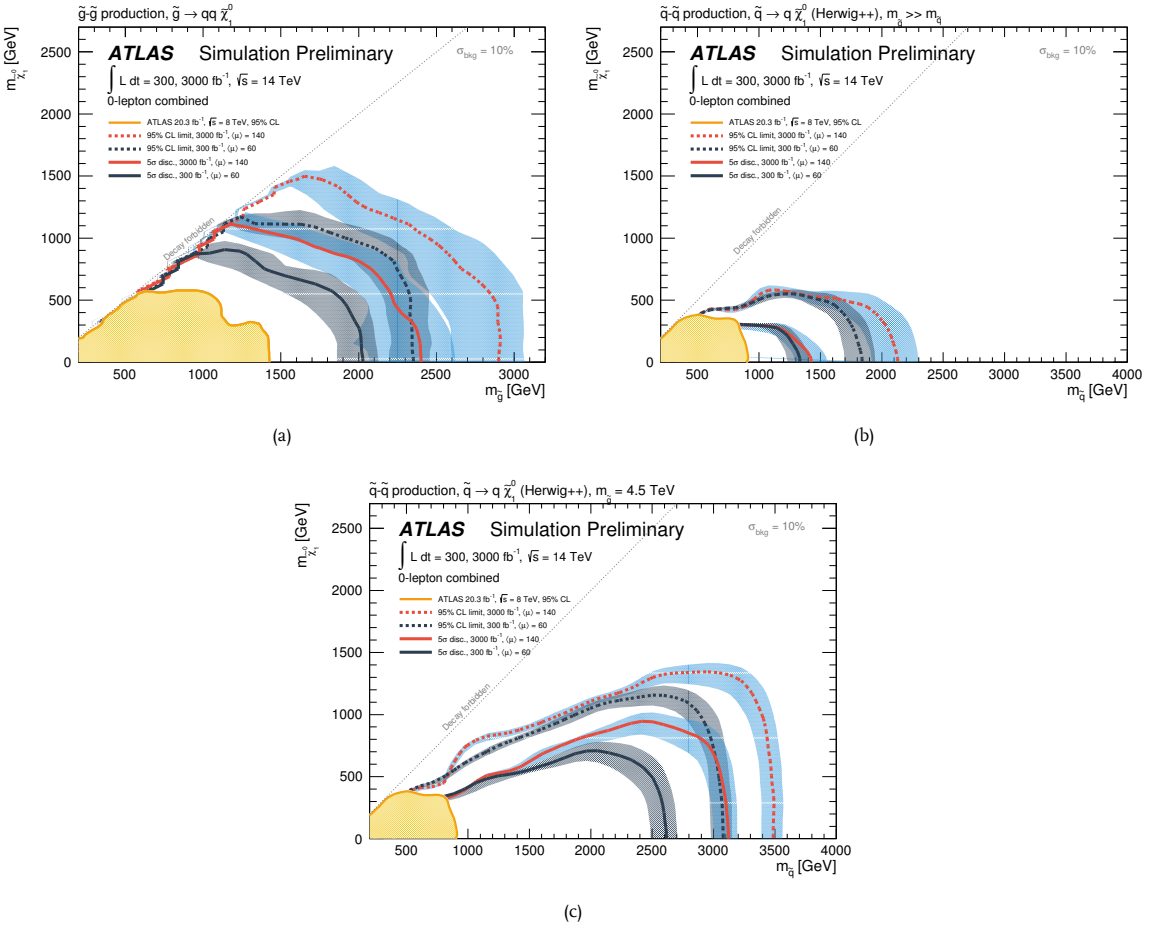

Fig. 7.6 · Expected 5σ discovery contours (solid) and exclusion contours at 95% CL (dashed) on simplified models of gluino-pair production with direct decays (a), squark-pair production with direct decays and decoupled gluinos (b), and squark-pair production with direct decays and $m_{\tilde{g}} = 4.5$ TeV (c). The contours are obtained under two luminosity assumptions: 300 fb^{-1} with $\langle\mu\rangle = 60$ (black) and 3000 fb^{-1} with $\langle\mu\rangle = 140$ (red). The shaded bands (grey and blue) indicate the 1σ theoretical uncertainty on the sparticle production cross section. The limits obtained with data collected at $\sqrt{s} = 8$ TeV [1] are shown in yellow.

limits obtained by the analysis performed at $\sqrt{s} = 8$ TeV [1] are shown. The more recent limits obtained with data collected at $\sqrt{s} = 13$ TeV [3] were not available at the time of these studies.

7.6.1 Expected Sensitivity of Gluino-pair Production

The expected sensitivity of gluino-pair production at the two luminosity scenarios is shown in Figure 7.6a. The large shaded areas indicate the uncertainty in the gluino-pair production cross

section. The uncertainty reaches 400 GeV for heavy gluinos and is dominated by uncertainties on the parton distribution functions.

It can be seen that with the full LHC dataset consisting of 300 fb^{-1} collected at $\sqrt{s} = 14$ TeV with an average pile-up of 60, gluinos with masses up to 2000 GeV can be discovered at 5σ significance for massless $\tilde{\chi}_1^0$. With the full dataset collected with the upgrade of the LHC to HL-LHC consisting of 3000 fb^{-1} with $\langle\mu\rangle = 140$, the 5σ discovery reach of gluinos when the $\tilde{\chi}_1^0$ is massless extends to 2400 GeV. With increasing mass of the neutralino, the sensitivity to heavy gluinos decreases. With a Neutralino mass of 900 GeV and 1100 GeV, gluinos with masses up to 1200 GeV can be discovered with the 300 fb^{-1} and 3000 fb^{-1} luminosity scenario, respectively. The discovery reach for both heavy gluinos and neutralinos extends beyond the current limits of $m_{\tilde{g}} = 1510$ GeV and $m_{\tilde{\chi}_1^0} = 800$ GeV obtained with the dataset collected at $\sqrt{s} = 13$ TeV [3].

If no excesses are observed, gluinos with masses of 2350 GeV and 2950 GeV can be excluded when the neutralino is massless with the full LHC and HL-LHC dataset, respectively. If the neutralino is not massless, then the exclusion reach in the gluino mass decreases. Gluino-pair production with direct decay with a neutralino mass up to 1100 GeV and a gluino mass of 1700 GeV can be excluded with the full LHC dataset, while the exclusion extends to models with a neutralino mass of 1500 GeV and a gluino mass of 1700 GeV with the full dataset of the HL-LHC.

7.6.2 Expected Sensitivity to Squark-pair Production

The expected sensitivity to squark-pair production with decoupled gluinos and gluinos with a mass of 4.5 TeV is shown in Figure 7.6b and 7.6c, respectively. As the acceptance efficiencies of the two squark scenarios were found to be comparable, they were assumed to be identical. The theoretical uncertainties on the production cross section of squarks indicated by the blue and grey shaded areas are smaller than the uncertainties on cross section of gluino production.

The discovery reach of squark-pair production with decoupled gluinos does not increase significantly with the full HL-LHC dataset of 3000 fb^{-1} compared to the reach obtained with the LHC dataset consisting of 300 fb^{-1}. The discovery reach extends to a squark mass of 1320 GeV when the neutralino is massless with the 300 fb^{-1} luminosity scenario, while the reach with the full HL-LHC dataset would be 1420 GeV. The discovery reach extends beyond the current limit on the mass of squarks which is 1030 GeV. If no excesses are observed, squarks with masses of 1850 GeV and 2000 GeV will be excluded with the full dataset of the LHC and HL-LHC, respectively. Neither the discovery nor exclusion reach of neutralinos extends beyond the current limits of 500 GeV. The poor exclusion reach and discovery sensitivity of heavy neutralinos is partly explained by the choice of generator, HERWIG++, which does not include initial state radiation in the matrix-element as MADGRAPH-5.0 does. Furthermore, the highly compressed scenarios where $m_{\tilde{q}} \approx m_{\tilde{\chi}_1^0}$ are hard to discover or exclude as the final is dominated by jets with low energy and low $E_{\mathrm{T}}^{\mathrm{miss}}$.

If the mass of the gluino is 4.5 TeV, it is beyond the reach even with the HL-LHC dataset. The cross section of squark-pair production does however increase significantly due to the availability of production through a t-channel exchange of a gluino. In this scenarios, squarks with masses up to 2600 GeV can be discovered with the full LHC dataset of 300 fb^{-1}. The discovery reach

increases to 3100 GeV with the HL-LHC dataset of 3000 fb^{-1}. Sensitivity to scenarios with heavier neutralinos is increasing as well compared to the sensitivity to the squark model with decoupled gluinos, though the diagonal where $m_{\tilde{q}} \approx m_{\tilde{\chi}_1^0}$ is still beyond reach. In case of no observed excesses, squarks with masses of 3100 GeV and 3500 GeV can be excluded using the 300 fb^{-1} dataset of the LHC and the 3000 fb^{-1} dataset of the HL-LHC, respectively.

The discovery and exclusion reaches of the squark model with $m_{\tilde{g}} = 4.5$ TeV cannot be be directly compared to exclusion limits obtained with data collected at $\sqrt{s} = 13$ TeV where the gluino is assumed to be decoupled.

7.7 Conclusion

The sensitivity study presented in this chapter is aiming to give an overall impression of the sensitivity to squarks and gluinos with an upgrade of the LHC and a ten-fold increase in integrated luminosity. The exact results should therefore be taken with a grain of salt. They are based on Monte Carlo samples generated at truth level subsequently smeared with parameterised functions based on assumptions on upgrades of the ATLAS detector. Furthermore, the analysis strategy and signal region selection is heavily inspired by previous analyses and no new variables have been studied. The background is estimated solely from simulation samples normalised to their respective cross section. However, it is seen with the use of control regions in the analyses presented in Chapter 5 and 6 that the transfer factors from control regions to signal regions are smaller than one for many backgrounds which leads to an overestimate of the background in these studies. The conservative assumption on the total uncertainty of the background will further decrease the discovery and exclusion reaches. The results do therefore represent a conservative estimate of what can be expected with an upgrade of the LHC to the HL-LHC.

The results of the sensitivity study indicate that the discovery and exclusion reach in simplified models of squark and gluino production with direct decay will increase significantly with the full dataset of the LHC consisting of an integrated luminosity of 300 fb^{-1} collected at a collision energy of 14 TeV with an average number of proton collisions per bunch crossing of 60. With an upgrade of the LHC to the HL-LHC and an integrated luminosity increase to 3000 fb^{-1}, the discovery reach will increase by up to 400 GeV in gluino mass and 500 GeV in squark mass if the gluino is not completely decoupled.

The study furthermore shows that the sensitivity to squark pair production depends heavily on the mass of gluino, even if the gluino is beyond reach of direct searches. With a gluino mass of 4.5 TeV, the discovery reach increased by 1700 GeV compared to the reach in a model with decoupled gluinos. Squark models with heavy, but not completely decoupled gluinos are thus interesting to study in the searches for strongly produced supersymmetry.

Even if supersymmetric particles have not yet been discovered, they can still exist and be produced at the LHC. With an upgrade of the LHC to the HL-LHC and the increase in the amount of data to 3000 fb^{-1}, the discovery reach will increase far beyond any current limits.

8

Conclusion and Outlook

The first run of the LHC ended in 2012. The climax was the discovery of the Higgs boson deeming the Standard Model complete. After two years scheduled shutdown, the LHC began its second run with an increased centre-of-mass energy of $\sqrt{s} = 13$ TeV. The increase in energy has opened up an entire new energy regime where the Standard Model can be tested at even higher energies and maybe new physics will be discovered.

In this thesis, searches for squarks and gluinos in events with jets and $E_{\mathrm{T}}^{\mathrm{miss}}$ with the full Run-1 dataset at $\sqrt{s} = 8$ TeV and with the first Run-2 dataset collected in 2015 at $\sqrt{s} = 13$ TeV are presented in Chapter 5 and Chapter 6. No hints of squarks and gluinos were seen in either of the 0-lepton analyses. This results in increasingly high exclusion limits on the masses of squarks and gluinos at 1030 GeV and 1519 GeV in simplified models with direct decays, respectively. Even with the prospects of being able to discover squarks and gluinos with the full HL-LHC dataset presented in Chapter 7, it is interesting to ask: What is the status of supersymmetry after the first run of the LHC and with the early data of the second run? Is supersymmetry dead and should we stop searching for it?

The short answer to the question would be: No, supersymmetry is still an interesting theory and we should keep on searching. The longer answer to this question is that there can be several reasons why supersymmetry has not been discovered yet.

Even though the production cross sections of squarks and gluinos are the highest amongst the supersymmetric particles, there can be several reasons why squarks and gluinos have not yet been discovered in events with jets and $E_{\mathrm{T}}^{\mathrm{miss}}$ even if they exist:

Squarks and gluinos are too heavy. If squarks and gluinos are heavier than the current exclusion limits, then the analyses are simply not sensitive. With an increase in the amount of data collected at $\sqrt{s} = 13$ TeV, the sensitivity reach will extend beyond the current limits.

The lightest supersymmetric particle is heavy. The analyses are optimised to discover heavy squarks and gluinos and they are therefore not very sensitive to high $\tilde{\chi}_1^0$ masses. This can be seen in the exclusion limits of simplified models of squark and gluino production with direct decays in Figure 6.16.

The mass difference between squarks or gluinos and $\tilde{\chi}_1^0$ is small. When the models are compressed, i. e. the mass of the squark or gluino is almost identical to the mass of $\tilde{\chi}_1^0$, then the

jets emerging from the decay will be soft. This will result in low $E_{\mathrm{T}}^{\mathrm{miss}}$ as well as there will be no high energy objects from which it can recoil. This will therefore result in events with soft jets and low $E_{\mathrm{T}}^{\mathrm{miss}}$ which are hard to distinguish from the Standard Model background. As the analyses presented in this thesis is based on events with high-p_{T} jets and high $E_{\mathrm{T}}^{\mathrm{miss}}$, they are not sensitive to these compressed models.

Squarks and gluinos can decay through other decay channels. If the squark or gluino decays through decay channels not studied, it could be that the analyses are not sensitive to these decays. Especially longer decay chains can result in many leptons or jets that are too soft to be selected in the analyses. Furthermore, as the exclusion limits on simplified models with direct decays increase, it begins to seem more likely that there could be heavier charginos and neutralinos that the squark and gluino would decay through resulting in longer decay channels.

One of the major motivations for supersymmetry is the solution to the hierarchy problem where the existence of sparticles will reduce the "un-natural" large virtual corrections to the mass of the Higgs boson as described in Section 1.4.1. However, if supersymmetry is to provide a solution to the hierarchy problem restrictions on the masses of some of the sparticles are placed. The first two generation of squarks can in general be heavy ($m_{\tilde{q}} > 1\,\mathrm{TeV}$) while the third generation squarks should be lighter. The top quark is the main contributor to the virtual correction of the Higgs mass in the Standard Model. In order to cancel the contribution from the top quark, the top squark must not be too heavy compared to its Standard Model counterpart. Another constraint is on the mass scale of the higgsinos, μ, which should be of the order of the mass of the Z boson in order not to introduce a new source of heavy fine-tuning in supersymmetry.

If the squarks and gluinos are too heavy to be produced, other supersymmetric particles could be lighter and might be discovered first. The searches for supersymmetry with the ATLAS detector are therefore many and each analysis is dedicated at searching for specific sparticle production mechanisms and decay. In Figure 8.1, a summary of excluded masses of supersymmetric particles by analyses performed with the data collected by the ATLAS experiment. The inclusive searches place high limits of the order of 1 TeV on both squark and gluino masses, while the searches for third generation squarks, $\tilde{b}$ and $\tilde{t}$, result in lower limits. The searches for charginos, neutralinos, and sleptons do in general result in lower limits due to their lower cross section.

Many of the limits presented in Figure 8.1 are based on simplified models. The simplified models are based on very simple assumptions and contain typically one type of sparticle production and a single possible decay. They are therefore not full supersymmetric models, but merely slices in the SUSY phase space. It is interesting to ask whether the searches are limited by the choice of using simplified models and which parts of the SUSY phase are not targeted by any of the ATLAS searches. It is therefore interesting to study the limits placed by the analyses in more "complete" supersymmetry models.

One of the models which was a prime candidate for supersymmetry before the startup of the LHC was MSUGRA/CMSSM with 5 free parameters. The limit on an MSUGRA/CMSSM model with a mass of the Higgs boson of ~ 125 GeV was presented in Chapter 5. Unfortunately, with the

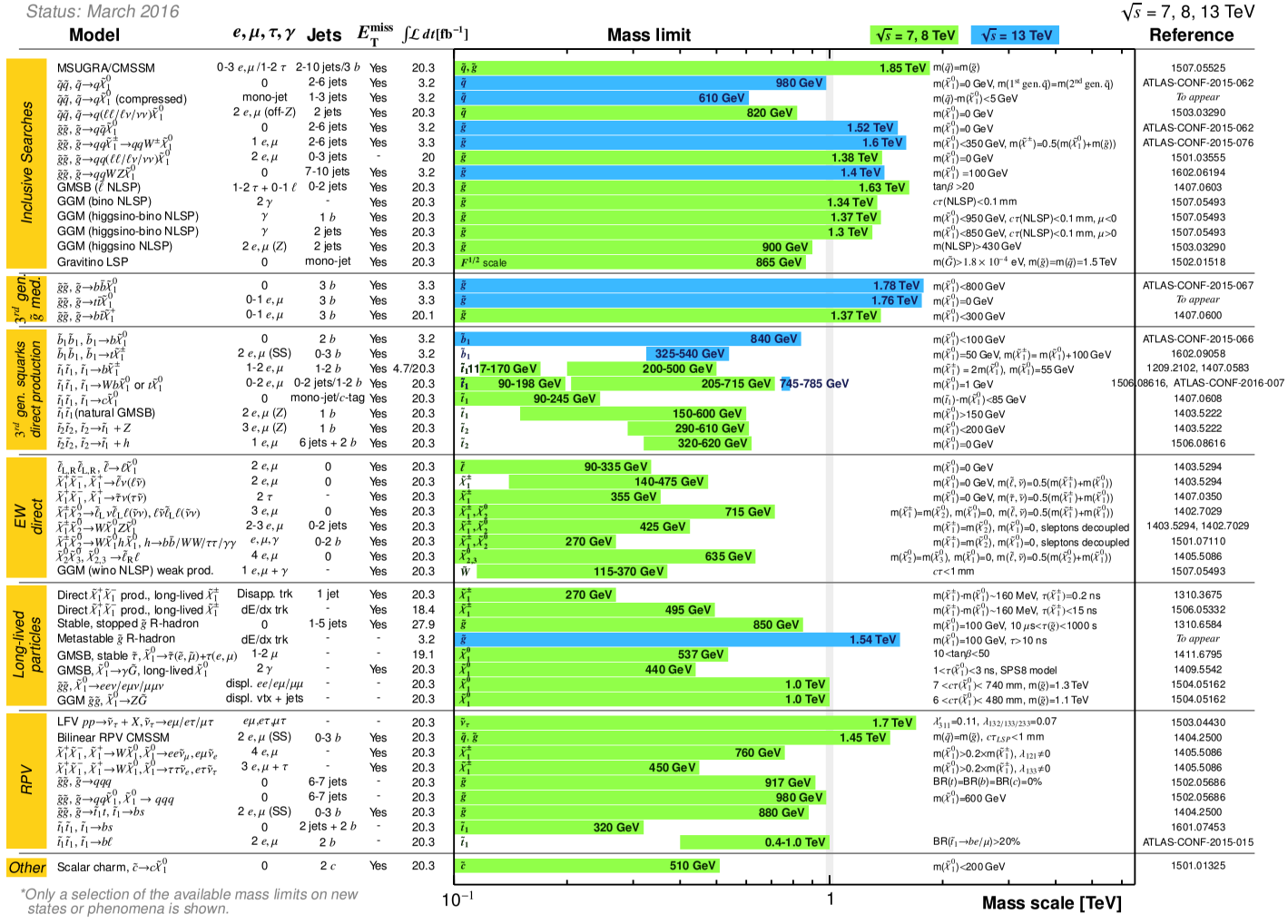

Fig. 8.1 · Masses of supersymmetric particles excluded by searches by ATLAS at $\sqrt{s} = 7$ TeV, 8 TeV, and 13 TeV. Only a subset of models are included in the figure. The figure is taken from Ref. [278].

high exclusion limits in this model of 1.85 TeV when $m_{\tilde{q}} = m_{\tilde{g}}$, MSUGRA/CMSSM does not look as attractive anymore.

Instead one could move to an even more complex SUSY model with more free parameters. An example of such a supersymmetric model could be pMSSM with 19 free parameters. The exclusion in the the pMSSM parameter space can be studied in slices of the parameter space as it was done in the analysis presented in Chapter 5 where limits on left-handed squark-pair production was presented.

Another possibility is to study a wider scan of the 19 free parameters of the pMSSM and check whether or not a point in the pMSSM parameter space is excluded by any of the ATLAS searches for supersymmetry. Such an analysis was performed on the full Run-I dataset using all searches for supersymmetry published by ATLAS [279]. In total more than 300.000 points in the pMSSM parameter space were generated and studied. The points were chosen to fulfill a set of constraints such as precision measurements of rare b-decays, the measured relic density of dark matter in the Universe, and the observed mass of the Higgs boson. For each generated point, it is checked whether it is excluded or not by any of the ATLAS searches for supersymmetry.

One of the most powerful analyses at excluding points in the pMSSM phase space is the analysis presented in Chapter 5. The 0-lepton analysis is very general as it selects events containing jets and $E_{\mathrm{T}}^{\mathrm{miss}}$ while vetoing events containing electrons and muons, and will therefore be sensitive to many models that contain light squarks or gluinos. In Figure 8.2, the fraction of excluded points models are presented in two-dimensional parameter spaces together with the limits in simplified models with direct decays placed by the 0-lepton analysis at $\sqrt{s} = 8$ TeV. It can be seen that the fraction of pMSSM points which are excluded in the $m_{\tilde{g}}$-$m_{\tilde{\chi}_1^0}$-plane shown in Figure 8.2b is close to 1 within the limit on the simplified model with direct decays. The fraction of pMSSM points in the squark-plane in Figure 8.2a that are excluded within the limit on a simplified model with direct squark decays are in ranges from 0.6 to 0.8. Hence, there are models with squark masses lower than the current limits placed on simplified models that have not been excluded by any of the ATLAS searches for supersymmetry.

The fraction of excluded models studied in the $m_{\tilde{q}}$-$m_{\tilde{g}}$-plane are shown in Figures 8.2c and 8.2d with wino-like and bino-like $\tilde{\chi}_1^0$, respectively, along with the limit placed by the 0-lepton analysis in a model with a massless $\tilde{\chi}_1^0$. It can be seen that still many models are not excluded by the searches for supersymmetry. In particular, the fraction of models with bino-like $\tilde{\chi}_1^0$ excluded by the supersymmetry searches is low. Due to the requirement on the relic density of Dark Matter, the models with bino-like $\tilde{\chi}_1^0$ are typically more compressed and the searches for supersymmetry are therefore not as sensitive. Hence, there are still many points in the SUSY phase space even with low squark or gluino masses which are not yet excluded.

A summary of the fraction of excluded model points for each type of sparticle as a function of their masses can be seen in Figure 8.3. It can be seen that many of the model points where the gluino is lighter than 1300 GeV or the first two generations of squarks are lighter than 600 GeV have been excluded. Not all model points with light charginos and neutralinos are excluded and with the increasing cross sections of supersymmetric particle production with the increase in collision energy, the search for electroweak supersymmetry becomes very interesting. The

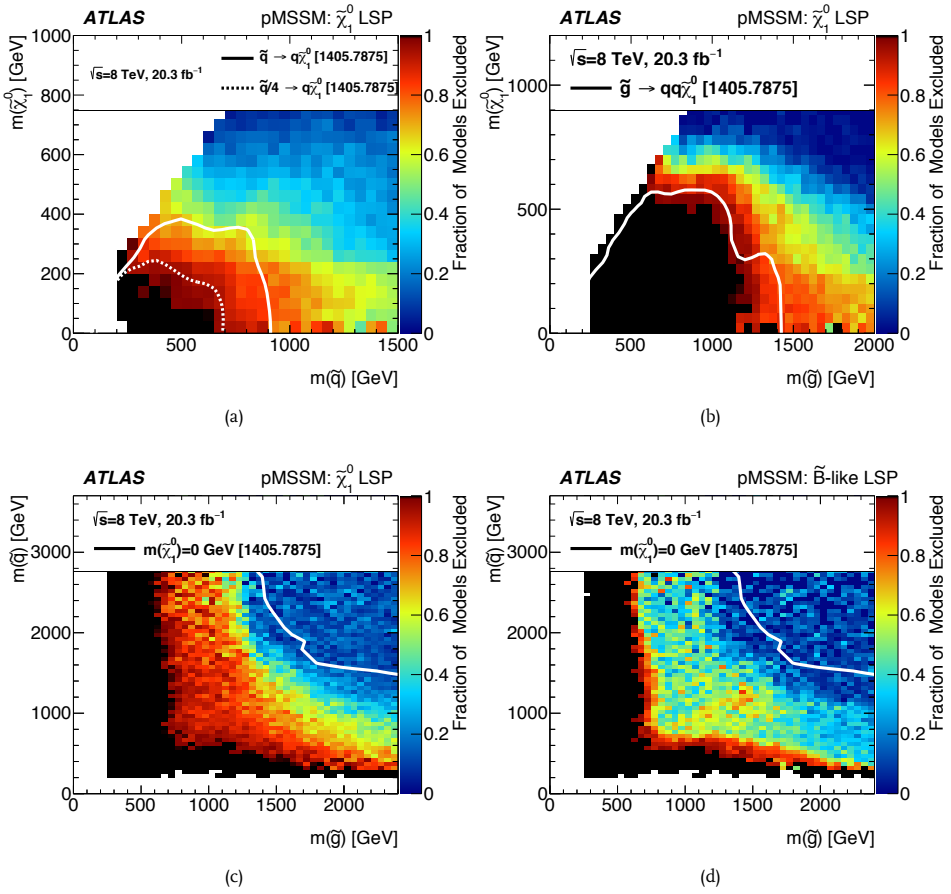

Fig. 8.2 · Fraction of pMSSM points excluded in the $m(\tilde{q})$-$m(\tilde{\chi}_1^0)$-plane (a), in the $m_(\tilde{g})$-$m(\tilde{\chi}_1^0)$-plane (b), and in the $m(\tilde{g})$-$m(\tilde{q})$-plane with a wino-like $\tilde{\chi}_1^0$ (c) and a bino-like $\tilde{\chi}_1^0$ (d). The overlaid line shows a limit for a simplified models obtained with the analysis presented in Chapter 5 selecting events with jets and $E_{\mathrm{T}}^{\mathrm{miss}}$. The figures are taken from Ref. [279].

excluded fraction of model points as a function if the mass of $\tilde{\chi}_1^{\pm}$ first decreases to ~ 0 around 1 TeV and then increases again at a mass of 1.5 TeV. This pattern is caused by the correlation of the mass of $\tilde{\chi}_1^{\pm}$ with the mass of a higgsino or wino-like LSP: when the $\tilde{\chi}_1^{\pm}$ gets heavier so does the higgsino or wino-like $\tilde{\chi}_1^0$. As the mass of $\tilde{\chi}_1^{\pm}$ increases beyond 1500 GeV, the higgsino or wino-like LSP becomes very heavy and the fraction is only representative of models with a bino-like $\tilde{\chi}_1^0$.

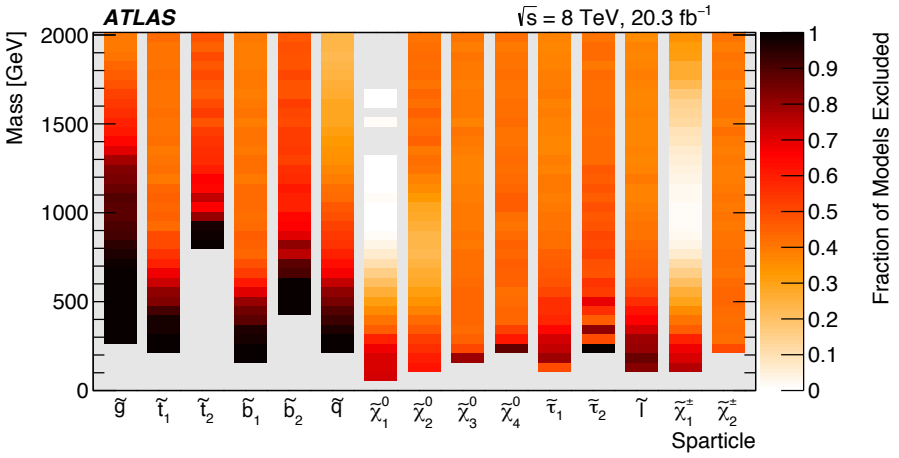

Fig. 8.3 · The fraction of model points excluded by the ATLAS supersymmetry searches for each sparticle in the pMSSM model point scan. The figure is taken from Ref. [278].

The search for supersymmetry at the LHC has just begun and the increase in collision energy has unlocked sensitivity to entire new parts of the SUSY phase-space. The LHC has resumed proton collisions in 2016, and the ATLAS experiment has already by August 2016 collected 20 fb^{-1}. The coming years will bring many more proton collisions and with the large increase in the amount data, the Standard Model will be facing a tough test. More data will show whether the Standard Model will hold or hints of new physics will show up. Supersymmetry is still an interesting theory meeting several shortcomings of the Standard Model and it has not yet been ruled out by the exclusion limits placed by the searches at the LHC.

Only time and more data will show whether or not hints of new physics beyond the Standard Model will be seen at the Large Hadron Collider.

B

Bibliography

[1] ATLAS Collaboration, *Search for squarks and gluinos with the ATLAS detector in final states with jets and missing transverse momentum using $\sqrt{s} = 8$ TeV proton–proton collision data*, JHEP **09** (2014) 176, arXiv:1405.7875 [hep-ex]. (Cited on pages 3, 85, 102, 109, 185, 190, 194, 196, and 200.)

[2] ATLAS Collaboration, *Summary of the searches for squarks and gluinos using $\sqrt{s} = 8$ TeV pp collisions with the ATLAS experiment at the LHC*, JHEP **10** (2015) 054, arXiv:1507.05525 [hep-ex]. (Cited on pages 3, 85, 102, 142, 143, 144, 177, 178, and 179.)

[3] ATLAS Collaboration, *Search for squarks and gluinos in final states with jets and missing transverse momentum at $\sqrt{s} = 13$ TeV with the ATLAS detector*, Eur. Phys. J. **C76** no. 7, (2016) 392, arXiv:1605.03814 [hep-ex]. (Cited on pages 3, 145, 195, 196, 200, and 201.)

[4] ATLAS Collaboration, *Search for Supersymmetry at the high luminosity LHC with the ATLAS experiment*, Tech. Rep. ATL-PHYS-PUB-2014-010, CERN, Geneva, Jul, 2014. (Cited on pages 3, 185, and 187.)

[5] S. Glashow, *Partial Symmetries of Weak Interactions*, Nucl. Phys. **22** (1961) 579–588. (Cited on pages 5 and 8.)

[6] S. Weinberg, *A Model of Leptons*, Phys. Rev. Lett. **19** (1967) 1264–1266. (Cited on pages 5 and 8.)

[7] A. Salam, *Weak and Electromagnetic Interactions*, Conf. Proc. **C680519** (1968) 367–377. (Cited on pages 5 and 8.)

[8] F. Englert and R. Brout, *Broken Symmetry and the Mass of Gauge Vector Mesons*, Phys. Rev. Lett. **13** (1964) 321–323. (Cited on pages 5 and 10.)

[9] P. W. Higgs, *Broken Symmetries and the Masses of Gauge Bosons*, Phys. Rev. Lett. **13** (1964) 508–509. (Cited on pages 5 and 10.)

[10] M. Gell-Mann, *A Schematic Model of Baryons and Mesons*, Phys. Lett. **8** (1964) 214–215. (Cited on pages 5 and 11.)

[11] G. Zweig, *An SU(3) model for strong interaction symmetry and its breaking*, Tech. Rep. CERN-TH-401, CERN, Geneva, 1964. (Cited on pages 5 and 11.)

[12] Particle Data Group Collaboration, K. A. Olive et al., *Review of Particle Physics*, Chin. Phys. **C38** (2014) 090001. (Cited on pages 6, 7, 22, and 62.)

[13] ATLAS Collaboration, *Observation of a new particle in the search for the Standard Model Higgs boson with the ATLAS detector at the LHC*, Phys. Lett. **B 716** (2012) 1–29, arXiv:1207.7214 [hep-ex]. (Cited on page 6.)

[14] CMS Collaboration, *Observation of a new boson at a mass of 125 GeV with the CMS experiment at the LHC*, Phys. Lett. **B 716** (2012) 30–61, arXiv:1207.7235 [hep-ex]. (Cited on page 6.)

[15] ATLAS, CMS Collaboration, *Combined Measurement of the Higgs Boson Mass in pp Collisions at $\sqrt{s} = 7$ and 8 TeV with the ATLAS and CMS Experiments*, Phys. Rev. Lett. **114** (2015) 191803, arXiv:1503.07589 [hep-ex]. (Cited on pages 6 and 7.)

[16] M. E. Peskin and D. V. Schroeder, *An Introduction to Quantum Field Theory*. Westview Press, Boulder, 1995. (Cited on pages 7 and 11.)

[17] UA1 Collaboration, *Experimental observation of isolated large transverse energy electrons with associated missing energy at $\sqrt{s}$ 540 GeV*, Phys. Lett. **B 122** (1983) 103–116. (Cited on page 8.)

[18] UA2 Collaboration, *Observation of single isolated electrons of high transverse momentum in events with missing transverse energy at the CERN $\bar{p}p$ collider*, Phys. Lett. **B 122** (1983) 476–485. (Cited on page 8.)

[19] UA1 Collaboration, *Experimental observation of lepton pairs of invariant mass around 95 GeV/c^2 at the CERN SPS collider*, Phys. Lett. **B 126** (1985) 398–410. (Cited on page 8.)

[20] UA2 Collaboration, *Evidence for $Z^0 \to e^+e^-$ at the CERN $\bar{p}p$ collider*, Phys. Lett. **B 129** (1983) 130–140. (Cited on page 8.)

[21] N. Cabibbo, *Unitary Symmetry and Leptonic Decays*, Phys. Rev. Lett. **10** (1963) 531–533. (Cited on page 9.)

[22] M. Kobayashi and T. Maskawa, *CP-Violation in the Renormalizable Theory of Weak Interaction*, Prog. Theor. Phys. **49** (1973) 652–657. (Cited on page 9.)

[23] C. N. Yang and R. L. Mills, *Conservation of Isotopic Spin and Isotopic Gauge Invariance*, Phys. Rev. **96** (1954) 191–195. http://link.aps.org/doi/10.1103/PhysRev.96.191. (Cited on page 9.)

[24] G. 't Hooft and M. Veltman, *Regularization and renormalization of gauge fields*, Nucl. Phys. **B 44** (1972) 189–213. (Cited on page 10.)

[25] D. Green, *High P_T Physics at Hadron Colliders*. Cambridge University Press, Cambride, 2005. (Cited on page 13.)

[26] H1 and ZEUS Collaboration, *Combined Measurement and QCD Analysis of the Inclusive e+- p Scattering Cross Sections at HERA*, JHEP **1001** (2010) 109, arXiv:0911.0884 [hep-ex]. (Cited on page 13.)

[27] H1 Collaboration, *Measurement of inclusive jet production in deep-inelastic scattering at high Q^2 and determination of the strong coupling*, Phys. Lett. **B 653** (2007) 134–144, arXiv:0706.3722 [hep-ex]. (Cited on page 13.)

[28] ZEUS Collaboration, *Inclusive-jet and dijet cross-sections in deep inelastic scattering at HERA*, Nucl. Phys. **B 765** (2007) 1–30, arXiv:hep-ex/0608048 [hep-ex]. (Cited on page 13.)

[29] DØ Collaboration, *Measurement of the inclusive jet cross-section in $p\bar{p}$ collisions at $\sqrt{s} = 1.96$ TeV*, Phys. Rev. Lett. **101** (2008) 062001, arXiv:0802.2400 [hep-ex]. (Cited on page 13.)

[30] CDF Collaboration, *Measurement of the Inclusive Jet Cross Section using the k_T algorithm in $p\bar{p}$ Collisions at $\sqrt{s} = 1.96$ TeV with the CDF II Detector*, Phys. Rev. **D 75** (2007) 092006, arXiv:hep-ex/0701051 [hep-ex]. (Cited on page 13.)

[31] ATLAS Collaboration, *Measurement of the Transverse Momentum Distribution of W Bosons in pp Collisions at $\sqrt{s} = 7$ TeV with the ATLAS Detector*, Phys. Rev. **D85** (2012) 012005, arXiv:1108.6308 [hep-ex]. (Cited on page 13.)

[32] CMS Collaboration, *Measurement of the muon charge asymmetry in inclusive $pp \to W + X$ production at $\sqrt{s} = 7$ TeV and an improved determination of light parton distribution functions*, Phys. Rev. **D90** no. 3, (2014) 032004, arXiv:1312.6283 [hep-ex]. (Cited on page 13.)

[33] LHCb Collaboration, *Measurement of the cross-section for $Z \to e^+e^-$ production in pp collisions at $\sqrt{s} = 7$ TeV*, JHEP **02** (2013) 106, arXiv:1212.4620 [hep-ex]. (Cited on page 13.)

[34] A. Martin, W. Stirling, R. Thorne, and G. Watt, *Parton distributions for the LHC*, Eur. Phys. J. **C 63** (2009) 189–285, arXiv:0901.0002 [hep-ph]. (Cited on pages 13, 96, and 146.)

[35] NNPDF Collaboration, *Parton distributions for the LHC Run II*, JHEP **04** (2015) 040, arXiv:1410.8849 [hep-ph]. (Cited on pages 13 and 14.)

[36] H.-L. Lai, M. Guzzi, J. Huston, Z. Li, P. M. Nadolsky, J. Pumplin, and C. P. Yuan, *New parton distributions for collider physics*, Phys. Rev. **D82** (2010) 074024, arXiv:1007.2241 [hep-ph]. (Cited on pages 13, 47, 95, 151, and 189.)

[37] J. Pumplin, D. R. Stump, J. Huston, H. L. Lai, P. M. Nadolsky, and W. K. Tung, *New generation of parton distributions with uncertainties from global QCD analysis*, JHEP **07** (2002) 012, arXiv:hep-ph/0201195 [hep-ph]. (Cited on pages 13, 47, 93, 95, and 189.)

[38] J. C. Collins, D. E. Soper, and G. F. Sterman, *Factorization of Hard Processes in QCD*, Adv. Ser. Direct. High Energy Phys. **5** (1989) 1–91, arXiv:hep-ph/0409313 [hep-ph]. (Cited on page 14.)

[39] G. F. Sterman, *Summation of Large Corrections to Short Distance Hadronic Cross-Sections*, Nucl. Phys. **B281** (1987) 310. (Cited on page 14.)

[40] Planck Collaboration, *Planck 2015 results. I. Overview of products and scientific results*, arXiv:1502.01582 [astro-ph.CO]. (Cited on page 15.)

[41] Planck Collaboration, *Planck 2015 results. XIII. Cosmological parameters*, arXiv:1502.01589 [astro-ph.CO]. (Cited on pages 15 and 27.)

[42] WMAP Collaboration, *Nine-Year Wilkinson Microwave Anisotropy Probe (WMAP) Observations: Final Maps and Results*, Astrophys. J. Suppl. **208** (2013) 20, arXiv:1212.5225 [astro-ph.CO]. (Cited on page 15.)

[43] WMAP Collaboration, *Nine-year Wilkinson Microwave Anisotropy Probe (WMAP) Observations: Cosmological Parameter Results*, Astrophys. J. Suppl. **208** (2013) 19, arXiv:1212.5226. (Cited on pages 15 and 27.)

[44] F. Zwicky, *Die Rotverschiebung von extragalaktischen Nebeln*, Helv. Phys. Acta **6** (1933) 110–127. (Cited on page 15.)

[45] Supernova Search Team Collaboration, *Observational evidence from supernovae for an accelerating universe and a cosmological constant*, Astron. J. **116** (1998) 1009–1038, arXiv:astro-ph/9805201 [astro-ph]. (Cited on page 15.)

[46] S. P. Martin, *A Supersymmetry primer*, arXiv:hep-ph/9709356v7 [hep-ph]. [Adv. Ser. Direct. High Energy Phys.18,1(1998)]. (Cited on pages 15, 18, 19, 21, and 22.)

[47] H. Georgi and S. L. Glashow, *Unity of All Elementary Particle Forces*, Phys. Rev. Lett. **32** (1974) 438–441. (Cited on page 16.)

[48] J. C. Pati and A. Salam, *Lepton Number as the Fourth Color*, Phys. Rev. **D10** (1974) 275–289. [Erratum: Phys. Rev.D11,703(1975)]. (Cited on page 16.)

[49] A. J. Buras, J. Ellis, M. K. Gaillard, and D. V. Nanopoulos, *Aspects of the grand unification of strong, weak and electromagnetic interactions*, Nuclear Physics B **135** (1978) 66–92. (Cited on page 16.)

[50] G. D. Coughlan, J. E. Dodd, and B. M. Gripaios, *The Ideas of Particle Physics*. Cambridge University Press, Cambridge, 1984. (Cited on page 16.)

[51] A. Riotto, *Theories of baryogenesis*, in *High energy physics and cosmology. Proceedings, Summer School, Trieste, Italy, June 29-July 17, 1998*. 1998. arXiv:hep-ph/9807454 [hep-ph]. http://inspirehep.net/record/473645/files/arXiv:hep-ph_9807454.pdf. (Cited on page 17.)

[52] S. Coleman and J. Mandula, *All Possible Symmetries of the S Matrix*, Phys. Rev. **159** (1967) 1251–1256. (Cited on page 17.)

[53] R. Haag, J. T. Łuposzański, and M. Sohnius, *All possible generators of supersymmetries of the S-matrix*, Nucl. Phys. **B 88** (1975) 257–274. (Cited on page 17.)

[54] L. Girardello and M. T. Grisaru, *Soft Breaking of Supersymmetry*, Nucl. Phys. B **194** (1982) 65. (Cited on page 19.)

[55] H. W. Baer and X. Tata, *Weak scale supersymmetry: from superfields to scattering events*. Cambridge Univ. Press, Cambridge, 2006. (Cited on page 19.)

[56] P. Fayet, *Supersymmetry and Weak, Electromagnetic and Strong Interactions*, Phys. Lett. B **64** (1976) 159. (Cited on page 20.)

[57] P. Fayet, *Spontaneously Broken Supersymmetric Theories of Weak, Electromagnetic and Strong Interactions*, Phys. Lett. B **69** (1977) 489. (Cited on page 20.)

[58] Super-Kamiokande Collaboration, *Search for proton decay via $p \to \nu\nu K^+$ using 260 kiloton·year data of Super-Kamiokande*, Phys. Rev. **D90** no. 7, (2014) 072005, arXiv:1408.1195 [hep-ex]. (Cited on page 21.)

[59] G. R. Farrar and P. Fayet, *Phenomenology of the Production, Decay, and Detection of New Hadronic States Associated with Supersymmetry*, Phys. Lett. **B76** (1978) 575–579. (Cited on page 21.)

[60] M. Drees, R. Godbole, and P. Roy, *Theory and phenomenology of Sparticles: an account of four-dimensional N=1 supersymmetry in high-energy physics*. World Scientific Publishing, Singapore, 2004. (Cited on page 23.)

[61] A. H. Chamseddine, R. L. Arnowitt, and P. Nath, *Locally Supersymmetric Grand Unification*, Phys. Rev. Lett. **49** (1982) 970. (Cited on pages 24 and 72.)

[62] R. Barbieri, S. Ferrara, and C. A. Savoy, *Gauge Models with Spontaneously Broken Local Supersymmetry*, Phys. Lett. B **119** (1982) 343. (Cited on pages 24 and 72.)

[63] G. L. Kane, C. F. Kolda, L. Roszkowski, and J. D. Wells, *Study of constrained minimal supersymmetry*, Phys. Rev. D **49** (1994) 6173–6210, arXiv:hep-ph/9312272 [hep-ph]. (Cited on pages 24 and 72.)

[64] M. Dine and W. Fischler, *A Phenomenological Model of Particle Physics Based on Supersymmetry*, Phys. Lett. B **110** (1982) 227. (Cited on page 24.)

[65] L. Alvarez-Gaume, M. Claudson, and M. B. Wise, *Low-Energy Supersymmetry*, Nucl. Phys. B **207** (1982) 96. (Cited on page 24.)

[66] C. R. Nappi and B. A. Ovrut, *Supersymmetric Extension of the SU(3) x SU(2) x U(1) Model*, Phys. Lett. B **113** (1982) 175. (Cited on page 24.)

[67] G. F. Giudice, M. A. Luty, H. Murayama, and R. Rattazzi, *Gaugino mass without singlets*, JHEP **12** (1998) 027, arXiv:hep-ph/9810442 [hep-ph]. (Cited on page 24.)

[68] L. Randall and R. Sundrum, *Out of this world supersymmetry breaking*, Nucl. Phys. B **557** (1999) 79–118, arXiv:hep-th/9810155 [hep-th]. (Cited on page 24.)

[69] MSSM Working Group Collaboration, A. Djouadi et al., *The Minimal supersymmetric standard model: Group summary report*, in *GDR (Groupement De Recherche) - Supersymetrie Montpellier, France, April 15-17, 1998*. 1998. arXiv:hep-ph/9901246 [hep-ph]. (Cited on page 24.)

[70] C. F. Berger, J. S. Gainer, J. L. Hewett, and T. G. Rizzo, *Supersymmetry Without Prejudice*, JHEP **02** (2009) 023, arXiv:0812.0980 [hep-ph]. (Cited on page 24.)

[71] J. Alwall, M.-P. Le, M. Lisanti, and J. G. Wacker, *Searching for Directly Decaying Gluinos at the Tevatron*, Phys. Lett. B **666** (2008) 34–37, arXiv:0803.0019 [hep-ph]. (Cited on page 25.)

[72] J. Alwall, P. Schuster, and N. Toro, *Simplified Models for a First Characterization of New Physics at the LHC*, Phys. Rev. D **79** (2009) 075020, arXiv:0810.3921 [hep-ph]. (Cited on page 25.)

[73] LHC New Physics Working Group Collaboration, D. Alves, *Simplified Models for LHC New Physics Searches*, J. Phys. G **39** (2012) 105005, arXiv:1105.2838 [hep-ph]. (Cited on page 25.)

[74] LEP2 SUSY Working group, *Combined LEP Chargino Results, up to 208 GeV for large m_0*, Tech. Rep. LEPSUSYWG/01-03.1, CERN, Geneva, 2001. (Cited on page 26.)

[75] LEP2 SUSY Working group, *Combined LEP Chargino Results, up to 208 GeV for low DM*, Tech. Rep. LEPSUSYWG/02-04.1, CERN, Geneva, 2002. (Cited on page 26.)

[76] DELPHI Collaboration, *Searches for supersymmetric particles in e^+ e^- collisions up to 208 GeV and interpretation of the results within the MSSM*, Eur. Phys. J. **C 31** (2003) 421–479, arXiv:hep-ex/0311019 [hep-ex]. (Cited on page 26.)

[77] ALEPH Collaboration, *Absolute lower limits on the masses of selectrons and sneutrinos in the MSSM*, Phys. Lett. **B 544** (2002) 73–88, arXiv:hep-ex/0207056 [hep-ex]. (Cited on page 26.)

[78] CDF Collaboration, *Inclusive Search for Squark and Gluino Production in $p\bar{p}$ Collisions at $\sqrt{s} = 1.96$ TeV*, Phys. Rev. Lett. **102** (2009) 121801. (Cited on page 26.)

[79] DØ Collaboration, *Search for squarks and gluinos in events with jets and missing transverse energy using 2.1 fb^{-1} of $p\bar{p}$ collision data at $\sqrt{s} = 1.96$ TeV*, Phys. Lett. **B 660** (2008) 449–457, arXiv:0712.3805 [hep-ex]. (Cited on page 26.)

[80] BaBar Collaboration, J. P. Lees et al., *Exclusive Measurements of $b \to s\gamma$ Transition Rate and Photon Energy Spectrum*, Phys. Rev. **D86** (2012) 052012, arXiv:1207.2520 [hep-ex]. (Cited on page 27.)

[81] CMS and L. Collaborations, *Observation of the rare $B_s^0 \to \mu^+\mu^-$ decay from the combined analysis of CMS and LHCb data*, Nature **522** (2015) 68–72, arXiv:1411.4413 [hep-ex]. (Cited on page 27.)

[82] A. Arbey, M. Battaglia, F. Mahmoudi, and D. Martinez Santos, *Supersymmetry confronts $B_s \to \mu^+\mu^-$: Present and future status*, Phys. Rev. **D 87** (2013) 035026, arXiv:1212.4887 [hep-ph]. (Cited on page 27.)

[83] Muon G-2 Collaboration, *Final Report of the Muon E821 Anomalous Magnetic Moment Measurement at BNL*, Phys. Rev. **D 73** (2006) 072003, arXiv:hep-ex/0602035 [hep-ex]. (Cited on page 27.)

[84] S. P. Martin and J. D. Wells, *Muon anomalous magnetic dipole moment in supersymmetric theories*, Phys. Rev. **D64** (2001) 035003, arXiv:hep-ph/0103067 [hep-ph]. (Cited on page 27.)

[85] A. Arbey, M. Battaglia, A. Djouadi, F. Mahmoudi, and J. Quevillon, *Implications of a 125 GeV Higgs for supersymmetric models*, Phys. Lett. **B708** (2012) 162–169, arXiv:1112.3028 [hep-ph]. (Cited on page 27.)

[86] R. Bernabei et al., *Final model independent results of DAMA/LIBRA-phase1 and perspectives of phase2*, Phys. Part. Nucl. **46** no. 2, (2015) 138–146. (Cited on page 27.)

[87] C. E. Aalseth et al., *Search for an Annual Modulation in a p-Type Point Contact Germanium Dark Matter Detector*, Phys. Rev. Lett. **107** (2011) 141301, arXiv:1106.0650 [astro-ph.CO]. (Cited on page 27.)

[88] O. Adriani et al., *Cosmic-Ray Positron Energy Spectrum Measured by PAMELA*, Phys. Rev. Lett. **111** (2013) 081102. (Cited on page 27.)

[89] AMS Collaboration, *Electron and Positron Fluxes in Primary Cosmic Rays Measured with the Alpha Magnetic Spectrometer on the International Space Station*, Phys. Rev. Lett. **113** (2014) 121102. (Cited on page 27.)

[90] AMS Collaboration, *High Statistics Measurement of the Positron Fraction in Primary Cosmic Rays of 0.5–500 GeV with the Alpha Magnetic Spectrometer on the International Space Station*, Phys. Rev. Lett. **113** (2014) 121101. (Cited on page 27.)

[91] XENON100 Collaboration, *Dark Matter Results from 225 Live Days of XENON100 Data*, Phys. Rev. Lett. **109** (2012) 181301, arXiv:1207.5988 [astro-ph.CO]. (Cited on page 27.)

[92] LUX Collaboration, *First results from the LUX dark matter experiment at the Sanford Underground Research Facility*, Phys. Rev. Lett. **112** (2014) 091303, arXiv:1310.8214 [astro-ph.CO]. (Cited on page 27.)

[93] S. Henrot-Versillé, R. Lafaye, T. Plehn, M. Rauch, D. Zerwas, S. Plaszczynski, B. Rouillé d'Orfeuil, and M. Spinelli, *Constraining Supersymmetry using the relic density and the Higgs boson*, Phys. Rev. **D89** no. 5,

(2014) 055017, arXiv:1309.6958 [hep-ph]. (Cited on page 27.)

[94] Prospino2. http://www.thphys.uni-heidelberg.de/~plehn/includes/prospino/prospino_lhc8.eps. Accessed: 2016-03-04. (Cited on page 29.)

[95] O. S. Bruning, P. Collier, P. Lebrun, S. Myers, R. Ostojic, J. Poole, and P. Proudlock, *LHC Design Report Vol.1: The LHC Main Ring,*. (Cited on pages 31 and 45.)

[96] O. Buning, P. Collier, P. Lebrun, S. Myers, R. Ostojic, J. Poole, and P. Proudlock, *LHC Design Report. 2. The LHC infrastructure and general services,*. (Cited on page 31.)

[97] M. Benedikt, P. Collier, V. Mertens, J. Poole, and K. Schindl, *LHC Design Report. 3. The LHC injector chain,*. (Cited on page 31.)

[98] L. Evans and P. Bryant, *LHC Machine*, JINST **3** (2008) S08001. (Cited on pages 31 and 33.)

[99] *LEP design report*. CERN, Geneva, 1984. https://cds.cern.ch/record/102083. (Cited on page 31.)

[100] C. Lefevre, *LHC: the guide (English version). Guide du LHC (version anglaise)*, https://cds.cern.ch/record/1165534, Feb, 2009. (Cited on page 32.)

[101] ATLAS Collaboration, *The ATLAS Experiment at the CERN Large Hadron Collider*, JINST **3** (2008) S08003. (Cited on pages 33, 34, 35, 36, 37, 40, and 41.)

[102] CMS Collaboration, *The CMS experiment at the CERN LHC*, JINST **3** (2008) S08004. (Cited on page 33.)

[103] ALICE Collaboration, *The ALICE experiment at the CERN LHC*, JINST **3** (2008) S08002. (Cited on page 33.)

[104] LHCb Collaboration, *The LHCb Detector at the LHC*, JINST **3** (2008) S08005. (Cited on page 33.)

[105] LHCf Collaboration, *The LHCf detector at the CERN Large Hadron Collider*, JINST **3** (2008) S08006. (Cited on page 33.)

[106] TOTEM Collaboration, *The TOTEM experiment at the CERN Large Hadron Collider*, JINST **3** (2008) S08007. (Cited on page 33.)

[107] MoEDAL Collaboration, *Technical Design Report of the MoEDAL Experiment*, Tech. Rep. CERN-LHCC-2009-006, CERN, Geneva, Jun, 2009. (Cited on page 33.)

[108] ATLAS Collaboration, *Luminosity Determination in pp Collisions at $\sqrt{s} = 7$ TeV Using the ATLAS Detector at the LHC*, Eur. Phys. J. **C71** (2011) 1630, arXiv:1101.2185 [hep-ex]. (Cited on page 34.)

[109] ATLAS Collaboration, *ATLAS detector and physics performance: Technical Design Report, 1*. No. ATLAS-TDR-14 in Technical Design Report ATLAS. CERN, Geneva, 1999. (Cited on page 34.)

[110] ATLAS Collaboration, *ATLAS detector and physics performance: Technical Design Report, 2*. No. ATLAS-TDR-15 in Technical Design Report ATLAS. CERN, Geneva, 1999. (Cited on page 34.)

[111] ATLAS Collaboration, *ATLAS magnet system: Technical Design Report, 1*. No. ATLAS-TDR-6 in Technical Design Report ATLAS. CERN, Geneva, 1997. (Cited on page 36.)

[112] ATLAS Collaboration Collaboration, *ATLAS central solenoid: Technical Design Report*. No. ATLAS-TDR-9 in Technical Design Report ATLAS. CERN, Geneva, 1997. (Cited on page 36.)

[113] ATLAS Collaboration, *ATLAS barrel toroid: Technical Design Report*. No. ATLAS-TDR-7 in Technical Design Report ATLAS. CERN, Geneva, 1997. (Cited on page 36.)

[114] ATLAS Collaboration, *ATLAS end-cap toroids: Technical Design Report*. No. ATLAS-TDR-8 in Technical Design Report ATLAS. CERN, Geneva, 1997. (Cited on page 36.)

[115] ATLAS Collaboration, *ATLAS inner detector: Technical Design Report, 1*. No. ATLAS-TDR-4 in Technical Design Report ATLAS. CERN, Geneva, 1997. (Cited on page 37.)

[116] ATLAS Collaboration, *ATLAS inner detector: Technical Design Report, 2.* No. ATLAS-TDR-5 in Technical Design Report ATLAS. CERN, Geneva, 1997. (Cited on page 37.)

[117] ATLAS Collaboration, *ATLAS pixel detector: Technical Design Report.* No. ATLAS-TDR-11 in Technical Design Report ATLAS. CERN, Geneva, 1998. (Cited on page 37.)

[118] ATLAS Collaboration, *ATLAS Insertable B-Layer Technical Design Report*, Tech. Rep. CERN-LHCC-2010-013. ATLAS-TDR-19, CERN, Geneva, Sep, 2010. http://cds.cern.ch/record/1291633. (Cited on page 38.)

[119] A. Abdesselam et al., *The barrel modules of the ATLAS semiconductor tracker*, Nucl. Instrum. Meth. **A 568** (2006) 642–671. (Cited on page 38.)

[120] A. Abdesselam et al., *The ATLAS semiconductor tracker end-cap module*, Nucl. Instrum. Meth. **A 575** (2007) 353–389. (Cited on page 38.)

[121] ATLAS TRT Collaboration, *The ATLAS TRT Barrel Detector*, JINST **3** (2008) P02014. (Cited on page 38.)

[122] ATLAS TRT Collaboration, *The ATLAS TRT end-cap detectors*, JINST **3** (2008) P10003. (Cited on page 38.)

[123] ATLAS Collaboration, *ATLAS liquid-argon calorimeter: Technical Design Report.* No. ATLAS-TDR-2 in Technical Design Report ATLAS. CERN, Geneva, 1996. (Cited on page 39.)

[124] ATLAS Collaboration, *ATLAS tile calorimeter: Technical Design Report.* No. ATLAS-TDR-3 in Technical Design Report ATLAS. CERN, Geneva, 1996. (Cited on page 39.)

[125] ATLAS Collaboration, *ATLAS muon spectrometer: Technical Design Report.* No. ATLAS-TDR-10 in Technical Design Report ATLAS. CERN, Geneva, 1997. (Cited on page 40.)

[126] ATLAS Collaboration, *ATLAS Forward Detectors for Luminosity Measurement and Monitoring*, Tech. Rep. CERN-LHCC-2004-010. LHCC-I-014, CERN, Geneva, Mar, 2004. (Cited on page 42.)

[127] ATLAS Collaboration, *ATLAS Forward Detectors for Measurement of Elastic Scattering and Luminosity.* No. ATLAS-TDR-18 in Technical Design Report ATLAS. CERN, Geneva, 2008. https://cds.cern.ch/record/1095847. (Cited on page 42.)

[128] ATLAS Collaboration, *Zero Degree Calorimeters for ATLAS*, Tech. Rep. LHCC-I-016. CERN-LHCC-2007-001, CERN, Geneva, Jan, 2007. (Cited on page 42.)

[129] R. Achenbach et al., *The ATLAS Level-1 Calorimeter Trigger*, JINST **3** (2008) P03001. (Cited on page 43.)

[130] ATLAS Collaboration, *2015 start-up trigger menu and initial performance assessment of the ATLAS trigger using Run-2 data*, Tech. Rep. ATL-DAQ-PUB-2016-001, CERN, Geneva, Mar, 2016. https://cds.cern.ch/record/2136007. (Cited on page 43.)

[131] ATLAS Collaboration, *ATLAS Data Summary Page.* https://atlas.web.cern.ch/Atlas/GROUPS/DATAPREPARATION/DataSummary, 2016. (Cited on page 45.)

[132] ATLAS Collaboration, *ATLAS Detector Status.* https://twiki.cern.ch/twiki/bin/view/AtlasPublic/ApprovedPlotsATLASDetector, 2016. (Cited on page 45.)

[133] T. Sjostrand, S. Mrenna, and P. Z. Skands, *PYTHIA 6.4 physics and manual*, JHEP **0605** (2006) 026, arXiv:0603175 [hep-ph]. (Cited on pages 47, 93, 95, 150, 151, and 152.)

[134] T. Sjostrand, S. Mrenna, and P. Z. Skands, *A Brief Introduction to PYTHIA 8.1*, Comput. Phys. Commun. **178** (2008) 852–867, arXiv:0710.3820 [hep-ph]. (Cited on pages 47, 96, 150, 151, and 152.)

[135] T. Gleisberg, S. Hoeche, F. Krauss, M. Schonherr, S. Schumann, et al., *Event generation with SHERPA 1.1*, JHEP **0902** (2009) 007, arXiv:0811.4622 [hep-ph]. (Cited on pages 47, 95, 151, and 189.)

[136] G. Corcella, I. Knowles, G. Marchesini, S. Moretti, K. Odagiri, et al., *HERWIG 6: An Event generator for hadron emission reactions with interfering gluons (including supersymmetric processes)*, JHEP **0101** (2001) 010, arXiv:hep-ph/0011363. (Cited on pages 47 and 95.)

[137] G. Corcella, I. G. Knowles, G. Marchesini, S. Moretti, K. Odagiri, P. Richardson, M. H. Seymour, and B. R. Webber, *HERWIG 6.5 release note*, arXiv:hep-ph/0210213 [hep-ph]. (Cited on pages 47 and 95.)

[138] M. Bahr, S. Gieseke, M. Gigg, D. Grellscheid, K. Hamilton, et al., *Herwig++ Physics and Manual*, Eur.Phys.J. **C58** (2008) 639–707, arXiv:0803.0883 [hep-ph]. (Cited on pages 47, 93, 151, and 188.)

[139] J. Alwall, M. Herquet, F. Maltoni, O. Mattelaer, and T. Stelzer, *MadGraph 5 : Going Beyond*, JHEP **06** (2011) 128, arXiv:1106.0522 [hep-ph]. (Cited on pages 47, 93, 95, 188, and 189.)

[140] M. L. Mangano, M. Moretti, F. Piccinini, R. Pittau, and A. D. Polosa, *ALPGEN, a generator for hard multiparton processes in hadronic collisions*, JHEP **0307** (2003) 001, arXiv:hep-ph/0206293. (Cited on pages 47 and 95.)

[141] P. Nason, *A New method for combining NLO QCD with shower Monte Carlo algorithms*, JHEP **0411** (2004) 040, arXiv:hep-ph/0409146. (Cited on pages 47, 95, and 151.)

[142] S. Frixione, P. Nason, and C. Oleari, *Matching NLO QCD computations with parton shower simulations: the POWHEG method*, JHEP **0711** (2007) 070, arXiv:0709.2092 [hep-ph]. (Cited on pages 47, 95, and 151.)

[143] S. Alioli, P. Nason, C. Oleari, and E. Re, *A general framework for implementing NLO calculations in shower Monte Carlo programs: the POWHEG BOX*, JHEP **1006** (2010) 043, arXiv:1002.2581 [hep-ph]. (Cited on pages 47, 95, and 151.)

[144] S. Frixione and B. R. Webber, *Matching NLO QCD computations and parton shower simulations*, JHEP **06** (2002) 029, arXiv:hep-ph/0204244 [hep-ph]. (Cited on pages 47, 95, and 151.)

[145] S. Frixione, P. Nason, and B. R. Webber, *Matching NLO QCD and parton showers in heavy flavor production*, JHEP **08** (2003) 007, arXiv:hep-ph/0305252 [hep-ph]. (Cited on pages 47, 95, and 151.)

[146] S. Frixione, E. Laenen, P. Motylinski, and B. R. Webber, *Single-top production in MC@NLO*, JHEP **03** (2006) 092, arXiv:hep-ph/0512250 [hep-ph]. (Cited on pages 47, 95, and 151.)

[147] S. Frixione, E. Laenen, P. Motylinski, B. R. Webber, and C. D. White, *Single-top hadroproduction in association with a W boson*, JHEP **07** (2008) 029, arXiv:0805.3067 [hep-ph]. (Cited on pages 47, 95, and 151.)

[148] GEANT4 Collaboration, S. Agostinelli et al., *GEANT4: A simulation toolkit*, Nucl. Instrum. Meth. A **506** (2003) 250–303. (Cited on pages 47, 93, and 150.)

[149] ATLAS Collaboration, *The simulation principle and performance of the ATLAS fast calorimeter simulation FastCaloSim*, Tech. Rep. ATL-PHYS-PUB-2010-013, CERN, Geneva, Oct, 2010. https://cds.cern.ch/record/1300517. (Cited on pages 47, 93, and 150.)

[150] J. Pequenao and P. Schaffner, *An computer generated image representing how ATLAS detects particles*, https://cds.cern.ch/record/1505342, Jan, 2013. (Cited on page 50.)

[151] T. Cornelissen, M. Elsing, S. Fleischmann, W. Liebig, E. Moyse, and A. Salzburger, *Concepts, Design and Implementation of the ATLAS New Tracking (NEWT)*, Tech. Rep. ATL-SOFT-PUB-2007-007. ATL-COM-SOFT-2007-002, CERN, Geneva, Mar, 2007. https://cds.cern.ch/record/1020106. (Cited on page 51.)

[152] ATLAS Collaboration, *Performance of the ATLAS Inner Detector Track and Vertex Reconstruction in the High Pile-Up LHC Environment*, Tech. Rep. ATLAS-CONF-2012-042, CERN, Geneva, Mar, 2012.

https://cds.cern.ch/record/1435196. (Cited on pages 51, 52, and 53.)

[153] ATLAS Collaboration, *The Optimization of ATLAS Track Reconstruction in Dense Environments*, Tech. Rep. ATL-PHYS-PUB-2015-006, CERN, Geneva, Mar, 2015. https://cds.cern.ch/record/2002609. (Cited on page 51.)

[154] R. Fruhwirth, *Application of Kalman filtering to track and vertex fitting*, Nucl. Instrum. Meth. **A262** (1987) 444–450. (Cited on page 51.)

[155] ATLAS Collaboration, *Early Inner Detector Tracking Performance in the 2015 data at $\sqrt{s} = 13$ TeV*, Tech. Rep. ATL-PHYS-PUB-2015-051, CERN, Geneva, Dec, 2015. https://cds.cern.ch/record/2110140. (Cited on page 52.)

[156] G. Piacquadio, K. Prokofiev, and A. Wildauer, *Primary vertex reconstruction in the ATLAS experiment at LHC*, J. Phys. Conf. Ser. **119** (2008) 032033. (Cited on page 52.)

[157] ATLAS Collaboration, *Vertex Reconstruction Performance of the ATLAS Detector at $\sqrt{s} = 13$ TeV*, Tech. Rep. ATL-PHYS-PUB-2015-026, CERN, Geneva, Jul, 2015. https://cds.cern.ch/record/2037717. (Cited on pages 52 and 53.)

[158] R. Fruhwirth, W. Waltenberger, and P. Vanlaer, *Adaptive vertex fitting*, J. Phys. **G34** (2007) N343. (Cited on page 52.)

[159] ATLAS Collaboration, *Topological cell clustering in the ATLAS calorimeters and its performance in LHC Run 1*, arXiv:1603.02934 [hep-ex]. (Cited on page 54.)

[160] ATLAS Collaboration, *Jet Calibration and Systematic Uncertainties for Jets Reconstructed in the ATLAS Detector at $\sqrt{s} = 13$ TeV*, Tech. Rep. ATL-PHYS-PUB-2015-015, CERN, Geneva, Jul, 2015. https://cds.cern.ch/record/2037613. (Cited on pages 54, 55, 56, and 168.)

[161] M. Cacciari, G. P. Salam, and G. Soyez, *The anti-k_t jet clustering algorithm*, JHEP **04** (2008) 063, arXiv:0802.1189 [hep-ph]. (Cited on pages 54 and 96.)

[162] M. Cacciari, G. P. Salam, and G. Soyez, *FastJet User Manual*, Eur. Phys. J. **C72** (2012) 1896, arXiv:1111.6097 [hep-ph]. (Cited on page 54.)

[163] M. Cacciari and G. P. Salam, *Dispelling the N^3 myth for the k_t jet-finder*, Phys. Lett. B **641** (2006) 57–61, arXiv:hep-ph/0512210. (Cited on page 54.)

[164] M. Cacciari, G. P. Salam, and G. Soyez, *The Catchment Area of Jets*, JHEP **04** (2008) 005, arXiv:0802.1188 [hep-ph]. (Cited on page 54.)

[165] ATLAS Collaboration, G. Aad et al., *Performance of pile-up mitigation techniques for jets in pp collisions at $\sqrt{s} = 8$ TeV using the ATLAS detector*, arXiv:1510.03823 [hep-ex]. (Cited on page 54.)

[166] ATLAS Collaboration, *Jet energy measurement and its systematic uncertainty in proton-proton collisions at $\sqrt{s} = 7$ TeV with the ATLAS detector*, Eur. Phys. J. **C75** (2015) 17, arXiv:1406.0076 [hep-ex]. (Cited on pages 54 and 55.)

[167] ATLAS Collaboration, *Jet energy measurement with the ATLAS detector in proton-proton collisions at $\sqrt{s} = 7$ TeV*, Eur. Phys. J. **C73** no. 3, (2013) 2304, arXiv:1112.6426 [hep-ex]. (Cited on pages 55, 123, and 168.)

[168] ATLAS Collaboration, *Jet energy resolution in proton-proton collisions at $\sqrt{s} = 7$ TeV recorded in 2010 with the ATLAS detector*, Eur. Phys. J. **C73** no. 3, (2013) 2306, arXiv:1210.6210 [hep-ex]. (Cited on pages 55, 123, and 168.)

[169] ATLAS Collaboration, *Commissioning of the ATLAS high-performance b-tagging algorithms in the 7 TeV collision data*, Tech. Rep. ATLAS-CONF-2011-102, CERN, Geneva, Jul, 2011. https://cds.cern.ch/record/1369219. (Cited on page 56.)

[170] ATLAS Collaboration, *Expected Performance of the ATLAS Experiment - Detector, Trigger and Physics*, arXiv:0901.0512 [hep-ex]. (Cited on pages 56 and 62.)

[171] ATLAS Collaboration, *Calibration of the performance of b-tagging for c and light-flavour jets in the 2012 ATLAS data*, Tech. Rep. ATLAS-CONF-2014-046, CERN, Geneva, Jul, 2014. https://cds.cern.ch/record/1741020. (Cited on page 56.)

[172] ATLAS Collaboration, *Performance of b-Jet Identification in the ATLAS Experiment*, JINST **11** no. 04, (2016) P04008, arXiv:1512.01094 [hep-ex]. (Cited on pages 57 and 96.)

[173] ATLAS Collaboration, *Expected performance of the ATLAS b-tagging algorithms in Run-2*, Tech. Rep. ATL-PHYS-PUB-2015-022, CERN, Geneva, Jul, 2015. https://cds.cern.ch/record/2037697. (Cited on pages 57 and 152.)

[174] ATLAS Collaboration, *Electron reconstruction and identification efficiency measurements with the ATLAS detector using the 2011 LHC proton-proton collision data*, Eur. Phys. J. **C74** no. 7, (2014) 2941, arXiv:1404.2240 [hep-ex]. (Cited on pages 58 and 96.)

[175] ATLAS Collaboration, *Electron efficiency measurements with the ATLAS detector using the 2012 LHC proton-proton collision data*, Tech. Rep. ATLAS-CONF-2014-032, CERN, Geneva, Jun, 2014. https://cds.cern.ch/record/1706245. (Cited on pages 58 and 60.)

[176] W. Lampl, S. Laplace, D. Lelas, P. Loch, H. Ma, S. Menke, S. Rajagopalan, D. Rousseau, S. Snyder, and G. Unal, *Calorimeter Clustering Algorithms: Description and Performance*, Tech. Rep. ATL-LARG-PUB-2008-002. ATL-COM-LARG-2008-003, CERN, Geneva, Apr, 2008. https://cds.cern.ch/record/1099735. (Cited on page 58.)

[177] ATLAS Collaboration, *Electron and photon energy calibration with the ATLAS detector using LHC Run 1 data*, Eur. Phys. J. **C74** no. 10, (2014) 3071, arXiv:1407.5063 [hep-ex]. (Cited on pages 58 and 59.)

[178] ATLAS Collaboration, *Electron identification measurements in ATLAS using $\sqrt{s}$ = 13 TeV data with 50 ns bunch spacing*, Tech. Rep. ATL-PHYS-PUB-2015-041, CERN, Geneva, Sep, 2015. https://cds.cern.ch/record/2048202. (Cited on pages 58, 60, and 152.)

[179] ATLAS Collaboration, *Measurements of the photon identification efficiency with the ATLAS detector using* 4.9fb^{-1} *of pp collision data collected in 2011*, Tech. Rep. ATLAS-CONF-2012-123, CERN, Geneva, Aug, 2012. https://cds.cern.ch/record/1473426. (Cited on pages 59, 61, 97, and 153.)

[180] ATLAS Collaboration, *Measurement of the photon identification efficiencies with the ATLAS detector using LHC Run-1 data*, arXiv:1606.01813 [hep-ex]. (Cited on pages 59 and 61.)

[181] ATLAS Collaboration, *Muon reconstruction efficiency and momentum resolution of the ATLAS experiment in proton-proton collisions at $\sqrt{s}$ = 7 TeV in 2010*, Eur. Phys. J. **C74** no. 9, (2014) 3034, arXiv:1404.4562 [hep-ex]. (Cited on pages 61 and 96.)

[182] ATLAS Collaboration, *Measurement of the muon reconstruction performance of the ATLAS detector using 2011 and 2012 LHC proton-proton collision data*, Eur. Phys. J. **C74** no. 11, (2014) 3130, arXiv:1407.3935 [hep-ex]. (Cited on pages 61, 62, and 63.)

[183] ATLAS Collaboration, *Muon reconstruction performance of the ATLAS detector in proton-proton collision data at $\sqrt{s}$ =13 TeV*, Eur. Phys. J. **C76** no. 5, (2016) 292, arXiv:1603.05598 [hep-ex]. (Cited on pages 61, 62, 63, 152, and 153.)

[184] ATLAS Collaboration, *Identification and energy calibration of hadronically decaying tau leptons with the ATLAS experiment in pp collisions at $\sqrt{s}$=8 TeV*, Eur. Phys. J. **C75** no. 7, (2015) 303, arXiv:1412.7086 [hep-ex]. (Cited on pages 63, 64, and 97.)

[185] ATLAS Collaboration, *Reconstruction, Energy Calibration, and Identification of Hadronically Decaying Tau Leptons in the ATLAS Experiment for Run-2 of the LHC*, Tech. Rep. ATL-PHYS-PUB-2015-045, CERN, Geneva, Nov, 2015. https://cds.cern.ch/record/2064383. (Cited on pages 63 and 64.)

[186] ATLAS Collaboration, *Performance of Missing Transverse Momentum Reconstruction in Proton-Proton Collisions at 7 TeV with ATLAS*, Eur. Phys. J. **C72** (2012) 1844, arXiv:1108.5602 [hep-ex]. (Cited on page 65.)

[187] ATLAS Collaboration, *Performance of Missing Transverse Momentum Reconstruction in ATLAS studied in Proton-Proton Collisions recorded in 2012 at 8 TeV*, Tech. Rep. ATLAS-CONF-2013-082, CERN, Geneva, Aug, 2013. https://cds.cern.ch/record/1570993. (Cited on pages 65, 66, and 67.)

[188] ATLAS Collaboration, *Expected performance of missing transverse momentum reconstruction for the ATLAS detector at $\sqrt{s} = 13$ TeV*, Tech. Rep. ATL-PHYS-PUB-2015-023, CERN, Geneva, Jul, 2015. https://cds.cern.ch/record/2037700. (Cited on page 65.)

[189] ATLAS Collaboration, *Performance of missing transverse momentum reconstruction for the ATLAS detector in the first proton-proton collisions at at $\sqrt{s}$= 13 TeV*, Tech. Rep. ATL-PHYS-PUB-2015-027, CERN, Geneva, Jul, 2015. https://cds.cern.ch/record/2037904. (Cited on pages 65 and 66.)

[190] ATLAS Collaboration, *Tagging and suppression of pileup jets with the ATLAS detector*, Tech. Rep. ATLAS-CONF-2014-018, CERN, Geneva, May, 2014. https://cds.cern.ch/record/1700870. (Cited on page 65.)

[191] C. Chen, *New approach to identifying boosted hadronically-decaying particle using jet substructure in its center-of-mass frame*, Phys. Rev. **D85** (2012) 034007, arXiv:1112.2567 [hep-ph]. (Cited on page 72.)

[192] I. Hinchliffe, F. E. Paige, M. D. Shapiro, J. Soderqvist, and W. Yao, *Precision SUSY measurements at CERN LHC*, Phys. Rev. **D55** (1997) 5520–5540, arXiv:hep-ph/9610544 [hep-ph]. (Cited on page 72.)

[193] D. R. Tovey, *Measuring the SUSY mass scale at the LHC*, Phys. Lett. **B498** (2001) 1–10, arXiv:hep-ph/0006276 [hep-ph]. (Cited on pages 72 and 73.)

[194] C. Rogan, *Kinematical variables towards new dynamics at the LHC*, arXiv:1006.2727 [hep-ph]. (Cited on page 73.)

[195] C. G. Lester and D. J. Summers, *Measuring masses of semiinvisibly decaying particles pair produced at hadron colliders*, Phys. Lett. **B463** (1999) 99–103, arXiv:hep-ph/9906349 [hep-ph]. (Cited on pages 73 and 181.)

[196] D. R. Tovey, *On measuring the masses of pair-produced semi-invisibly decaying particles at hadron colliders*, JHEP **04** (2008) 034, arXiv:0802.2879 [hep-ph]. (Cited on page 73.)

[197] L. Randall and D. Tucker-Smith, *Dijet Searches for Supersymmetry at the Large Hadron Collider*, Phys. Rev. Lett. **101** (2008) 221803. http://link.aps.org/doi/10.1103/PhysRevLett.101.221803. (Cited on page 73.)

[198] G. Cowan, K. Cranmer, E. Gross, and O. Vitells, *Asymptotic formulae for likelihood-based tests of new physics*, Eur. Phys. J. **C71** (2011) 1554, arXiv:1007.1727 [physics.data-an]. [Erratum: Eur. Phys. J.C73,2501(2013)]. (Cited on pages 74, 81, and 131.)

[199] A. L. Read, *Presentation of search results: the CL_s technique*, Journal of Physics G: Nuclear and Particle Physics **28** no. 10, (2002) 2693. http://stacks.iop.org/0954-3899/28/i=10/a=313. (Cited on pages 75 and 81.)

[200] M. Baak, G. J. Besjes, D. Cote, A. Koutsman, J. Lorenz, et al., *HistFitter software framework for statistical data analysis*, arXiv:1410.1280 [hep-ex]. (Cited on page 79.)

[201] ROOT Collaboration, K. Cranmer, G. Lewis, L. Moneta, A. Shibata, and W. Verkerke, *HistFactory: A tool for creating statistical models for use with RooFit and RooStats*, Tech. Rep. CERN-OPEN-2012-016, CERN, Geneva, Jan, 2012. (Cited on page 79.)

[202] L. Moneta, K. Belasco, K. S. Cranmer, S. Kreiss, A. Lazzaro, et al., *The RooStats Project*, PoS **ACAT2010** (2010) 057, arXiv:1009.1003 [physics.data-an]. (Cited on page 79.)

[203] W. Verkerke and D. P. Kirkby, *The RooFit toolkit for data modeling*, eConf **C0303241** (2003) MOLT007, arXiv:physics/0306116. (Cited on page 79.)

[204] R. Brun and F. Rademakers, *ROOT: An object oriented data analysis framework*, Nucl. Instrum. Meth. **A 389** (1997) 81–86. (Cited on page 79.)

[205] I. Antcheva, M. Ballintijn, B. Bellenot, M. Biskup, R. Brun, et al., *ROOT: A C++ framework for petabyte data storage, statistical analysis and visualization*, Comput. Phys. Commun. **182** (2011) 1384–1385. (Cited on page 79.)

[206] R. Bruneliere, M. Baak, J. Lundberg, M. C. Rammensee, and T. J. Khoo, *Setting exclusion limits in ATLAS supersymmetry searches with a likelihood ratio based method*, Tech. Rep. ATL-PHYS-INT-2011-032, CERN, Geneva, Apr, 2011. https://cds.cern.ch/record/1342545. (Cited on page 79.)

[207] C. Gutschow and Z. Marshall, *Setting limits on supersymmetry using simplified models*, arXiv:1202.2662 [hep-ex]. (Cited on page 83.)

[208] T. J. LeCompte and S. P. Martin, *Large Hadron Collider reach for supersymmetric models with compressed mass spectra*, Phys. Rev. **D84** (2011) 015004, arXiv:1105.4304 [hep-ph]. (Cited on page 86.)

[209] T. J. LeCompte and S. P. Martin, *Compressed supersymmetry after 1/fb at the Large Hadron Collider*, Phys. Rev. **D85** (2012) 035023, arXiv:1111.6897 [hep-ph]. (Cited on page 86.)

[210] W. Beenakker, R. Hopker, M. Spira, and P. M. Zerwas, *Squark and gluino production at hadron colliders*, Nucl. Phys. **B492** (1997) 51–103, arXiv:hep-ph/9610490 [hep-ph]. (Cited on pages 86, 146, 147, 150, and 188.)

[211] A. Kulesza and L. Motyka, *Threshold resummation for squark-antisquark and gluino-pair production at the LHC*, Phys. Rev. Lett. **102** (2009) 111802, arXiv:0807.2405 [hep-ph]. (Cited on pages 86, 146, 147, 150, and 188.)

[212] A. Kulesza and L. Motyka, *Soft gluon resummation for the production of gluino-gluino and squark-antisquark pairs at the LHC*, Phys. Rev. **D80** (2009) 095004, arXiv:0905.4749 [hep-ph]. (Cited on pages 86, 146, 147, 150, and 188.)

[213] W. Beenakker, S. Brensing, M. Kramer, A. Kulesza, E. Laenen, and I. Niessen, *Soft-gluon resummation for squark and gluino hadroproduction*, JHEP **12** (2009) 041, arXiv:0909.4418 [hep-ph]. (Cited on pages 86, 146, 147, 150, and 188.)

[214] W. Beenakker, S. Brensing, M. Kramer, A. Kulesza, E. Laenen, L. Motyka, and I. Niessen, *Squark and Gluino Hadroproduction*, Int. J. Mod. Phys. **A26** (2011) 2637–2664, arXiv:1105.1110 [hep-ph]. (Cited on pages 86, 146, 147, 150, and 188.)

[215] A. Djouadi, M. Muhlleitner, and M. Spira, *Decays of supersymmetric particles: The Program SUSY-HIT (SUspect-SdecaY-Hdecay-InTerface)*, Acta Phys.Polon. **B38** (2007) 635–644, arXiv:hep-ph/0609292 [hep-ph]. (Cited on pages 87, 88, 90, and 91.)

[216] B. Allanach, *SOFTSUSY: a program for calculating supersymmetric spectra*, Comput.Phys.Commun. **143** (2002) 305–331, arXiv:hep-ph/0104145 [hep-ph]. (Cited on pages 87 and 88.)

[217] M. Muhlleitner, A. Djouadi, and Y. Mambrini, *SDECAY: A Fortran code for the decays of the supersymmetric particles in the MSSM*, Comput. Phys. Commun. **168** (2005) 46–70, arXiv:hep-ph/0311167 [hep-ph]. (Cited on pages 87 and 90.)

[218] W. Beenakker, R. Hopker, and M. Spira, *PROSPINO: A Program for the production of supersymmetric particles in next-to-leading order QCD*, arXiv:hep-ph/9611232 [hep-ph]. (Cited on pages 87, 90, 146, 147, and 188.)

[219] ATLAS Collaboration, *Improved luminosity determination in pp collisions at sqrt(s) = 7 TeV using the ATLAS detector at the LHC*, Eur. Phys. J. **C73** no. 8, (2013) 2518, arXiv:1302.4393 [hep-ex]. (Cited on pages 93, 123, and 149.)

[220] S. Catani, L. Cieri, G. Ferrera, D. de Florian, and M. Grazzini, *Vector boson production at hadron colliders: a fully exclusive QCD calculation at NNLO*, Phys. Rev. Lett. **103** (2009) 082001, arXiv:0903.2120 [hep-ph]. (Cited on pages 95 and 148.)

[221] ATLAS Collaboration, *First tuning of HERWIG/JIMMY to ATLAS data*, Tech. Rep. ATL-PHYS-PUB-2010-014, CERN, Geneva, Oct, 2010. https://cds.cern.ch/record/1303025.

(Cited on page 95.)

[222] M. Czakon, P. Fiedler, and A. Mitov, *Total Top-Quark Pair-Production Cross Section at Hadron Colliders Through $O(\alpha_S^4)$*, Phys. Rev. Lett. **110** (2013) 252004, arXiv:1303.6254 [hep-ph]. (Cited on pages 95, 148, and 151.)

[223] M. Czakon and A. Mitov, *Top++: A Program for the Calculation of the Top-Pair Cross-Section at Hadron Colliders*, Comput. Phys. Commun. **185** (2014) 2930, arXiv:1112.5675 [hep-ph]. (Cited on pages 95, 148, and 151.)

[224] B. Cooper, J. Katzy, M. L. Mangano, A. Messina, L. Mijovic, and P. Skands, *Importance of a consistent choice of alpha(s) in the matching of AlpGen and Pythia*, Eur. Phys. J. **C72** (2012) 2078, arXiv:1109.5295 [hep-ph]. (Cited on page 95.)

[225] P. Z. Skands, *Tuning Monte Carlo Generators: The Perugia Tunes*, Phys. Rev. **D82** (2010) 074018, arXiv:1005.3457 [hep-ph]. (Cited on pages 95 and 151.)

[226] B. P. Kersevan and E. Richter-Was, *The Monte Carlo event generator AcerMC versions 2.0 to 3.8 with interfaces to PYTHIA 6.4, HERWIG 6.5 and ARIADNE 4.1*, Comput. Phys. Commun. **184** (2013) 919–985, arXiv:hep-ph/0405247 [hep-ph]. (Cited on page 95.)

[227] N. Kidonakis, *Next-to-next-to-leading-order collinear and soft gluon corrections for t-channel single top quark production*, Phys. Rev. **D83** (2011) 091503, arXiv:1103.2792 [hep-ph]. (Cited on pages 95 and 151.)

[228] N. Kidonakis, *NNLL resummation for s-channel single top quark production*, Phys. Rev. **D81** (2010) 054028, arXiv:1001.5034 [hep-ph]. (Cited on page 95.)

[229] N. Kidonakis, *Two-loop soft anomalous dimensions for single top quark associated production with a W- or H-*, Phys. Rev. **D82** (2010) 054018, arXiv:1005.4451 [hep-ph]. (Cited on pages 95 and 151.)

[230] A. Lazopoulos, T. McElmurry, K. Melnikov, and F. Petriello, *Next-to-leading order QCD corrections to $t\bar{t}Z$ production at the LHC*, Phys. Lett. **B666** (2008) 62–65, arXiv:0804.2220 [hep-ph]. (Cited on pages 95 and 151.)

[231] M. V. Garzelli, A. Kardos, C. G. Papadopoulos, and Z. Trocsanyi, *$t\bar{t}\,W^{\pm}$ and $t\bar{t}\,Z$ Hadroproduction at NLO accuracy in QCD with Parton Shower and Hadronization effects*, JHEP **11** (2012) 056, arXiv:1208.2665 [hep-ph]. (Cited on page 95.)

[232] J. M. Campbell and R. K. Ellis, *$t\bar{t}W^{\pm}$ production and decay at NLO*, JHEP **07** (2012) 052, arXiv:1204.5678 [hep-ph]. (Cited on pages 95 and 151.)

[233] J. M. Campbell and R. K. Ellis, *An Update on vector boson pair production at hadron colliders*, Phys. Rev. **D60** (1999) 113006, arXiv:hep-ph/9905386 [hep-ph]. (Cited on pages 95, 148, and 151.)

[234] J. M. Campbell, R. K. Ellis, and C. Williams, *Vector boson pair production at the LHC*, JHEP **07** (2011) 018, arXiv:1105.0020 [hep-ph]. (Cited on pages 95, 148, and 151.)

[235] ATLAS Collaboration, *Measurements of top quark pair relative differential cross-sections with ATLAS in pp collisions at $\sqrt{s} = 7$ TeV*, Eur. Phys. J. **C73** no. 1, (2013) 2261, arXiv:1207.5644 [hep-ex]. (Cited on pages 94 and 150.)

[236] ATLAS Collaboration, *Measurements of normalized differential cross sections for $t\bar{t}$ production in pp collisions at $\sqrt{s} = 7$??TeV using the ATLAS detector*, Phys. Rev. **D90** no. 7, (2014) 072004, arXiv:1407.0371 [hep-ex]. (Cited on pages 94 and 150.)

[237] ATLAS Collaboration, *Further ATLAS tunes of PYTHIA6 and Pythia 8*, Tech. Rep. ATL-PHYS-PUB-2011-014, CERN, Geneva, Nov, 2011. (Cited on page 96.)

[238] ATLAS Collaboration, *Selection of jets produced in proton-proton collisions with the ATLAS detector using 2011 data*, Tech. Rep. ATLAS-CONF-2012-020, CERN, Geneva, Mar, 2012. https://cds.cern.ch/record/1430034. (Cited on page 100.)

[239] ATLAS Collaboration, *Search for squarks and gluinos with the ATLAS detector in final states with jets and missing transverse momentum and 20.3 fb^{-1} of $\sqrt{s} = 8$ TeV proton-proton collision data*, Tech. Rep. ATLAS-CONF-2013-047, CERN, Geneva, May, 2013. https://cds.cern.ch/record/1547563. (Cited on page 101.)

[240] ATLAS Collaboration, *Search for squarks and gluinos with the ATLAS detector in final states with jets and missing transverse momentum using 4.7 fb^{-1} of $\sqrt{s} = 7$ TeV proton-proton collision data*, Phys. Rev. **D87** no. 1, (2013) 012008, arXiv:1208.0949 [hep-ex]. (Cited on pages 117, 135, 136, 137, and 138.)

[241] ATLAS Collaboration, *Single hadron response measurement and calorimeter jet energy scale uncertainty with the ATLAS detector at the LHC*, Eur. Phys. J. **C73** no. 3, (2013) 2305, arXiv:1203.1302 [hep-ex]. (Cited on pages 123 and 168.)

[242] ATLAS Collaboration, *Search for squarks and gluinos in events with isolated leptons, jets and missing transverse momentum at $\sqrt{s} = 8$ TeV with the ATLAS detector*, JHEP **04** (2015) 116, arXiv:1501.03555 [hep-ex]. (Cited on page 142.)

[243] James Stirling Collaboration, *13/8TeVLHC luminosity ratios*. http://www.hep.ph.ic.ac.uk/~wstirlin/plots/lhclumi7813_2013_v1.pdf, 2016. (Cited on page 146.)

[244] J. Butterworth, E. Dobson, U. Klein, B. Mellado Garcia, T. Nunnemann, J. Qian, D. Rebuzzi, and R. Tanaka, *Single Boson and Diboson Production Cross Sections in pp Collisions at sqrts=7 TeV*, Tech. Rep. ATL-COM-PHYS-2010-695, CERN, Geneva, Aug, 2010. https://cds.cern.ch/record/1287902. (Cited on page 148.)

[245] M. Aliev, H. Lacker, U. Langenfeld, S. Moch, P. Uwer, and M. Wiedermann, *HATHOR: HAdronic Top and Heavy quarks crOss section calculatoR*, Comput. Phys. Commun. **182** (2011) 1034–1046, arXiv:1007.1327 [hep-ph]. (Cited on pages 148, 151, and 189.)

[246] P. Kant, O. M. Kind, T. Kintscher, T. Lohse, T. Martini, S. Mölbitz, P. Rieck, and P. Uwer, *HatHor for single top-quark production: Updated predictions and uncertainty estimates for single top-quark production in hadronic collisions*, Comput. Phys. Commun. **191** (2015) 74–89, arXiv:1406.4403 [hep-ph]. (Cited on pages 148 and 151.)

[247] J. Alwall et al., *The automated computation of tree-level and next-to-leading order differential cross sections, and their matching to parton shower simulations*, JHEP **2014** (2014) 158, arXiv:1405.0301 [hep-ph]. (Cited on pages 150 and 151.)

[248] R. D. Ball et al., *Parton distributions with LHC data*, Nucl. Phys. **B867** (2013) 244–289, arXiv:1207.1303 [hep-ph]. (Cited on pages 150, 151, and 152.)

[249] ATLAS Collaboration, *The ATLAS Simulation Infrastructure*, Eur. Phys. J. **C70** (2010) 823–874, arXiv:1005.4568 [physics.ins-det]. (Cited on page 150.)

[250] ATLAS Collaboration, *Monte Carlo Generators for the Production of a W or Z/γ^* Boson in Association with Jets at ATLAS in Run 2*, Tech. Rep. ATL-PHYS-PUB-2016-003, CERN, Geneva, Jan, 2016. https://cds.cern.ch/record/2120133. (Cited on page 150.)

[251] ATLAS Collaboration, *Simulation of top quark production for the ATLAS experiment at sqrt(s) = 13 TeV*, Tech. Rep. ATL-PHYS-PUB-2016-004, CERN, Geneva, Jan, 2016. https://cds.cern.ch/record/2120417. (Cited on pages 150 and 151.)

[252] ATLAS Collaboration, *Modelling of the $t\bar{t}H$ and $t\bar{t}V$ ($V = W, Z$) processes for $\sqrt{s} = 13$ TeV ATLAS analyses*, Tech. Rep. ATL-PHYS-PUB-2016-005, CERN, Geneva, Jan, 2016. https://cds.cern.ch/record/2120826. (Cited on pages 150 and 151.)

[253] ATLAS Collaboration, *Multi-Boson Simulation for 13 TeV ATLAS Analyses*, Tech. Rep. ATL-PHYS-PUB-2016-002, CERN, Geneva, Jan, 2016. https://cds.cern.ch/record/2119986. (Cited on pages 150 and 152.)

[254] K. Melnikov and F. Petriello, *Electroweak gauge boson production at hadron colliders through O(alpha(s)**2)*, Phys. Rev. D **74** (2006) 114017, arXiv:hep-ph/0609070. (Cited on pages 151 and 189.)

[255] R. Gavin, Y. Li, F. Petriello, and S. Quackenbush, *FEWZ 2.0: A code for hadronic Z production at next-to-next-to-leading order*, Comput. Phys. Commun. **182** (2011) 2388–2403, arXiv:1011.3540 [hep-ph]. (Cited on pages 151 and 189.)

[256] ATLAS Collaboration, *ATLAS Pythia 8 tunes to 7 TeV data*. ATL-PHYS-PUB-2014-021, 2014. http://cdsweb.cern.ch/record/1966419. (Cited on page 151.)

[257] ATLAS Collaboration, *ATLAS Run 1 Pythia8 tunes*, Tech. Rep. ATL-PHYS-PUB-2014-021, CERN, Geneva, Nov, 2014. https://cds.cern.ch/record/1966419. (Cited on page 151.)

[258] ATLAS Collaboration, *Selection of jets produced in 13TeV proton-proton collisions with the ATLAS detector*, Tech. Rep. ATLAS-CONF-2015-029, CERN, Geneva, Jul, 2015. https://cds.cern.ch/record/2037702. (Cited on page 155.)

[259] CMS Collaboration, *Search for supersymmetry in the multijet and missing transverse momentum final state in pp collisions at 13 TeV*, Phys. Lett. **B758** (2016) 152–180, arXiv:1602.06581 [hep-ex]. (Cited on page 181.)

[260] CMS Collaboration, *Search for new physics with the MT2 variable in all-jets final states produced in pp collisions at sqrt(s) = 13 TeV*, arXiv:1603.04053 [hep-ex]. (Cited on pages 181 and 182.)

[261] ATLAS Collaboration, *Expected sensitivity studies for gluino and squark searches using the early LHC 13 TeV Run-2 dataset with the ATLAS experiment*, Tech. Rep. ATL-PHYS-PUB-2015-005, CERN, Geneva, Mar, 2015. https://cds.cern.ch/record/2002608. (Cited on page 182.)

[262] L. Rossi and O. Brüning, *High Luminosity Large Hadron Collider A description for the European Strategy Preparatory Group*, Tech. Rep. CERN-ATS-2012-236, CERN, Geneva, Aug, 2012. https://cds.cern.ch/record/1471000. (Cited on page 185.)

[263] I. Bejar Alonso and L. Rossi, *HiLumi LHC Technical Design Report: Deliverable: D1.10*, Tech. Rep. CERN-ACC-2015-0140, CERN, Geneva, Nov, 2015. https://cds.cern.ch/record/2069130. (Cited on pages 185 and 186.)

[264] ATLAS and CMS Collaboration, *Expected pileup values at the HL-LHC*, Tech. Rep. ATL-UPGRADE-PUB-2013-014, CERN, Geneva, Sep, 2013. https://cds.cern.ch/record/1604492. (Cited on page 187.)

[265] ATLAS Collaboration, *Physics at a High-Luminosity LHC with ATLAS*, Tech. Rep. ATL-PHYS-PUB-2013-007, CERN, Geneva, Jul, 2013. http://cds.cern.ch/record/1564937. (Cited on page 187.)

[266] ATLAS Collaboration, *ATLAS Phase-II Upgrade Scoping Document*, Tech. Rep. CERN-LHCC-2015-020. LHCC-G-166, CERN, Geneva, Sep, 2015. http://cds.cern.ch/record/2055248. (Cited on page 187.)

[267] ATLAS Collaboration, *Projections for measurements of Higgs boson signal strengths and coupling parameters with the ATLAS detector at a HL-LHC*, Tech. Rep. ATL-PHYS-PUB-2014-016, CERN, Geneva, Oct, 2014. http://cds.cern.ch/record/1956710. (Cited on page 187.)

[268] ATLAS Collaboration, *Search for the Standard Model Higgs and Z Boson decays to $J/\psi\,\gamma$: HL-LHC projections*, Tech. Rep. ATL-PHYS-PUB-2015-043, CERN, Geneva, Sep, 2015. http://cds.cern.ch/record/2054550. (Cited on page 187.)

[269] ATLAS Collaboration, *Update of the prospects for the $H \to Z\gamma$ search at the High-Luminosity LHC*, Tech. Rep. ATL-PHYS-PUB-2014-006, CERN, Geneva, May, 2014. http://cds.cern.ch/record/1703276. (Cited on page 187.)

[270] ATLAS Collaboration, *Prospects for measuring Higgs pair production in the channel $H(\to \gamma\gamma)H(\to b\bar{b})$ using the ATLAS detector at the HL-LHC*, Tech. Rep. ATL-PHYS-PUB-2014-019, CERN, Geneva, Oct, 2014. http://cds.cern.ch/record/1956733. (Cited on page 187.)

[271] ATLAS Collaboration, *Higgs Pair Production in the $H(\to \tau\tau)H(\to b\bar{b})$ channel at the High-Luminosity LHC*, Tech. Rep. ATL-PHYS-PUB-2015-046, CERN, Geneva, Nov, 2015. http://cds.cern.ch/record/2065974. (Cited on page 187.)

[272] ATLAS Collaboration, *Studies of Vector Boson Scattering And Triboson Production with an Upgraded ATLAS Detector at a High-Luminosity LHC*, Tech. Rep. ATL-PHYS-PUB-2013-006, CERN, Geneva, Jun, 2013. http://cds.cern.ch/record/1558703. (Cited on page 187.)

[273] ATLAS Collaboration, *Letter of Intent for the Phase-I Upgrade of the ATLAS Experiment*, Tech. Rep. CERN-LHCC-2011-012. LHCC-I-020, CERN, Geneva, Nov, 2011. https://cds.cern.ch/record/1402470. (Cited on page 190.)

[274] ATLAS Collaboration, *Letter of Intent for the Phase-II Upgrade of the ATLAS Experiment*, Tech. Rep. CERN-LHCC-2012-022, LHCC-I-023, CERN, Geneva, Dec, 2012. https://cds.cern.ch/record/1502664. (Cited on page 190.)

[275] ATLAS Collaboration, *Performance assumptions for an upgraded ATLAS detector at a High-Luminosity LHC*, Tech. Rep. ATL-PHYS-PUB-2013-004, CERN, Geneva, Mar, 2013. http://cds.cern.ch/record/1527529. (Cited on pages 190, 191, 192, and 194.)

[276] ATLAS Collaboration, *Performance assumptions based on full simulation for an upgraded ATLAS detector at a High-Luminosity LHC*, Tech. Rep. ATL-PHYS-PUB-2013-009, CERN, Geneva, Sep, 2013. http://cds.cern.ch/record/1604420. (Cited on pages 190, 191, 192, and 193.)

[277] J. T. Linnemann, *Measures of Significance in HEP and Astrophysics*, arXiv:physics/0312059. (Cited on page 196.)

[278] ATLAS Collaboration, *Summary plots from the ATLAS Supersymmetry physics group*. https://atlas.web.cern.ch/Atlas/GROUPS/PHYSICS/CombinedSummaryPlots/SUSY/, 2016. (Cited on pages 205 and 208.)

[279] ATLAS Collaboration, *Summary of the ATLAS experiment's sensitivity to supersymmetry after LHC Run 1 - interpreted in the phenomenological MSSM*, JHEP **10** (2015) 134, arXiv:1508.06608 [hep-ex]. (Cited on pages 206 and 207.)

Summary

One of the ultimate theoretical goals in physics is to construct a theory that can describe everything through interactions of the four fundamental forces: electromagnetism, the weak force, the strong force, and gravity. The theory of particle physics, the Standard Model, gets close by describing three of the four fundamental forces, electromagnetism, the weak force, and the strong force, through interactions of elementary particles . The fourth fundamental force, gravity, is not included in the Standard Model.

The elementary particles can be divided into two groups: fermions and bosons. Among the fermions one can find six leptons such as the electron and the electron neutrino, and the six quarks where the two lightest are the building blocks of the protons and neutrons. There are five types of bosons: the scalar Higgs boson and the four types of force-carrying vector bosons. The Higgs boson is introduced by the Higgs mechanism which gives rise to the masses of the elementary particles. The four types of vector bosons are the neutral Z boson and the charged $W^{\pm}$ bosons of the weak force, the photon responsible for electromagnetic interactions, and the gluons tightening together the quarks through the strong force. The mediator of the gravitational force, the graviton, has not yet been observed and is not included in the Standard Model.

The Standard Model has overall been very successful and with the discovery of the Higgs boson by the ATLAS and CMS experiments in 2012, it passed a very important milestone. However, despite its great success in very accurately predicting many experimental outcomes, the Standard Model is not the theory of everything. One of the shortcomings of the Standard Model is that it does not include the fourth fundamental force, gravity. Furthermore, observations of distant galaxies and supernovae as well as the cosmic microwave background show that only $\sim 5\%$ of the Universe is made of the matter described by the Standard Model – the remaining 95% consists of Dark Matter and Dark Energy. Clearly, the Standard Model does not provide the full picture.

The basis of the Standard Model is a set of symmetries. A symmetry of a theory is a transformation that leaves the theory unchanged. The Standard Model is built on different kinds of symmetries: global symmetries, e. g. space-time symmetries, and local gauge symmetries through which the force-carrying vector bosons are introduced. It is possible to extend the symmetry group of the Standard Model with an entire new type of symmetry: supersymmetry which is a symmetry between fermions and bosons. Supersymmetry predicts a bosonic superpartner of each fermion and vice-versa. It thus doubles the number of particles. Many supersymmetric models predict a

particle that can act as a candidate for Dark Matter, the lightest supersymmetric particle ($\tilde{\chi}_1^0$) that only interacts through the weak force, and thereby providing a solution to one of the problems of the Standard Model. However, the supersymmetric partners of the Standard Model particles have not yet been observed, and supersymmetry can therefore not be an exact symmetry at our energy scale. Hence, it must be broken resulting in a higher mass of the supersymmetric particles and in a very large number of free parameters.

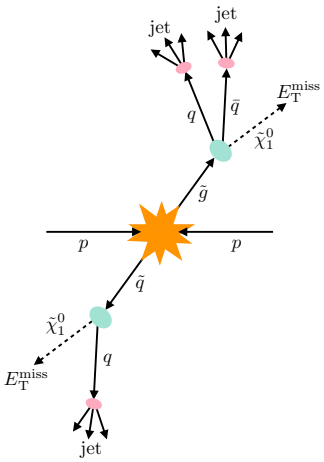

Fig. S.1 · Illustration of squark and gluino production in pp collisions with direct decays: $\tilde{q} \to q\tilde{\chi}_1^0$ and $\tilde{g} \to q\bar{q}\tilde{\chi}_1^0$.

In this thesis, searches for the supersymmetric partners of the quarks and gluons, the squarks ($\tilde{q}$) and gluinos ($\tilde{g}$), are presented. If squarks and gluinos are light, they have the highest probability among the supersymmetry particles to be produced in proton collisions because they carry colour charge and participate in the strong interaction - they, so to say, are the lowest hanging fruits on the tree. The squarks and gluinos are likely to be unstable and will decay. There are many possible decays depending on the values of the masses of the other supersymmetric particles, but all decays will contain quarks, a $\tilde{\chi}_1^0$, and possibly the decay products of bosons of the Standard Model. The simplest decay of squarks and gluinos are $\tilde{q} \to q\tilde{\chi}_1^0$ and $\tilde{g} \to q\bar{q}\tilde{\chi}_1^0$, respectively. The signature when searching for the production and decay of squarks and gluinos will therefore primarily be several jets originating from quarks and a measured imbalance in the transverse momentum, $E_{\mathrm{T}}^{\mathrm{miss}}$, caused by the escaping $\tilde{\chi}_1^0$. The topic of this thesis is the search for squarks and gluinos in events without any electrons or muons, but with many jets and $E_{\mathrm{T}}^{\mathrm{miss}}$. An illustration of squark and gluino production with direct decays into quarks and $\tilde{\chi}_1^0$ can be seen in Figure S.1.

If squarks and gluinos exist and are sufficiently light, they can be produced in very energetic proton-proton collisions. The largest man-built, proton accelerator and collider, the Large Hadron Collider (LHC), is located deep underground at the international particle physics laboratory CERN. It is designed to collide protons at an unprecedented centre-of-mass energy of $\sqrt{s} = 14$ TeV, and is an ideal collider to perform searches for supersymmetry. Four large experiments are located at four different points of the LHC to measure the results of the highly energetic proton collisions.

One of the four large experiments is the ATLAS detector. It has a cylinder shape and is 44 m long and 25 m tall and wide. The ATLAS detector consists of many different kinds of subdetector systems each with a specific task in identifying and measuring the energy and momentum of the particles originating from the proton collisions. The ATLAS detector is designed to study the

Standard Model and search for physics beyond the Standard Model in highly energetic proton collisions.

Operation of the LHC began in 2010 with proton collisions at a centre-of-mass energy of $\sqrt{s} = 7$ TeV. In 2012, the energy was increased to $\sqrt{s} = 8$ TeV. The end of 2012 marked the end of a very successful first run of the LHC, Run-1, with a dataset consisting of 20.3 fb^{-1} of proton-proton collisions. After a two year shutdown of the LHC where maintenance was performed, the second run of the LHC, Run-2, commenced and proton collisions were resumed in 2015 at an even higher energy of $\sqrt{s} = 13$ TeV. By the end of 2015, the ATLAS experiment had collected a dataset consisting of 3.2 fb^{-1} at $\sqrt{s} = 13$ TeV.

This thesis contains searches for squarks and gluinos in events without electrons or muons with the full Run-1 dataset and with the early Run-2 collected by the ATLAS experiment.

The two analyses at different energies are both selecting events with 2–6 jets and $E_{\mathrm{T}}^{\mathrm{miss}}$. The Standard Model background processes are therefore the same. There are several Standard Model processes that result in a final state identical to the one targeted in the analyses: W+jets, $Z(\rightarrow \nu\nu)$+jets, pair- and single-production of the heaviest quark, the top quark (t), diboson production, and multijet events produced by the strong interaction.

With the increase in the proton collision energy from $\sqrt{s} = 8$ TeV to $\sqrt{s} = 13$ TeV, the expected production cross section of squarks or gluinos increases by up to a factor of 1000 depending on their mass. The increase in the production cross sections of the Standard Model background processes range from 1.7 to 3.3 depending on the process. The sensitivity to squarks and gluinos does therefore increase significantly with the increase in energy, and even with the smaller dataset of 2015 new parts of the phase space of supersymmetry can be explored.

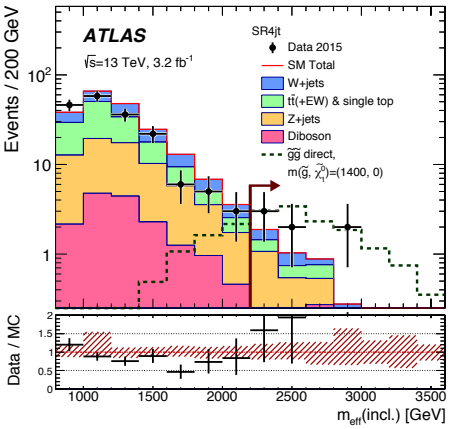

Fig. S.2 · Observed and expected m_{eff}(incl.) distributions of the Standard Model background (filled) overlaid with a supersymmetric model (dashed) of one signal region (4jt) at $\sqrt{s} = 13$ TeV.

The strategy of the two analyses is very similar: a set of signal regions is defined by a set of cuts on kinematical variables where one expects a significant amount of signal over background. As the masses of the supersymmetric particles are unknown, multiple signal regions are needed to target the different combinations of masses and decays. The effective mass, m_{eff}(incl.), which is the scalar sum of the p_{T} of the jets and $E_{\mathrm{T}}^{\mathrm{miss}}$ is a powerful variable at discriminating between supersymmetric particle production and the Standard Model backgrounds as shown in Figure S.2.

The number of observed events in a signal region is compared to the number of events expected from the Standard Model backgrounds. An excess of observed events over the expected background is measured in terms of the number of standard deviations, σ. An excess is said to be an "observation" if it deviates by more than 3σ and a "discovery" if it deviates more than 5σ from the estimated number of background events which are equivalent to a 0.1% and a 2.87×10^{-7} probability of obtaining such an excess from statistical fluctuations of the background. If no excesses are found, the results are interpreted as exclusion limits on supersymmetric models. In this summary, exclusion limits on very simple models where only squarks or gluinos are light enough to be produced and decay only directly into quarks and $\tilde{\chi}_1^0$ are presented. The limits are presented in a two-dimensional supersymmetric parameter space where the parameters typically are the mass of the squark or gluino and the mass of $\tilde{\chi}_1^0$. Different combinations of masses are analysed to see whether they are excluded or not, i. e. whether the number of events predicted by the supersymmetric model is too large to be covered by the uncertainty on the number of estimated background events.

As the existence of supersymmetry will show itself as an excess over the expected number of Standard Model background events in a signal region, it is very important to correctly estimate the number of expected events. The dominant backgrounds are therefore normalised in a set of dedicated control regions which are designed to enhance a specific background while being as kinematically close as possible yet mutually exclusive to the signal regions. Not only is it important to estimate the number of background events in the signal regions correctly, it is also very important to know the accuracy of that estimate as this will influence the significance of an excess. To properly take into account all sources of uncertainty and their correlations, a fit to data is performed simultaneously in all control regions. The background estimates are validated in dedicated validation regions that are orthogonal to both signal and control regions, i. e. there are no overlap between the regions.

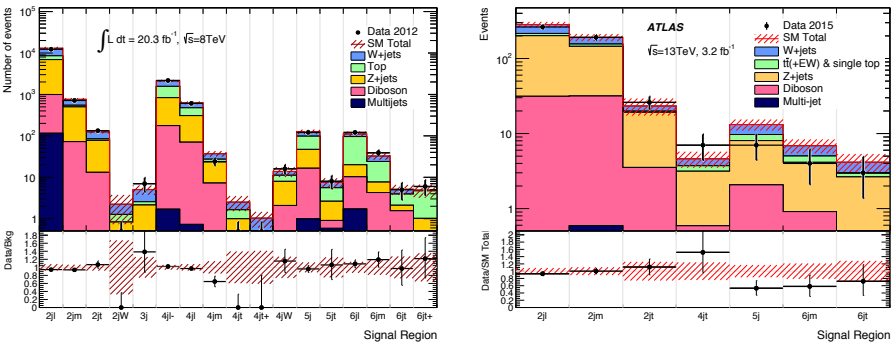

Fig. S.3 · A comparison of the observed number of events and the number of events expected from the Standard Model background in all signal regions at $\sqrt{s} = 8$ TeV and $\sqrt{s} = 13$ TeV.

In total 17 signal regions were defined at $\sqrt{s} = 8$ TeV and 7 at $\sqrt{s} = 13$ TeV. A comparison between the observed number of events and the number of events expected from the Standard Model background can be seen in Figure S.3. The largest excess seen in any of the signal regions was $\sim 1\sigma$ in the 4jt region at $\sqrt{s} = 13$ TeV shown in detail in Figure S.2. Alas, no significant excesses and thereby no hints of supersymmetry were seen in any of the signal regions neither at $\sqrt{s} = 8$ TeV nor at $\sqrt{s} = 13$ TeV. The results of the analyses are therefore presented as exclusion limits on supersymmetric models.

The result of the analyses is presented as limits on many supersymmetric models with squark and gluino production and various decays. As an example, the limits on supersymmetric models of squark-pair and gluino-pair production decaying directly to quarks and $\tilde{\chi}_1^0$ obtained with the full Run-1 dataset and the early Run-2 dataset are shown in Figure S.4. The grey area is excluded by the full Run-1 dataset while the area within the solid red line is excluded by the early Run-2 dataset. When the mass of the squark or gluino is larger than the mass of $\tilde{\chi}_1^0$, the $\tilde{\chi}_1^0$ is no longer the lightest supersymmetric particle and the direct decay is no longer possible. Any points above the diagonal $m_{\tilde{q},\tilde{g}} = m_{\tilde{\chi}_1^0}$ are therefore excluded. The limits on the mass of squarks and gluinos decaying directly to quarks and $\tilde{\chi}_1^0$ are 1030 GeV and 1510 GeV, respectively, when $\tilde{\chi}_1^0$ is massless.

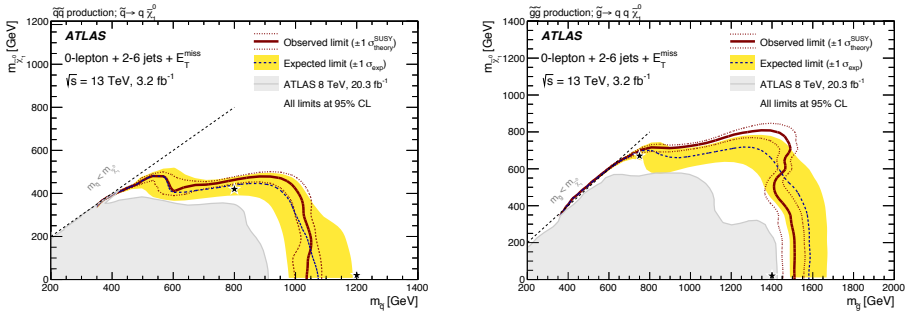

Fig. S.4 · Limits on squark-pair production with direct decay, $\tilde{q} \to q\tilde{\chi}_1^0$, and gluino-pair production with direct decay, $\tilde{g} \to q\bar{q}\tilde{\chi}_1^0$, at $\sqrt{s} = 8$ TeV (grey area) and at $\sqrt{s} = 13$ TeV (red line).

Despite the no-show of supersymmetric particles in the entire Run-1 and early Run-2 datasets, all hope of the existence of supersymmetry should not be abandoned. It could be that squarks and gluinos are not light enough to be seen in the data or they decay differently than assumed. The sensitivity to supersymmetry will increase with a larger dataset.

The LHC is scheduled to operate for many years to come. By 2023, the LHC is foreseen to have delivered an integrated luminosity of 300 fb^{-1} at a proton collision energy of $\sqrt{s} = 14$ TeV. From 2024 to 2026, the LHC will undergo a major upgrade to the High Luminosity-LHC (HL-LHC) which is expected to have delivered an integrated luminosity of 3000 fb^{-1} at $\sqrt{s} = 14$ TeV by 2036. The increase in the size of the dataset will naturally increase the sensitivity to searches for supersymmetry, as well.

As an upgrade of the LHC to the HL-LHC is a costly affair, it is interesting to quantify the expected sensitivity to squark and gluino-pair production with the full LHC and HL-LHC datasets corresponding to an integrated luminosity of 300 fb^{-1} and 3000 fb^{-1}, respectively. The sensitivity to two supersymmetric models, squark-pair production with direct decays and gluino-pair production with direct decays, are studied in events containing 2-6 jets, $E_{\mathrm{T}}^{\mathrm{miss}}$, and no electrons or muons, just like analyses performed with the full Run-1 and early Run-2 datasets described earlier. The studies are performed on simulations of the supersymmetric processes and the Standard Model backgrounds smeared with the expected performance of the ATLAS detector. The signal regions are designed based on the same strategy as the previous analyses to optimise the discovery reach in the two models, i. e. to have the best ratio of expected number of signal events to expected number of events coming from the Standard Model backgrounds.

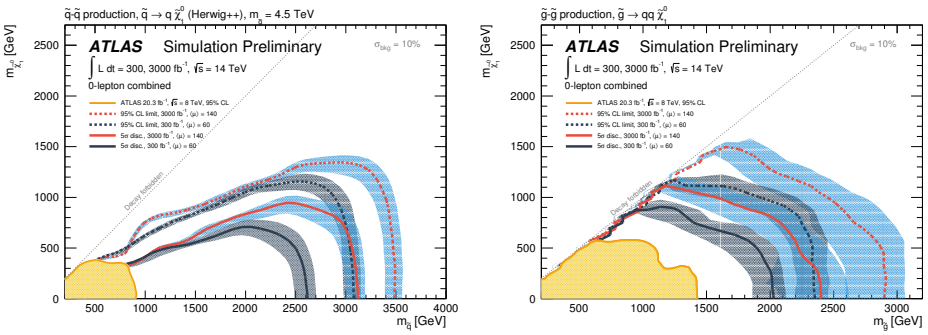

Fig. S.5 · The expected discovery (solid) and exclusion reach (dashed) at $\sqrt{s} = 14$ TeV with an integrated luminosity of 300 fb^{-1} (black) and 3000 fb^{-1} (red) and the observed limit at $\sqrt{s} = 8$ TeV (yellow) in a supersymmetric models with squark-pair production with direct decay and gluino-pair production with direct decay.

The expected discovery reach of the two supersymmetry models extend far beyond the limits placed with the full Run-1 dataset as can be seen in Figure S.5. In the squark-model the discovery reach is 2600 GeV with an integrated luminosity of 300 fb^{-1} and 3100 GeV with the full HL-LHC dataset of 3000 fb^{-1}. The discovery reach in the gluino-model is 2000 GeV and 2400 GeV with 300 fb^{-1} and 3000 fb^{-1}, respectively. If no excesses are seen, the limits will reach 3100 GeV and 3500 GeV in the squark-model and 2350 GeV and 2900 GeV in the gluino-model with the full LHC dataset of 300 fb^{-1} and the full HL-LHC dataset of 3000 fb^{-1}.

With the increasing size of the dataset provided by the LHC, the Standard Model is facing a tough test. Maybe it will pass it and come out with flying colours or maybe hints of new physics beyond the Standard Model, e. g. supersymmetry, will be seen. One thing is certain: many interesting years in particle physics lie ahead...

S

Samenvatting

Een van de uiteindelijke doelen van de theoretische natuurkunde is een theorie die alle interacties in de natuur met vier fundamentale krachten kan beschrijven: elektromagnetisme, de zwakke kernkracht, de sterke kernkracht en zwaartekracht. De huidige theorie in de deeltjesfysica, het Standaardmodel, komt daar dicht bij in de buurt: ze beschrijft drie van de vier fundamentele krachten (elektromagnetisme, de zwakke kernkracht en de sterke kernkracht) door middel van interacties tussen elementaire deeltjes. De laatste kracht, zwaartekracht, is geen onderdeel van het Standaardmodel.

De elementaire deeltjes van het Standaardmodel kunnen in twee groepen worden onderverdeeld: fermionen en bosonen. De fermionen bestaan uit zes leptonen, waaronder het elektron en het elektronneutrino, en zes quarks. De lichtste twee quarks zijn de bouwstenen van protonen en neutronen. Daarnaast zijn er vijf bosonen: het scalaire Higgsdeeltje en vier typen krachtdragende vectordeeltjes. Het Higgsdeeltje is een gevolg van het Higgsmechanisme, dat er voor zorgt dat elementaire deeltjes hun massa krijgen. De vier vectorbosonen zijn het neutrale Z-boson en de geladen $W^{\pm}$-bosonen, die de zwakke kernkracht beschrijven; het foton, dat elektromagnetische interacties beschrijft; en het gluon dat quarks door middel van de sterke kernkracht bij elkaar houdt. Een mogelijke mediator voor zwaartekracht, het graviton, is nog nooit waargenomen en is geen onderdeel van het Standaardmodel.

Het Standaardmodel is over het algemeen een zeer succesvolle theorie. De ontdekking van het Higgsboson door de ATLAS- en CMS-experimenten in 2012 was een belangrijke mijlpaal. Ondanks het grote succes van de nauwkeurige voorspellingen voor experimentele resultaten die de theorie doet is het Standaardmodel echter geen theorie van alles. Een van de tekortkomingen is dat de zwaartekracht niet beschreven wordt. Bovendien tonen observaties van vergelegen sterrenstelsels en supernova's en metingen van de kosmische achtergrondsttraling aan dat slechts 5% van het universum bestaat uit de materie beschreven door het Standaardmodel. De resterende 95% bestaat uit zogenaamde donkere materie en donkere energie. Het Standaardmodel is daarmee niet het complete antwoord.

Aan de basis van het Standaardmodel staan verschillende symmetrieën. Een symmetrie van een theorie is een transformatie die haar onveranderd laat. Het Standaardmodel is gebouwd op een aantal typen symmetrieën: globale symmetrieën, bijvoorbeeld ruimte-tijd symmetrieën, en lokale ijksymmetrieën die de vectorbosonen beschrijven. De combinatie van alle symmetrieën

van het Standaardmodel, de symmetriegroep, kan uitgebreid worden met een totaal nieuwe symmetrie: een tussen fermionen en bosonen, die supersymmetrie heet. Supersymmetrie voorspelt het bestaan van een bosonische superpartner voor elk fermion, en vice versa. Daarmee verdubbelt het het aantal bestaande deeltjes. Veel supersymmetrische modellen voorspellen het bestaan van een lichtste supersymmetrisch deeltje dat alleen via de zwakke kernkracht kan interageren, en daarmee het een kandidaat voor een donkere-materiedeeltje is. Daarmee lost het één van de tekortkomingen van het Standaardmodel op. Supersymmetrische deeltjes zijn echter nooit waargenomen: de nieuwe symmetrie kan dus niet exact bij de energieschaal van het Standaardmodel zijn, maar is een gebroken symmetrie. Als gevolg zijn de supersymmetrische deeltjes zwaarder dan hun partners in het Standaardmodel en heeft de theorie een zeer groot aantal vrije parameters.

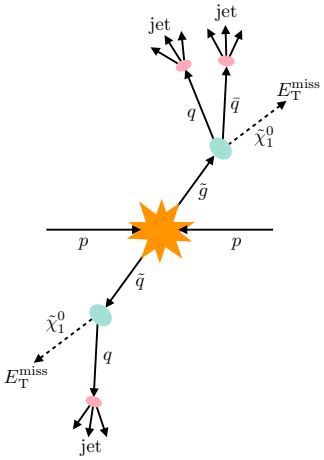

Fig. S.1 · Een illustratie van squark- en gluinoproductie in pp-botsingen met directe vervallen: $\tilde{q} \to q\tilde{\chi}_1^0$ en $\tilde{g} \to q\bar{q}\tilde{\chi}_1^0$.

In dit proefschrift wordt een zoektocht naar de supersymmetrische partners van quarks en gluonen, de squarks ($\tilde{q}$) en gluinos ($\tilde{g}$), gepresenteerd. Indien deze squarks en gluinos licht zijn, zijn ze van alle supersymmetrische deeltjes dankzij hun kleurlading en interactie via de sterke kernkracht het eenvoudigst te produceren in protonbotsingen. Ze zijn zogezegd het laaghangende fruit. Omdat zowel squarks en gluinos naar alle waarschijnlijkheid onstabiel zijn vervallen ze vrijwel direct na geproduceerd te zijn. Er zijn veel mogelijke vervalscenario's, die afhangen van de precieze massa's van supersymmetrische deeltjes, maar allemaal bevatten ze quarks, een neutralino $\tilde{\chi}_1^0$, en mogelijke vervalsproducten van andere geproduceerde Standaardmodeldeeltjes. De eenvoudigst denkbare vervallen zijn die waar squarks en gluino's direct naar quarks vervallen: $\tilde{q} \to q\tilde{\chi}_1^0$ en $\tilde{g} \to q\bar{q}\tilde{\chi}_1^0$. Om die vervallen te bestuderen worden botsingen gebruikt met meerdere jets, afkomstig van de quarks, en een grote onbalans in de tranversale impuls $E_{\mathrm{T}}^{\mathrm{miss}}$, afkomstig van het neutralino $\tilde{\chi}_1^0$ dat niet gedetecteerd kan worden. Het onderwerp van dit proefschrift is een zoektocht naar squarks en gluino's in events zonder elektronen of muonen, maar met meerdere jets en $E_{\mathrm{T}}^{\mathrm{miss}}$. Een voorbeeld van squark- en gluinoproductie met directe vervallen is weergeven in figuur S.1.

Wanneer squarks en gluino's bestaan en licht genoeg zijn kunnen ze geproduceerd worden in hoogenergetische proton-protonbotsingen. De grootste door mensen gebouwde protonversneller ter wereld, de Large Hadron Collider (LHC), ligt diep ondergrond bij het internationale deeltjesfysicalaboratorium CERN. De LHC is ontworpen op protonen op elkaar te botsen met een ongeëvenaarde massamiddelpuntsenergie van $\sqrt{s} = 14$ TeV en is daarmee een ideale omgeving

om te zoeken naar supersymmetrie. Op vier verschillende punten langs de LHC-ring staan grote experimenten om het resultaat van de hoogenergetische botsingen te meten.

Één van die vier grote experimenten is de ATLAS-detector. De detector is cylindervormig en ongeveer 44 m lang en 25 m hoog en breed. Hij bestaat uit veel verschillende typen subdetectoren, die elk een specifieke rol hebben: elk subsysteem wordt gebruikt om bepaalde typen deeltjes te meten en hun energie en impuls te kunnen bepalen. ATLAS is ontworpen om met hoogenergetische protonbotsingen het Standaardmodel nader te bestuderen en te zoeken naar het bestaan van het fysica voorbij het Standaardmodel.

In 2010 vonden de eerste botsingen bij de LHC plaats met een energie van $\sqrt{s} = 7$ TeV. Die energie werd in 2012 verhoogd tot $\sqrt{s} = 8$ TeV. Het einde van 2012 markeerde het einde van de eerste zeer succesvolle *run* van de LHC (Run-1), met een dataset van 20,3 fb^{-1} aan gemeten proton-protonbotsingen. Na een pauze van twee jaar waarin onderhoud aan de versneller werd gepleegd begon in 2015 Run-2 van de LHC, ditmaal met een nog hogere botsingsenergie van $\sqrt{s} = 13$ TeV. Ten tijde van eind 2015 had ATLAS een dataset van 3,2 fb^{-1} aan gemeten proton-protonbotsingen bij deze energie.

Dit proefschrift beschrijft zoektochten naar squarks en gluino's met events zonder elektronen of muonen gebruikmakende van de volledige Run-1-dataset en de eerste Run-2-data gemeten bij het ATLAS-experiment.

Hoewel beide analyses bij verschillende botsingsenergieën gedaan zijn maken beide gebruik van events met 2–6 jets en $E_{\mathrm{T}}^{\mathrm{miss}}$. De Standaardmodelachtergrondprocessen zijn daarom in elk van de analyses hetzelfde. Een aantal processen met Standaardmodeldeeltjes geven precies hetzelfde resultaat in de detector als de supersymmetrische deeltjes waarnaar gezocht is: productie van W+jets en van $Z(\rightarrow \nu\nu)$+jets, productie van enkele top-quarks (het zwaarste quark) en paarproductie van topquarks, dibosonproductie, en multijet events waar meedere jets door middel van de sterke kernkracht geproduceerd zijn.

Met de toename in de botsingsenergie van $\sqrt{s} = 8$ TeV naar $\sqrt{s} = 13$ TeV neemt de verwachte botsingsdoorsnede voor squark- en gluinoproductie, afhankelijk van de deeltjesmassa's, met een factor 10000 toe. De botsingsdoorsnede voor de achtergrondprocessen neemt echter met slechts een factor 1,7 tot 3,3 toe. De sensitiviteit om squarks en gluino's te kunnen meten neemt daarmee dus significant toe. Zelfs met de kleinere dataset gemeten in in 2015 kunnen dus nieuwe delen van de faseruimte van supersymmetrie worden verkend.

De analysestrategie is in beide analyses grotendeels hetzelfde. Een aantal signaalgebieden wordt gedefinieerd aan de hand van snedes op kinematische variabelen waar een grote hoeveelheid signaal ten opzichte van de achtergrond wordt verwacht. Omdat de massa's van supersymmetrische deeltjes onbekend zijn worden meerdere gebieden gebruikt, om zo verschillende scenario's en combinaties massa's te kunnen detecteren. De effectieve massa m_{eff}(incl.) is de scalaire som van de transversale jetimpulsen (p_{T}) en de ontbrekende transversale energie $E_{\mathrm{T}}^{\mathrm{miss}}$ en is een krachtige variabele om supersymmetrische deeltjes van de achtergronden te kunnen scheiden, zoals geïllustreerd in figuur S.2.

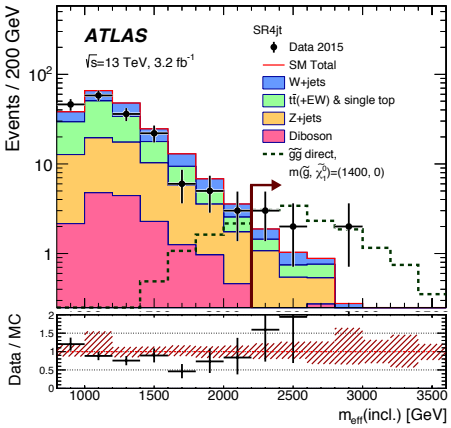

Fig. S.2 · Verwachtte en gemeten m_{eff}(incl.)-distributies van het Standaardmodel (gevuld) met daaroverheen een getekend het verwachtte signaal van een bepaald supersymmetrisch model (gestreept) in een specifiek signaalgebied (4jt) bij $\sqrt{s} = 13$ TeV.

Het aantal gemeten events in elk signaalgebied wordt vervolgens vergeleken met het verwachtte aantal van bekende Standaardmodelprocessen. Een mogelijk overschot aan events wordt daarna uitgedrukt in aantallen standaarddeviaties van een normaalverdeling, aangeduid met σ. Wanneer het overschot groter is dan 3σ wordt het een *observatie* genoemd. Een *ontdekking* vindt pas plaats bij een overschot groter dan 5σ. Dat correspondeert respectievelijk met een waarschijnlijkheid dat door middel van een statistische fluctuatie van het aantal verwachtte aantal events het overschot wordt gezien van 0,1% en $2{,}87 \times 10^{-7}$. Wanneer geen overschot wordt gevonden kunnen de resultaten geïnterpreteerd worden in verschillende supersymmetrische modellen en kunnen limieten op deze modellen gesteld worden.

In deze samenvatting worden limieten gepresenteerd op eenvoudige modellen, waar alleen squarks en gluinos licht genoeg zijn om te produceren bij de LHC en ze direct vervallen naar quarks en $\tilde{\chi}_1^0$. Deze limieten worden grafisch weergegeven als een lijn in de tweedimensionale supersymmetrische parameterruimte, waar de parameters typisch de massa van het squark danwel gluino en de massa van $\tilde{\chi}_1^0$ zijn. Van verschillende combinaties van massa's wordt getest of ze uitgesloten zijn of niet; dat wil zeggen, of het model zoveel events exta voorspeld dat een gebrek eraan, daarbij rekening houdend met systematische onzekerheden, betekent dat het uitgesloten is.

Omdat het bestaan van supersymmetrisch aangetoond wordt door middel van een overschot aan events in een signaalgebied is het belangrijk te weten hoeveel events verwacht worden door Standaardmodelprocessen. De belangrijkste achtergronden worden daarom genormaliseerd in een aantal daarvoor ontworpen controlegebieden. Elk controlegebied heeft snedes zodat het gedomineerd wordt door één bepaalde achtergrond en dicht bij het signaalgebied ligt, maar er niet mee overlapt. Het is echter niet alleen belangrijk om het aantal verwachtte achtergrondevents te weten: ook de onzekerheid op die verwachting is belangrijk, aangezien ze de significantie van een mogelijk overschot beïnvloed. Om alle onzekerheden en hun correlaties op een juiste manier te modelleren wordt in alle controlegebieden tegelijkertijd een statistische fit uitgevoerd om de normalisaties en hun onzekerheden te bepalen. De zo gevonden normalisaties worden in speciale validatiegebieden gevalideerd. Deze gebieden overlappen met de controle- noch signaalgebieden. Pas daarna wordt naar data in de signaalgebieden gekeken.

In totaal zijn 17 signaalgebieden voor $\sqrt{s} = 8$ TeV en 7 voor $\sqrt{s} = 13$ TeV gedefinieerd. Een vergelijking tussen het gemeten aantal events in het verwachtte aantal events van achter-

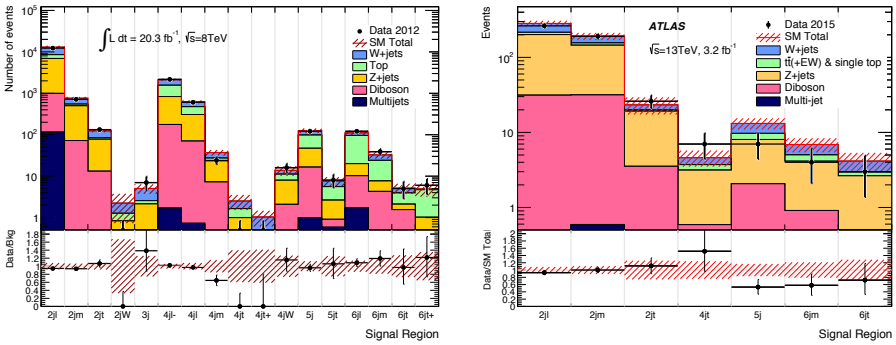

Fig. S.3 · Een vergelijking met het aantal gemeten events en het aantal verwachtte events van Standaardmodelprocessen in alle signaalgebieden voor data gemeten bij $\sqrt{s} = 8$ TeV en $\sqrt{s} = 13$ TeV.

grondprocessen is weergegeven in figuur S.3. Het grootste gemeten overschot in een van de signaalgebieden was $\sim 1\sigma$ in het $4jt$-gebied bij $\sqrt{s} = 13$ TeV. Dit gebied is in detail weergegeven in figuur S.2. Helaas zijn er derhalve geen significante overschotten gezien bij $\sqrt{s} = 8$ TeV noch bij $\sqrt{s} = 13$ TeV. De resultaten van beide analyses worden daarom weergegeven als limieten op supersymmetrische modellen.

Meerdere modellen worden gebruikt om de resultaten van de analyses te interpreteren. Een voorbeeld van een limiet op een dergelijk model is weergeven in figuur S.4, waarin de limieten op squark- en gluinoproductie met directe vervallen naar quarks en $\tilde{\chi}_1^0$ worden gepresenteerd. Zowel het resultaat voor de volledige Run-1-dataset als de eerste Run-2-data is weergegeven. Het grijze gebied is uitgesloten met de Run-1-dataset; de rode lijn geeft aan welk gebied uitgesloten is na de eerste Run-2-data. Omdat wanneer de massa van $\tilde{\chi}_1^0$ kleiner is dan die van het squark danwel gluino het verval niet meer mogelijk is zijn punten boven de diagonaal automatisch uitgesloten. In het geval van massaloze neutralino's zijn de limieten op de massa van het squark en het gluino respectivelijk 1030 GeV en 1510 GeV.

Ondanks het gebrek aan supersymmetrische deeltjes in de gebruikte datasets moet niet alle hoop op hun bestaan opgegeven worden. Wanneer squarks en gluino's te zwaar zijn om te produceren bij de gebruikte energieën of anders dan verwacht vervallen is het negatieve resultaat verklaarbaar. De sensitiviteit van de analyse zal vanzelf verbeteren met een grotere dataset.

Ook staat voor de LHC gepland dat er nog vele jaren botsingen zullen plaatsvinden. Rond 2023 wordt een totale geïntegreerde luminositeit van 300 fb^{-1} verwacht bij een botsingsenergie van $\sqrt{s} = 14$ TeV. Vervolgens zal tussen 2024 en 2026 een grote upgrade naar de High Luminosity-LHC (HL-LHC) plaatsvinden. Bij deze HL-LHC zal uiteindelijk een dataset van 3000 fb^{-1} gemeten worden, naar verwachting rond 2036. De grotere botsingsenergie en de veel grotere dataset zullen vanzelfsprekend ook de sensitiviteit van zoektochten naar supersymmetrie vergroten.

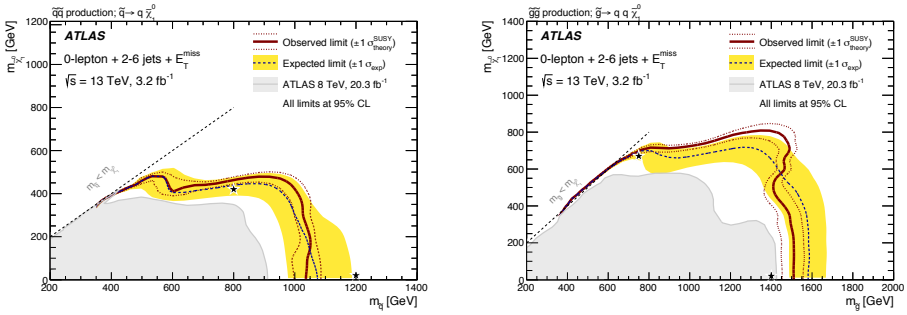

Fig. S.4 · Limieten op paarproductie van squarks die direct vervallen ($\tilde{q} \to q\tilde{\chi}_1^0$) en van gluinos die direct vervallen ($\tilde{g} \to q\bar{q}\tilde{\chi}_1^0$), bij zowel $\sqrt{s} = 8$ TeV (grijs gebied) als $\sqrt{s} = 13$ TeV (rode lijn).

Omdat de upgrade van de LHC naar de HL-LHC niet goedkoop is, is het interessant de verwachtte sensitiviteit van de analyse voor squark- en gluinoproductie met de volledige LHC- en HL-LHC-datasets van 300 fb^{-1} en 3000 fb^{-1} te bepalen. Daartoe is de sensitiviteit voor twee supersymmetrische modellen bestudeerd: squark- en gluino-paarproductie waar zowel squarks als gluinos direct vervallen. Er is gebruik gemaakt van events met 2–6 jets, $E_{\mathrm{T}}^{\mathrm{miss}}$ en geen elektronen of muonen, net als de eerder beschreven analyses in Run-1 en met de eerste Run-2-data. De studies zijn verricht op simulaties waar de verwachtte toekomstige meetonzekerheden van het ATLAS-experiment gebruikt zijn om het effect van de detector te simuleren. Voor beide modellen zijn signaalgebieden volgens dezelfde strategie als eerder gebruikt: dat wil zeggen dat gepoogd is het bereik van modellen dat ontdekt kan worden zo groot mogelijk te houden; de verhouding verwachtte signaalevents tegenover verwachtte achtergrondevents moet zo groot mogelijk zijn.

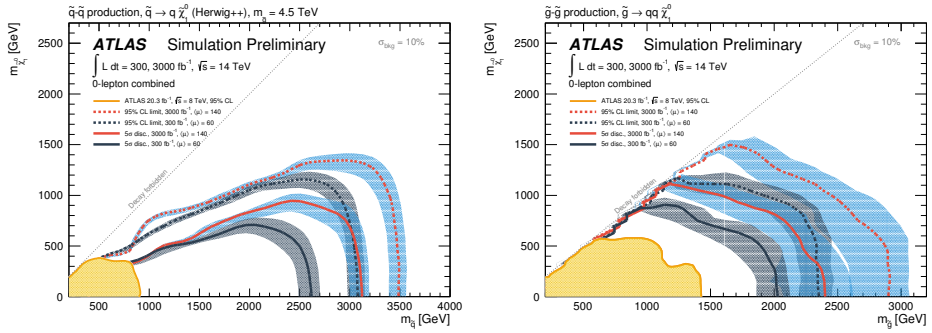

Fig. S.5 · Het verwachtte bereik voor ontdekkingen (dichte lijn) en limieten (gestreepte lijn) bij $\sqrt{s} = 14$ TeV voor een geïntegreerde luminositeit van 300 fb^{-1} (zwart) en 3000 fb^{-1} (rood) en de gemeten limiet bij $\sqrt{s} = 8$ TeV (geel) voor supersymmetrische modellen van squark- en gluino-paarproductie waar de squarks en gluino's direct vervallen.

Het verwachtte bereik van supersymmetrische modellen die ontdekt kunnen worden is weergegeven in figuur S.5 en ligt ver voorbij de tot dusver na Run-I uitgesloten modellen. Paargeproduceerde squarks kunnen ontdekt worden tot 2600 GeV met een geïntegreerde luminositeit van 300 fb^{-1} en tot 3100 GeV met de volledige HL-LHC-dataset van 3000 fb^{-1}. Voor gluino's liggen deze waarden bij 2000 GeV en 2400 GeV voor respectivelijk 300 fb^{-1} en 3000 fb^{-1}. Indien geen overschotten worden waargenomen kunnen limieten voor squarks tot 3100 GeV en 3500 GeV en voor gluino's tot 2350 GeV and 2900 GeV gesteld worden voor dezelfde luminositeiten.

Met de steeds groter wordende gemeten datasets bij de LHC komt het Standaardmodel voor hete vuren te staan. Wellicht slaagt het met vlag en wimpel voor alle tests, of wellicht worden hints van fysica voorbij het Standaardmodel, zoals supersymmetrie, gezien. Één ding zal in ieder geval zeker zijn: er liggen vele interessante jaren in de deeltjesfysica in het verschiet...

R

Resumé

Et af de ultimative mål i fysik er at konstruere en teori, der kan beskrive alting gennem vekselvirkningerne af de fire fundamentale naturkræfter: elektromagnetisme, den svage kernekraft, den stærke kernekraft og tyngdekraften. Teorien bag partikelfysik, standardmodellen, kommer tæt på målet ved gennem vekselvirkninger mellem elementarpartikler at beskrive tre af de fire fundamentale naturkræfter: elektromagnetisme, den svage kernekraft og den stærke kernekraft. Den fjerde fundamentale kraft, tyngdekraften, er ikke beskrevet af standardmodellen.

Elementarpartiklerne kan inddeles i to grupper: fermioner og bosoner. Blandt fermioner finder man de seks leptoner som for eksempel elektronen og elektronneutrinoen, og de seks kvarker af hvilke de to letteste er byggestene for protoner og neutroner. Der er fem typer bosoner: den skalare Higgs-boson og de fire forskellige kraftformidlende vektor-bosoner. Higgs-bosonen er introduceret gennem Higgs-mekanismen, som giver ophav til de massen af elementarpartikler. De fire typer kraftformidlende vektor-bosoner er den neutrale Z-boson og den ladede $W^{\pm}$-boson, der hører til den svage kernekraft, fotonen, der er ansvarlig for elektromagnetiske vekselvirkninger, og gluonerne, der holder kvarkerne sammen ved den stærke kernekraft. Formidleren af tyngdekraften, gravitonen, er endnu ikke observeret og er derfor ikke inkluderet i standardmodellen.

Standardmodellen har generelt været meget succesfuld og med opdagelsen af Higgs-bosonen af ATLAS- og CMS-eksperimenterne i 2012 passerede standardmodellen en vigtig milepæl. På trods af sin store succes med meget akkurat at forudsige udfaldet af mange eksperiment er standardmodellen ikke den endegyldige teori, der beskriver alting. En af standardmodellens mangler er at den fjerde fundamentalkraft, tyngdekraften, ikke er inkluderet. Endvidere viser observationer af fjerne galakser og supernovaer såvel som den kosmiske baggrundsstråling at kun $\sim$ 5% af universet består stof beskrevet standardmodellen – de resterende 95% består af mørkt stof og mørk energi. Standardmodellen giver tydeligvis ikke et fuldstændigt billede.

Standardmodellens base er et sæt af symmetrier. En symmetri i en teori er en transformation der efterlade teorien uforandret. Standardmodellen er bygget af forskellige slags symmetrier: globale symmetrier, som for eksempel rumtids-symmetrier, og lokale gauge-symmetrier gennem hvilke de kraftformidlende vektor-bosoner bliver introduceret. Det er muligt at udvide standardmodellens symmetrigruppe med en helt ny type symmetri: supersymmetri, der er en symmetri mellem fermioner og bosoner. Supersymmetri forudsiger en bosonisk superpartner for hver fermion og omvendt. Supersymmetri fordobler derved antallet af partikler. Mange supersymmetriske

modeller forudsiger en partikel, der kan fungere som en kandidat for mørkt stof: den letteste, supersymmetriske partikel ($\tilde{\chi}_1^0$), der kun vekselvirker gennem den svage kernekraft og derved løser et af standardmodellens problemer. De supersymmetriske partnere til standardmodel-partiklerne er dog ikke blevet observeret endnu, og supersymmetry kan derfor ikke være en eksakt symmetri ved vores energiniveau. Supersymmetri må derfor være brudt, hvilket fører til, at massen af de supersymmetriske partikler er højere og et meget stort antal frie paramtre.

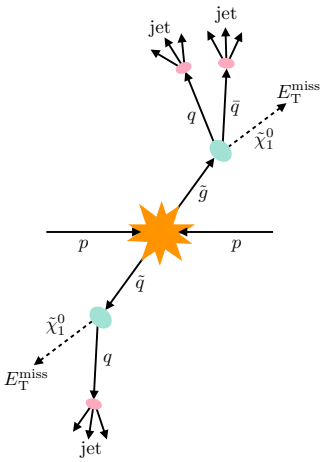

Fig. R.1 · Illustration af skvark- og gluinoproduktion i pp-kollisioner med direkte henfald: $\tilde{q} \to q\tilde{\chi}_1^0$ og $\tilde{g} \to q\bar{q}\tilde{\chi}_1^0$.

I denne afhandling er søgninger efter kvarkernes og gluonernes supersymmetriske partnere, skvarker ($\tilde{q}$) og gluinoer ($\tilde{g}$), præsenteret. Hvis skvarker og gluinoer er lette, har de den højeste sandsynlighed blandt de supersymmetriske partikler for at blive produceret i protonkollisioner fordi de er farveladede og deltager i den stærke vekselvirkning - man kan sige at de er de lavest hængende frugter. Skvarker og gluinoer vil sandsynligvis være ustabile og henfalde. Der er mange mulige henfald afhængigt af masserne af de andre supersymmetriske partikler, men alle henfald vil indeholde kvarker, en $\tilde{\chi}_1^0$, og muligvis henfaldsprodukter af standardmodel-bosoner. Det simpleste henfald af skvarker og gluinoer er henholdsvis $\tilde{q} \to q\tilde{\chi}_1^0$ og $\tilde{g} \to q\bar{q}\tilde{\chi}_1^0$. Kendetegnet, når man leder efter produktion of henfald af skvarker og gluinoer, vil derfor primært være flere jets, der stammer fra kvarker, og en målt ubalance i den tværgående impuls, $E_{\mathrm{T}}^{\mathrm{miss}}$, forårsaget af den undslupne $\tilde{\chi}_1^0$. Emnet for denne afhandling er en søgen efter skvarker og gluinoer i begivenheder uden nogen elektroner eller myoner, men med mange jets og $E_{\mathrm{T}}^{\mathrm{miss}}$. En illustration af skvark- og gluinoproduktion med direkte henfald til kvarker og $\tilde{\chi}_1^0$ kan ses i Figur R.1.

Hvis skvarker og gluinoer findes og er tilstrækkeligt lette, kan de produceres i meget energirige proton-proton-kollisioner. Den største menneskeskabte proton-accelerator og -collider, Large Hadron Collider (LHC), er placeret dybt under jorden ved det internationale partikelfysiklaboratorium CERN. Den er designet til at kollidere protoner ved en hidtil uset massemidtpunktsenergi på $\sqrt{s} = 14$ TeV og er en ideel collider til at foretage søgninger efter supersymmetri. Fire store eksperimenter er placeret ved fire forskellige stedet på LHC for at måle resultaterne af de meget energirige protonkollisioner.

Et af de fire store eksperimenter er ATLAS-detektoren. Den har form som en cylinder og er 44 m lang og 25 m høj og bred. ATLAS-detektoren består af mange forskellige slags underdetektorsystemer hver især med en bestemt opgave om at identificere og måle energi og impuls af

partiklerne der stammer fra protonkollisionerne. ATLAS-detektoren er designet til at studere standardmodellen og lede efter fysik udover standardmodellen i meget energirige protonkollisioner.

Driften af LHC påbegyndte i 2010 med protonkollisioner ved en massemidtpunktsenergi på $\sqrt{s} = 7$ TeV. I 2012 blev energien øget til $\sqrt{s} = 8$ TeV. Slutningen på 2012 markerede enden på et meget succesfuldt første omgang af LHC, Run-1, med et datasæt bestående af 20.3 fb^{-1} af proton-proton-kollisioner. Efter to års nedlukning af LHC hvor vedligeholdelse blev udført, påbegyndtes den anden omgang af LHC, Run-2, og protonkollisioner blev genoptaget i 2015 ved en endnu højere energi på $\sqrt{s} = 13$ TeV. Ved udgangen af 2015 havde ATLAS-eksperimentet samlet et datasæt bestående af 3.2 fb^{-1} ved $\sqrt{s} = 13$ TeV.

Den afhandling indeholder søgninger efter skvarker og gluinoer i begivenheder uden elektroner eller myoner med det fulde Run-1 datasæt og det tidlige Run-2 datasæt opsamlet af ATLAS-eksperimentet.

De to analyser udført ved forskellige energier udvælger begge begivenheder indeholdende 2-6 jets og $E_{\mathrm{T}}^{\mathrm{miss}}$. Standardmodelbaggrundsprocesserne er derfor de samme. Der er flere standardmodelprocesser, der resulterer i en sluttilstand identisk med den, analysen er målrettet efter: W+jets, $Z(\to \nu\nu)$+jets, par- og singleproduktion af den tungeste kvark, top-kvarken (t), dibosonproduktion, og multijet begivenheder produceret gennem den stærke vekselvirkning.

Med den øgede protonkollisionsenergi fra $\sqrt{s} = 8$ TeV til $\sqrt{s} = 13$ TeV forøges det forventede produktionstværsnit af kvarker og gluinoer med op til en faktor 1000 afhængigt af deres masse. Forøgelsen i produktionstværsnit af standardmodelbaggrundsprocesserne går fra 1.7 til 3.3 afhængigt af processes. Følsomheden over for kvarker og gluinoer bliver derfor forøget signifikant med forøgelsen i energi, og selv med det mindre datasæt fra 2015 kan nye dele af det supersymmetriske faserum blive udforsket.

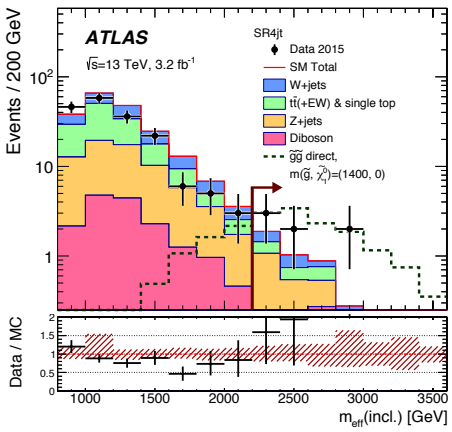

Fig. R.2 · Observeret og forventet m_{eff}(incl.)-fordeling af standardmodelbaggrunden (fyldt) overlagt med en supersymmetrisk model (stiplet) af en signalregion (4jt) ved $\sqrt{s} = 13$ TeV.

Strategien bag de to analyser er meget ens: et sæt af signalregioner defineres ved et sæt af snit i kinematiske variabler hvor man forventer en signifikant mængde af signal over baggrund. Da masserne af de supersymmetriske partikler er ukendte, er der behov for flere signal regioner til at målrette de forskellige kombinationer af masser og henfald. Den effektive mass, m_{eff}(incl.), som er den skalare sum af $E_{\mathrm{T}}^{\mathrm{miss}}$ og p_{T} af jets, er en kraftfuld variabel til at se forskel på produktion af supersymmetriske partikler og standardmodelbaggrundende som vist i Figur R.2.

Det observerede antal af begivenheder i en signalregion sammenlignes med antallet af begivender som forventes fra standardmodelbaggrundene. Et overskud af observerede begivenheder sammenlignet med den forventede baggrund måles i antallet af standardafvigelser, σ. Et overskud benævnes som "evidens" hvis det afviger med mere en 3σ og en "opdagelse" hvis det afviger med mere end 5σ fra det estimerede antal baggrundsbegivenheder svarende til en 0.1% og en 2.87×10^{-7} sandsynlighed for at opnå et lignende overskud fra en statistisk fluktuation af baggrunden. Hvis der ikke ses noget overskud, bliver resultaterne tolket som udelukkede afgræsninger i supersymmetriske modeller. De udelukkede afgrænsninger, der præsenteres i denne opsummering, er givet i meget simple modeller hvor kun skvarker eller gluinoer er tilstrækkeligt lette til at blive produceret og henfalder kun direkte til kvarker og $\tilde{\chi}_1^0$. Afgrænsningerne præsenteres i et todimensionelt, supersymmetrisk parameterrum, hvor parametrene typisk er massen af skvarken eller gluinoen og massen af $\tilde{\chi}_1^0$. Forskellige massekombinationer bliver analyseret for at undersøge om de er udelukkede eller ej, det vil sige om antallet af begivenheder forudsagt af den supersymmetriske model er for stort til at være dækket af usikkerheden på det estimerede antal baggrundsbegivenheder.

Da eksistensen af supersymmetri vil vise sig som et overskud af begivenheder i en signalregion sammenlignet med det forventede antal af begivenheder fra standardmodellenbaggrunden, er det meget vigtigt at estimere antallet af forventede begivenheder korrekt. Der dominerende baggrunde bliver derfor normaliseret i et set a dedikerede kontrolregioner, com er designed til at øge en bestemt baggrund og samtidig være så kinematisk tæt på, men dog gensidigt udelukkende til signalregionerne. Ikke alene er det vigtigt at estimere antallet af baggrundsbegivenheder i signalregionerne korrekt, det er også meget vigtigt at kende nøjagtigheden af estimatet da det vil påvirke signifikansen af et overskud af begivenheder. For korrekt at tage højde for alle usikkerhedskilderne og deres korrelationer, udføres et fit til data i alle kontrolregioner samtidigt. Baggrundsestimaterne valideres i dedikerede valideringsregioner, der er ortogonale til både signal- og kontrolregionerne, det vil sige at der intet overlap er mellem regionerne.

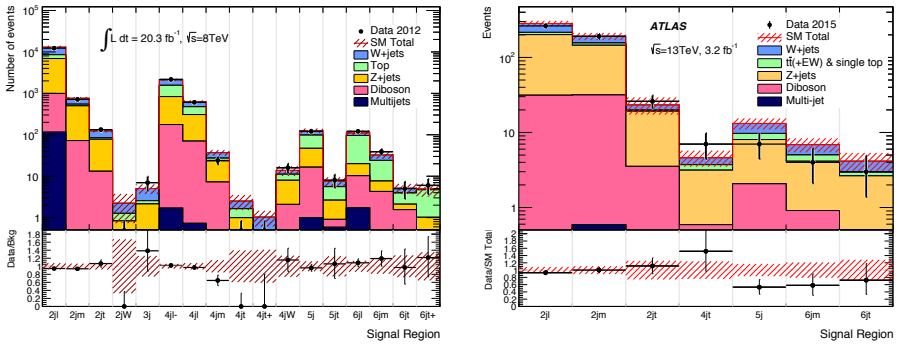

Fig. R.3 · En sammenligning mellem det observerede antal begivenheder og det forventede antal begivenheder fra standardmodelbaggrunden i alle signalregionerne ved $\sqrt{s} = 8$ TeV og $\sqrt{s} = 13$ TeV.

I det hele blev 17 signalregioner defineret ved $\sqrt{s} = 8$ TeV og 7 ved $\sqrt{s} = 13$ TeV. En sammenligning mellem det observerede antal begivenheder og antallet af begivenheder, som forventes fra standardmodelbaggrunden, kan ses i Figur R.3. Det største overskud af begivenheder set i nogen af signalregioner var $\sim 1\sigma$ i 4jt-regionen ved $\sqrt{s} = 13$ TeV, som er vist i større detalje i Figur R.2. Ak, ingen signifikante overskud i begivenheder og dermed ingen antydninger af supersymmetri blev siet i nogen af signalregionerne hverken ved $\sqrt{s} = 8$ TeV eller ved $\sqrt{s} = 13$ TeV. Resultaterne af analyserne bliver derfor præsenteret som udelukkede områder i supersymmetriske modeller.

Resultatet af analyserne er præsenteret som udelukkede områder i mange supersymmetriske modeller med skvark- og gluinoproduktion og forskellige henfald. Som et eksempel er de udelukkede områder i supersymmetriske modeller med produktion af skvark- og gluinopar, der henfalder direkte til kvarker og $\tilde{\chi}_1^0$, ved brug af det fulde Run-1 datasæt og det tidlige Run-2 datasæt vist i Figur R.4. Det grå område er udelukket af det fulde Run-1 datasæt, mens arealet indenfor den røde linje er udelukket af det tidlige Run-2 datasæt. Når massen af skvarken eller gluinoen bliver større end massen af $\tilde{\chi}_1^0$, er $\tilde{\chi}_1^0$ ikke længere den letteste supersymmetriske partikel, og det direkte henfald er ikke længere muligt. Ethvert punkt over diagonalen $m_{\tilde{q},\tilde{g}} = m_{\tilde{\chi}_1^0}$ er derfor udelukket. De udelukkede masser af skvarker og gluinoer, der henfalder direkte til kvarker og $\tilde{\chi}_1^0$, er henholdvis 1030 GeV og 1510 GeV, når $\tilde{\chi}_1^0$er masseløs.

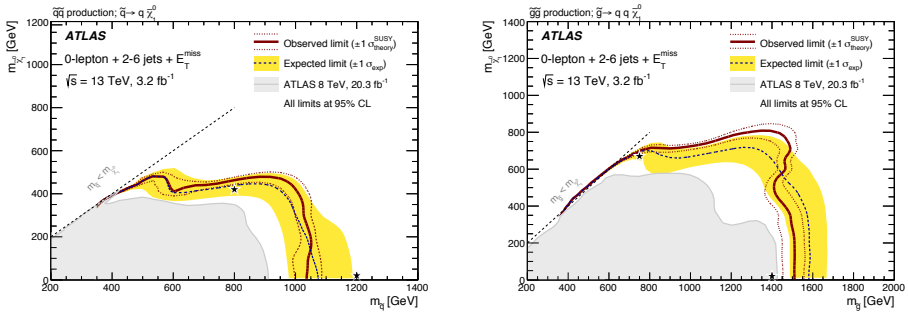

Fig. R.4 · Udelukkede områder i produktion af skvarkpar med direkte henfald, $\tilde{q} \to q\tilde{\chi}_1^0$, og produktion af gluinopar med direkte henfald, $\tilde{g} \to q\bar{q}\tilde{\chi}_1^0$, ved $\sqrt{s} = 8$ TeV (gråt område) og ved $\sqrt{s} = 13$ TeV (rød linje).

Påtrods af udeblivelsen af supersymmetriske partikler i hele datasættet fra Run-1 og det tidlige Run-2 datasæt, bør alt håb om eksistensen af supersymmetri ikke opgives. Det kunne være, at skvarker og gluinoer ikke er lette nok til at blive set i data eller deres henfald er anderleders end antaget. Følsomheden over for supersymmetri vil stige med et større datasæt.

Driften af LHC er planlagt i mange år fremover. I 2023, forventes LHC at have leveret en integreret luminositet på300 fb^{-1} ved en protonkollisionsenergi på $\sqrt{s} = 14$ TeV. Fra 2024 til 2026, vil LHC gennemgå en større opgradering til High Luminosity-LHC (HL-LHC) som forventes at have leveret en integreret luminositet på 3000 fb^{-1} ved $\sqrt{s} = 14$ TeV i 2036. Forøgelsen i størrelsen af datamængden vil naturligvis ligeleder forøge følsomheden i søgen efter supersymmetri.

Da en opgradering fra LHC til HL-LHC er en bekostelig affære, er det interesant at sætte tal på den forventede følsomhed over for produktion af skvark- og gluinopar med det fulde LHC- og HL-LHC-datasæt, som svarer til en integreret luminositet på henholdsvis 300 fb^{-1} og 3000 fb^{-1}. Følsomheden over for to supersymmetriske modeller, produktion af skvarkpar og gluinopar begge med direkte henfald, studeres i begivenheder med 2-6 jets, $E_{\mathrm{T}}^{\mathrm{miss}}$ og uden elektroner eller myoner meget lig analyserne udført med det fulde Run-1 og det tidlige Run-2 datasæt, som er beskrevet tidligere. Studierne er udført med simuleringer af de supersymmetriske processer og standardmodelbaggrundene udglattet med den forventede ydeevne af ATLAS-detektoren. Signalregionerne er designet efter samme strategi som i de tidligere analyser for at optimere opdagelsespotentialet i de to modeller, det vil sige for at have det bedste forhold mellem det forventede antal signalbegivenheder og det forventede antal begivenheder, der kommer fra standardmodelbaggrundene.

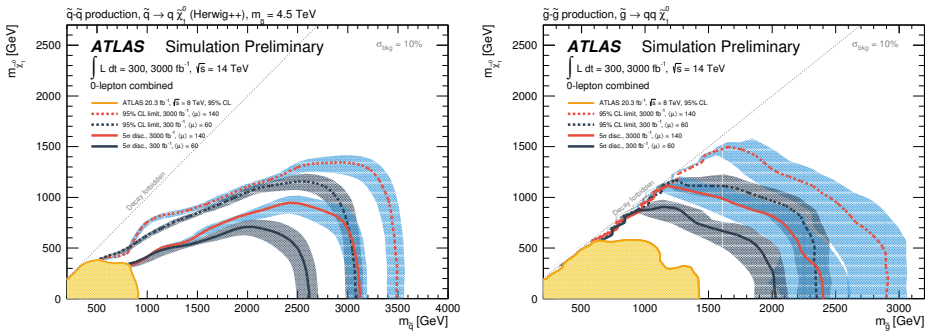

Fig. R.5 · Den forventede opdagelses- (fuld) og udelukkelsesrækkevidde (stiplet) ved $\sqrt{s} = 14$ TeV med en integreret luminositet på 300 fb^{-1} (sort) og 3000 fb^{-1} (rød), og den observerede grænse ved $\sqrt{s} = 8$ TeV (gul) i supersymmetrisk modeller med produktion af skvarkpar og gluinopar med direkte henfald.

Den forventede opdagelsesrækkevidde i de to supersymmetriske modeller rækker langt ud over grænserne der er sat med det fulde Run-1 datasæt, som det ses i Figur R.5. I skvarkmodellen, er opdagelsesrækkevidden 2600 GeV med en integreret luminositet på 300 fb^{-1} og 3100 GeV med det fulde HL-LHC-datasæt på 3000 fb^{-1}. Opdagelsesrækkevidden i gluinomodellen er 2000 GeV og 2400 GeV med henholdsvis 300 fb^{-1} og 3000 fb^{-1}. Hvis ingen overskud af begivenheder ses, vil de udelukkede område nå 3100 GeV og 3500 GeV i skvarkmodellen og 2350 GeV og 2900 GeV i gluinomodellen med det fulde LHC-datasæt på 300 fb^{-1} og det fulde HL-LHC-datasæt på 3000 fb^{-1}.

Med den øgede mængde data leveret af LHC, står standardmodellen overfor en hård prøve. Måske vil den bestå til ug med kryds og slange, eller måske vil antydninger er ny fysik udover standardmodellen, som for eksempel supersymmetry, vise sig. En ting er sikkert: Mange interessante år ligger forude for partikelfysik...

A

Acknowledgements

Four years and a bit has passed since I had my first working day at Nikhef. In some sense it feels just like yesterday, I had my first coffee in the Spectrum, and in another way it feels like a long time ago. One thing is certain: I have enjoyed my years as a PhD student at Nikhef and it would not have been half as enjoyable had it not been for the nice and welcoming atmosphere. Although ultimately writing a PhD thesis is a one-(wo)man job, it is important to have people in your corner to push you forward and cheer you up when things get tough. I would like to thank all the people who helped me and made my time at Nikhef and in the Netherlands such a great experience. It is hard to remember everybody, so please bear with me if I forget a few names - it is not intentionally.

First and foremost I would like to thank Paul, my promotor, for giving me the chance to do a PhD with the Nikhef ATLAS group and for introducing me to the search for supersymmetry without leptons. You have provided great guidance and always took your time to talk to me whenever I had any questions or doubts. Thank you for your help in the process of writing this thesis and all your useful comments.

Another person I owe a huge "thank you" is my supervisor, Marija. From the moment I joined the Nikhef o-lepton team you have been a source of help and advice. You started out as the postdoc in our group and I was extremely happy when you agreed to become my supervisor after you moved back to Serbia - it at least made me feel less bad asking all my questions. It is rare to find someone who gets as excited as me about new emoticons on Skype and who also uses the word "sorry" in every other sentence even if there is nothing to be sorry about.

I would also like to thank the members of my committee: Eric, Olya, Paul, Marcel, Ivo, Sascha, and David. Thank you for accepting the task of reading my thesis and for being part of my graduation. One thing I have learned while writing my thesis is that I do not keep it brief so my apologies for the length of the thesis.

I knew that I would like the ATLAS Nikhef group already when I visited for the interview for the PhD position. The atmosphere in the group is relaxed and creates an environment for discussions about everything and nothing. Thank you to the entire ATLAS group: Stan, Wouter, Pamela, Bob, Peter, Marcel, Gerjan, Ivo, Sascha, Nicolo, Frank, Hella, Olya, David, David, Magdalena, Dominik, Sara, Snezana, Jochen, Marcus, Sami, Peter, Tim, Broos, Matteo, Gabriele, Hartger, Remco, Daan, Marc, Ivan, Wouter, Angelantonio, Nikos, Antonia, Rogier, Rosemarie, Robin, John, and Ido.

Thank you all for creating such a great work atmosphere where there is always room for a Friday "borrel". The nice atmosphere at Nikhef is of course not only attributed to the ATLAS group - Roel, Serena, Chiara, Veerle, Pieter, Rose, Suvayu, Vasilis, Jeroen, Elena, Jacco, Rolf, Stergios, and Panos: thank you all for making my years in the Netherlands so enjoyable! A special thanks to my office mates who have joined for countless teas and talks through the past four years: Priscilla, Afroditi, Stefan, Jörn, Lydia, and Sarah.

It was clear from the beginning of my PhD that I was to join the Nikhef o-lepton team which at that time consisted of Robin, Marija, Geert-Jan, and Sascha and later Antonia joined as well. I would especially like to thank Geert-Jan for his help with HistFitter, LaTeX, and the dutch summary. I would also like to thank Geert-Jan for the collaboration on all the projects we ended up doing together often resulting in discussions on colour choices with the conveners.

As a foreigner in a new country it is important to build a network of friends. I found a basis for new friendships among my fellow PhD students and postdocs at Nikhef. Thank you Nika for your bubbly happiness, Pierfrancesco for your jokes, Pier-Olivier for macarons, cakes, port, and rally games, Koen for trips, Vince for wine and Black Books evenings, and Faab for the countless bingo nights.

My year in Geneva was spent in the office on physics (of course), in the mountains skiing, and biking around the lake. In Geneva, I had the great pleasure of living together with a girl that has taught me the wonders of pickling and sprouting. Thank you, Jane, for all the evenings spent trying out new recipes and being potatoes on the couch. I got my dose of danish from the idiots just around the corner who always provided hospitality for an evening with Dr. Phil, an all-danish fastelavns party with matching banana outfits, or simply a cup of coffee. Gorm, Chris og Maria: Tak for at være idioter! Også et tak til Sune for utallige kopper kaffe på dit kontor og frokoster i Ri.

To my paranymphs, Lydia and Anne Mette: Thank you for agreeing to stand up there with me during my defence. Lydia, thank you for always bringing the good (christmas) mood to the office. Your optimism and positive outlook on almost everything is admirable. Anne Mette, yndlingsdame ♡, tak for dine besøg og din heppen fra Danmark og - det har betydet meget! Jeg glæder mig til dameaftner i det kommende år.

Siim, even though you have not lived in Amsterdam in the last year you have still been a great support. You have always tried to get me to calm down and see the bigger picture whenever I got upset. You did not always succeed, but I am grateful that you tried every time. Thank you for always being on my side.

Sidst, men ikke mindst, vil jeg gerne sige en stor tak til mine venner og familie i Danmark. Tak til min familie og især til min mor og far for altid at støtte og hjælpe mig - det betyder alverden! Tak til jer alle sammen fordi I stadig er der på trods af at jeg ikke har været en del af jeres dagligdag i fire år. Jeg glæder mig til der igen skal spises lagkage til aftensmad, synges Jon og ABBA for fuld udblæsning, lolles rundt i København og drikkes mandagsøl.

Ingrid Deigaard
Amsterdam, October 2016